A Biophysical Approach to Understanding the Temperature-dependence of Enzyme Catalysis

Jones, Hannah

Award date:
2019

Awarding institution:
University of Bath

A Biophysical Approach to Understanding the Temperature-dependence of Enzyme Catalysis

Jones, Hannah

Award date:
2019

Awarding institution:
University of Bath

A Biophysical Approach to Understanding the Temperature-dependence of Enzyme Catalysis

Hannah Beatrice Louise Jones

A thesis submitted for the degree of Doctor of Philosophy

University of Bath

Department of Biology and Biochemistry

January 2019

Declaration of any previous submission of the work

The material presented here for examination for the award of a higher degree by research has / has not been incorporated into a submission for another degree

H B L Jones

H B L Jones

Acknowledgements

First and foremost, I would like to thank my supervisor Dr Christopher Pudney, who recognised I was able to undertake a PhD before I did, and who has always encouraged me to go further than I thought I could. His enthusiasm for science and his ability to patiently talk through this research even in the busiest times has both motivated and supported me over the last few years. My thanks also go to Prof. Vickery Arcus, for sharing his work with us, and whose enthusiasm for this research was felt from half-way across the world.

I would also like to thank Dr Marc van der Kamp, who bravely agreed to supervise and collaborate with me in computational chemistry, an area in which I had no experience. He has always been patient and willing to get involved with projects, that have benefited greatly from his expertise. For similar reasons I acknowledge and thank Rory Crean, who I have collaborated with for the majority of my PhD, and who I have learnt a lot from.

To all of the lab members of what was labs 1.33 and 1.28, specifically Dragana Catici and Rory Crean, I would like to thank for the camaraderie over the years, and all of the support I've received both in research and more generally. I was always made to feel welcome.

I would also like to acknowledge my family and friends. Especially my parents, who would have supported me unwaveringly in whatever it was I decided to do in life and who have made me feel like anything is possible. Finally, I would like to thank Sam, for everything.

Contents

Abbreviations and symbols

$\Delta G^{\ddagger}_{\mathrm{cat}}$ - activation energy of catalysis

$\Delta G^{\ddagger}_{\mathrm{inact}}$ - thermal inactivation of catalysis

[A][B] - concentration of the reactants

[E_0] - total enzyme concentration

[$X^{\ddagger}$] - concentration of reactants at the transition state

$\langle(\delta H)^2\rangle$ - the mean squared distribution of enthalpies

° - unfolding

‡ - over the reaction coordinate

A - amplitude

A - pre-exponential factor

BMMY - buffered methanol-complex medium

BZA - benzylamine

C_p - heat capacity

CSM - centre of spectral mass

Cα - alpha carbon

Cβ - beta carbon

D_1 - D-glucose (1-D)

D_1 - D-xylose (1-D)

D_{12} - D-glucose (1,2,3,4,5,6,6-D7) + D_2O

D_2O - deuterium oxide

D_5 - D-glucose + D_2O

D_7 - D-glucose (1,2,3,4,5,6,6-D7)

DFT - density functional theory

DHFR - dihydrofolate reductase

E - enzyme

E_a - activation energy

Ecuts - energy cut offs

EPR - electron paramagnetic resonance

ESI-Q TOF - electrospray ionization quadrupole time-of-flight

FAD - flavin adenine dinucleotide

FEL - free energy landscape

FIRST - floppy inclusions and rigid substructure topography

G - Gibbs free energy

GDH - glucose dehydrogenase

H - enthalpy

h - Planck's constant

HEPES - 4-(2-hydroxyethyl)-1-piperazineethanesulfonic acid

HLADH - horse liver alcohol dehydrogenase

k - rate constant

$K^{\ddagger}$ - equilibrium of reactants at the transition state

k_B - Boltzmann's constant

k_{cat} - catalytic constant

K_{eq} - reversible inactivation of the enzyme

KIE - kinetic isotope effect

k_{inact} - enzymes thermal inactivation rate constant

KSI - Ketosteroid isomerase

KYN - kynuramine dihydrobromide

MalL - Oligo-1,6-glucosidase 1

MAO - monoamine oxidase

MD - molecular dynamics

MM - minimal methanol

MM - molecular mechanics

MMRT - macromolecular rate theory

N - Avogadro's constant

$NAD(P)^+$ - nicotinamide adenine dinucleotide (phosphate)

NMR - nuclear magnetic resonance

NPT - number of atoms, volume, energy, temperature and pressure isolated – isothermal-isobaric ensemble

NVE - number of atoms, volume and energy isolated – microcanonical ensemble

NVT – number of atoms, volume, energy and temperature isolated – canonical ensemble

P - product

p/T - pressure-temperature

PCA - principle component analysis

PES - potential energy surface

PME - particle-mesh Ewald

pNP - 4-nitrophenol

pNPG - 4-nitrophenyl β-D-glucopyranoside

POPC - palmitoyloleoylphosphatidylcholine

POPE - palmitoyloleoyl-phosphatidylethanolamine

POR - protochlorophyllide oxidoreductase

QMT - quantum mechanical tunnelling

R - curvature

R - gas constant

RCD - rigid cluster decomposition

RCs - rigid clusters

REES - red edge excitation shift

RMSD - root-mean-square deviation

RMSF - root-mean-square fluctuation

ROS - reactive oxygen species

S - entropy

S - substrate

SET - single electron transfer

SKIE - solvent kinetic isotope effect

SMA - styrene maleic acid co-polymer

T - temperature

t - time

T_0 - reference temperature

T_{eq} - temperature at which E_{act} and E_{inact} are in equal concentration

T_{opt} - Optimum temperature

Trp - tryptophan

TST – transition state theory

V - volume

V_{max} - catalytic maximum velocity

WT - wild-type

ZPE - zero point energy

α - expansivity

β – compressibility

Δ - change

ΔH_{eq} - change in enthalpy upon the enzyme becoming inactive

ΔS_{eq} - change in entropy upon the enzyme becoming inactive

ρ - density

Equations list

1. $v_0 = \frac{V_{\max}[\mathrm{S}]}{K_\mathrm{m}}$
2. $k = Ae^{-\frac{E_a}{RT}}$
3. $[X^{\ddagger}] = K^{\ddagger}[A][B]$
4. $\Delta G^{\ddagger} = RTlnK^{\ddagger}$
5. $\Delta G^{\ddagger} = \Delta H^{\ddagger} - T\Delta S^{\ddagger}$
6. $[X^{\ddagger}] = [A][B]e^{\Delta S^{\ddagger}/R}e^{-\Delta H^{\ddagger}/RT}$
7. $k = \frac{RT}{Nh}e^{\Delta S^{\ddagger}/R}e^{-\Delta H^{\ddagger}/RT}$
8. $\Delta H^0 = \Delta H_R^0 + \Delta C_p(T - T_R)$
9. $\Delta S^0 = \Delta S_R^0 + \Delta C_p ln\, T/T_R$
10. $k_{obs} = \frac{A\, exp\left(\frac{-E_a}{RT}\right)}{1+\exp\left(\frac{\Delta S^0}{R} - \frac{\Delta H^0}{RT}\right)}$
11. $k_{obs} = A_2 e^{-\left(\frac{E_2}{RT}\right)} - A_D e^{-\left(\frac{E_D}{RT}\right)}$
12. $V_{\max} = \frac{k_\mathrm{B}T}{h} \cdot e^{-\left(\frac{\Delta G_{\mathrm{cat}}^{\ddagger}}{RT}\right)} \cdot [\mathrm{E}_0]e^{-\frac{k_B T}{h}\cdot e^{-\left(\frac{\Delta G_{\mathrm{inact}}^{\ddagger}}{RT}\right)}\cdot \mathrm{t}}$
13. $\mathrm{E_{act}} \overset{K_{\mathrm{eq}}}{\rightleftharpoons} \mathrm{E_{inact}} \overset{k_{\mathrm{inact}}}{\rightarrow} \mathrm{E_{denat}}$
14. $\ln\left(K_{\mathrm{eq}}\right) = \frac{\Delta H_{\mathrm{eq}}}{R}\left(\frac{1}{T_{\mathrm{eq}}} - \frac{1}{T}\right)$
15. $T_{\mathrm{eq}} = \frac{\Delta H_{\mathrm{eq}}}{\Delta S_{\mathrm{eq}}}$
16. $k' = \frac{k_1}{1+\exp\left(-\frac{\Delta G}{RT}\right)} + \frac{k_2}{1+\exp\left(-\frac{\Delta G}{RT}\right)}$
17. $\Delta H^{\ddagger} = \Delta H_{T_R}^{\ddagger} + \Delta C_p^{\ddagger}(T - T_R)$
18. $\Delta S^{\ddagger} = \Delta S_{T_R}^{\ddagger} + \Delta C_p^{\ddagger} ln\, T/T_R$
19. $lnk = ln\frac{k_B T}{h} - \left[\frac{\Delta H_{T_R}^{\ddagger} + \Delta C_P^{\ddagger}(T - T_R)}{RT}\right] + \left[\frac{\Delta S_{T_R}^{\ddagger} + \Delta C_P^{\ddagger}(lnT - lnT_R)}{R}\right]$
20. $T_{opt} = \frac{\Delta H_{T_0}^{\ddagger} - \Delta C_p^{\ddagger} T_0}{-\Delta C_p^{\ddagger} - R}$
21. $\Delta C_p^{\ddagger} = \frac{\Delta\langle \partial H^2\rangle^{\ddagger}}{k_B T^2}$
22. $-\left(\frac{\partial \Delta V^{\ddagger}}{\partial T}\right)_P = -\left(\frac{\partial \Delta S^{\ddagger}}{\partial P}\right)_T$
23. $\Delta V^{\ddagger} - T\left(\frac{\partial \Delta V^{\ddagger}}{\partial T}\right)_P = \left(\frac{\partial \Delta H^{\ddagger}}{\partial P}\right)_T$
24. $\Delta G_{P,T} = \Delta V_0(P - P_0) + \Delta\alpha'(P - P_0)(T - T_0) + \frac{\Delta\beta'}{2}(P - P_0)^2 + \Delta G_0 - \Delta S_0(T - T_0) - \Delta C_P\left[T\left(ln\left(\frac{T}{T_0}\right) - 1\right) + T_0\right]$
25. $\Delta\alpha = \left(\frac{1}{\Delta V}\frac{\delta \Delta V}{\delta T}\right)_P,\ \Delta\beta = -\left(\frac{1}{\Delta V}\frac{\delta \Delta V}{\delta P}\right)_T$

26. $\Delta G_{P,T} = \Delta G_{P_0,T_0} + \Delta V_{T_0}\left[exp[\Delta\alpha(T - T_0)]\right](P - P_0) - \frac{\Delta V_{P_0}}{\Delta\beta}\left[1 - exp[-\Delta\beta(P - P_0)]\right]$
27. $\Delta G_{P,T} = \Delta G_{P_0,T_0} + \Delta V_{T_0}\Delta\alpha(T - T_0)(P - P_0) + \frac{\Delta V_{P_0}\Delta\beta}{2}(P - P_0)^2$
28. $lnk = lnA - \frac{\Delta H^{\ddagger}_{T_0}}{RT} + \frac{\Delta C^{\ddagger}_P}{R}\left[ln\left(\frac{T}{T_0}\right) - 1 + T_0/T\right] - \frac{\Delta V^{\ddagger}_{T_0}}{RT}(exp[\Delta\alpha^{\ddagger}(T - T_0)])(P - P_0) + \frac{\Delta V^{\ddagger}_{P_0}}{\Delta\beta^{\ddagger}RT}\left[1 - exp[-\Delta\beta^{\ddagger}(P - P_0)]\right]$
29. $\left(\frac{dC_P}{dP}\right)_T = -T\left(\frac{d^2V}{dT^2}\right)_P = -T\left(\frac{d\alpha V}{dT}\right)_P = -TV\left[\alpha^2 + \left(\frac{d\alpha}{dT}\right)_P\right]$
30. $-T\left(\frac{d\Delta\alpha^{\ddagger}}{dT}\right)_P \Delta V^{\ddagger}_{P_0} \sim 1.3 \times 10^{-5}\, J.mol^{-1}.K^{-1}.Pa^{-1}$
31. $CSM = CSM_0 + Ae^{R\Delta\lambda_{Ex}}$
32. $k_{obs} = \frac{k_B T}{h}\left(\frac{1+\sigma}{\eta+\sigma}\right) exp\left(\frac{\Delta S^{\ddagger}}{R}\right) exp\left(\frac{-\Delta H^{\ddagger}}{RT}\right)$
33. $CSM = \frac{\sum(f_i x\, \lambda_{Em})}{\sum(f_i)}$
34. $k = (k_B T/h)e^{\Delta S^{\ddagger}/R}e^{-\Delta H^{\ddagger}/RT}$

List of Figures

List of Tables

List of Schemes

Abstract

The concept of the heat capacity of an enzyme changing over its reaction coordinate ($\Delta C_p^{\ddagger}$) had not been considered before 2013. However, the large size and associated dynamics of macromolecules such as enzymes, lends them to a large heat capacity, a property that could change significantly during enzyme turnover. The macromolecular rate theory (MMRT)[1] proposed that the temperature-dependence of changes in enthalpy and entropy associated with enzyme turnover, occurring as a result of a change in heat capacity, can lead to curvature in the temperature-dependence of enzymatic rates. Notionally, the main contribution to $\Delta C_p^{\ddagger}$ is altered vibrational motion. The work presented in this thesis aimed to validate the MMRT, and to investigate the utilization of $\Delta C_p^{\ddagger}$ as a probe of enzyme dynamics linked to catalysis. This was achieved by perturbing the vibrational motion of two different enzyme systems, using high-pressure, viscosity and kinetic isotope effects, and monitoring the subsequent effect of this on the value of $\Delta C_p^{\ddagger}$. The results demonstrate that the value of $\Delta C_p^{\ddagger}$ is sensitive to perturbations in enzyme dynamics, simultaneously validating the MMRT, and the importance of dynamical contributions to catalysis. The approach is also applied to a medically relevant enzyme, with values of $\Delta C_p^{\ddagger}$ revealing that the catalysis of this system is sensitive to its membrane environment. This directed further analysis of the influence of the membrane environment on its turnover. Consequently, molecular dynamic simulations were used to identify previously unknown substrate entrances, and thus new drug targets, for the enzyme. The necessity to acknowledge the effect of $\Delta C_p^{\ddagger}$ when investigating the temperature-dependence of enzymatic rates, is therefore highlighted by this work. Ultimately, it will aid in future work to engineer the optimum temperature, and rate at the optimum temperature, of enzymes. This will be valuable in both medical and industrial enzyme applications.

Chapter 1:
Introduction and Background

Harnessing the catalytic abilities of enzymes for applications in medicine and industry[2–4] is a widespread and invaluable practice. The study of enzymology for these applications is often focused on gaining mechanistic insight into specific enzymes. Research focuses on establishing druggable targets,[3,4] altering the reactant catalysed,[5] or stabilising enzymes[6] for which the applications are of value. Whilst there are previous cases where these research aims have proven successful, the methodology often involves large screening studies, such as inhibitor screening[7] or directed evolution[8], which take time and resource. Rational engineering of enzymes has a mixed success rate[6,9], and arguably the progression of applied enzymology is held back by our lack of fundamental understanding on how enzymes act as catalysts.

In addition to these current applications an unrealised goal of enzymology is the ability to accurately tune the optimum temperature (T_{opt}) and rate of turnover at T_{opt}. The relationship between rate and temperature has been quantified since 1889 by the Arrhenius equation,[10] and progressed in 1934 by the Eyring equation.[11] Whilst these equations give some insight into the thermodynamics behind the reaction of study, they fail to address the decrease in rate commonly seen after the T_{opt} of enzymatic reactions. Arguably, this lack of understanding regarding the temperature-dependence of enzymatic reactions is preventing the engineering of the T_{opt} and rate of enzymes. Thus, an insight into this relationship would be extremely valuable.

1.1 Enzyme kinetics

To investigate the temperature dependence of enzyme reactions, enzyme kinetics are monitored via colourimetric assays throughout this work. Numerous variables can influence the rate of an enzyme reaction, such as temperature, substrate concentration, and pH. Here, the relationship between rate and temperature is the variable of interest, with the rate of an enzyme roughly doubling every 10 K due to an increase in energy.[12] To ensure that the availability of substrate is not limiting the rate of reaction studied, Michaelis-Menten kinetics are measured throughout this work. Michaelis-Menten kinetics describe the relationship between enzyme rate and substrate concentration, which increases up until a saturating point, according to the Michaelis-Menten equation (Eq 1).

$$v_0 = \frac{V_{\max}[\mathrm{S}]}{K_{\mathrm{m}}} \qquad \text{(Eq1)}$$

Where v_0 is the initial velocity of a reaction, V_{max} is maximal velocity of the enzyme at a specific concentration, [S] is the substrate concentration, and K_m is the Michaelis constant

(the substrate concentration at which V_{max} is half).[12] To ensure substrate concentration is not limiting the rate of the reactions monitored, the substrate concentration is always kept to a minimum of 10 x the K_m. Other variables such as pH are kept constant, unless otherwise stated.

1.2 The Arrhenius equation

The Arrhenius equation (Eq 2) relates the rate of a reaction to the temperature of the reaction, allowing for the pre-exponential factor (A) and the activation energy (E_a) to be determined.

$$k = Ae^{-\frac{E_a}{RT}} \quad \text{(Eq2)}$$

Where k is the rate constant, R is the gas constant and T is the temperature. Based on collision theory the pre-exponential factor corresponds to the frequency of collisions in a catalytic orientation occurring.[12] The formation of the Arrhenius equation was an important first step towards describing the temperature-dependence of reactions. However, the equation describes an empirical relationship and can only report on gas-phase kinetics.[13] Contrastingly, the Eyring equation is not empirical and can be applied to condensed phase reactions, meaning it is preferred for the study of enzyme temperature-dependences.

1.3 Transition state theory and the Eyring equation

The Eyring equation arose from the development of transition state theory, which describes the energy barrier that is overcome during the transition from reactant to product[11] (Figure 1). This forms the classical understanding of enzyme reactions.

According to transition state theory, the concentration at the transition state [$X^{\ddagger}$] is in equilibrium ($K^{\ddagger}$) with the concentration of the reactants [A][B] (Eq 3).

$$[X^{\ddagger}] = K^{\ddagger}[A][B] \quad \text{(Eq3)}$$

This means $K^{\ddagger}$ can be treated as follows to give the Gibbs free energy of activation ($\Delta G^{\ddagger}$) (Eq 4).

$$\Delta G^{\ddagger} = RTlnK^{\ddagger} \quad \text{(Eq4)}$$

Which can be expanded to obtain the change in enthalpy ($\Delta H^{\ddagger}$) and entropy terms ($\Delta S^{\ddagger}$) between the ground and transition state of the reaction (Eq 5). Here enthalpy reflects the

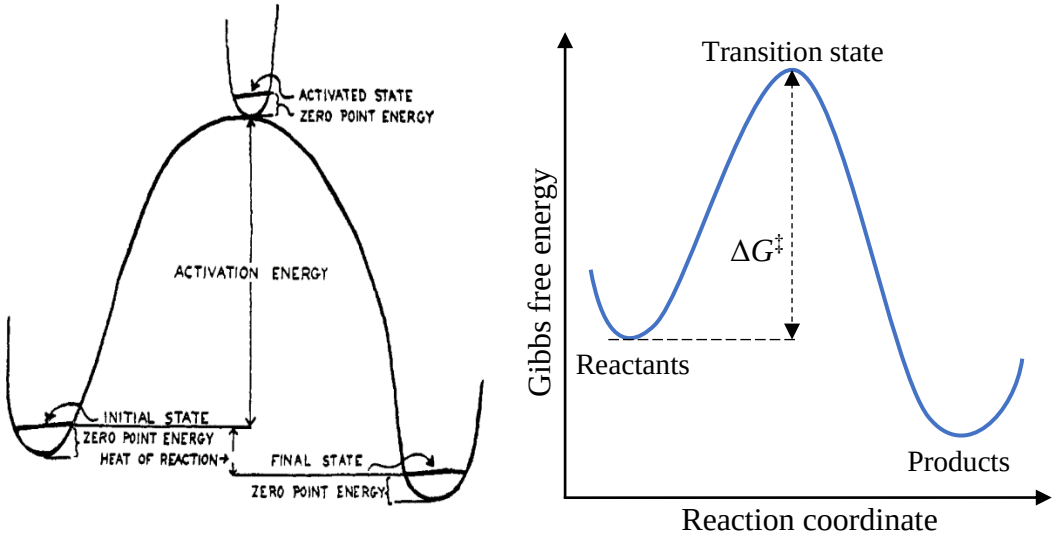

Figure 1. Left: Original transition state theory diagram by Eyring (1935).[11] Right: Diagram of the current understanding of transition state theory with the change in Gibbs free energy ($\Delta G^{\ddagger}$) in the Eyring equation replacing activation energy in the Arrhenius equation, to demonstrate the energy barrier.

amount of stretching, squeezing or breaking of chemical bonds, and the entropy reflects the change in enzyme conformations required for the enzyme reaction to occur.[12]

$$\Delta G^{\ddagger} = \Delta H^{\ddagger} - T\Delta S^{\ddagger} \qquad \text{(Eq5)}$$

When equations 3, 4 and 5 are combined, the concentration of $X^{\ddagger}$ is as follows (Eq 6).

$$[X^{\ddagger}] = [A][B]e^{\Delta S^{\ddagger}/R}e^{-\Delta H^{\ddagger}/RT} \qquad \text{(Eq6)}$$

Despite being in equilibrium, once $X^{\ddagger}$ is reached, the back-reaction to A and B is essentially non-existent. Following this, the breakdown of $X^{\ddagger}$ to products is assumed to occur primarily through the breaking of a single bond. Thus, including the Avogadro (N) and Planck's (h) constants into the equation to include vibrational bond frequency, the rate for the complete reaction is given as the Eyring equation (Eq 7).

$$k = \frac{RT}{Nh}e^{\Delta S^{\ddagger}/R}e^{-\Delta H^{\ddagger}/RT} \qquad \text{(Eq7)}$$

This can be related to the Arrhenius equation by interpreting the entropy term ($\Delta S^{\ddagger}$) as the collision frequency pre-exponential factor and interpreting the enthalpy term ($\Delta H^{\ddagger}$) as the temperature independent value of the activation energy. This breakdown of the transition state theory is commonly used in various textbooks, with the information presented here found in the 'Fundamentals of Enzyme Kinetics'.[12]

1.4 Enzyme denaturation leading to curvature in enzyme temperature-dependences

Whilst the Eyring equation describes an increase in rate in relation to an increase in temperature, it fails to address the decrease in rate seen after a certain temperature is reached in enzymatic rates. A widely accepted reasoning for this decrease in rate is that denaturation of the enzyme is occurring after a certain temperature is reached. This was formally described in 1949[14] (Figure 2).

Thermal denaturation is a process that occurs in all proteins, with the effect on enzyme rates varying, depending on the stability of the protein. Extreme examples of this include highly stable thermophilic/hyper-thermophilic enzymes[15] and unstable psychrophilic enzymes.[16] It occurs due to the weakening of non-covalent interactions between different amino acids, such as hydrogen bonding and electrostatics, which are imperative to the correct folding and retention of a proteins unique tertiary structure.[17] The stability of folded enzymes with respect to temperature is directly linked to the enthalpic and entropic terms of the enzyme at ground state. Upon protein unfolding these terms are temperature-dependent due to the change in heat capacity (ΔC_p) (Eq 8 & 9), resulting in a curved ΔG^0 (free energy of unfolding) with respect to temperature.[17] Heat capacity relates the temperature change of a system with respect to heat change.[18]

$$\Delta H^0 = \Delta H_R^0 + \Delta C_p(T - T_R) \quad \text{(Eq8)}$$

$$\Delta S^0 = \Delta S_R^0 + \Delta C_p ln\, T/T_R \quad \text{(Eq9)}$$

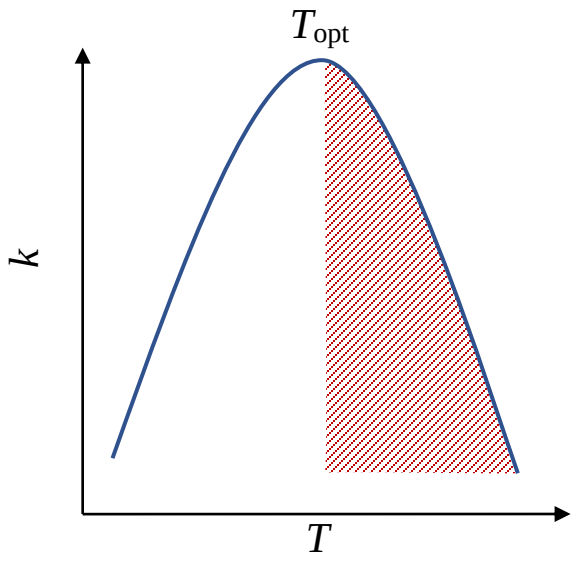

Figure 2. Schematic of the temperature-dependence of an enzyme reaction. The shaded red area demonstrates a drop in rate, which is ordinarily attributed to thermal denaturation, after the T_{opt} of the enzyme has been reached.

Here, ΔH_R^0 and ΔS_R^0 are the unfolding entropy and enthalpy at a reference temperature (T_R). This translates into Equation 10 with respect to enzyme rates,[12] with the ΔS^0 becoming detrimental to rate at higher temperatures (Terms here are the same as those defined at Eq 2).

$$k_{obs} = \frac{A\ exp\left(\frac{-E_a}{RT}\right)}{1 + \exp\left(\frac{\Delta S^0}{R} - \frac{\Delta H^0}{RT}\right)} \quad \text{(Eq10)}$$

In 1979 a term for the reduction in enzymatic rates due to denaturation was incorporated into the Arrhenius equation[14] (Eq 11).

$$k_{obs} = A_2 e^{-\left(\frac{E_2}{RT}\right)} - A_D e^{-\left(\frac{E_D}{RT}\right)} \quad \text{(Eq11)}$$

Where Kobs is the observed rate, $A_2 e^{-\left(\frac{E_2}{RT}\right)}$ is the Arrhenius equation as described at Eq 2, and $A_D e^{-\left(\frac{E_D}{RT}\right)}$ is the rate of denaturation. Whilst this correction could be applied where the rate of denaturation has been experimentally established, a more common practice is to use the initial velocity of a reaction and limit the temperature range studied.[12] This ensures temperature-dependence linearity and avoids the convolving factor of denaturation on the rate.

1.5 Other contributions to curvature in enzyme temperature-dependences

Whilst enzyme denaturation is clearly a contributing factor to a reduction in rate after a specific optimum temperature, it is not the sole contributor to this curvature. For example, quantum mechanical tunnelling (QMT) can result in the upward curvature of enzymatic temperature-dependences at low temperatures, where it is contributing significantly to the reaction.[19] Additionally, the temperature-dependences of some reactions are convolved by a change in the rate-limiting step of a reaction, which can lead curvature.[20] Conversely, a change in the rate-limiting step can also conceal curvature in the temperature-dependence of an enzyme reaction.[21] This highlights the importance of establishing the temperature-dependence of the rate-limiting step, when interpreting the temperature-dependence of a reaction.

Sharp breaks in the linearity of enzyme temperature-dependences have been reported, which are too sharp for a change in the rate-limiting step[22] and significant curvature has been found even where QMT is not occurring.[19] Work by Truhlar & Kohen in 2001 suggests non-linearity is a result of the balance of energy over all systems, subtracted from the energy over all reacting systems, which gives the value of the activation energy. When this balance is temperature-dependent it can result in convex or concave Arrhenius plots.[23]

They use this explanation as a rationale for findings by Massey *et al*., which suggest that curvature in temperature-dependence plots may be attributable to temperature-dependent reversible changes in protein structure.[24]

The hypothesis that reversible changes in protein structure can influence the curvature of the temperature-dependence of enzyme reactions regularly appears in the literature. In addition to Massey *et al.*, Kavanau also proposed that there are inactive reversible enzymatic states, and attributed this to hydrogen bonding at low temperatures.[25] Additionally, in 1998, Thomas and Scopes demonstrated that the temperature-dependence of the rate of enzyme 3-phosphoglycerate kinase was not exponential as expected by the Arrhenius equation. They found that the reduction in rate at higher temperatures could not be fully attributed to irreversible denaturation and again proposed that there are intermediates within the denaturation process that are capable of reversible unfolding.[26]

A separate hypothesis for non-linearity in Arrhenius plots was proposed by Masgrau *et al.*[19] They propose that in the absence of tunnelling, curvature occurs because of temperature-dependent variation in the activation energy of the reaction, as suggested by Truhlar & Kohen, which they attribute to temperature-dependent differences in the vibrational modes associated with the transition state of a reaction.[19]

Curvature in enzymatic dependences, that is not attributable to protein denaturation, presents itself more clearly when the extremes of psychrophilic or thermophilic enzymatic rates are studied. It has been found that there is a drop in the rate of both psychrophilic[27] and thermophilic[28] enzymes at temperatures much lower than the temperature of protein denaturation. To fully understand the temperature-dependence of enzymatic rates, the phenomena behind the decrease in rate after T_{opt}, that is not attributable to denaturation, changes in the rate-limiting step, or QMT, needs to be identified. Arguably, the ability to reliably and rationally tune the rate and T_{opt} of enzymes can only be achieved with more insight into this phenomenon. At present, there are three numerical models that have been proposed that address the curvature in the temperature-dependence of enzymatic rates. The equilibrium model[29], the N-state model[9] and the macro-molecular rate theory[1].

1.6 The equilibrium model

The equilibrium model, proposed in 2001 by Daniel *et al.*[30] was the first comprehensive model to address the curvature in the temperature-dependence of enzyme reactions. It builds on work by Sizer[31] and others[24–26] who proposed that the equilibrium of active/inactive enzyme is reversible, and of Wright and Schomaker[32] who examined denaturation with respect to time. The equilibrium model combines these concepts of reversible inactivation and the effect of time with the hypothesis by Thomas and Scopes[26] that there are intermediates in the denaturation process that are reversibly inactivated before irreversible denaturation occurs. It builds on the classic model of accounting for the rate of enzyme denaturation using the Eyring equation (rather than the Arrhenius equation at Eq 11) with respect to time (Eq 12).

$$V_{\max} = \frac{k_{\mathrm{B}}T}{h} \cdot e^{-\left(\frac{\Delta G^{\ddagger}_{\mathrm{cat}}}{RT}\right)} \cdot [\mathrm{E}_0] e^{-\frac{k_B T}{h} \cdot e^{-\left(\frac{\Delta G^{\ddagger}_{\mathrm{inact}}}{RT}\right)} \cdot \mathrm{t}} \quad \text{(Eq12)}$$

Where the first term is representative of the enzyme's catalytic rate constant (k_{cat}), and the second term is representative of the enzymes thermal inactivation rate constant (k_{inact}). V_{max} is the enzymes maximum velocity, k_B is the Boltzmann constant, h is the Planck's constant, R is the gas constant, T is the temperature, $\Delta G^{\ddagger}_{\mathrm{cat}}$ and $\Delta G^{\ddagger}_{\mathrm{inact}}$ are the activation energies of catalysis and thermal inactivation respectively, $[E_0]$ is the total enzyme concentration, and t is time.[33]

When modelled, this equation presents no T_{opt} at the zero timepoint of biologically relevant temperatures. Instead rate exponentially increases with temperature and a T_{opt} only presents with increasing time, due to denaturation.

However, when Eq 12 was further expanded to quantify the thermal parameter K_{eq}, as outlined by Eq 13-15), it was found that the zero timepoint presented a T_{opt}.[34,35]

$$\mathrm{E}_{\mathrm{act}} \overset{K_{\mathrm{eq}}}{\rightleftharpoons} \mathrm{E}_{\mathrm{inact}} \overset{K_{\mathrm{inact}}}{\longrightarrow} \mathrm{E}_{\mathrm{denat}} \quad \text{(Eq13)}$$

$$\ln(K_{\mathrm{eq}}) = \frac{\Delta H_{\mathrm{eq}}}{R}\left(\frac{1}{T_{\mathrm{eq}}} - \frac{1}{T}\right) \quad \text{(Eq14)}$$

$$T_{\mathrm{eq}} = \frac{\Delta H_{\mathrm{eq}}}{\Delta S_{\mathrm{eq}}} \quad \text{(Eq15)}$$

Where T_{eq} is the temperature at which E_{act} and E_{inact} are in equal concentration (Eq 14&15) and ΔH_{eq} and ΔS_{eq} (Eq 15) are the change in enthalpy and entropy upon the enzyme becoming inactive. This model was found to fit to experimental data, where the classical model could not.[33–35] It was proposed that the reversible inactivation (K_{eq}) of the enzyme was happening on a much faster time scale than the denaturation of the enzyme, resulting in curvature of the rate at the zero timepoint. Rates then become increasingly lower with respect to time at high temperatures, as a result of denaturation.[35] Whilst this model is upheld by the fit of experimental data, the molecular basis and specific timescales for the K_{eq} are yet to be determined.[29] Arguably, without this insight, it cannot be used to fully explain the curvature of temperature-dependence plots.

1.7 The N-state model

The N-State model was hypothesized by Glowacki *et al*. in 2012,[9] and presents another expansion of the Eyring equation to further the understanding of the temperature-dependence of enzymatic reactions. The model addresses the role of the dynamical motions of enzymes and the implications they may have on the rate of catalysis. It states

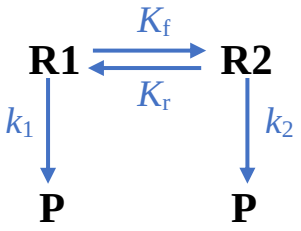

Figure 3. A schematic of the premise of the N-state model, with different catalytic rates (k_1 and k_2) occurring as a result of different conformers (R1 and R2) (adapted from Glowaki *et al*., 2012).[9]

that where the conformational change of an enzyme is slower than the change upon reaction coordinates, then using statistical rate theories that assume an averaged dynamical motion, such as the transition state theory, do not suffice. In this case, the different reactant conformers aren't necessarily driving catalysis, but they may be influencing the rate at which catalysis proceeds (Figure 3). Thus, they need to be accounted for when studying the temperature-dependence of enzyme-driven reactions.

The model builds on a previous model from 1983 that investigated the effect of the potential energy surface (PES) of an enzyme on the temperature-dependence of catalysis.[36] The N-state model progresses this by accounting for the additional effect of quantum-tunnelling on catalytic rate. The model is applied to, and supported by, kinetic isotope effect (KIE) studies, in cases where there is disparity between the expected temperature-dependences of k_H and k_D (Eq 16).

$$k' = \frac{k_1}{1 + \exp\left(-\frac{\Delta G}{RT}\right)} + \frac{k_2}{1 + \exp\left(-\frac{\Delta G}{RT}\right)} \qquad \text{(Eq16)}$$

Where the rate is separated into two different rates (k_1 and k_2) by the change in free energy (ΔG) between two enzyme conformations, ascertained from the equilibrium constant of K_f and K_r (Figure 3).

When applied to the temperature-dependence of KIEs that previously presented a poor fit to the traditional TST model, the N-state model fit well to the data. This suggests that in some cases, differing enzyme conformations can affect the temperature-dependence of enzyme catalysis. It is noted however that the model contains multiple constraints and assumptions that potentially weaken the integrity of the fit. Thus, the inclusion of multiple terms, for multiple conformations, into Eq 16, may weaken the fit further, ultimately limiting its application.

Denaturation, the equilibrium model and the N-state model all provide some explanation as to why enzymes present a specific T_{opt}. However, none of these explanations consider the effect that substrate binding has on the heat-capacity of enzymes. The influence of the change in heat-capacity between the ground and transition states of an enzyme reaction,

($\Delta C_p^{\ddagger}$) on the temperature-dependence of enzyme reactions, was first hypothesized and explored in 2013.[1] It was termed the macromolecular rate theory (MMRT).

1.8 Macromolecular rate theory (MMRT) background

Whilst the change in heat-capacity during protein unfolding, resulting in temperature-dependent changes in enthalpy and entropy, has been well documented,[17,37] the change in the heat-capacity of an enzyme over its reaction coordinate had not been fully considered until 2013.[1]

Many proteins are intrinsically disordered in nature, meaning they adopt multiple conformations, and in some cases become more ordered upon ligand binding.[38] This has been demonstrated specifically in numerous systems,[39,40] with enzymes being no exception.[41] Often, this rigidification allows crystallographers to obtain crystal structures, where otherwise the protein would have been too disordered.[42]

Molar heat capacity increases with increasing molecular weight, with each amino acid of a folded protein contributing around 45 J $mol^{-1} \cdot K^{-1}$ to its heat capacity.[43] This means that macromolecules with relatively large molecular weights such as enzymes, when compared to small reactant systems, bear a substantial heat-capacity.[42] Consequently this leads to a transient change in heat capacity at the transition-state of an enzymatic reaction, attributable to the aforementioned increase in rigidification,[1,42] that is variable with temperature (Figure 4).

Because of this change in enzyme heat capacity between the ground and transition state of the reaction coordinate, Eq 8&9 can now be applied to describe the temperature-dependence of enthalpy and entropy over the reaction coordinate ($\Delta H^{\ddagger}$ and $\Delta S^{\ddagger}$ respectively) (Eq 17&18).

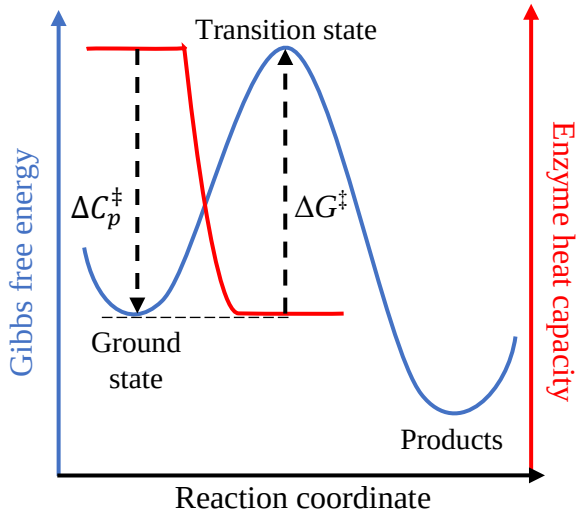

Figure 4. Schematic of the variation in heat capacity of an enzyme over the reaction coordinate.

$$\Delta H^{\ddagger} = \Delta H^{\ddagger}_{T_R} + \Delta C^{\ddagger}_p (T - T_R) \quad \text{(Eq17)}$$

$$\Delta S^{\ddagger} = \Delta S^{\ddagger}_{T_R} + \Delta C^{\ddagger}_p ln\, T/T_R \quad \text{(Eq18)}$$

Eq 17&18 can then be incorporated into the Eyring equation, to give the MMRT equation (Eq 19).

$$lnk = ln\frac{k_B T}{h} - \left[\frac{\Delta H^{\ddagger}_{T_R} + \Delta C^{\ddagger}_P (T - T_R)}{RT}\right] + \left[\frac{\Delta S^{\ddagger}_{T_R} + \Delta C^{\ddagger}_P (lnT - lnT_R)}{R}\right] \quad \text{(Eq19)}$$

Here the $\Delta C^{\ddagger}_p$ is representative of the curvature in the temperature-dependence of the enzyme reaction. According to the MMRT, the curvature is hypothesized to occur due to the decrease in enthalpy and an increase in entropy between the ground and transition state of the reaction as temperature increases, resulting in a curved $\Delta G^{\ddagger}$ [42] (Figure 5A). The magnitude of $\Delta C^{\ddagger}_p$ therefore increases with more significant curvature (Figure 5B).

From this, as the value of $\Delta C^{\ddagger}_p$ becomes increasingly negative, the more curved the temperature-dependence is. In order to confirm whether $\Delta C^{\ddagger}_p$ is responsible for curvature in temperature-dependence plots, it is important to postulate and experimentally investigate what is responsible for varying $\Delta C^{\ddagger}_p$ values in enzymes.

Around 85 % of a proteins heat capacity originates from the change in energy of the system with temperature. The energy can be split into translational, rotational, vibrational and electronic modes. Electronic energy does not vary within the range of biologically relevant temperatures, and so is not considered in the context of the MMRT.[42] The

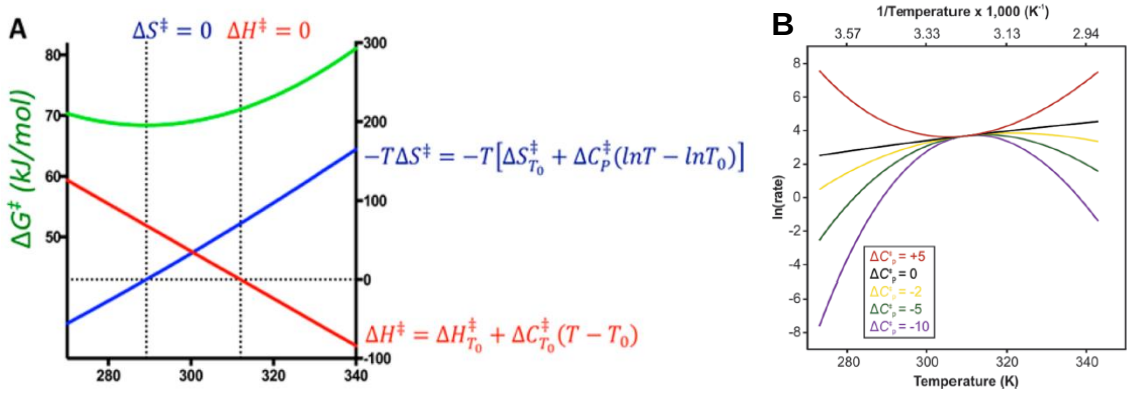

Figure 5. A The hypothesized variation in $\Delta H^{\ddagger}$ and $\Delta S^{\ddagger}$ with respect to temperature, leading to curvature in $\Delta G^{\ddagger}$, and consequently the enzymatic rate. **B** Examples of variation in $\Delta C^{\ddagger}_p$ values with variation in the curvature of temperature-dependences (from Arcus *et al.,* 2016).[42]

remaining 15 % is composed of the proteins hydration term.[44] Throughout this thesis the words 'dynamics' 'flexibility/rigidity' and 'Vibrational motions/modes' are used interchangeably to refer to these translational, rotational and vibrational modes, and larger scale motions that stem from them.

As a result of this, notionally the majority (85 %) of the measured $\Delta C_p^{\ddagger}$ of an enzyme is composed of its dynamics, which means that the MMRT can be validated by perturbing the dynamics of the system and ascertaining whether $\Delta C_p^{\ddagger}$ is consequently affected. It also provides the potential for the metric of $\Delta C_p^{\ddagger}$ to be applied as a novel tool to measure the extent to which enzyme dynamics are linked to its catalysis in comparative situations. This could be applied to gain further insight into specific enzyme systems, as well as directing the engineering of enzyme dynamics to enable the tuning of rates and optimum temperature.

1.9 Current literature on MMRT

1.9.1 Point mutations to investigate MMRT

When MMRT was first proposed in 2013 by Hobbs *et al.*[1] they probed the model by making 268 point mutations of a model enzyme 'MalL' (Oligo-1,6-glucosidase 1). Here they identified four mutations that increased the T_{opt} of MalL. They correlated T_{opt} to varying $\Delta C_p^{\ddagger}$ values of these mutants, and other enzymes, accounting for varying levels of vibrational modes by dividing $\Delta C_p^{\ddagger}$ by the mass of the different enzymes.

Of the four point mutations that led to an increase in the T_{opt} of MalL, V200S and G202P resulted in the largest increase in T_{opt}, with V200S resulting in an increased k_{cat} (min^{-1}) and G202P resulting in a decreased k_{cat}. Wildtype (WT), V200S and G202P MalL were subsequently crystallised and molecular dynamics (MD) simulations were run to assess the source of the differences in their $\Delta C_p^{\ddagger}$ values. MD simulations ascertained that G202P MalL had similar levels of flexibility to WT MalL, with the assumption that the heat capacity at the transition state is reduced, consequently reducing the $\Delta C_p^{\ddagger}$. The flexibility of V200S MalL was significantly reduced, meaning the heat capacity of the mutant at the ground state was reduced, giving rise to the reduced $\Delta C_p^{\ddagger}$ of the reaction.

This work was an important first step towards validating the hypothesis of the MMRT. However, point mutations could influence the stability, and therefore the proteins propensity to denature, despite the short assay times used here. Whilst this work was a vital step towards demonstrating that $\Delta C_p^{\ddagger}$ is influencing the curvature of enzymatic reactions, further investigation in a more comparative setting was required to provide definitive evidence of the influence of $\Delta C_p^{\ddagger}$.

1.9.2 Applying MMRT to kinetic isotope effects

The hypothesis that $\Delta C_p^{\ddagger}$ may be reflective of enzyme dynamics linked to catalysis was further examined in 2015 by Arcus and Pudney using 10 existing primary KIE data sets.[45] They found significant curvature in the temperature-dependence plots that had previously been assumed to be linear. To ascertain if this curvature was arising from enzyme dynamics, the temperature-dependence of the KIEs were examined.

Specifically, the enthalpy change between the ground and transition states of the reaction were compared for protiated and deuterated hydride transfer reactions ($\Delta\Delta H^{\ddagger}$). Where $\Delta\Delta H^{\ddagger}$ values are less than around 5 kJ mol^{-1}, the KIE is primarily comprised of the temperature-dependence associated with the reduction of deuterated hydrogen on the reactions zero point energy (ZPE) when compared to protiated hydrogen. However, when the $\Delta\Delta H^{\ddagger}$ is larger than ~ 5 kJ mol^{-1} it is thought that the reaction is influenced by significant vibrational coupling.

They found a correlation between the positive $\Delta\Delta H^{\ddagger}$ values and negative $\Delta C_p^{\ddagger}$ values for seven out of the ten data sets studied. The three outliers, that presented a negative $\Delta C_p^{\ddagger}$ and a small $\Delta\Delta H^{\ddagger}$ value, were found to have separate evidence for significant vibrational coupling to the reaction coordinate. Thus, the data demonstrated that negative $\Delta C_p^{\ddagger}$ values reflect when significant enzyme dynamics are contributing to catalysis.

They considered that substantial QMT, denaturation and the hydration term, could be contributing to the curvature seen in the temperature-dependences studied here. However, they found no correlation between the extent of QMT and $\Delta C_p^{\ddagger}$. Additionally, denaturation would be of the same impact for both protiated and deuterated data sets, thus cancelling itself out. Finally, the hydration state change also reflects protein dynamics, due to its alteration upon conformational change.

1.9.3 Furthering the theory of MMRT

MMRT was summarised as a new concept in 2016 by Arcus *et al.*[42] Here the relationship between $\Delta C_p^{\ddagger}$ and T_{opt} is formally described by Eq 20.

$$T_{opt} = \frac{\Delta H_{T_0}^{\ddagger} - \Delta C_p^{\ddagger} T_0}{-\Delta C_p^{\ddagger} - R} \qquad \text{(Eq20)}$$

The relationship between enzymatic temperature-dependence curvature and the evolution of psychrophilic and thermophilic enzymes was examined in further detail. Eq 20 demonstrates that as T_{opt} decreases, so does $\Delta C_p^{\ddagger}$, representing an increase in the curvature of the temperature-dependence. Here, the idea of a 'psychrophilic trap' is introduced, with the curvature increasing to the point where slight deviations from the T_{opt} lead to a

detrimental impact on rate, when compared to mesophilic or thermophilic enzymes. This means there may be a lower limit on the T_{opt} of enzymes, as explained by $\Delta C_p^{\ddagger}$.

Additionally, the hypothesis that enzymes are large to deal with difficult chemistry is proposed, with increasing enzymatic mass correlated to increasingly difficult chemistry (in terms of $\ln(k_{cat}/k_{non})$. However, it should be noted that this is based on correlation, not causation and has yet to be experimentally explored in more detail.

1.9.4 Investigating MMRT using molecular dynamics simulations

MMRT was further validated in 2018 by van der Kamp *et al*.[46] using MD simulations. Here, extensive simulations (in the μs range) were carried out on two enzymes (Ketosteroid isomerase (KSI) and MalL). The difference in the mean squared fluctuation in the enthalpy $\langle \partial H^2 \rangle$ was calculated for both enzymes with and without a transition state analogue, to represent the ground and transition states of the reaction. This can then be converted to $\Delta C_p^{\ddagger}$ by Eq 21.

$$\Delta C_p^{\ddagger} = \frac{\Delta \langle \partial H^2 \rangle^{\ddagger}}{k_B T^2} \qquad \text{(Eq21)}$$

Here the computational $\Delta C_p^{\ddagger}$ values were found to match the experimentally determined $\Delta C_p^{\ddagger}$ values within error, validating the origin of experimentally measured $\Delta C_p^{\ddagger}$ calculated via the MMRT equation (Eq 19).

Additionally, they found that the origins of $\Delta C_p^{\ddagger}$ were not just located around the active sites of the enzyme, but also in distal areas. The catalytic monomer of the KSI dimer presented an increase in C_p between the ground and transition state, whereas the non-catalytic monomer presented a decrease in C_p between the ground and transition state, resulting in an overall slightly negative $\Delta C_p^{\ddagger}$. MalL also demonstrated a similar trend, with the catalytic side of its TIM barrel contributing a to positive increase C_p, with other remote parts of the protein and the other half of the TIM barrel contributing to a negative decrease in C_p.

This is related to other studies that have suggested that the reduction in entropy around the active site at the transition state of the reaction is compensated for by an increase in entropy in areas distal to the active site.[46–48] Van der Kamp *et al*. suggest that this may provide further explanation for the large mass of enzymes and for the aforementioned link between $\Delta C_p^{\ddagger}$, enzyme mass, and difficulty of chemistry outlined by Arcus *et al*.[42]

1.10 Assumptions of catalysis made by MMRT

Although MMRT presents a strong rationale for the temperature-dependence of enzyme catalysis, it makes two assumptions about the contribution of enzymes to catalysis. The first assumption is that there are significant contributions from both entropy and enthalpy

to catalysis, regardless of whether they are positive or negative contributions. Without this assumption, the temperature-dependence of these parameters would not affect the curvature of the enzymatic temperature-dependences. Secondly, although not implicit to MMRT, the study by Arcus and Pudney[45], and the work of this thesis examines whether the value of $\Delta C_p^{\ddagger}$ is reflective of dynamic motion linked to the reaction coordinate. However, this assumes that enzyme dynamics are linked to catalysis. Both assumptions are highly contentious in the literature, with strong evidence for and against their roles in catalysis.

1.10.1 Enthalpy/Entropy driven catalysis

Various studies reveal that the contribution of either enthalpy or entropy to catalysis can vary between different enzyme systems, with some finding no contribution of these factors at all. For example, computational studies by Åqvist *et al*. examine the contribution of entropy to catalysis and compare them to entropy contributions without a catalyst present. In some systems, such as cytidine deaminase, they found that the entropy penalty of enzyme turnover is incurred by substrate binding, and that the change in entropy for the catalytic step is minimal.[49] In other cases, both experimental and computational studies validate both positive and negative catalytic $\Delta S^{\ddagger}$ in a trGTPase and a Ras-RasGAP complex respectively.[50]

Work by Wolfenden proposes that in terms of evolution, most modern enzyme catalysis is driven by an enthalpic contribution, when compared to uncatalyzed reactions.[51] Whilst contributions from entropy and enthalpy vary depending on the system, there is clear evidence that both terms contribute to catalysis, with the entropy-enthalpy compensation theory presenting itself in the case of psychrophilic enzymes.[50] In the case of psychrophilic enzymes, it is found that the $\Delta S^{\ddagger}$ is large and negative when compared to mesophilic enzymes, whilst the $\Delta H^{\ddagger}$ is smaller.[52] Åqvist *et al.* found that this large change in entropy was due to the surface of psychrophilic enzymes being more flexible, contributing to the entropy of the system.[50] This corroborates the aforementioned increase in $\Delta C_p^{\ddagger}$ and shift in T_{opt} of psychrophilic enzymes, presented by Arcus *et al*.[42] Overall, the literature suggests that whilst it is system specific, there are contributions of both entropy and enthalpy to catalysis, with Cornish-Bowden even suggesting that the two properties may be one and the same, due to the entropy-enthalpy compensation correlation being so unified.[53]

1.10.2 Dynamics linked to catalysis

The equilibrium model, the N-state model and MMRT discussed above all imply that enzyme dynamics are linked to catalysis.[9,29,45] However, it should be noted that there is much debate in the literature about the extent to which dynamics influence catalysis, and whether they directly affect the catalytic step of a reaction at all. Dynamics can range from small vibrations on the ps-ns timescale, to larger scale conformational movement on

the μs-s timescale (Figure 6). This has been documented by various experimental and computational techniques such as nuclear magnetic resonance (NMR)[54,55] and MD simulations.[56]

Large scale enzymatic dynamics (milliseconds) have been found to contribute to various phases of enzyme turnover, such as substrate capture[57], and can be rate-limiting in some cases.[58] In the case of an RNase, NMR was utilized to suggest that the chemical step is rate-limited by these dynamics.[59] However, some researchers maintain that although these motions exist as part of turnover, they are not linked directly to the catalytic chemical step.[60]

There is a similar discourse in the literature regarding small scale dynamics on the picosecond scale, which represent the proteins vibrational modes. As previously mentioned, large $\Delta\Delta H^{\ddagger}$ values (> ~5-6 kJ mol^{-1}) are used to imply vibrational motions directly linked to the catalytic step.[45,61] This occurs where KIEs are temperature-dependent, outside of the Bell-correction model for tunnelling occurring in addition to classical TST catalysis. This is attributed to significant compression of the Hydrogen/Deuterium (H/D) bond being examined, as a consequence of vibration linked to catalysis.[61]

KIEs are also invoked in combination with other techniques to provide evidence of vibrational motions linked to catalysis. For example the use of pressure to compress the donor-acceptor distance of a reaction has been used to demonstrate that a non-linear pressure dependence of a KIE is indicative of vibrational coupling.[62] Mutagenesis has also provided evidence of catalytic vibrational coupling, with the mutation of Soybean Lipoxygenase-1, which is thought to catalyse reactions purely through QMT due to its large KIE.[63] Here, a model of environmentally modulated hydrogen tunnelling was applied to rationalize the data. The Soybean Lipoxygenase-1 mutation I553A led to a significant increase in the temperature-dependence of the KIE, which was attributed to an

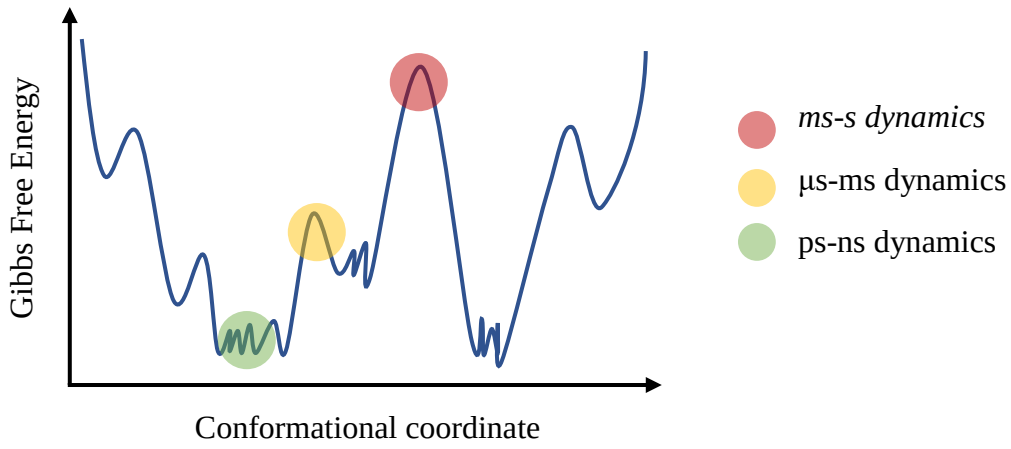

Figure 6. Schematic of the relationship between the energy, conformation and time scale of protein dynamics (Adapted from [54,55]).

increase in vibrational coupling to the reaction coordinate, and specifically to motions involved in the chemical step of the reaction, termed 'active dynamics'.

KIEs are one of the few ways to study the effect of vibrational motions on catalysis, as the picosecond timescale of dynamics is largely inaccessible experimentally. Due to the indirect nature of these experiments, researchers have also turned to computational simulations/calculations to gain further atomistic insight into these vibrations. For example, work by Schwartz *et al*., has demonstrated a role for vibrational coupling in human lactate dehydrogenase and horse liver alcohol dehydrogenase, using spectral density from MD simulations.[64,65] This has also been investigated via QM/MM calculations on Catechol O-Methyltransferase.[66]

However, other computationalists argue that there is no clear evidence of dynamics linked to the catalytic chemical step and that catalysis is instead driven by electrostatic preorganisation of the active site.[67,68] A review of the lack of clarity and consensus regarding the involvement of dynamics in catalysis by Tuñón *et al.*, concludes that dynamics do not have an effect on rate, as the various states are in equilibrium. They add that the temperature-dependence of reactions may reflect a shift in this equilibrium, rather than being directly attributable to dynamical effects. This is reaffirmed by a statement that dynamical effects generally do not have a significant impact on catalysis, and as a result of this, transition state theory holds.[69]

There is extensive research arguing for and against this point, indicating that we are not yet at a stage where either experimental or computational methods can conclusively establish the extent to which dynamics are involved in the catalytic chemical step of enzyme driven reactions. Further contributing to this discourse, is system dependent variation in enzyme dynamics, with studies inferring dynamical contributions based on select examples. This is evident from the work by Pudney & Arcus,[45] whereby some enzymes presented no evidence, and some enzymes presented significant evidence, for contributions of dynamics to catalysis.

This work aims to explore the premise that enzyme dynamics are contributing to catalysis, regardless of whether they are directly linked to the catalytic step. This is achieved by perturbing enzyme dynamics and investigating the effect this has on the value of $\Delta C_p^{\ddagger}$ in comparative cases. This builds on the initial link of enzyme dynamics and the value of $\Delta C_p^{\ddagger}$ presented by Pudney & Arcus,[45] and aims to further the understanding of MMRT whilst also investigating $\Delta C_p^{\ddagger}$ as a potential novel probe for dynamics linked to catalysis.

1.11 Caveats to the application of MMRT

Comparative cases are presented in this work, as although the value of $\Delta C_p^{\ddagger}$ may be reflecting the dynamics of an enzyme reaction linked to its catalysis, it is also influenced by other variables. For example, the hydration term that is thought to represent ~ 15 % of the heat capacity of a protein,[1] may convolve data that aims to examine the vibrational

contribution of heat capacity during enzyme turnover. It has been suggested that the change in the hydration term of an enzyme between the ground and transition state of a reaction is indicative of enzyme dynamics linked to catalysis in itself.[45] Despite this, different enzymatic systems may present differing contribution levels of hydration and vibration to heat capacity. For consistency of the hydration term, the enzymes studied in this work, are either perturbed by single point mutations, or influenced by external factors, such as isotope effects or the membrane environment, all of which should have minimal impact on the hydration term.

Another confounding variable that needs to be accounted for when measuring $\Delta C_p^{\ddagger}$ is protein denaturation. Arcus *et al*., suggest that establishing the effect of denaturation on rate, by including the proteins unfolding rate, is important to obtain an accurate value of $\Delta C_p^{\ddagger}$.[42] Although this is necessary to obtain true $\Delta C_p^{\ddagger}$ values, in this work the unfolding rate was not incorporated into the rate of turnover, as the error on the unfolding rate may convolve subtle changes in $\Delta C_p^{\ddagger}$ upon the perturbation of dynamics. Instead, initial rates were measured to avoid denaturation over time, and conservative temperatures were used. Work was also carried out on a hyper-thermophilic glucose dehydrogenase (GDH), which is incredibly stable at high temperatures.[70] Additionally, all experimentation was done using comparative systems as mentioned above, which are expected to have similar denaturation rates that essentially cancel each other out.

It is also important to note that the phenomenon of MMRT is temperature-dependent in itself. That is, as the value of $\Delta C_p^{\ddagger}$ reflects the curvature of the temperature-dependence of enzymatic reactions, its value will be smaller at lower temperatures, and larger at high temperatures, where curvature in the plot becomes more pronounced. This issue is currently being addressed, with plans to further adapt the MMRT equation to include a term to account for this temperature-dependence. However, an additional parameter will make the values obtained from the equation less stringent. In this work, within the comparative systems, the temperature ranges studied are kept consistent, to avoid this issue.

Finally, to directly analyse the rate of a reaction, the rate-limiting step needs to be studied. For the cases presented here, product formation was spectroscopically followed, in steady-state, to establish rates. For all systems presented in this work, the evidence suggests that product formation is the rate-limiting step. This was demonstrated via stopped-flow studies for MalL, by QM calculations for GDH, and was already established for Monoamine Oxidase B (MAO-B). It is acknowledged that the rate-limiting step of a reaction can also be temperature-dependent.[71,72] However, it is assumed that the comparative cases used here would minimise convolution of rates by a temperature-dependent change in the rate-limiting step. In the case of GDH the rate-limiting step was found to be temperature-independent by QM calculations. In any case, if the rate-limiting step is altered by perturbing the dynamics of the enzyme, this in itself links dynamics to catalysis, and demonstrates that they are reflected in the value of $\Delta C_p^{\ddagger}$.

1.12 Aims and objectives

To further explore the temperature-dependence of enzymatic reactions, and the catalytic-dynamics of enzymatic reactions, in the context of the MMRT outlined above, the following research objectives were investigated, and are presented in this thesis:

Objective one:

To perturb the free energy landscape (FEL) of MalL using pressure and viscosity and assess the effect of this perturbation on the value of $\Delta C_p^{\ddagger}$. Here, the wildtype, which is known to have a substantial $\Delta C_p^{\ddagger}$ value, was compared to a mutant (V200S MalL), which has a small $\Delta C_p^{\ddagger}$ value, to account for the previously outlined caveats. MalL acts as model enzyme system here, with this work building on the existing investigations into both the WT and V200S mutations carried out by Hobbs *et al*.[1]

Objective two:

To explore the sensitivity of $\Delta C_p^{\ddagger}$ to enzyme dynamics at the level of vibrational motion. To assess whether the sensitivity of $\Delta C_p^{\ddagger}$ to vibrational motion extends to the substrate. The promiscuous and hyper-thermophilic nature of GDH allows for this objective to be investigated, whilst minimising convolution of the data from denaturation. Here, GDH is used with various substrates, as well as with progressively deuterated glucose in order to directly assess what the value of $\Delta C_p^{\ddagger}$ is reflecting, using KIEs.

Objective three:

To apply MMRT to a medically relevant enzyme system (MAO-B), in order to assess the effect of the membrane environment on the dynamics of the enzyme. This builds on existing MD simulations of MAO-B, which demonstrate that the membrane environment influences the dynamics and therefore potentially the catalysis of the enzyme.[73] This work highlights the importance of accounting for the effect of the membrane on MAO-B when designing and discovering drugs for the inhibition of the enzyme.

Chapter 2:
Theory of Methodology

Various methods are used to investigate MMRT throughout this thesis. In order to perturb dynamics to examine the effect on the value of $\Delta C_p^{\ddagger}$, high pressure, viscosity and KIEs were implemented. Additionally, computational calculations (Floppy Inclusions and Rigid Substructure Topography (FIRST)) and simulations (MD), were used to gain insight into the origin of $\Delta C_p^{\ddagger}$. This chapter presents some of the theory behind these methods, to demonstrate why and how they were applied in this work.

2.1 The effect of pressure on enzyme catalysis

Enzyme catalysis is much less sensitive to changes in pressure when compared to changes in temperature.[12] Thus, the high-pressure work presented in this thesis uses a pressure range of 1-2000 bar. The application of extreme pressure can provide an insight into the role of the FEL of proteins.[74] Additionally, the effect of pressure changes on the rate of enzymatic reactions can report on the change in volume of the enzyme during turnover. From this, comparative studies where the enzymes environment is altered can give specific information about the reaction. Such as contributions from hydration, polarity and charge development etc.[20] Additionally, the application of pressure to enzymes in conjunction with KIEs is also valuable to investigate vibrational motion linked to catalysis.[62,75]

2.1.1 Volume changes over enzyme turnover

The partial molar volume (*V*) of an enzyme consists of the volume of atoms, the volume of cavities, and the associated solvation volume due to the hydration term of solvent exposed amino acids.[76] The hydration term of the enzyme describes the blanket of water that surrounds the protein and involves polar interactions, hydrophobic interactions, and hydrogen bonding.[20] Whilst the volume of atoms is unchanged during a reaction, the volume can be altered due to intrinsic changes attributable to chemical interactions being broken and formed, structural conformational changes, and changes in the solvation volume of the enzyme.[76]

During a simplistic enzymatic reaction of E+S ⇌ ES ⇌ E + P, where E is enzyme, S is substrate and P is product, there are three main alterations in volume. The initial hydration of the enzyme, which determines a large part of its energy level; the binding of substrate,

which can displace water molecules, form bonds and lead to the rearrangements of amino acids; and the catalytic step itself, with continual water rearrangement occurring until the transition state is reached.[20]

The value of $\Delta V^{\ddagger}$ for an enzymatic reaction can be obtained by analysing the relationship between rate and pressure.[20] When looking at the change in activation volume over the reaction coordinate ($\Delta V^{\ddagger}$), the starting volume can be considered to be the volume at ES, when S is saturating.[20] Where protein denaturation has been ruled out, the value of $\Delta V^{\ddagger}$ reflects the change in volume between the ground and transition state of the reaction.[77]

Enzymes can undergo both negative and positive changes in activation volume during a reaction ($\Delta V^{\ddagger}$). Thus, depending on the reaction type, pressure can either increase or decrease the rate of reaction. For example, a reaction that undergoes a negative $\Delta V^{\ddagger}$ presents an increase in rate with an increase in pressure, as the pressure favours the transition state that has a smaller volume.[12]

2.1.2 Applying pressure and temperature to enzyme turnover

Pressure can be combined with temperature to give a rich dataset that can determine multiple thermodynamic parameters of a reaction. Often $\Delta V^{\ddagger}$ is temperature-dependent and is directly linked to the pressure dependence of $\Delta H^{\ddagger}$ and $\Delta S^{\ddagger}$, which can be described using the Maxwell relations of Eq 22&23 respectively.[20,76]

$$-\left(\frac{\partial \Delta V^{\ddagger}}{\partial T}\right)_P = -\left(\frac{\partial \Delta S^{\ddagger}}{\partial P}\right)_T \qquad \text{(Eq22)}$$

$$\Delta V^{\ddagger} - T\left(\frac{\partial \Delta V^{\ddagger}}{\partial T}\right)_P = \left(\frac{\partial \Delta H^{\ddagger}}{\partial P}\right)_T \qquad \text{(Eq23)}$$

The value of $\Delta V^{\ddagger}$ is related to temperature by an expansivity term ($\Delta \alpha^{\ddagger}$) and can be used to obtain a value for isothermal compressibility ($\Delta \beta^{\ddagger}$) during a reaction. Adiabatic compressibility represents changes in the imperfect atomic packing volume, and the change in volume as a result of solvation, which positively and negatively affects compressibility respectively. A value for isothermal compressibility can be obtained by including terms for thermal expansivity (α) density (ρ) and heat capacity (C_p). The isothermal compressibility is reflective of fluctuations in the volume of a protein, and thus, it can report on protein dynamics. Increase in pressure generally increases isothermal compressibility as a result of decreased protein flexibility, due to cavity compression, protein packing and an increase in hydration. However, the release of solvent, and an increase in entropy can decrease isothermal compressibility. The information above is summarised from a review by Masson and Balny.[76]

2.1.3 Application of pressure and temperature to investigate $\Delta C_p^{\ddagger}$

Non-linearity in the pressure-dependence of enzymatic rates, where tunnelling is not contributing significantly, can occur because of protein denaturation,[78] changes in compressibility ($\Delta\beta^{\ddagger}$),[76] and changes in the rate-limiting step.[20] The use of pressure in this work investigated a non-linearity in the pressure-temperature (P/T) dependence of WT MalL. Here, WT MalL exhibited significant decreases in rate, with increasing pressure, which was reversible, and therefore not attributable to denaturation. This was compared to the P/T dependence of V200S MalL, so that the data were comparative, to try and minimize convolution through potential changes in rate-limiting step over the P/T plane.

WT MalL is known to have a larger $\Delta C_p^{\ddagger}$ value than V200S MalL, so to investigate whether it is reflective of dynamics linked to turnover, the dynamics of both systems were perturbed with pressure. WT MalL was found to have a larger $\Delta\beta^{\ddagger}$ than V200S MalL, reflective of WT MalL presenting higher levels of dynamics linked to turnover. Additionally, the $\Delta C_p^{\ddagger}$ value was found to be highly pressure dependent in WT MalL, and pressure independent in V200S MalL. The $\Delta\alpha^{\ddagger}$ value was found to be negative for WT mall and essentially zero for V200S MalL. The effect of pressure here is attributable to changes to the ruggedness of the FEL, which alters the accessibility of conformations of MalL, whilst retaining the size of the energy barriers (Figure 7). This demonstrated that the dynamics of V200S MalL are not linked to its catalysis to the same extent as WT MalL.

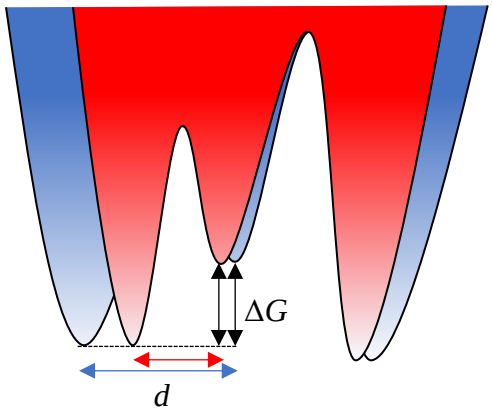

Figure 7. Schematic of the effect of pressure on the FEL of a protein (Blue: Before pressure, Red: After pressure). While ΔG remains unchanged, the structural differences of the protein are reduced (adapted from Librizzi *et al.*[74]).

2.2 The effect of viscosity on enzyme catalysis

In addition to pressure, the dynamics of WT and V200S MalL were also perturbed by viscosity, to further explore the effect of altered dynamics on $\Delta C_p^{\ddagger}$. At a simplistic level, viscosity can be thought of an increase in friction experienced by protein dynamics, with increases in friction affecting protein-solvent interactions and protein-protein intramolecular interactions.[79] According to Kramer's theory, the rate of an enzymes reaction is inversely proportional to a frictional coefficient, which is represented by the solvent viscosity according to Stokes' law.[79,80] However, the effect of increased viscosity on enzymatic rate cannot always be fully attributed to solvent friction, and the additional effect of internal friction is also considered.[79] In 1992 Ansari *et al.* presented an equation that can be applied to the viscosity dependence of an enzymes rate, to quantify the contribution of its internal friction[80] (this is detailed further in chapter 3, Eq 32).

It should be noted that the internal friction value presented by the Ansari equation is not the solely accepted interpretation of the influence of viscosity on enzymatic rates. The existence of internal friction is rivalled by the notion that all protein dynamics are linked to the solvent,[81] although this does not explain movements that can occur in the absence of solvent.[79] Additionally, where the Ansari equation does not hold, an equation containing a power function has been proposed.[82] Whilst there are arguments for and against the use of either equation, it is difficult to tell which is valid in the narrow viscosity range available for accurate experimental study.[79] In this work the Ansari equation is applied successfully to the data and is used to report on the internal friction of WT and V200S MalL.

In terms of conformational change, viscosity effects have been found to affect slower dynamics more significantly than faster (fs-ps) dynamics.[83] Parallels can be drawn between the effect of viscosity on protein dynamics, when compared to pressure. For example, internal friction caused by viscosity is also thought to affect the ruggedness of the protein FEL.[84] Furthermore, it has been proposed, that like pressure, viscosity affects the volume and consequentially the compressibility of a protein, by altering the cavities and solvation of the protein.[85]

Priev *et al*. proposed this viscosity driven alteration in volume and compressibility and found that large molecules such as proteins are dominated by the internal friction effect and not the co-solvent effect of viscosity. With this increase in viscosity, there was a negative impact on volume and apparent adiabatic compressibility of the protein. The reverse was true for small molecules such as single amino acids, where the co-solvent viscosity effect dominated.[85] To explain these findings, Priev *et al*. explored the effects of glycerol on the friction of protein dynamics. At the solvent surface of a protein, the presence of glycerol is generally unfavourable.[86] It is thought that the hydrogen bonding of glycerol to water, leads to ordered solvent around the protein, in turn reducing the volume and adiabatic compressibility of a protein.[85] As a consequence of this increased compression, water is pushed out of the protein core, leading to intramolecular bonding,

and an increase in internal friction. This reduction/collapse in cavities decreases the volume and compressibility of a protein.[85]

Whilst variation in co-solvents and enzyme systems will lead to different effects of viscosity on turnover, mutations of an enzyme offer a viable way to probe the link between the free energy landscape and enzyme turnover.[79] In this work, glycerol is used as a viscogen, with the absence of competitive inhibition, and consistent substrate saturation ensured by Michaelis-Menten plots. Both WT and V200S MalL present a significant value for internal friction at 20 °C. Additionally, $\Delta C_p^{\ddagger}$ is found to be sensitive to increases in viscosity for WT MalL, but not for V200S MalL outside of error. This further validated the findings on the sensitivity of $\Delta C_p^{\ddagger}$ to pressure.

2.3 Kinetic isotope effects

A more precise and direct way to perturb enzyme dynamics, and specifically their vibrational motion, is the application of KIEs. The scope and history of the field of studying KIEs on enzyme reactions is vast. In the context of this work, KIEs are applied to specifically perturb the vibrational motion of a reaction, to investigate the effect on the value of $\Delta C_p^{\ddagger}$, and the implications that can be drawn from this regarding the MMRT.

2.3.1 The effect of deuteration on the potential energy surface

The deuteration of hydrogen is appealing in the study of vibrational motion, due to the minimal impact deuteration has on the potential energy surface (PES) of hydrogen. As aforementioned in the context of heat capacity, energy can be partitioned into vibrational, rotational, translational and electronic contributions.[42] As a consequence of this split of energy, according to the Born-Oppenheimer approximation[87], the potential energy surface of a molecule consists of the electronic energy of nuclei at a certain position.[88] Therefore, in the case of deuteration, the electronic energy contribution from electrons and nuclei remains the same, retaining the PES.[88] By process of elimination, the energy differences contributing to enzymatic kinetic isotope effects are vibrational, rotational, and translational, with vibrational energy being the main contributor to changes in rate.[88]

2.3.2 The effect of deuteration on zero-point energy (ZPE)

The vibrational frequency of a bond is made of up of stretching and bending modes, with the bending mode being more energetically favourable than the stretching mode, meaning the oscillation is anharmonic (Figure 8).[88,89] The additional mass of deuterium, when compared to hydrogen, reduces the frequency of the stretching mode of this oscillation.[90] This means that the heavier isotope does not stretch as far or as frequently, and thus the bond is less likely to break.[88] If the bond frequency that is affected is broken during a reaction, it is known as a primary KIE.[88]

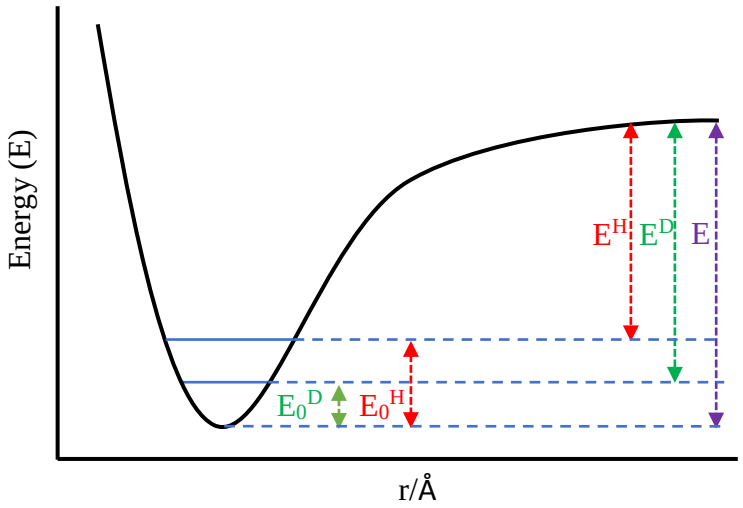

Figure 8 Schematic of an anharmonic bond stretch, demonstrating the effect of ZPE on the energy of a X-H and X-D bond. Adapted from Bell.[91]

Knowing the difference in this frequency allows for the calculation of the alteration in ZPE of the bond, from which the expected reduction in reaction rate can be calculated (Figure 9). For example, the wavenumber of a C-H bond is ~2900 cm^{-1}, which results in a 4.52 kJ mol^{-1} difference in ZPE for an unassisted reaction, and a KIE of ~ 6.2 at 298 K.[91] When accounting for the contribution of bending modes, the absolute maximum difference in ZPE is 5.66 kJ mol^{-1}, resulting in a KIE of around ~10 at 298 K.[91] However, these values do not account for the vibrational modes and ZPE of the transition state,

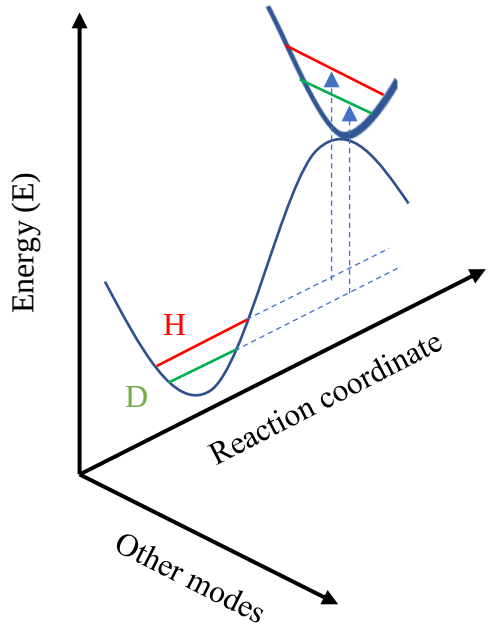

Figure 9. The effect of the ZPE of hydrogen and deuterium on the energy required to move from the ground to the transition state of the reaction coordinate. At the transition state the frequencies not directly correlated to that of the ground state are shown as an energy well. Adapted from Kohen.[90]

which can act to reduce the KIE.[91] In cases where the transition state is reactant/product-like, transition state vibrations can result in an inverse KIE if the force constants are larger than in the reactant.[88] Although this makes it difficult to assign a minimum expected KIE, it does mean that there is a maximum expected KIE in the semi-classical model.[91] Where this is exceeded, the presence of QMT can be inferred.[91]

2.3.3 Quantum mechanical tunnelling in enzyme reactions

QMT occurs due to the probability distribution of a particle's location, as described by Heisenberg's uncertainty principle. The principle states that the exact location of a particle cannot be known and will fall somewhere within this distribution.[92] This is because of the wave-particle duality principle, which means that particles have properties of both a particle with mass and of a wave. The wavelength of the particle is directly related to its mass and speed according to the de Broglie equation.[93] Where mass is large, the wavelength is small, meaning that the location of the particle is less variable in terms of distance. However, for reactions where small particles are transferred, such as hydrogen, the wavelength is large enough that it may be larger than the width of the energy barrier of a reaction.[94] This means that the reaction does not have to reach the height of the free energy barrier for it to occur, and instead can tunnel through the energy barrier.

2.3.4 Implications drawn from KIE temperature-dependences

Whilst significant QMT was ruled out in the application of KIEs to study the reaction of GDH in this work, it is worth noting some of the applications of KIEs to study the QMT of a reaction. Tunnelling predominates reactions at lower temperatures, meaning the KIE effect is large here. As temperature increases, the KIE approaches unity, as the reaction increasingly occurs by the classical energy barrier route.[95] The effect of the temperature-dependence of tunnelling was formally described by the Bell tunnel correction model.[91] However, as mentioned previously, the model does not hold true in all cases, and where large $\Delta\Delta H^{\ddagger}$ values are present, the discrepancy in temperature-dependence is explained by vibrational-modes linked to catalysis.[61] Extremely large kinetic isotope effects, where QMT is thought to be extensive, are also explained by additional vibrational modes linked to catalysis.[63]

2.3.5 Secondary kinetic isotope effects

Secondary kinetic isotope effects occur where an isotope is introduced distally from the bond being broken during a reaction. Immediate secondary kinetic isotope effects can be split into α and β effects, where in the case of a C-H bond, the deuterium is on either the α or β carbon of a molecule in relation to the hydrogen being transferred.[90] Secondary kinetic isotope effects can also have an effect more distally, but the impact is reduced with distance.[90] The effects of α secondary isotope effects originate from in plane and out of plane bending,[90] whereas the effects of β secondary isotope effects are attributable to

hyperconjugation at the transition state of the reaction.[88] In this work, β secondary kinetic isotope effects are applied, to additively affect the vibrational frequency of the sugar molecule being studied, thus restricting the vibrational modes linked to the turnover of GDH.

2.3.6 KIEs in the context of investigating the MMRT

The absence of QMT contributing to rate in the case of GDH allowed for KIEs to be applied in a very direct way. The progressive deuteration of glucose catalysed by GDH allowed for cumulative restriction of the vibrational motion of the sugar, and any vibrational modes that link it with GDH. The effect on the value of $\Delta C_p^{\ddagger}$ was also cumulative, with the application of KIEs demonstrating the link between $\Delta C_p^{\ddagger}$ and dynamics linked to catalysis, further validating MMRT.

2.4 Molecular dynamics simulations

In this work, MD simulations were used to sample the hydride transfer distance between glucose/xylose and GDH. They were also used extensively to probe the dynamics of MAO-B and to explore the influence of the membrane on these dynamics. MD simulations can be applied to known structures of biological systems, such as proteins, to computationally examine the movement of atoms at timescales of femtoseconds to milliseconds.[96] In MD simulations, bonds do not form or break, and so once the topology of the system is defined, then it is studied as a constant over time, with a consequential constant pH.[97] The dynamics of the system are established by applying the rules of classical mechanics, usually Hamiltonian mechanics.[97] Equations of motion are repeatedly solved, by calculating the forces acting on the atoms of a system, which are obtained from the potential energy of the atoms.[98] This is achieved by applying a force field to the system, which defines the parameters of the system, in terms of bonded and non-bonded interactions, to allow for the potential energy to be accurately calculated.[97]

2.4.1 MD force fields

Force field parameters for bonded interactions include bond lengths, angles and torsions, whilst parameters for non-bonded interactions include van der Waals interactions and electrostatic interactions.[99] Bonds are often described by harmonic potentials but can include anharmonic potentials in some cases.[97] Force-fields can implement exclusions and reductions to varying degrees, to ensure the interactions are accurately represented. For example, where a bonded interaction occurs, non-bonded interactions are often discounted to ensure that the properties of the interaction are upheld.[97] Additionally, the non-bonded interactions between the terminal atoms of a torsion are often reduced, to prevent them from overpowering long-range interactions.[97] The way in which force fields parameterize these interactions varies, and are not necessarily interchangeable.[99] The choices behind

the mathematics invoked by various force fields are often driven by balancing speed and accuracy, with applications also dependent on the type of system being studied.[97]

2.4.2 MD conditions

MD simulations often seek to represent experimental findings as accurately as possible. Thus, proteins are solvated and placed in periodic boundary conditions.[97] Although proteins cannot directly interact, due to the zero momentum assigned to the centre-of-mass, the solvent of a periodic box can perturb the solvent of other periodic boxes, representing experimental bulk behaviour.[97] Depending on the aim of the study, proteins can be studied at a constant number of atoms, volume and energy (NVE), have additional temperature regulation (NVT) or have additional temperature and pressure regulation (NPT).[97]

In this work, NVT was used for heating systems, and NPT was used for equilibration and production MD simulations. MAO-B MD simulations used a Langevin thermostat/Monte Carlo barostat, and GDH MD simulations using a Langevin thermostat/Berendsen barostat. The Langevin thermostat introduces the effect of solvent friction and random collision to the equations of motion, which represents the dynamical dampening of the protein that would occur at a specific temperature.[97] The Monte Carlo barostat intermittently adjusts the volume of the system using Monte Carlo moves, whereas the Berendsen barostat couples the system to a pressure bath that scales the volume.[97]

Both simulations used particle-mesh Ewald (PME) summation for long-range electrostatics. Electrostatic interactions occur over long ranges and are therefore computationally expensive.[97] This is of particular issue when simulating a membrane lipid bilayer, as phospholipids have high charge density's and low dielectric constants, resulting in important long range electrostatics.[100] Rather than using an electrostatic cut off that can misrepresent the properties of a system, the use of PME is popular.[100] Through treatment of the Ewald summation, long range electrostatics decay much more rapidly.[97] Additionally, PME applies a grid to this treatment of the electrostatics, with each part representing the electrostatics for that area.[97] Both of these differences mean that although there is not a strict cut-off, PME results in a less computationally demanding calculation of long range electrostatics.[97]

2.4.3 The process of MD simulations

The general process of MD simulations can be broken down into five main stages: system preparation, minimization, heating, equilibration and production.[97] In the case of MAO-B and GDH, preparation involved modelling missing loop and termini regions, and placing MAO-B into a lipid bilayer. Hydrogens were added to the structures, and the correct protonation states were determined. Finally, the structures were solvated ready for minimization. Minimization relaxes the system into a local energy minima, so that when the simulation begins, the movement is not too large compared to the selected timestep.[97]

Time is then allowed for the system to equilibrate so that the MD simulations that are analysed are representative of the average movement of the system in equilibrium.[97] When a membrane is present, this equilibration needs to be relatively extensive (on the ns scale).[100] In the case of MAO-B, the system was equilibrated for 50 ns, by which time the route-mean-square deviation (RMSD) and area per lipid measurements had settled. After this point, the simulation can be used for analysis, and is referred to as production MD simulation.

2.4.4 Applications of MD simulations

There are numerous analyses that can be carried out on MD simulations. In the case of MAO-B, route-mean-square fluctuation (RMSF) and principle component analysis (PCA) were used to examine the differences in flexibility of different mutations. PCA extracts the different eigenvectors that are present during the MD simulation, allowing for the largest movements to be examined and compared.[101] Additionally, caver 3.0[102] was applied to numerous snapshots of the MAO-B MD simulations, to examine the size and frequency of tunnels that allow accessibility to the substrate binding site of the enzyme. This enabled analysis of the symmetry of the dimer, substrate entrances, and the influence on these properties when substrate was present in the active site. In addition to MD simulations being utilized in this work to validate and investigate experimental MMRT findings, computational FIRST calculations were also applied.

2.5 Floppy Inclusions and Rigid Substructure Topography

.

FIRST is a high throughput computational algorithm, which applies graph theory to establish areas of rigidity and flexibility in a protein. When it was conceived it was ~ 1 million times faster computationally than the application of MD simulations.[103] Where MD simulations assess movement with respect to time using a force field, FIRST applies a constraint network to a protein, highlighting areas of rigidity and flexibility by determining which dihedral bonds are rotatable/locked.[104] However, whilst FIRST is computationally less demanding than MD simulations, the lack of solvation, and inclusion of only specific constraints instead of a fully considered force field, mean that the technique forgoes some accuracy in return for increased speed and reduced cost.

FIRST defines areas of flexibility and rigidity by applying pebble game to assign degrees of freedom to atoms (pebbles) and their constraints (bonds), with each atom represented as three pebbles.[103] Of the six degrees of freedom available to each atom, two are lost for hydrophobic interactions, five are lost for a covalent bond or hydrogen bond and all six are lost where the interaction is deemed locked, which is the case for double, peptide or aromatic covalent bonds.[104] Long range electrostatic and van der Waals are weak and lack directionality, so are not considered in FIRST calculations.[103]

Rigid cluster decomposition (RCD) is the application of FIRST over a range of energy cut offs (Ecuts), which means that at a zero-energy cut off the protein is mostly rigid, but

when the energy cut off is increased, only the strongest hydrogen bonds and salt bridges remain.[105] From this, a protein can be assessed over a range of Ecuts, giving richer information on the breakdown of its rigidity, by informing on the fraction of residues in rigid clusters at each Ecut. This application of FIRST is applied to compare the rigidity of WT and V200S MalL. Additionally, FIRST RCD was used as a high throughput screen of MAO-B, detailed in chapter 5, to identify: the contribution of each residue to the rigidity of the protein, mutations that subsequently increased this rigidity, and areas distal to the mutation site that were affected by the mutations. The sensitivity of MAO-B to rigidification was then demonstrated by the experimental ablation of the activity of these mutants.

Chapter 3:
Linking MMRT to the Free Energy Landscape

The first step in validating the MMRT and its potential reflection of enzyme dynamics involved in catalysis entailed perturbing the free energy landscape of an enzyme and monitoring the effect of this on the value of $\Delta C_p^{\ddagger}$. In this study, the aforementioned WT and V200S MalL were used, to provide comparative examples of enzymes with a large (−4.5 kJ mol^{-1}1 K^{-1}) and a small (−0.9 kJ mol^{-1} K^{-1}) $\Delta C_p^{\ddagger}$ value respectively. Reduced dynamics in the ground state of V200S MalL when compared to WT MalL were established using FIRST calculations and red edge excitation shift (REES) fluorescence experimentation. To ascertain if these dynamical differences were linked to catalysis, and therefore the difference in the $\Delta C_p^{\ddagger}$ of the two enzymes, the FEL was perturbed by both pressure and viscosity, and the temperature-dependence of the turnover of both enzymes in these different conditions was measured. The sensitivity of the WT MalL $\Delta C_p^{\ddagger}$ value and the insensitivity of the V200S MalL $\Delta C_p^{\ddagger}$ value, to viscosity and pressure, demonstrated that dynamics are influencing the curvature of enzyme temperature-dependences. This in turn validates the MMRT and its implication that the difference in heat capacity between the ground and transition state of an enzyme, the majority of which is composed of differences in vibrational modes, is directly affecting the curvature and subsequent T_{opt} of enzymatic temperature-dependences.

This declaration concerns the article entitled:									
A complete thermodynamic analysis of enzyme turnover links the free energy landscape to enzyme catalysis									
Publication status (tick one)									
draft manuscript		**Submitted**		**In review**		**Accepted**		**Published**	✓
Publication details (reference)	Jones, H.B., Wells, S.A., Prentice, E.J., Kwok, A., Liang, L.L., Arcus, V.L. and Pudney, C.R., 2017. A complete thermodynamic analysis of enzyme turnover links the free energy landscape to enzyme catalysis. *The FEBS journal*, *284*(17), pp.2829-2842.								
Candidate's contribution to the paper (detailed, and also given as a percentage).	The candidate contributed to/ considerably contributed to/predominantly executed the… Formulation of ideas: Pressure and viscosity experiments formulated by HBLJ and CRP Pressure analysis carried out by VA, LLL and CRP REES and Stopped flow experiments formulated by CRP FIRST calculations formulated by SW (30%) Design of methodology: Methodology for pressure experiments designed by HBLJ and CRP Methodology for viscosity experiments designed by HBLJ Methodology for stopped-flow and REES designed by CRP Methodology for FIRST calculation designed by SW (50%) Experimental work: Protein expression and purification by HBLJ Pressure and viscosity steady-state enzyme experimentation by HBLJ Stopped-flow experimentation by CRP and HBLJ REES experimentation by AK FIRST calculations by SW Formulation of equations and analysis of pressure experiments by VA, LLL and CRP (70%) Presentation of data in journal format: Paper was written by CRP and reviewed/edited by all authors Methodology by HBLJ (15 %)								

Statement from Candidate	This paper reports on original research I conducted during the period of my Higher Degree by Research candidature.		
Signed	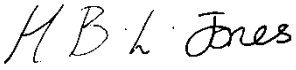	**Date**	17/01/19

A complete thermodynamic analysis of enzyme turnover links the free energy landscape to enzyme catalysis

Hannah BL Jones[‡], Stephen A Wells[§], Erica J Prentice[†], Anthony Kwok[‡], Liyin L Liang[†], Vickery L Arcus[†]* and Christopher R Pudney[‡]*

[†]School of Science, Faculty of Science and Engineering, University of Waikato, Hamilton 3240, New Zealand.

[‡]Department of Biology and Biochemistry, [§]Department of Chemical Engineering, Faculty of Science, University of Bath, Bath, BA2 7AY, United Kingdom

Running title: *Linking energy landscapes to enzyme catalysis*

Keywords: *Enzyme, heat capacity, expansivity, free energy landscape, pressure.*

Abbreviations: FEL; free energy landscape, pNPG; 4-nitrophenyl β-D-glucopyranoside, CSM; centre of spectral mass, REES; red edge excitation shift

Abstract: Our understanding of how enzymes work is colored by static structure depictions where the enzyme scaffold is presented as either immobile, or in equilibrium between well-defined static conformations. Proteins however exhibit a large degree of motion over a broad range of timescales and magnitudes and this is defined thermodynamically by the enzyme free energy landscape (FEL). The role and importance of enzyme motion is extremely contentious. Much of the challenge is in the experimental detection of so called 'conformational sampling' involved in enzyme turnover. Herein we apply combined pressure and temperature kinetics studies to elucidate the full suite of thermodynamic parameters defining an enzyme FEL as it relates to enzyme turnover. We find that the key thermodynamic parameters governing vibrational modes related to enzyme turnover are the isobaric expansivity term and the change in heat capacity for enzyme catalysis. Variation in the enzyme FEL affects these terms. Our analysis is supported by a range of biophysical and computational approaches that specifically capture information on protein vibrational modes and the FEL (all atom flexibility calculations, red edge excitation shift spectroscopy and viscosity studies) that provide independent evidence for our findings. Our data suggest that restricting the enzyme FEL may be a powerful strategy when attempting to rationally engineer enzymes, particularly to alter thermal activity. Moreover, we demonstrate how rational predictions can be made with a rapid computational approach.

Understanding the structure and motion of proteins lies at the heart of our understanding of how enzymes achieve spectacular rate enhancements.[106] In recent years detailed computational studies have clearly demonstrated the importance of the electrostatic environment.[107] Enzymes appear to pre-organise the electrostatics of the active site to promote formation of the transition state.[108] Similarly, innovative experimental approaches have demonstrated the importance of conformational sampling of proteins in mediating substrate binding and formation of the reactive complex geometry that precedes the chemical step.[45,109,110] However, the presence and effect of conformational sampling on enzyme turnover is highly contentious. The FEL for an enzyme is a description of protein structure as a multidimensional energy surface, composed of a series of 'hills' and 'valleys' separating energetic minima. Discrete conformational sub-states lie within these minima. Alternative sub-states are accessed by crossing the energetic barriers between minima or altering the FEL itself. That is, the FEL describes the equilibrium of conformational states a protein can adopt. Vibrational free energy contributes very significantly to the shape of the FEL by affecting the distribution of conformational sub-states within this equilibrium.[111] The frequency of vibrational modes and their population distribution affects the ruggedness of the FEL.[111] For enzyme turnover, it is the specific features of the FEL that affect the rate of enzyme turnover that are important. However, accessing this level of information in a quantitative manner is typically the preserve of high level simulation studies.

Defining the thermodynamics of an enzyme with respect to its chemical turnover can be achieved by monitoring the change in observed rate in a matrix of pressure/temperature conditions. Numerically fitting these data then gives $\Delta H^{\ddagger}$, $\Delta S^{\ddagger}$, $\Delta G^{\ddagger}$, $\Delta C_P^{\ddagger}$, $\Delta V^{\ddagger}$, $\Delta\beta^{\ddagger}$ and $\Delta\alpha^{\ddagger}$ reflecting the changes enthalpy, entropy, Gibbs free energy, heat capacity, activation volume, compressibility and expansivity between the enzyme-substrate complex and the enzyme transition-state complex, respectively. The enzyme kinetics for only a relatively few enzymes has been treated by combined *p*/*T* studies.[112–114] In these cases, the *p*/T plane has not been fitted with a numerical model meaning at least $\Delta C_P^{\ddagger}$ and $\Delta\alpha^{\ddagger}$ are not determined. We have recently explored the use of a new model that defines the temperature-dependence of enzyme catalyzed rates, that we have called termed macromolecular rate theory (MMRT),

$$lnk = ln\frac{k_B T}{h} - \left[\frac{\Delta H^{\ddagger}_{T_R} + \Delta C_P^{\ddagger}(T - T_R)}{RT}\right] + \left[\frac{\Delta S^{\ddagger}_{T_R} + \Delta C_P^{\ddagger}(lnT - lnT_R)}{R}\right] \qquad \text{(Eq19)}$$

where T_0 is an arbitrary reference temperature. $\Delta C_P^{\ddagger}$ determines the change in $\Delta H^{\ddagger}$ and $\Delta S^{\ddagger}$ with temperature and defines the temperature-dependence of the Gibbs free energy between the ground state and the transition state ($\Delta G^{\ddagger}$). The dominant contribution to $\Delta C_P^{\ddagger}$ for enzymes is the distribution and frequency[115,116] of the large number of vibrational modes of the molecule and its closely associated solvent molecules. Finding that $\Delta C_P^{\ddagger}$ is non-zero for enzyme catalysis demonstrates (in the absence of other contributing

factors[42]) a change in the distribution of vibrational modes between the enzyme-substrate complex and the enzyme-transition state complex. Equivalently, a negative value of $\Delta C_P^{\ddagger}$ implies that $<(\delta H)^2>$ (the mean squared distribution of enthalpies) for the enzyme substrate complex is greater than $<(\delta H^{\ddagger})^2>$ for the enzyme-transition state complex at a given temperature. The magnitude of $\Delta C_P^{\ddagger}$ can therefore be used as an excellent proxy for changes to the enzyme FEL, and more specifically for the changes in vibrational modes during enzyme turnover (conformational sampling). Pressure effects are system specific[113] but should perturb a large $\Delta C_P^{\ddagger}$ since pressure affects the pre-existing equilibrium of conformational states, favouring smaller volumes.[117,118]

Hobbs *et al* have studied a model sugar cleaving enzyme oligo-1,6-glucosidase 1 (MalL; EC 3.2.1.10) and have found that the wild-type (WT) enzyme displays a significant negative $\Delta C_P^{\ddagger}$ ($\Delta C_P^{\ddagger}$ = -11.6 kJ mol^{-1} K^{-1}) that is dramatically reduced in the V200S variant enzyme ($\Delta C_P^{\ddagger}$ = -5.9 kJ mol^{-1} K^{-1}) as well as a significant increase in the optimum temperature (T_{opt}) where k_{cat} is maximal. These changes are not accompanied by a structurally different enzyme form, with the X-ray crystal structures of the wild-type (WT) and V200S enzymes being essentially invariant.[1] Molecular dynamics simulations suggest that the origin of the difference in $\Delta C_P^{\ddagger}$ is due to rigidification of the ground state relative to the transition state for V200S MalL when compared to the WT enzyme.[1] That is, the FEL for the enzyme substrate complex is greatly constrained at the transition state implying significant changes to the distribution of vibrational modes along the reaction coordinate. WT MalL and the V200S variant therefore presents a powerful model system with which to probe the distribution of vibrational modes during enzyme turnover and the relationship to the protein FEL.

Herein, we compare WT and V200S MalL and find that $\Delta C_P^{\ddagger}$ is only pressure-dependent for the WT enzyme and that this is correlated with a more flexible protein, with a broader equilibrium of protein conformational states in the enzyme substrate complex; a broader FEL. Our findings suggest that the vibrational modes of the protein do significantly affect enzyme turnover and that this can be achieved through modulation of $\Delta\alpha^{\ddagger}$. V200S has higher T_{opt} and a faster rate at T_{opt}. Therefore, our findings suggest that, at least in this case, the faster enzyme has a restricted FEL that minimises $\Delta C_P^{\ddagger}$ and thus changes the temperature-dependence of the rate. Contrary to many assertions, for at least some enzymes, decreasing the contribution from conformational sampling for the enzyme substrate complex is a potential path to achieving more effective (faster) enzymes.

Results and Discussion

Combined pressure/temperature-dependence studies

We have measured the combined pressure and temperature-dependence of WT and V200S MalL steady-state turnover by monitoring the conversion of 4-nitrophenyl β-D-glucopyranoside (pNPG) to 4-nitrophenol (pNP), monitoring the increase in absorption at 420 nm attributable to product formation. Figure 10 shows that substrate binding is accompanied by an increase in MalL tryptophan (Trp) fluorescence emission. We find a decrease in Trp emission that occurs in the dead-time of the stopped-flow instrument (meaning a process > 2000 s^{-1}). This time-scale is far faster than the evolution of the absorption feature at 420 nm at the same enzyme concentration, suggesting that substrate binding is fast relative to enzyme turnover (Figure 10 *inset*). Moreover, from Figure 10, we find that the decrease in Trp emission saturates with an equilibrium constant (K = 0.07 ± 0.1 mM) similar to the measured K_m value (K_m = 0.012 ± 0.001 mM) and so we suggest that this signal reflects ligand binding. On longer-timescales, we find an increase in Trp emission that is kinetically similar to the rate of product formation and we suggest reflects a small amount of fluorescence attributable to formation of the product. We therefore infer that ligand binding represents an extremely fast step relative to product formation and so our kinetic data are not convolved of ligand binding. Without a full binding study we cannot unequivocally determine that our steady-state kinetic data are not convolved of ligand binding steps, but based on the evidence in Figure 10 this seems the most likely conclusion. Therefore, given the direct nature of the assay, we infer the observed kinetics reflect product formation. We perform the p/T turnover studies in 4-(2-hydroxyethyl)-1-piperazineethanesulfonic acid (HEPES) buffer so that there is only minor change in pK_a across the p/T range, $\Delta pK_a/\Delta T = -0.014$ ($°C^{-1}$)[119] and $\Delta pK_a/\Delta p = 0.0008$ (MPa^{-1})[120]. In

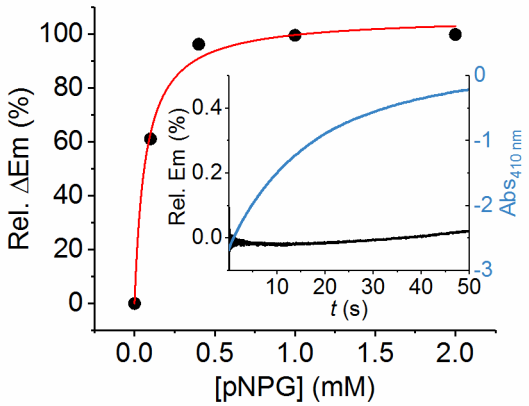

Figure 10. The concentration dependence of the relative change in emission of MalL trp residues vs ligand concentration. The red fitted line is the fit to a simple weak binding isotherm. Inset, stopped-flow studies of ligand binding following the change in MalL Trp emission in rapid-mixing with pNPG. The evolution of the absorbance feature attributable to product formation (blue) in the presence of a high concentration of enzyme (10 μM) and the emission of MalL trp residues (black).

Table 1. Extracted parameters from kinetic and thermodynamic studies.

	WT MalL		V200S MalL
Steady-state kinetics			
k_{cat} (s^{-1})[a]	47.2 ± 1.2		60.7 ± 1.6
Km (mM)[b]	0.012 ± 0.001		0.12 ± 0.01
T_{opt} (K)	330.8		348.4
p/T dependence			
	Eq 28	Eq 28[c]	Eq 28
$\Delta V^{\ddagger}_{P_0}$ (10^{-5}cm^3 mol^{-1})	−8.8 ± 7.1	−2.7 ± 2.3	−4.0 ± 3.1
$\Delta\beta^{\ddagger}$ (10^{-9} Pa^{-1})	−5.5 ± 4.0	−6.1 ± 3.0	−2.6 ± 8.5
$\Delta\alpha^{\ddagger}$ (K^{-1})	−0.03±0.02	−0.04 ± 0.03	0.02 ± 0.06
$\Delta C_P^{\ddagger}$ (kJ mol^{-1} K^{-1})	−4.50±1.5	−	−0.9 ± 0.6
$H^{\ddagger}$ (kJ mol^{-1})	107.0±9.8	111.7±13.7	80.1±4.8
R^2, RMSE	0.97 ± 0.02, 0.18 ± 0.06	0.98 ± 0.02, 0.15 ± 0.06	1.0 ± 0.01, 0.05 ± 0.04
Viscosity dependence			
σ (cP)[b]	1.58 ± 0.76		4.48 ± 1.31
$\Delta S^{\ddagger}$ (kJ K^{-1} mol^{-1})	1.44 ± 0.02		1.30 ± 0.01
$\Delta H^{\ddagger}$ (kJ mol^{-1})	98.7 ± 6.0		55.5 ± 4.3
$\Delta\Delta C_P^{\ddagger}$ (kJ mol^{-1} K^{-1} ŋ$^{-1}$)	1.82 ± 1.41		1.1 ± 1.1

[a], calculated at *T*opt. [b], measured at 20 °C. c, Eq 28 modified as in Figure 12B. Error reported at standard error and standard deviation (for *p*/*T* data).

this buffer system and at pH 7 we find that k_{cat} = 32.5 s^{-1} at 20 °C and that the magnitude of $\Delta C_P^{\ddagger}$ = −5.9 kJ mol^{-1} K^{-1}. We have previously used a phosphate buffer system (pH 8) where, $\Delta C_P^{\ddagger}$ = −11.6 kJ mol^{-1} K^{-1} and regardless of buffer the trend between the wild-type and V200S variant remains. That is, $\Delta C_P^{\ddagger}$ is approximately halved, the temperature where the rate is maximal (T_{opt}) is higher and k_{cat} at T_{opt} is ~30% larger for V200S compared to WT MalL (Table 1). We note that K_m is essentially temperature independent for both WT and V200S MalL and our initial rate plots are entirely linear under all conditions studied (example plots shown in Figure 11A and 11B). Moreover, our extracted initial rates are fully reversible with changes in pressure. We are therefore saturating the enzyme under all conditions studied and there is no evidence for protein denaturation. The *p*/*T* dependence on MalL turnover kinetics are shown in Figure 11C and 11D (two-dimensional plots) and Figure 12 (three-dimensional plots) and the resulting data given in Table 1. A contour plot in the *p*/*T* plane shows elliptical contours familiar from the *p*/*T* studies for protein folding/unfolding at equilibrium (Figure 12D-F).

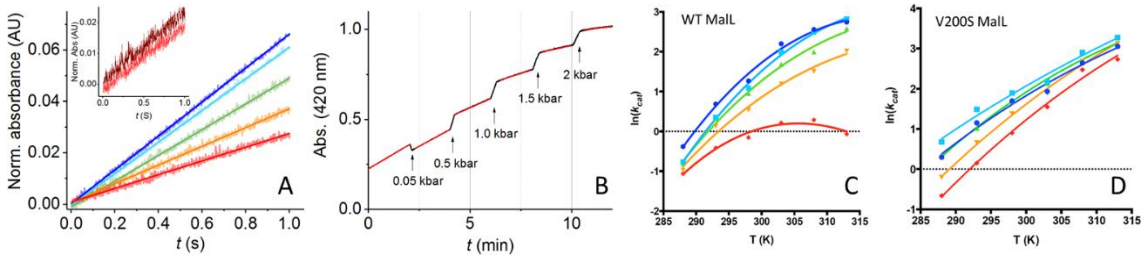

Figure 11 (A) Example absorption traces from pressure experiments. The normalised absorption is shown for each pressure and the solid line is the fit to a linear equation. The gradient of the fitted line then gives rise to the extracted initial rate. Note that based on this analysis, the data are entirely linear at each pressure studied and the signal-to-noise of the raw data is small. Inset, comparison of traces before (red) and after (dark red) high-pressure incubation to show reversibility. (B) The measured initial rate does not exhibit curvature throughout high-pressure experiments. Arrows illustrate the point at which the pressure is increased. Notice that the absorption changes as the optics of the cell equilibrate to the new pressure. The red line is the fit of a linear equation to the initial rate data and illustrates there is essentially no curvature over the time course of the measurement or at any pressure. (C and D) Combined pressure/temperature-dependence of k_{cat} for WT Mall (Panel C) and V200S MalL (Panel D). Solid lines are the fits as in the main text corresponding to Fig. 12.

A great deal of research has been described on the pressure-temperature (*p/T*) dependence of protein *stability* beginning with pioneering work by Brandts[121,122] and Hawley.[123] Hawley presented an equation for the free energy difference between the native and denatured states of a protein in the *p/T* plane by integration of the thermodynamic relationship $d\Delta G = \Delta V dP - \Delta S dT$ giving:

$$\Delta G_{P,T} = \Delta V_0(P - P_0) + \Delta\alpha'(P - P_0)(T - T_0) + \frac{\Delta\beta'}{2}(P - P_0)^2 + \Delta G_0 - \Delta S_0(T - T_0) - \Delta C_P\left[T\left(ln\left(\frac{T}{T_0}\right) - 1\right) + T_0\right] \quad \text{(Eq24)}$$

where $\Delta\alpha'$ and $\Delta\beta'$ are related to the coefficients of adiabatic thermal expansion ($\Delta\alpha$) and isothermal compression ($\Delta\beta$) respectively. Explicitly, $\Delta\alpha' = \Delta\alpha.\Delta V$ and $\Delta\beta' = \Delta\beta.\Delta V$. Eq 24 has been used by nearly all investigators since.[124] An important assumption of Eq 24 is that the coefficients $\Delta\alpha'$, $\Delta\beta'$ and ΔC_P are independent of temperature and pressure.

We have derived an equation for $\Delta G_{P,T}$ by starting with the formal definitions of $\Delta\alpha$ and $\Delta\beta$:

$$\Delta\alpha = \left(\frac{1}{\Delta V}\frac{\delta\Delta V}{\delta T}\right)_P, \qquad \Delta\beta = -\left(\frac{1}{\Delta V}\frac{\delta\Delta V}{\delta P}\right)_T \quad \text{(Eq25)}$$

Using $d\Delta G = \Delta V dP$ and integrating we arrive at:

$$\Delta G_{P,T} = \Delta G_{P_0,T_0} + \Delta V_{T_0}\left[exp[\Delta\alpha(T - T_0)]\right](P - P_0) - \frac{\Delta V_{P_0}}{\Delta\beta}\left[1 - exp[-\Delta\beta(P - P_0)]\right] \quad \text{(Eq26)}$$

Expanding using the Taylor series around T_0 and P_0 we arrive at the familiar terms from Eq 24:

$$\Delta G_{P,T} = \Delta G_{P_0,T_0} + \Delta V_{T_0}\Delta\alpha(T - T_0)(P - P_0) + \frac{\Delta V_{P_0}\Delta\beta}{2}(P - P_0)^2 \qquad \text{(Eq27)}$$

Transposing Eq 26 onto Eq 24 and substitution into an Eyring rate equation gives:

$$\begin{aligned} lnk = lnA - \frac{\Delta H^{\ddagger}_{T_0}}{RT} + \frac{\Delta C^{\ddagger}_{P}}{R}\left[ln\left(\frac{T}{T_0}\right) - 1 + T_0/T\right] \\ - \frac{\Delta V^{\ddagger}_{T_0}}{RT}(exp[\Delta\alpha^{\ddagger}(T - T_0)])(P - P_0) \\ + \frac{\Delta V^{\ddagger}_{P_0}}{\Delta\beta^{\ddagger}RT}\left[1 - exp[-\Delta\beta^{\ddagger}(P - P_0)]\right] \end{aligned} \qquad \text{(Eq28)}$$

Fitting Eq 28 to pressure, temperature, ln(k_{cat}) data for V200S MalL gives good agreement between theory and experimental data (Figure 12C, R^2=0.98, SSE=0.66). However, Eq 28 does not describe the same pressure, temperature, ln(k_{cat}) data for WT MalL (Figure 12A,12D with irregular elliptical contours). We have therefore fitted the temperature-dependence of ln(k_{cat}) data for WT MalL (using the 1st three terms of Eq 28) at the 5

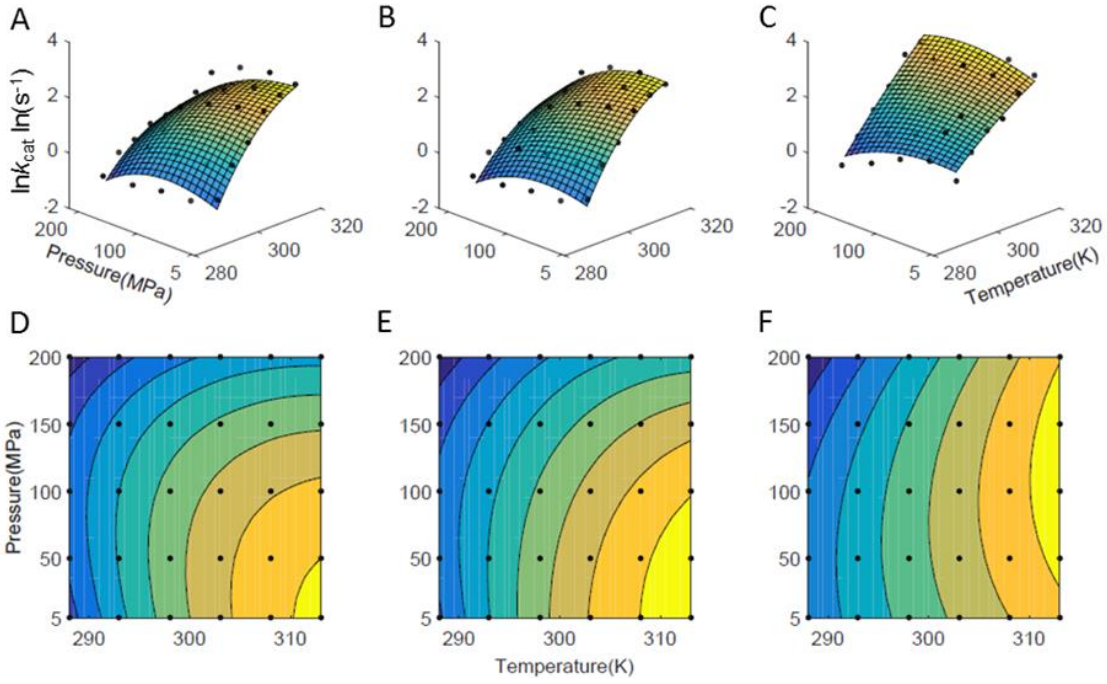

Figure 12 Combined pressure and temperature-dependence of the rate of (A; fit to Eqn (28) and B; fit to a modified Eqn (28) with a pressure-dependent term $\Delta C_p^{\ddagger}$ taken from Fig. 13) WT and (C; fit to Eqn (28)) V200S MalL turnover and with the associated contour plots, panels (D and E) and (F) respectively. The experimentally extracted data points are shown in black and the continuous coloured plane shows the fit as described in the main text. The colouring is to aid the eye.

different pressures and we find a strongly pressure-dependent $\Delta C_P^{\ddagger}$ for WT MalL with an essentially pressure-independent $\Delta C_P^{\ddagger}$ for V200S MalL (Figure 13). The extracted parameters (Figure 14) are given in Table 1. We note that the structures of WT and V200S MalL are essentially invariant[1] and so the difference in the pressure dependence is not due to different conformational states but must arise from another source. Pressure perturbs the pre-existing equilibrium of states on the FEL and so will affect any conformational sampling. The relationship we observe therefore suggests that the magnitude of $\Delta C_P^{\ddagger}$ reflects the role of conformational sampling and we explore this in more detail below.

Our *p*/*T* data allow us to further interrogate the relationship between pressure and $\Delta C_P^{\ddagger}$ to identify the thermodynamic driver for this relationship and so again link conformational sampling to the enzyme FEL. Using Maxwell's relations, the pressure dependence of $\Delta C_P^{\ddagger}$ is:

$$\left(\frac{dC_P}{dP}\right)_T = -T\left(\frac{d^2V}{dT^2}\right)_P = -T\left(\frac{d\alpha V}{dT}\right)_P = -TV\left[\alpha^2 + \left(\frac{d\alpha}{dT}\right)_P\right] \qquad \text{(Eq29)}$$

Acknowledging the linear pressure dependence up to high pressures (blue line, Figure 13 and the fact that α^2 is small and positive, the linear coefficient for Eq 28 is:

$$-T\left(\frac{d\Delta\alpha^{\ddagger}}{dT}\right)_P \Delta V_{P_0}^{\ddagger} \sim 1.3 \times 10^{-5}\, J.mol^{-1}.K^{-1}.Pa^{-1} \qquad \text{(Eq30)}$$

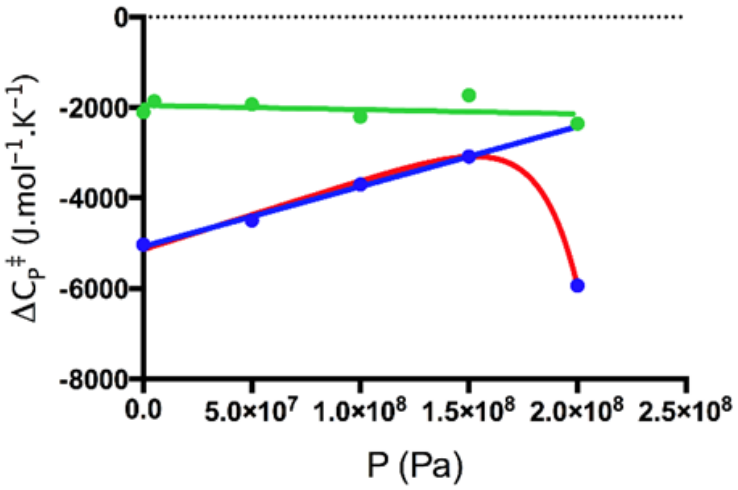

Figure 13 The pressure dependence of $\Delta C_p^{\ddagger}$ for both WT (blue data points) and V200S MalL (green data points). The solid lines are fits as described in the text. The green and blue lines are linear fits to the data and the red line is fitted as described in the text.

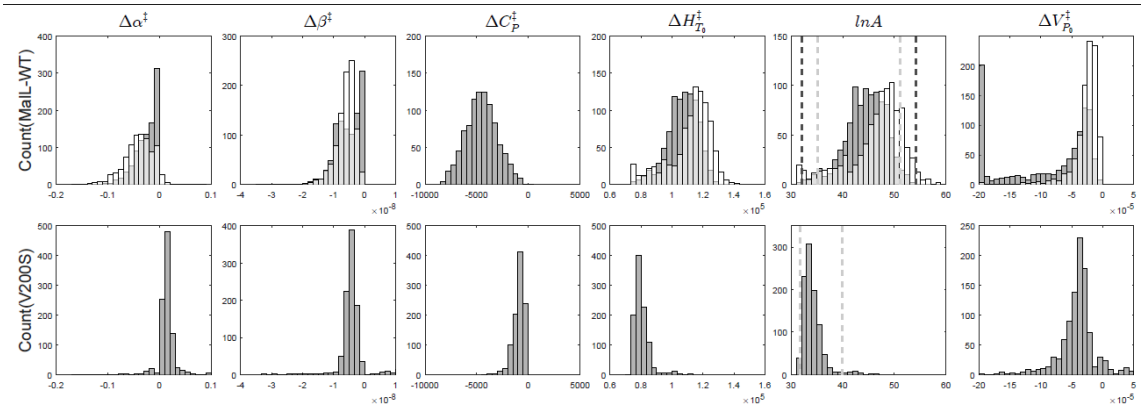

Figure 14 The statistical distribution of parameters from a 1000-iterations bootstrap analysis by fitting the measurements on MalL WT and V200S using Eqn (28) (clear bins). We also fitted MalL WT using a temperature-dependent $\Delta C_p^{\ddagger}$ term calculated from Fig. 13 to assess the difference in the parameters using the same 1000-iterations bootstrap analysis (grey bins).

These data imply that for WT MalL $\left(\frac{d\Delta\alpha^{\ddagger}}{dT}\right)_P > 0$ and this translates into a pressure-dependent $\Delta C_P^{\ddagger}$. Changes in the temperature-dependence of $\Delta\alpha$ have been seen previously for ligand binding using pressure perturbation calorimetry.[125] The red line in Figure 13 shows a curve of the expected shape for the integral of Eq 29, although there are insufficient points to justify fitting parameters using this more complex equation. Thus, when the parameters $\left(\frac{d\Delta\alpha^{\ddagger}}{dT}\right)_P$ and the corresponding $\left(\frac{\Delta C_P^{\ddagger}}{dP}\right)_T$ are non-zero, this gives rise to very complex behaviour for ln(k_{cat}) in the *p/T* plane and non-elliptical *p/T* contour plots (Figure 12) for enzyme turnover.

We therefore find that for V200S MalL both the absolute values of $\Delta\alpha^{\ddagger}$ and $\Delta C_P^{\ddagger}$ are less negative, the temperature and pressure dependence is dramatically decreased and k_{cat} at T_{opt} is larger compared to WT MalL. The magnitude of $\Delta\alpha^{\ddagger}$ is not outside of error for the comparison of WT and V200S MalL. However, the WT $\Delta\alpha^{\ddagger}$ is measurably negative within error as one expects for a pressure-dependent $\Delta C_P^{\ddagger}$ (Figure 13) and the V200S $\Delta\alpha^{\ddagger}$ is measurably zero within error as one expects for a pressure-independent $\Delta C_P^{\ddagger}$ (Figure 13) and this is the key point. The strong pressure dependence on $\Delta C_P^{\ddagger}$ for WT MalL therefore provides an independent line of evidence that $\Delta C_P^{\ddagger}$ reflects conformational sampling through protein vibrational modes and by definition the ruggedness of the FEL, but crucially that these modes are themselves able to affect enzyme turnover.

Experimental and Computational evidence for the role of global conformational sampling

We have recently demonstrated that the red edge excitation shift (REES) phenomenon for protein Trp residues can potentially report on intramolecular protein dynamics, reflecting

information on the 'ruggedness' of the free energy landscape (FEL).[126,127] That is, a larger REES effect reflects an increase in number of discrete species within the available equilibrium of conformational states; i.e. a more flexible protein.[126] The REES effect arises from photoselection of discrete conformational states reflected by differing solvent-solute interaction energies and has been described in depth recently.[126–129] The effect manifests as a red shift in emission spectra (increased inhomogenous broadening) as the energy of the exciting photons is decreased (Figure 15A). We use a model free approach to capture these data as the change in the centre of spectral mass (CSM) *versus* the change in excitation wavelength, $\Delta\lambda_{Ex}$ (Figure 15B). In proteins the fluorophore is tryptophan (selectively excited from 292 nm upwards) and the REES effect arises where the Trp exhibits a range of discrete solvation states. A large apparent REES effect should arise as a trivial consequence of multiple Trp residues in a single protein. However, *changes* to the REES effect for the same protein can be used to reflect changes in the protein FEL.[126] From Figure 15B, WT MalL shows a large REES effect as expected given its 17 Trp residues. We fit the experimental REES data (Figure 15B) to a phenomenological model based on an exponential function, similar to our previous fitting, primarily to capture the curvature that is always apparent in protein REES data sets.[126]

$$CSM = CSM_0 + Ae^{R\Delta\lambda_{Ex}} \qquad \text{(Eq31)}$$

Where CSM_0 is the CSM value independent of the excitation wavelength, λ_{Ex}, determined by the amplitude, *A*, of an exponential with a curvature, *R*. The magnitude of *A* and *R* characterise the REES effect and the ratio of these values is shown in Figure 15C and allows a useful comparison between data sets. An increase in *A* and a decrease in *R* (a larger *A*/*R* value) reflect a more pronounced REES effect and from our previous work, a more flexible protein characterised by a more rugged FEL. [126]

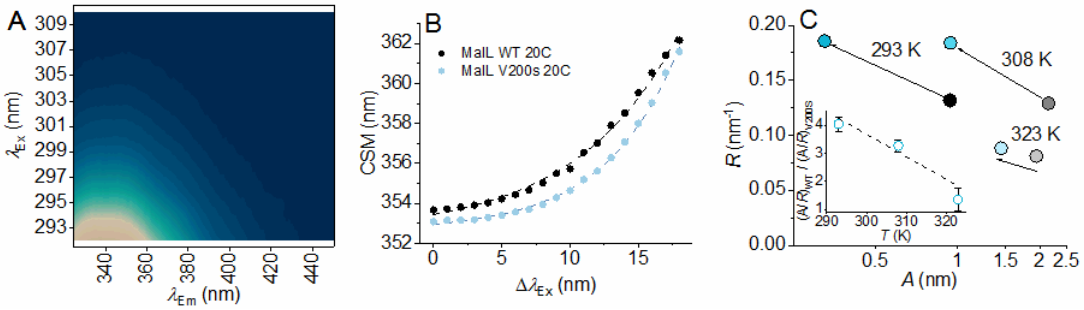

Figure 15 Fluorescence edge-shift data expose the difference in molecular flexibility between MalL and V200S MalL. (A) Example of the combined emission/excitation matrix of MalL Trp emission. The data are contoured from high (beige) to low (blue) emission intensity. (B) Example of the resulting edge-shift data extracted from panel A for MalL (black) and V200S MalL (light blue) at 20 °C. The dashed line is the fit to Eqn (31). (C) Plot of the parameters extracted from panel B showing the data for WT MalL and V200S MalL at 20, 35 and 50 °C, shown as shades of black and shades of blue respectively. Inset, ratio of the A/R value for WT and V200S MalL at each temperature studied. The dashed line is the fit to a simple linear equation and serves to show the trend in the data.

From Figure 15C we find that WT MalL gives a rather larger REES effect compared to V200S MalL with ΔA = 0.93 ± 0.14 and 0.32 ± 0.03 nm and ΔR = 0.13 ± 0.01 and 0.19 ± 0.01 nm^{-1} at 20 °C, respectively. Protein flexibility is strongly influenced by temperature and so we have monitored the REES effect at elevated temperatures that approach T_{opt} (Table 1) for both WT MalL and V200S MalL as shown in Figure 15C. From Figure 15C *inset*, the ratio of *A* and *R* values becomes more similar for WT and V200S MalL (A/R_{WT} / $A/R_{V200S} \rightarrow 1$) as the temperature tends towards the T_{opt}. These data show that the REES effect becomes more similar for WT MalL and V200S MalL at elevated temperatures, but also that the REES effect is consistently smaller for V200S MalL compared to WT MalL. These findings are consistent with comparisons between mesophilic and thermophilic proteins, where the protein flexibility is found to be similar at the respective T_{opt} of the enzymes.[33,130] The edge-shift data therefore suggest that V200S MalL is less flexible than WT MalL at the same reference temperature. That is, in line with our previous molecular dynamics simulations, we find that a smaller magnitude of $\Delta C_P^{\ddagger}$ (V200S MalL) is correlated with a less flexible protein in the ground state.

The edge-shift data above capture global changes and differences in protein flexibility. To achieve atomistic insight into protein flexibility, on a relevant timescale, we have turned to all atom flexible motion calculations from available X-ray crystal structures of WT and V200S MalL. These calculations capture information on protein rigidity and flexible motion, reflecting low frequency motions on the ~ microsecond timescale. Such timescales are often functionally relevant and so these calculations significantly augment our previous MD simulations, both temporally and in terms of structural analysis. We have analysed the rigidity of the MalL structure using pebble-game rigidity analysis as implemented in the program "FIRST" (see methods). The main control parameter is the energy cutoff (E_{cut}) which controls the inclusion of polar interactions in the constraint network. Both WT and V200S MalL display typical rigidity behaviour for a mixed alpha/beta structure,[130] as shown in Figure 16. From Figure 16A, MalL is largely rigid at

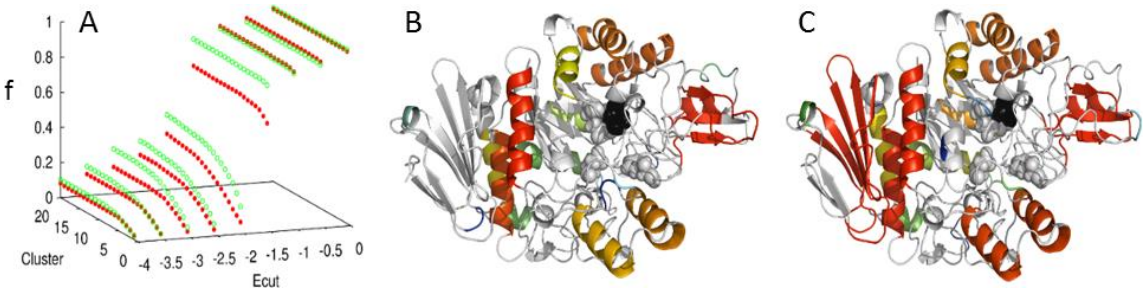

Figure 16 (A) The fraction of the protein main chain lying in the N largest RCs, for N = 1–20, as a function of the hydrogen bond energy cut-off E_{cut}, for the wild-type (red filled circles) and V200S mutant (green open circles) MalL structures. (B) Rigidity in the wild-type structure at E_{cut} = −2.0 kcal·mol^{-1}. Structure shown in light grey cartoon; the 20 largest RCs are shown in rainbow colour. Residue V200 is shown as black spheres, and active site glucose-binding residues are shown as white spheres. (C) Rigidity in the V200S mutant with the same cut-off and colouring as in panel B.

small E_{cut} values, and then becomes largely flexible as E_{cut} goes from -1 to -2 kcal mol^{-1} (Figure 16A). However, V200S MalL retains a higher fraction of rigidity than MalL at large negative E_{cut} values (Figure 16A). These data are then consistent with previous evidence from X-ray crystal data, molecular dynamics simulations, and with the current edge-shift data (above), in suggesting that MalL has more conformational freedom than V200S MalL. Most importantly, despite the V200S variant being located in the active site, the calculations show the difference in rigidity between MalL and V200S MalL is due to retention of rigidity in the extensive beta-sheet region (shown in Figure 16B and 16C), rather than the active site.

We have explored the flexibility of MalL and V200S MalL using geometric simulation, implemented in the FRODA module of FIRST.[131] Eigenvectors of low-frequency motion were generated by coarse-grained elastic network modelling implemented in ElNemo.[132] We focus on the lowest-frequency non-trivial modes of motion, which represent large scale motions that are likely to be on relatively long (microsecond) time-scales. Recent studies[105,133] have shown excellent agreement between flexible motion simulations and

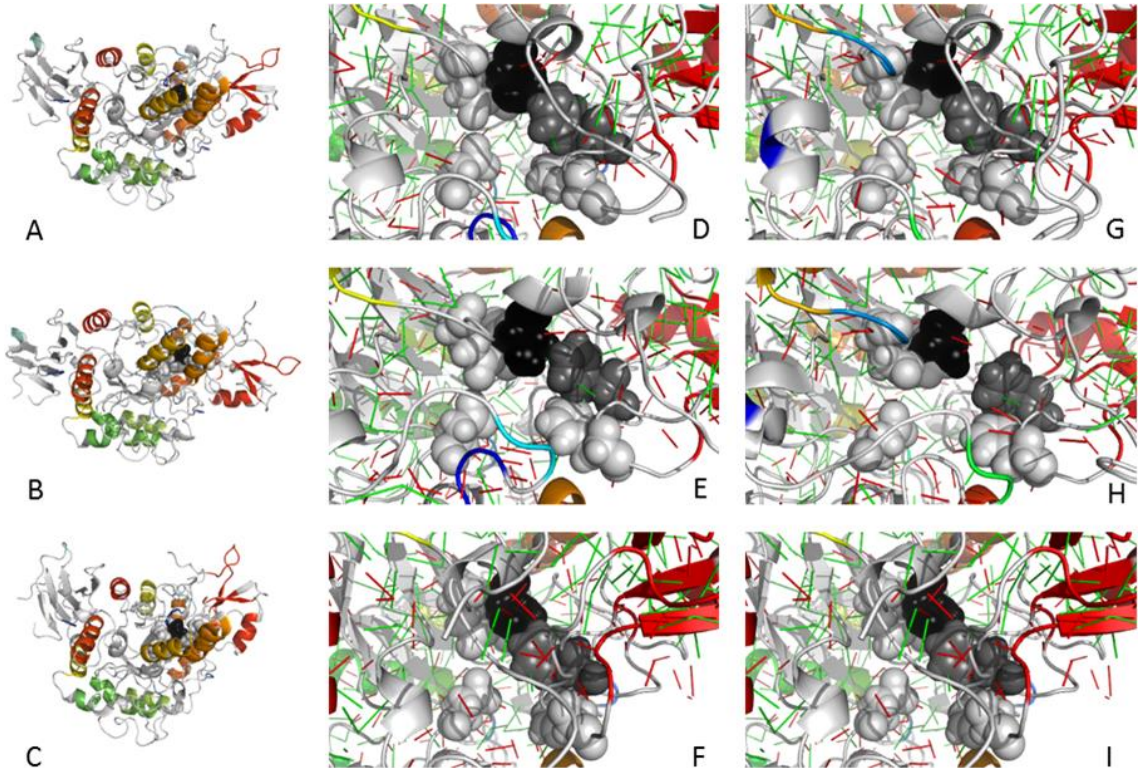

Figure 17 (A) MalL structure (PDB 4M56) coloured according to the presence of RCs. (B and C) MalL structure exploring motion biased parallel (B) and antiparallel (C) to its lowest frequency nontrivial elastic mode eigenvector in a geometric simulation using an E_{cut} value of −2.0 kcal·mol^{-1}. RMSD relative to the starting structure is ~ 4.2 Angstroms. (D) A close-up of the active site of MalL. The glucose-binding residues F144, D199, D332 and E255 are shown as light grey spheres; residue V200 is shown as black spheres; residue F163 shown as dark grey spheres. E and F close-up of active site of MalL structure during motion as in panel B (E) and panel C (F). G, a close-up of the active site of V200S MalL (PDB 4MAZ). H and I close-up of active site of V200S MalL structure during motion as in panel B (H) and panel C (I). Colouring is to aid the eye unless otherwise stated.

large-scale functional motion in enzymes, with results from the calculations found to be consistent with those produced by molecular dynamic simulations.[134] Example results are shown in Figure 17. These data show that both MalL and V200S MalL structures are capable of large amplitudes of flexible motion while retaining the network of covalent and noncovalent constraints[135] identified in the input structure (Figure 17A-C). The global character of this mode is essentially identical between WT and V200S MalL, as expected from the close similarity of the structures. We find that this lowest frequency mode couples large-scale motion of the entire structure with local variations in the geometry of the active site (Figure 17D-F for WT MalL). In the WT protein, a network of noncovalent (hydrophobic) interactions surrounds the active site, including an interaction between V200 and F163. The V200S mutation disrupts this interaction. This alters the variations in the active site geometry in the course of the protein's flexible motion, as shown in Figure 17G-I; note the opening of a gap between S200 and F163 in the mutant structure, which cannot occur in the WT protein.

Our rigidity analysis and modelling of flexible motion thus indicate that the V200S mutation, despite its minimal effect on the crystal structure, affects the enzyme dynamics in two ways: firstly, by an increase in rigidity distal to the mutation site, which will affect the global slow-mode dynamics; and secondly, by a change in the constraint network in the active site, altering the coupling between global slow dynamics and the active site. Our findings therefore suggest that there is a network of vibrational modes in the enzyme that couple directly to the active site volume. The observation of long range networks of vibrational modes in enzymes have been reported for a number of enzymes, for example horse liver alcohol dehydrogenase (HLADH),[136] dihydrofolate reductase (DHFR)[137] and protochlorophyllide oxidoreductase (POR).[138,139]

The combination of our *p/T* studies, REES data and structure-based calculations suggests that the distribution of vibrational modes is sensitive to changes in pressure for WT MalL but not V200S MalL and, consistent with our hypothesis, this correlates with a large and small magnitude of a negative $\Delta C_P^{\ddagger}$, respectively. More specifically, the finding that the distribution of vibrational modes related to enzyme turnover ($\Delta C_P^{\ddagger}$) is sensitive to pressure links the FEL to conformational sampling of the enzyme *and* also enzyme turnover.

Experimental evidence of the role of local versus global conformational dynamics.

Our all-atom calculations do not differentiate between conformational dynamics involved in enzyme turnover that are localised to the active site or involving a global network of residues that define the conformational dynamics. Varying solution viscosity is an established experimental tool to probe the involvement of global protein flexibility and is used extensively to study gated electron transfer, where significant conformational change (gating) is required to control the rate of an electron transfer step. We wished to provide experimental evidence for the role of global conformational sampling inferred from our structure-based calculations and so we have turned to viscosity dependence studies (by varying the concentration of glycerol) with MalL and V200S MalL, shown in Figure 18.

We note that varying glycerol concentration alone can only infer a viscosity change. We were concerned that the observed rates might be convolved of competitive inhibition with the viscogen and so for this reason we measured individual Michaelis-Menten curves to extract the reported k_{cat} values (example plots are shown in Figure 19). By definition, competitive inhibition will only affect the magnitude of K_m, but not V_{max} (and therefore k_{cat}). Our data are not therefore convolved of issues of competitive inhibition. The viscosity dependence of the extracted k_{cat} is fit to Eq 32 as described by Ansari *et al*,[80]

$$k_{obs} = \frac{k_B T}{h}\left(\frac{1+\sigma}{\eta+\sigma}\right) exp\left(\frac{\Delta S^{\ddagger}}{R}\right) exp\left(\frac{-\Delta H^{\ddagger}}{RT}\right) \quad \text{(Eq32)}$$

Where the observed rate varies according to an internal friction coefficient, σ, that reflects the contribution of the protein friction to the total friction of the system,[140,141] $\Delta S^{\ddagger}$ and $\Delta H^{\ddagger}$. Fitting our viscosity dependence data shown in Figure 18A, we find σ = 1.58 ± 0.76 and σ = 4.48 ± 1.31 cP for MalL and V200S MalL at 20 °C, respectively. This magnitude of σ is typically observed for gated electron transfer enzymes where very large protein conformational changes occur, typically falling in the range σ = 0.1-10 cP.[140–142] These data suggest that, consistent with flexible motion calculations, MalL does exhibit a significant role for *global* protein vibrational modes during turnover. We have monitored the temperature-dependence of k_{cat} at a range of experimentally accessible (given the viscosity dependence of k_{cat}) solution viscosities as shown in Figure 18B and 18C to give the viscosity dependence of $\Delta C_P^{\ddagger}$. The resulting parameters are given in Table 1 and shown in Figure 18E. The concentration of the viscogen is adjusted at each temperature to ensure the viscosity is the same at each temperature studied.[143] We find that $\Delta C_P^{\ddagger}$ is viscosity-dependent outside of experimental error with WT MalL and viscosity-independent within experimental error for V200S MalL, giving $\Delta\Delta C_P^{\ddagger}$ = 1.82 ± 1.41 and 1.10 ± 1.10 kJ mol^{-1} K^{-1} ŋ$^{-1}$, respectively. That is, viscosity (an increase in protein fictional coefficient) affects

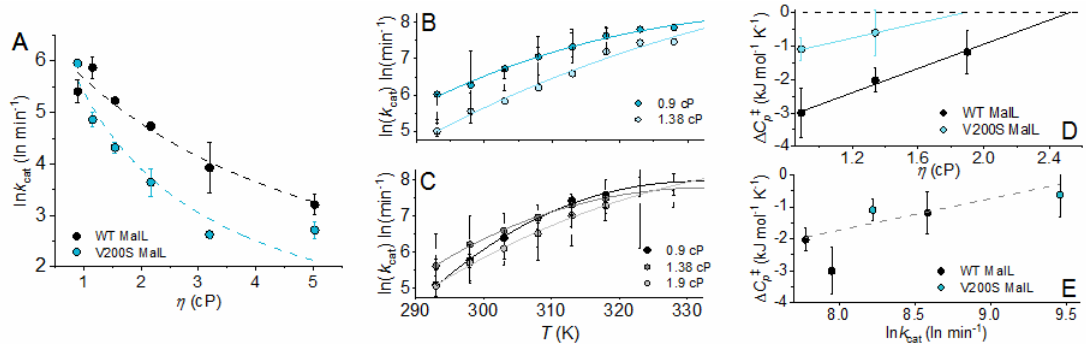

Figure 18 MalL- and V200S MalL-catalysed pNPG turnover are differently affected by increased solution viscosity. (A) The viscosity dependence of k_{cat} for MalL and V200S MalL at 20 °C. Dashed lines are the fit to Eqn (32). (B,C) The temperature-dependence of V200S MalL (top panel B; blue) and WT MalL (bottom panel C; black) catalysed pNPG turnover at a range of solution viscosities, each data point determined from individual Michaelis–Menten curves. Solid lines are the fit to Eqn (19). (D) Variation in $\Delta\Delta C_p^{\ddagger}$ with increasing solution viscosity for MalL (WT, black; V200S, blue). Solid lines are to aid the eye only, illustrating the trend in the $\Delta C_p^{\ddagger}$ vs viscosity data and extraction of $\Delta\Delta C_p^{\ddagger}$ (Table 1). E, Variation in $\Delta C_p^{\ddagger}$with k_{cat} at Topt (WT, black; V200S, blue). Solid lines are to aid the eye only.

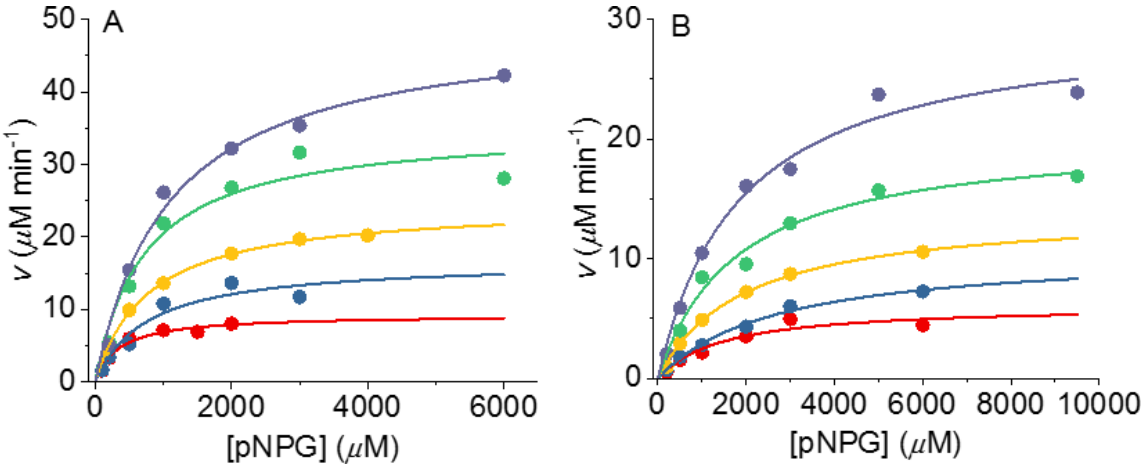

Figure 19 Example Michaelis–Menten plots for WT (A) and V200S (B) MalL at a range of temperatures (20–40 °C) and a viscosity of 1.38 cP. Note that the K_m is essentially invariant within error at each temperature, similar to the data at ambient viscosity.

the conformational sampling in WT MalL but not V200S MalL and this directly correlates with the increased rigidity we observe from our structure-based calculations and REES data above. Therefore, from these data we infer that V200S MalL has a less significant contribution from the global protein vibrational modes compared to MalL. We acknowledge the large error range on these values but we would point out these findings are entirely consistent with the observed lack of a measurable pressure and temperature-dependence for V200S MalL on $\Delta C_P^{\ddagger}$ and $\Delta\alpha^{\ddagger}$, respectively.

The only consistent way to compare rate constants for enzyme turnover is to consider the observed rate at T_{opt} since the temperature-dependence of the rate may vary. From our viscosity studies, the observed rate of MalL turnover (k_{cat} at T_{opt}) shows a trend to increase with increasing $\Delta C_P^{\ddagger}$ as $\Delta C_P^{\ddagger}$ gets closer to zero (Figure 18). We observe a similar trend with the V200S variant *versus* the wild-type enzyme (Figure 11 and Table 1). Therefore, based on the logic we establish above, we find that the rate of turnover increases where the protein FEL is made narrower and the contribution from protein vibrational modes is diminished. We note that the observed changes in k_{cat} are not very large (but significantly different) but are accompanied by relatively large changes in $\Delta C_P^{\ddagger}$. Moreover, the effect of altering the FEL either with viscogen or through amino acid variants must be small and illustrates the extreme sensitivity of $\Delta C_P^{\ddagger}$ to changes in the FEL that are linked to enzyme turnover.

Potential applications of modulating protein flexibility and $\Delta C_P^{\ddagger}$

Retaining the precision of the electrostatic environment of the enzyme active site is the key requirement for the catalytic effect and the massive rate enhancement achieved by

enzymes. However, engineering enzyme variants often destroys the precision of the electrostatic environment, abrogating enzyme activity. A number of studies have illustrated the importance of enzyme motions and have suggested the presence of networks of vibrational modes that enable conformational sampling of productive substrate binding and/or reaction geometries (for example refs [144–147]). Modulating such a network would then have the potential to tune enzyme activity without altering the fine detail of the electrostatic environment at the active site, which is the key requirement for catalysis. In the present example, we have captured a complete thermodynamic analysis of enzyme turnover, providing insight into the relationship between enzyme turnover and the protein FEL. Based on the insights from our study we find that 'rigidifying' the enzyme, specifically decreasing the distribution of vibrational modes (smaller $\Delta C_P^{\ddagger}$) that affect enzyme turnover by decreasing the absolute value of the expansivity, increases not only T_{opt}, but also the observed rate of turnover at T_{opt}. Moreover, we show that the difference arises from both an increase in enzyme rigidity distal to the active site, and from a change in the coupling between the local binding-site geometry and the global network of vibrational modes that extend throughout the enzyme. This trend is borne out by solvent studies which show a similar trend for a faster rate of turnover with a smaller $\Delta C_P^{\ddagger}$ value. Our study therefore illustrates the potential for rationally altering enzymes based on their network of vibrational modes, without affecting the enzyme structure. This is an even more attractive possibility given that networks of vibrational modes may extend throughout the protein structure, meaning that variants can be identified that are not localised to the active site, minimising disruption to the active site and by extension the electrostatic environment. Thus, we suggest that rigidification of those modes that affect enzyme turnover *versus* vibrational modes in the protein in general, is a powerful strategy for biocatalysis applications, where increased operating temperatures are routinely required. Moreover, our study illustrates that it is entirely possible to identify these modes within the enzymes using established structure-based calculations. As an example, in the present study we find that T_{opt} increases significantly though a single amino acid variant (Table 1). From a biocatalysis point-of-view this may be the more important finding compared to the observed increase in the rate of enzyme turnover.

Methods

Protein expression purification.

Full length *Bacillus subtilis* 168 MalL was expressed and purified as described previously.[1] Purified protein was dialyzed against a buffer of 20 mM HEPES pH 7.0. All measurements were made in this buffer unless otherwise stated.

Enzyme assays.

Steady-state kinetic measurements were performed using a UV/ Vis spectro-photometer (Agilent Cary 60 UV-Vis spectrometer) in a 1 cm cuvette, or mounted in the high-pressure cell (see below). For pressure/temperature measurements a saturating concentration of pNPG was used (4 mM). MalL turnover was monitored as the increase in absorption at 420 nm reflecting product formation. Initial rates were calculated using $\varepsilon = 18\ mM^{-1}\ cm^{-1}$. Initial velocity data were fit to the models described in the manuscript using either OriginPro 2016 (MicroCal) or Matlab (Mathworks). Viscosity studies were conducted with increasing concentrations of glycerol and for combined temperature viscosity studies the glycerol concentration was adjusted at each temperature to ensure a consistent viscosity.

An ISS high-pressure cell (ISS, Champaign, UL, USA), fitted with a custom mounting to an absorbance spectrometer, connected to a circulating water bath for temperature regulation (± 1 °C), was used to record all combined pressure/temperature measurements. To fit the surface to p/T versus $\ln k_{cat}$ data, we used a bootstrap method by randomly resampling our measurements (n=30, 6 thermal and 5 baric gradients) with replacement. The bootstrap method provides better information on the characteristics of the parameters than the one-set fitted parameters from the full dataset and it further produces the statistical distribution of the parameters. The goodness of fit are simply controlled by discarding those fit with a R^2 less than 0.9, where only happened ~5% of a 1000-iterations bootstrapping. Results from the bootstrap analysis are reported as the mean and standard deviation (mean±std).

Red edge excitation shift measurements.

All fluorescence measurements were performed using a Perkin Elmer LS50B Luminescence Spectrometer (Perkin Elmer, Waltham, MA, USA) connected to a circulating water bath for temperature regulation (± 1 °C). Samples were thermally equilibrated for 3 minutes at the specified temperature. Excitation and emission slit widths were 5 nm. Tryptophan emission was monitored from 325 to 500 nm. The excitation wavelength was subsequently increased in 1 nm steps for a total of 19 scans. 3 sets of individual scans were averaged. The corresponding buffer control was subtracted from the spectra for each experimental condition and this also removes the Raman peak water peak. The centre of spectral mass (CSM) was calculated using the following equation:

$$CSM = \frac{\sum(f_i x\ \lambda_{Em})}{\sum(f_i)} \qquad \text{(Eq33)}$$

Where f_i is the measured fluorescence intensity and λ_{Em} is the emission wavelength. We would stress the importance of using a consistent wavelength range when reporting CSM data, as the magnitude will be dependent on the wavelength range chosen. The QUBES data are extracted by fitting the CSM *versus* λ_{Ex} data as described in the manuscript. Data fitting and plotting was performed using OriginPro 2016 (Microcal).

Rigidity analysis

Pebble-game rigidity analysis[103] divides a protein structure into a number of rigid clusters (RCs) depending on the distribution of constraints in the system and the inclusion of hydrogen bonds in the constraint network is controlled by an energy cutoff parameter E_{cut}. As E_{cut} is decreased from zero to negative values, weaker hydrogen bonds are excluded from the constraint network and the structure becomes less rigid. We track the rigidity by considering the fraction (F) of mainchain residues which lie within the N largest rigid clusters (for N = 1 to 20) for E_{cut} values lying in the range from 0 kcal mol^{-1}, where the structure is largely rigid, to -4 kcal mol^{-1}, where the structure is largely flexible.[148] Template-based geometric simulation[104] uses rigid cluster information to rapidly generate new protein conformations with the same local bonding geometry as the original.

Acknowledgments. CRP acknowledges the EPSRC for funding. HBLJ is funded by a University of Bath Doctoral Scholarship. EJP is funded by a University of Waikato Doctoral Scholarship.

Author Contributions. HBLJ, SAW, EJP and AK performed experiments. HBLJ, VLA and CRP planned the study. All authors analysed data and wrote the paper.

Chapter 4:
Linking MMRT to Vibrational Coupling Through Kinetic Isotope Effects

The pressure and viscosity experiments shown in chapter 4 demonstrated that the value of $\Delta C_P^{\ddagger}$ was sensitive to perturbations of global enzyme dynamics, clearly influencing the curvature of enzymatic temperature-dependences. This led to further investigation into the sensitivity and extent to which $\Delta C_P^{\ddagger}$ can report on dynamics linked to catalysis, which is reported in this chapter. To cleanly examine the influence of vibrational motion linked to catalysis on $\Delta C_P^{\ddagger}$, KIE studies were carried out on a hyper-thermophilic promiscuous enzyme (GDH). These studies demonstrated that the effect of altered vibrational motion on catalysis extends to the substrates vibrational motion, and that $\Delta C_P^{\ddagger}$ is cumulatively sensitive to both primary and secondary KIEs. Whilst this is likely a system specific effect, the sensitivity of $\Delta C_P^{\ddagger}$ to a single bond frequency being altered, demonstrates that in the absence of other variables that can affect the curvature of an enzymatic temperature-dependence, vibrational motion is altering the temperature-dependence of the reaction in this study. It cannot be unequivocally stated that the magnitude of $\Delta C_P^{\ddagger}$ is reflective of direct dynamics linked to the catalytic step, and not just temperature influenced alterations in the equilibrium of states. Despite this, the alteration of the frequency of the bond that is broken during the reaction, significantly affecting the temperature-dependence of enzymatic rates, provides valuable insight into the significant influence enzyme dynamics can have on catalysis. This evidence suggests that $\Delta C_P^{\ddagger}$ may be a valid probe for dynamics involved in catalysis. It also further validates the MMRT, and the necessity to acknowledge changes in heat capacity during catalysis, when studying enzymatic temperature-dependences.

This declaration concerns the article entitled:									
Uncovering the relationship between the change in heat capacity for enzyme catalysis and vibrational frequency through isotope effect studies									
Publication status (tick one)									
draft manuscript		**Submitted**		**In review**		**Accepted**		**Published**	✓
Publication details (reference)	Jones, H.B., Crean, R.M., Matthews, C., Troya, A.B., Danson, M.J., Bull, S.D., Arcus, V.L., Van der Kamp, M.W. and Pudney, C.R., 2018. Uncovering the Relationship between the Change in Heat Capacity for Enzyme Catalysis and Vibrational Frequency through Isotope Effect Studies. *ACS Catalysis*, *8*(6), pp.5340-5349.								
Candidate's contribution to the paper (detailed, and also given as a percentage).	The candidate contributed to/ considerably contributed to/predominantly executed the… Formulation of ideas: Laboratory experiments formulated by HBLJ and CRP Computational experiments formulated by RC, MvdK and CRP (25%) Design of methodology: Laboratory experiments designed by HBLJ and CRP Computational experiments designed by RC and MvDK (25%) Experimental work: Protein expression and purification by HBLJ and CM Comparison of different sugars with GDH by HBLJ and CM Different isotopologue substrates with GDH by HBLJ Structure preparation for MD simulations by HBLJ MD simulations were carried out by MvdK QM cluster calculations were carried out by RC and AT (40%) Presentation of data in journal format: CRP wrote main text HBLJ made figures, wrote laboratory methodology and referenced text RC formulated SI and wrote computational methodology (25%)								
Statement from Candidate	This paper reports on original research I conducted during the period of my Higher Degree by Research candidature.								
Signed	H B L Jones				**Date**	17/01/19			

The following is the author accepted manuscript of an article published in final form in Jones, HBL, Crean, RM, Matthews, C, Troya, AB, Danson, MJ, Bull, SD, Arcus, VL, Van Der Kamp, MW & Pudney, CR 2018, 'Uncovering the relationship between the change in heat capacity for enzyme catalysis and vibrational frequency through isotope effect studies', ACS Catalysis, vol. 8, no. 6, pp. 5340-5349 and available online via: https://doi.org/10.1021/acscatal.8b01025.

Uncovering the relationship between the change in heat capacity for enzyme catalysis and vibrational frequency through isotope effect studies

Hannah BL Jones[†Δ], Rory M Crean[#†Δ], Christopher Matthews[†], Anna B Troya[†], Michael J Danson[†], Steven D Bull[‡], Vickery L Arcus[§]*, Marc W Van der Kamp[%]* and Christopher R Pudney[†]*

[†]Department of Biology and Biochemistry, [‡]Department of Chemistry, [#]Doctoral Training Centre in Sustainable Chemical Technologies, University of Bath, Bath BA2 7AY, United Kingdom

[§]School of Science, Faculty of Science and Engineering, University of Waikato, Hamilton 3240, New Zealand

[%]School of Biochemistry, University of Bristol, Biomedical Sciences building, University Walk, Bristol BS8 1TD, United Kingdom.

Abstract: Understanding how enzyme catalysis varies with temperature is key to understanding catalysis itself, and ultimately, how to tune temperature optima. Temperature-dependence studies inform on the change in heat capacity during the reaction, $\Delta C_P^{\ddagger}$, and we have recently demonstrated that this can expose links between the protein free energy landscape and enzyme turnover. By quantifying $\Delta C_P^{\ddagger}$, we capture information on the changes to the distribution of vibrational frequencies during enzyme turnover. The primary experimental tool to probe the role of vibrational modes in a chemical/biological process is isotope effect measurements, since isotopic substitution primarily affects the frequency of vibrational modes at/local to the position of isotopic substitution. We have monitored the temperature-dependence of a range of isotope effects on the turnover of a hyper-thermophilic glucose dehydrogenase. We find a progressive effect on the magnitude of $\Delta C_P^{\ddagger}$ with increasing isotopic substitution of D-glucose. Our experimental findings, combined with molecular dynamics simulations and quantum mechanical calculations, demonstrate that $\Delta C_P^{\ddagger}$ is sensitive to isotopic substitution. The magnitude of the change in $\Delta C_P^{\ddagger}$ due to substrate isotopic substitution indicates that small changes in substrate vibrational modes are 'translated' into relatively large changes in the (distribution and/or magnitude of) enzyme vibrational modes along the reaction. Therefore, the data suggest that relatively small substrate isotopic changes are causing a significant change in the temperature-dependence of enzymatic rates.

KEYWORDS Heat capacity, isotope effect, enzyme, catalysis, temperature-dependence

Isotope effects are one of the most powerful tools to investigate chemical mechanism and the physical chemical underpinnings of catalysis.[149] Enzyme mechanistic studies often employ kinetic and binding isotope effects, KIE and BIE, to access information on

specific steps in enzyme catalysis and to test the role of protein 'dynamics' in enzyme turnover.[150–152] The power of isotope effects lies in the simplicity of their physical origin. That is, isotopic substitution decreases the frequency of all vibrational modes, but does not affect the electronic structure of the molecule.[88] Therefore, where one observes an isotope effect, the physical chemical interpretation of the experimental observation is much less ambiguous compared to mutagenesis studies, for example.

In enzymatic studies, the temperature-dependence of the KIE is often used to infer the presence or absence of protein motions that affect the rate of enzymatic turnover.[63,153] The microscopic interpretation of these studies is controversial (see e.g. ref. [154]), but at least at a basic level these studies seem to validate the notion that protein motions can affect enzyme turnover (if not necessarily the catalytic step itself). Recently, the potential role of protein 'dynamical' effects on the reaction catalyzed by dihydrofolate reductase (DHFR) or HIV-1 protease, have been assessed based on simulations with mass modulated (isotopically substituted) enzymes.[155–157] In both systems, a small contribution from these dynamical effects to reducing the free energy profile around the transition state of the order ~2 kJ mol^{-1} was found. These authors interpret this difference as arising from the coupling between the reaction coordinate and the degrees of freedom of the system. However, the major contributor to reducing the free energy barrier arises from electrostatic effects.[150,158–160] In addition, Åqvist used simulation to reveal the molecular origin of entropic effects in catalysis with respect to temperature, and illustrated the importance of considering not just the immediate active site, but also remote parts of the protein (and surrounding solvent).[50] We further point out that others have argued that fast (sub-picosecond), local active site protein modes play a role in transition state formation (and thereby catalysis).[161] A further alternative view is that so-called protein dynamical effects are coupled to the reaction coordinate, but provide a small contribution to barrier reduction relative to, e.g., the electrostatic contribution via preorganisation.[150,158–160] Although not a catalytic 'dynamical effect', when strictly defined,[68] differences in enzyme fluctuations (or vibrations) that cause a change in heat capacity along the reaction can affect the temperature-dependence of enzyme activity.[46] Understanding this effect in detail may provide new tools to manipulate enzyme optimal temperatures.

We have recently demonstrated how capturing information on the change in heat capacity for activation $\Delta C_P^{\ddagger}$, informs on differences in the distribution of frequencies of vibrational modes between the enzyme-substrate and enzyme-transition state complex.[45,162] Typically, the temperature-dependence of enzyme rate constants is fitted to the Eyring equation.

$$k = (k_{\mathrm{B}}T/h)e^{\Delta S^{\ddagger}/R}e^{-\Delta H^{\ddagger}/RT} \qquad \text{(Eq34)}$$

This model assumes that $\Delta H^{\ddagger}$ and $\Delta S^{\ddagger}$ are temperature independent. However, if $\Delta H^{\ddagger}$ and $\Delta S^{\ddagger}$ are temperature-dependent, then this implies a non-zero value for $\Delta C_P^{\ddagger}$. $\Delta C_P^{\ddagger}$ can be extracted from temperature-dependence studies of enzymes fitted using a model that

incorporates temperature-dependence of $\Delta H^{\ddagger}$ and $\Delta S^{\ddagger}$, which we have termed macromolecular rate theory (MMRT): [1,42]

$$lnk = ln\frac{k_B T}{h} - \left[\frac{\Delta H^{\ddagger}_{T_R} + \Delta C_P^{\ddagger}(T - T_R)}{RT}\right] + \left[\frac{\Delta S^{\ddagger}_{T_R} + \Delta C_P^{\ddagger}(lnT - lnT_R)}{R}\right] \qquad \text{(Eq19)}$$

where T_0 is an arbitrary reference temperature. $\Delta C_P^{\ddagger}$ is the difference in heat capacity between the ground and transition states. $\Delta C_P^{\ddagger}$ determines the change in $\Delta H^{\ddagger}$ and $\Delta S^{\ddagger}$ with temperature and thereby defines the non-linearity of the temperature-dependence of the Gibbs free energy difference between the ground state and the transition state ($\Delta G^{\ddagger}$). Indeed, Roy *et al.* point to a temperature-dependent activation entropy as the source of non-linear temperature-dependence plots.[154] Other models that move beyond Eq 34 have been proposed, primarily relating to equilibria of different functional/non-functional states.[9,33] Whilst we do not discount these models, it appears, based on the range of recently published work from different labs,[42,45,46,162] that Eq 34 is useful and broadly accurate.

We expect that the dominant contribution to $\Delta C_P^{\ddagger}$ in enzymes is the difference in distribution and frequency[1,42] of the large number of vibrational modes of the molecule and its closely associated solvent molecules in the ground and transition states. Alternatively, a negative value of $\Delta C_P^{\ddagger}$ implies that $<(\delta H)^2>$ (the mean squared distribution of enthalpies) for the enzyme substrate complex is greater than $<(\delta H)^2>$ for the enzyme-transition state complex at a given temperature.[42] We suggest that the magnitude of $\Delta C_P^{\ddagger}$ can therefore be used as a proxy for the changes in vibrational modes (distribution, frequency) during enzyme turnover.

The origin of isotope effects lies in the difference in the frequency of vibrational modes between isotope changes. Observing a relationship between (i) increasing isotopic substitution of the substrate, (ii) an isotope effect on the rate of turnover, and (iii) $\Delta C_P^{\ddagger}$ would suggest that the enzymatic $\Delta C_P^{\ddagger}$ is sensitive to (substrate) vibrational modes that affect the observed reaction rate. Bigeleisen considered the effect of isotopic substitution on heat capacity, though not for hydrogen.[163] More recently, Tjahjono and Garland[164] have directly measured the difference in apparent molar heat capacity, C_P^0, for a series of model compounds with different levels of deuterium substitution. As with other reports,[165] the authors find that the deuterium isotope effect on C_P^0 was always positive, i.e. C_P^0 increases with the increasing number of deuterium substitutions (Nd) and that the relationship was essentially linear: ΔC_P^0 (J mol^{-1} K^{-1}) = 2.75Nd – 1.52. The increase in C_P^0 is attributed to the increased mass of the isotopologue and the concomitant decrease in frequencies of the affected bonds.

In a recent appraisal of a range of previously published experimental enzyme systems,[45] we found that there was potentially an isotope effect on $\Delta C_P^{\ddagger}$. Longbotham *et al*[166] recently

performed a study exploring a range of isotope effects on labelling the flavin in a model flavoenzyme and found their data could only be adequately fitted using Eq 19. These authors find a small isotope effect on $\Delta C_P^{\ddagger}$ outside experimental error for some, but not all, labelling patterns. Based on these intriguing findings we are inspired to explore the potential for isotope effects combined with Eq 19 to inform on changes in enzyme vibrational modes along the chemical reaction coordinate and their relationship to temperature-dependence. Herein, we use a hyperthermophilic enzyme, *Sulfolobus solfataricus* glucose dehydrogenase (*ss*GDH) as a model system to explore the contribution of enzymatic isotope effects on heat capacity differences during the reaction. Our data provide an experimental link between the temperature-dependence of enzyme turnover and (low frequency) vibrational modes. Importantly, the results raise the question of how subtle localized changes (through isotopic substitutions in the substrate) can lead to a significant change in the enzymatic heat capacity (and thus $<(\delta H)^2>$) during the reaction.

Results and discussion

Hydride transfer in ssGDH is rate determining.

*ss*GDH is a promiscuous hyperthermophilic enzyme that reduces nicotinamide adenine dinucleotide (phosphate) ($NAD(P)^+$), with a variety of sugars.[167] Milburn *et al*[70] solved the X-ray crystal structure with both $NADP^+$ and glucose/xylose bound using a catalytically inactive variant (T41A). Notionally the reduction of the nicotinamide (C4) occurs as a hydride transfer from C1 of the sugar, concomitant with a proton transfer from the C1 hydroxyl (Scheme S1) to a water molecule or hydroxide ion coordinated by a Zn^{2+} ion. We have performed molecular dynamics simulations of *ss*GDH (Figure 20A) in complex with both glucose and xylose (four independent runs of 50 ns, with all four active sites occupied). From our MD simulations, consistent with the X-ray crystal structures, we find that the hydride donor-acceptor (D-A) distance is very similar for glucose and xylose, but not identical, with the xylose D-A being ~0.2 Å longer (Figure 20B; Supporting information). Specifically, the averages are 2.77 +/- 0.287 Å and 2.93 +/- 0.310 Å; medians are 2.725 Å and 2.895 Å.

Quantum chemical cluster calculations (Figure 20C – 20G) on a 148 atom model of the active site of *ss*GDH in complex with glucose (Figure 20C) suggest a stepwise chemical mechanism, whereby proton abstraction from a Zn^{2+} coordinated hydroxide forms a stable alkoxide intermediate on the sugar C1 prior to hydride transfer. When a water molecule is modelled as coordinated to the Zn^{2+} ion (Figure 20C), the D-A distance is 2.49 Å, consistent with our MD simulations (above, Figure 20B). When instead a hydroxide ion is modelled as coordinated to the Zn^{2+} ion, the proton on the sugar C1 hydroxyl is readily abstracted upon geometry optimization (Figure 20D) to form a reactive intermediate, with the resulting anion stabilised by hydrogen bonding interactions to the now Zn^{2+} bound water and T41. This reactive intermediate has a reduced D-A distance of 2.22 Å, which reduces further as the glucose and $NADP^+$ rings pucker to form a transition state (Figure 20F) with a predicted free energy barrier relative to the reactive intermediate of 32.6 kJ

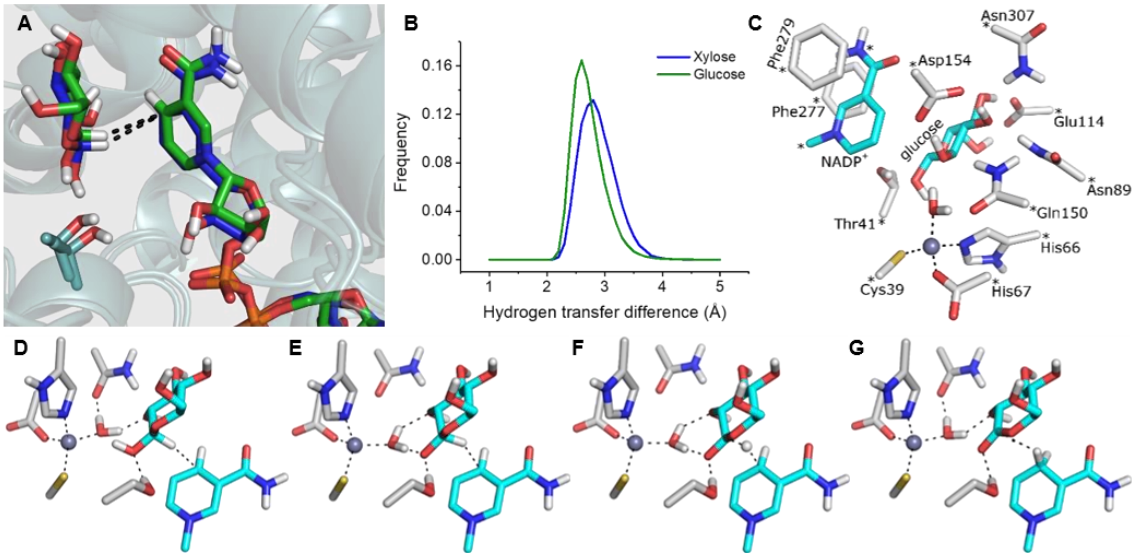

Figure 20. A, Representative structures of glucose (green) and xylose (blue) from our MD simulations demonstrating they have the same binding interface with $NADP^+$. **B,** Normalized histograms (bin width 0.1 Å) of the hydrogen transfer distance of glucose and xylose from MD simulations of ssGDH. **C,** QM cluster model created of glucose in complex with $NADP^+$, with asterisks indicating atoms fixed throughout the optimisation process. **D – G,** Reaction mechanism obtained from the QM model, starting from the reactant (**D**), to the deprotonated reactive intermediate (**E**), the transition state (**F**), and finally the product

mol^{-1} at 298 K. In synchrony with the hydride transfer, the Zn^{2+} bound water rotates away from glucose, returning to its original position of hydrogen bonding with Q150 and the C2 hydroxyl of glucono-D-lactone. In order to compare the predicted and experimental activation energies, one must consider the initial deprotonation into the bulk milieu (Reactant to Reactive Intermediate; Figure 20D and E, respectively), which cannot be determined reliably with the cluster based approach due to the importance of inhomogeneous long range interactions in modulating pK_a values.[168] Instead, one can subtract the hydride transfer barrier from the experimental barrier to obtain a predicted pK_a of 7.2 (Full calculation details can be found in the Supporting Information), which is in good agreement with the experimental pH optimum of 8.[169] Finally, we note that there is no obvious role for water in the rate determining step (deprotonated water acts as a base for proton abstraction, whereas the subsequent hydride transfer is rate limiting, see below) and so at least this route is not giving rise to a primary solvent isotope effect (see below).

Our combined computational and kinetic data (discussed below) provide evidence for the mechanistic step observed from our kinetic data. The slightly larger D-A distance in the Michaelis complex for xylose *versus* glucose, calculated from MD simulations, correlates with a ~1.6-fold larger k_{cat} value (k_{cat} = 95 and 58 s^{-1} at 90 °C; Figure 21) and a ~5-fold larger K_m (K_m = 2.5 ±0.3 and 0.5 ± 0.2 mM at 85 °C; Figure S1A and S1B) for glucose *versus* xylose, respectively. This magnitude increase in rate seems reasonable for a hydride transfer given a ~0.2 Å difference in D-A distance[170,171] (Figure 20B) and implies that the observed rate is primarily capturing the hydride transfer step. Similarly, the difference in K_m is likely reflective of the difference in binding geometry and bonding

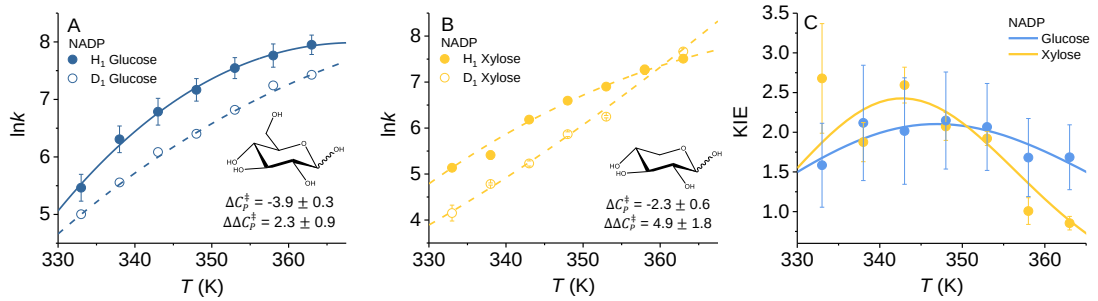

Figure 21. The temperature-dependence of NADP+ reduction by glucose (A) and xylose (B). Solid and dashed lines show the fitted to Eq 18 for the protiated and deuterated Glucose/xylose (D^1), respectively. C, the resulting KIE extracted from the lnk_{cat} (ln min^{-1}) in panels A and B. The solid line is the modelled KIE based on the parameters extracted from Eq 18 (Solid lines in panels A and B)

(discussed below). Our QM cluster calculations provide a reasonable mechanism in which a Zn^{2+} coordinated hydroxide ion can deprotonate the glucose C1 hydroxyl to form a reactive intermediate. The direct nature of the enzyme assay ($NADP^+$ reduction to NADPH), our QM calculations and the observation of a significant primary kinetic isotope effect (KIE, see below) suggests that the kinetic data primarily reflect the hydride transfer step.

Heat capacity changes during enzyme reaction.

We have measured the temperature-dependence of k_{cat} for both glucose and xylose, fitted to Eq 19, shown in Figure 21A and 21B. For both glucose and xylose, the temperature vs. ln(k_{cat}) data are clearly curved and are therefore appropriately fitted to Eq 19 instead of Eq 34. *ss*GDH is extremely thermally stable[169] and we do not find evidence for unfolding on the timescales of our assays at any temperature. To capture the curvature in temperature-dependence plots accurately, and to capture the experimental system at its natural operating temperature (77 °C)[169], we have focused on the temperature range 60-90 °C. From Figure 21A and 21B we find a significant difference in the magnitude of $\Delta C_P^{\ddagger}$ with $\Delta C_P^{\ddagger} = -3.9 \pm 0.3$ and -2.3 ± 0.6 kJ mol^{-1} K^{-1}, for glucose and xylose, respectively.

Potentially, the difference in $\Delta C_P^{\ddagger}$ between glucose and xylose could arise through a difference in the chemical structure of the sugars, i.e. the additional CH_2OH group of glucose. For example, the hydroxyl of the hydroxymethyl group can form hydrogen bonding interactions with either E114 or H297. This additional interaction may cause a general rigidification of the glucose and the active site, and thus decrease the absolute heat capacity of the ground and transition state. We cannot, however, confidently project how this would change $\Delta C_P^{\ddagger}$ (i.e. how the heat capacity of the ground state is affected differently from the heat capacity of the transition state), and thus cannot assign the physical origin of the observed differences in $\Delta C_P^{\ddagger}$ between glucose and xylose.

Change in $\Delta C_P^{\ddagger}$ with substrate isotopic substitutions.

To explore the relation between $\Delta C_P^{\ddagger}$ and substrate vibrational states, we determine the effects of substrate isotope substitutions on $\Delta C_P^{\ddagger}$ for sugar dehydrogenation by *ss*GDH. Figure 21A and 21B show the temperature-dependence of the primary kinetic isotope effect (1° KIE) for hydride transfer for both glucose and xylose using D-glucose (D^1) and D-xylose (D^1), respectively. For both sugars, the KIE is temperature-dependent (Figure 21C) and similar in magnitude (~2 – 2.5). Despite the similar magnitude of the KIE for both sugars, the isotope effect (IE) on the magnitude of $\Delta C_P^{\ddagger}$ is significantly different. The 1° IE on $\Delta C_P^{\ddagger}$ is very large for xylose [D-Xylose (D^1)], bringing the $\Delta C_P^{\ddagger}$ value to ~0 within error ($\Delta\Delta C_P^{\ddagger}$ = 4.9 ± 1.8 kJ mol^{-1} K^{-1}). However, for glucose the 1° IE is smaller: D-glucose (D_1) $\Delta C_P^{\ddagger}$ = −1.6 ± 0.6 kJ mol^{-1} K^{-1} ($\Delta\Delta C_P^{\ddagger}$ = 2.3 ± 0.9 kJ mol^{-1} K^{-1}). We note that this trend in the data is recapitulated when omitting 'outlier' data points (Figure S2). Moreover, these data do not appear to be due to significant differences in the structure or bonding of the reactive complex, since the K_m values are the same within error for the protiated and deuterated substrate, K_m = 3.2 ± 0.4 and 0.7 ± 0.1 mM at 85 °C *c.f.* K_m = 2.5 ±0.3 and 0.5 ± 0.2 mM at 85 °C for glucose *versus* xylose, respectively. The magnitude of $\Delta\Delta C_P^{\ddagger}$ for both xylose and glucose is surprising, as these differences are much larger than can be expected from effects on (substrate) heat-capacity for isotopic substitutions alone (discussed below). It indicates some (unknown) interaction between the reacting species and the enzyme enthalpy distribution that can be perturbed by isotopic substitution.

As discussed previously, the difference in $\Delta C_P^{\ddagger}$ between glucose and xylose could arise through a difference in the sugar-enzyme interactions. However, isotope effects arise from differences in the frequency of vibrational modes,[88] and not from changes in electronic structure that can lead to additional interactions. At a phenomenological level, our data therefore provide evidence that $\Delta C_P^{\ddagger}$ can be significantly perturbed by the frequency of bond vibrations in the reacting species. Figure 21C shows the KIE as a curve resulting from the temperature-dependence parameters extracted from the fits in Figures 21A and 21B.

The temperature-dependence of the KIE for both glucose and xylose show a qualitatively similar relationship; curvature with a maximum at 346 and 343 K, respectively. Typically, one observes a decrease in the magnitude of the KIE with respect to temperature when fitting data using the Eying/Arrhenius equation (as shown in Figure S3). Figure 22 shows a numerical model of the data shown in Figure 21C (using Eq 19), where the magnitude of $\Delta C_P^{\ddagger}$ for the isotopolgue is varied to explore a range of $\Delta\Delta C_P^{\ddagger}$ values and the resulting effect on the KIE. From this model, we find that the curvature in the KIE plots is a direct result of the isotope effect on $\Delta C_P^{\ddagger}$. That is, as $\Delta\Delta C_P^{\ddagger}$ tends towards zero (no isotope effect on $\Delta C_P^{\ddagger}$), the KIE plot will become 'normal', showing a decrease in magnitude with increasing temperature (Figure 22). These data show that a consequence of *any* significant

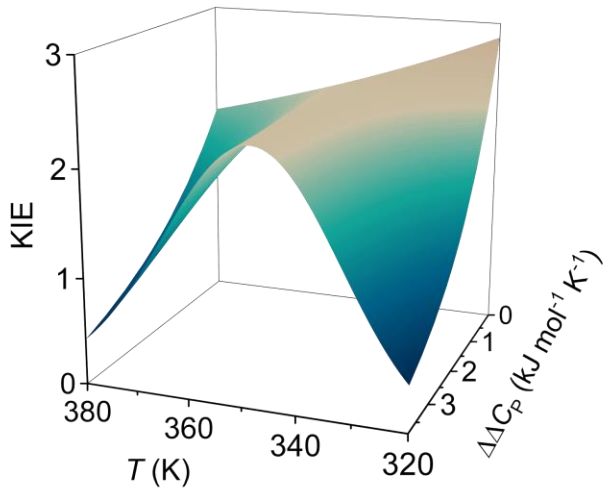

Figure 22. Numerical model showing how the magnitude of the glucose 1° KIE versus temperature is affected by differences in the isotope effect on $\Delta C_P^{\ddagger}$. $\Delta H^{\ddagger}$ and $\Delta S^{\ddagger}$ values used for modelling given in Table 2.

isotope effect on $\Delta C_P^{\ddagger}$ is that the KIE will tend towards unity and this is also true for all temperature-dependent KIEs fitted using e.g. Eq 34. The difference when accounting for plot curvature is that the KIE will approach unity at both low and high temperatures. It is therefore not surprising that both sugars show a KIE that tends towards 1 at low and high temperatures and this will be the case for all isotope effects on $\Delta C_P^{\ddagger}$.

Effect of increasing isotopic substitution on $\Delta C_P^{\ddagger}$.

To explore the relationship between substrate vibrational modes and $\Delta C_P^{\ddagger}$ further, we use glucose to find if there is an isotopic mass dependence on the magnitude of $\Delta C_P^{\ddagger}$. We have increased the isotopic substitution of glucose using both per-deuterated glucose and in combination with deuterium oxide (D_2O) and monitored the temperature-dependence of k_{cat} as shown in Figure 23A. The temperature-dependence of the KIE is shown in Figure 23B with the corresponding labeled structures shown in Figure 23D. Given that the *ss*GDH mechanism involves a concomitant hydride and proton transfer (discussed above and Figure 20C-G), we have essentially two possible 1° KIEs for the hydride (1^{o}_{H}) and proton (1^{o}_{P}) transfer. However, we note that our combined experimental and computational evidence above suggests that the proton transfer is fast relative to the hydride transfer, indicating that there would be no primary KIE for proton transfer and the experimental assay thus essentially captures the hydride transfer step.

Labelling of sites distal to the transferred hydride are a secondary (2°) KIE. In the present case, this 2° KIE will be composed of many microscopic 2° KIEs for each labelled position (shown in green in Figure 23D). Finally, to label the exchangeable OH groups we have performed our experiments in D_2O and this will lead to deuteration of *all* exchangeable protons (including amino acid side chains) that are immediately solvent

accessible. Note that the enzyme itself is not incubated in D_2O, only the substrate and so the enzyme deuteration occurs only on the timescale of the steady-state assay (~1 min), see *Materials and Methods*. The resulting kinetic parameters are given in Table 2 and for the substrate isotope effects.

One expects an increase in mass of the substrate to alter the frequency of the C-H stretch in both the ground and transition state, but whether the expected change still manifests in the presence of the active site amino acids is not obvious. Therefore, we have performed frequency calculations on the stationary points obtained from the above cluster model (Figure 20C), for each of the isotopically substituted states shown in Figures 23 and S1. The resulting frequencies are given in Table S1. We find a large decrease in stretching frequencies of both the TS and ground state on deuteration of the transferred hydride. On additional isotopic substitution there is generally a small decrease in the C-H stretching frequency for both the ground state and the TS. Again, one expects small changes in frequency on increasing mass through isotopic substitution and our calculations suggest this expected trend is preserved when the first shell of protein amino acids is also present (as in Figure 20C). It is interesting to note that where the amino acids are deuterated (solvent exchangeable positions as with our experiments conducted in D_2O), the frequencies show an additional and significant effect on the calculated frequencies in the order of ~1 cm^{-1}. We would stress that clearly elucidating the relationship between the change in frequencies at the ground/TS, the protein and $\Delta\Delta C_P^{\ddagger}$ would require very extensive (QM/MM) simulation studies.

Table 2. Kinetic parameters extracted from fits of Eq 34 and 19 to the temperature-dependence data shown in Figure 23A

	$\Delta H^{\ddagger}$ (kJ mol^{-1}) [a]	$\Delta S^{\ddagger}$ (kJ mol^{-1} K^{-1}) [a]	$\Delta C_P^{\ddagger}$ (kJ mol^{-1} K^{-1})	KIE [a]	KIE_{calc} [a,d]	$\Delta\Delta H^{\ddagger}$ (kJ mol^{-1} K^{-1})[b] - MMRT	$\Delta\Delta H^{\ddagger}$ (kJ mol^{-1} K^{-1})[c] – Eyring
D-glucose	76.0 ± 2.3	1.33 ± 0.01	-3.8 ± 0.5	–	–	–	–
D_1	78.0 ± 2.1	1.33 ± 0.01	-1.6 ± 0.5	2.1 ± 0.6	2.8	2.0 ± 4.4	1.6 ± 11.7
D_5	86.1 ± 2.5	1.35 ± 0.01	-0.6 ± 0.5	4.0 ± 1.2	0.9	10.1 ± 4.8	7.2 ± 10.6
D_7	80.4 ± 2.0	1.34 ± 0.01	0.0 ± 0.5	2.4 ± 0.9	2.7	4.4 ± 4.4	3.8 ± 9.5
D_{12}	80.4 ± 1.5	1.33 ± 0.01	0.3 ± 0.4	3.7 ± 1.1	2.3	4.4 ± 4.4	0.9 ± 9.5

[a], Data at 348 K. [b], from fits to Eq 19 (MMRT) at 348 K. [c], From fits to Eq 34 (Eyring equation). [d], Calculated from the QM cluster model.

There is a significant effect of increased isotope substitution on both the magnitude of the observed rate but also the magnitude of $\Delta C_P^{\ddagger}$ (Figure 23A and Table 2). From Figure 23B, the KIE increases with increasing isotopic substitution, but not in a linear fashion. The absolute magnitude of the KIE depends on the temperature at which the value is reported, the different contributions from substitutions at different positions and the fact that the temperature-dependence of the isotope effects is different for different isotopic substitutions (Table 2). Therefore, one does not necessarily expect the values to follow an obvious e.g. linear trend. That said, the maximal KIE does tend to increase with increased isotopic substitution, except in the case of Gluc-D_7 (Figure 23D) and we note the relatively large error on these values. As with the 1° KIE, we observe curvature in the magnitude of the KIE for all our isotopic labelling patterns. Figure S3 shows the resulting curve from both fits of the data to Eq 34 and Eq 19, and the corresponding extracted data are given in Table 2.

Given the complex nature of the isotopic labelling pattern for each isotopologue, we do not wish to overinterpret the microscopic contributions to the absolute magnitude of the KIEs. However, it is worth noting that comparison of Gluc-D12 with Gluc-D1 should reveal the combined influence of the secondary substitutions, where a 'normal' secondary KIE would be in the region ~1.1. These effects should be additive, i.e. the individual KIEs should be multiplied: 2.1 ± 0.6 × 1.1 × 1.1 ≈ 2.5 ± 0.6 which differs from the result observed (~3.7 ± 1.1). The large value suggests a significant contribution from secondary effects (~1.3 – 1.4). Huskey and Schowen have suggested that large enzyme secondary

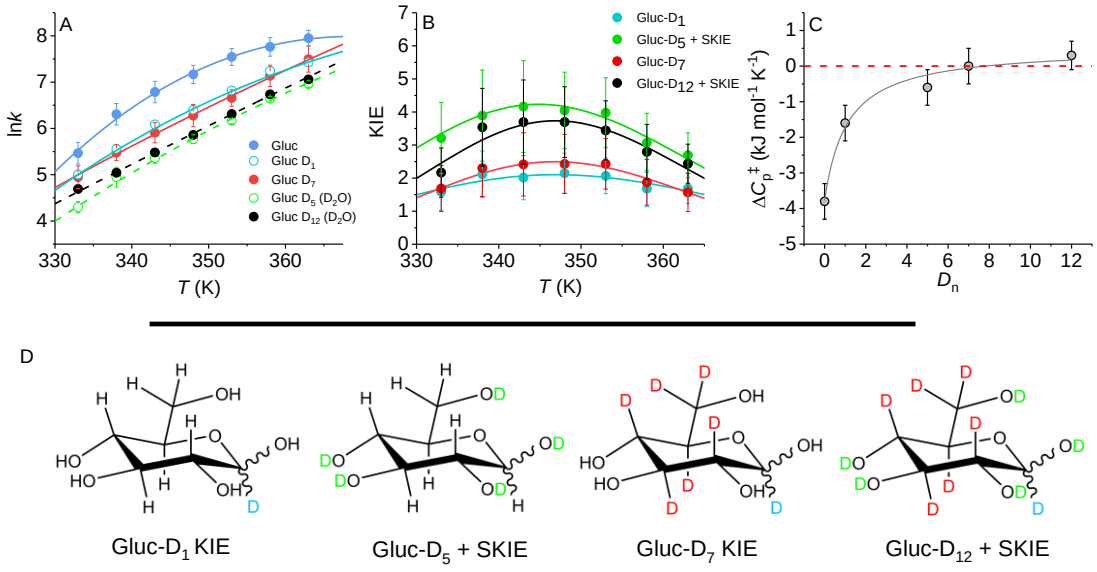

Figure 23. The effect of isotopic labelling on $\Delta\Delta C_P^{\ddagger}$. **A,** The temperature-dependence of k_{cat} for each isotopolgue of glucose. Solid lines are fits to Eq 19. **B,** Resulting KIEs extracted from the fits in panel A. **C,** correlation between the increase in molecular mass (through isotopic substitution) and the extracted magnitude of $\Delta\Delta C_P^{\ddagger}$. The solid line is a simple rectangular hyperbola and is to aid the eye only to illustrate the trend. **D**, structures of each isotopolgue used in the panel A.

KIEs reflect strong 'vibrational coupling' of the secondary sites to the reaction coordinate at the transition state.[172] More recent studies combining density functional theory (DFT) calculations of a model enzyme secondary KIE with high pressure measurements have similar findings.[173] We note that the notion of vibrational coupling is itself problematic and we do not suggest that our data reflect such coupling, not least because no study has provided unequivocal evidence for so called vibrational coupling. Given our data we cannot confidently assign the origin of these apparently exalted secondary KIEs.

The calculated KIEs from our QM cluster model (Table 2), suggest an expected secondary KIE of ~3.4 (2.8 × 1.1 × 1.1), which differs from the calculated value of 2.3 (Table 2). That is, the secondary KIE value is not as expected for either the experimental measurements or QM calculations. Given the excellent agreement between the experimentally measured and calculated 1° KIE (Table 2), the data may indicate that the limitations of the (static) QM cluster model and the importance of enzyme KIEs being calculated using as full a structural model, including conformational sampling, as possible. However, we note that the differences in the absolute magnitude of the experimental KIEs are in fact relatively small, particularly when taking into account the experimental error as shown in Figure 23B. As we state above, given this limitation, we prefer a more conservative interpretation of the labelling study, focusing on the increase in isotopic mass rather than the absolute contributions to the KIE from each labelled atom. Figure 23C shows the relationship between the extracted $\Delta C_P^{\ddagger}$ values (from Figure 23A) and the increase in isotopic mass of the substrate. From Figure 23C, the isotope effect on $\Delta C_P^{\ddagger}$ appears to increase with respect to the mass of the glucose. These data appear to show saturation behavior, with $\Delta C_P^{\ddagger}$ trending towards zero with increasing isotopic mass. Whilst the initial change in $\Delta C_P^{\ddagger}$ is relatively large for just one mass unit increase (Gluc-D_1. $\Delta\Delta C_P^{\ddagger}$ = 2.2 ± 1 kJ mol^{-1} K^{-1}), we find large (~1 kJ mol^{-1} K^{-1}) changes in $\Delta C_P^{\ddagger}$ associated with further isotopic substitutions.

Frequency calculations from the QM cluster model indicate these additional increases in mass (D_5-D_{12}) should only change the frequencies of the reacting species (and immediate surrounding) at the ground and transition state by at most a few wavenumbers (Table S1). Moreover, the calculated $\Delta C_P^{\ddagger}$ values are 3 orders of magnitude smaller than measured experimentally (Table S2). Finally, the calculated KIEs from the QM cluster model show essentially no curvature (Figure S4) compared to the clear curvature observed experimentally (Figure 23B) and shown by comparative fitting of Eq 34 and Eq 19 in Figure S3. A simplistic conclusion from these data would be that our experimental data are not reflecting vibrational frequency changes on isotopic substitution. However, the difference between experimental and computational values is that the QM cluster model neglects nearly all the protein. Recent molecular dynamics simulations that correctly predict significant enzyme $\Delta C_P^{\ddagger}$ values (~kJ mol^{-1} K^{-1}) have shown that the $\Delta C_P^{\ddagger}$ arises from energetic fluctuations across the whole molecule, including domains distant from the active site.[46] It therefore seems likely that the large isotope effect on $\Delta C_P^{\ddagger}$ has a major

component arising from changes in protein fluctuations further removed from the active site.

Conclusions

We have monitored the isotope effect on $\Delta C_P^{\ddagger}$ for a hypethermophilic enzyme, finding a very large primary isotope effect on the magnitude of $\Delta C_P^{\ddagger}$ for two different substrates (glucose and xylose). The size of the isotope effect on $\Delta C_P^{\ddagger}$ is very much larger than predicted based on a QM cluster model. Further we illustrate an additive effect of increase the isotopic mass of glucose on the magnitude of $\Delta C_P^{\ddagger}$. Taken together, our data shows that the change in $\Delta C_P^{\ddagger}$ is coincident with an increase in isotopic mass. These significant changes in $\Delta C_P^{\ddagger}$ (~ 1-2 kJ mol^{-1} K^{-1}) are accompanied by only small (~1 cm^{-1}) changes in vibrational frequency of the reacting species. If the change in $\Delta C_P^{\ddagger}$ arises from these small-scale frequency changes there would need to be some significant 'amplification' of the small local effect. Therefore, the key question arising from the mass modulation data presented here is what is behind the isotopic mass dependence on $\Delta C_P^{\ddagger}$ (Figure 23C). Specifically, if a significant change in enzymatic $\Delta C_P^{\ddagger}$ (and $\Delta H^{\ddagger}$; Table 2), on the ~kJ mol^{-1} K^{-1} scale arises when there are only small changes (on the ~1 cm^{-1} scale) in the vibrational frequency of the ground and transition states of the reacting species, how might this occur?

A similar conceptual challenge arises from protein mass modulation studies where changing the mass of a protein by isotopic substitution (mass change of ~10%) gives rise to very large changes in the temperature-dependence of the rate (isotope effect on $\Delta H^{\ddagger}$, $\Delta\Delta H^{\ddagger}$, changes by ~0-10 kJ mol^{-1}). These very large changes are difficult to rationalize since the expected change in the frequency of protein vibrational modes (for a protein that is ~10 % increase in mass) is on the scale of only a few wavenumbers. Previous efforts to interpret such data have suggested that large changes in $\Delta H^{\ddagger}$ might be achieved where protein vibrational modes become 'decoupled' from the enzyme catalyzed chemistry.[109,166,174] Ranasinghe *et al* have recently extended this rationale by suggesting that mass modulation not only affects protein motions coupled to the enzyme catalyzed chemical step, but also the electrostatics associated with longer time-scale events during turnover.[175] We note that these works have not considered $\Delta C_P^{\ddagger}$. Moreover, there have been a significant number of studies that suggest that protein 'dynamics' do not affect enzyme catalysis[60,68,176–178] and are not in any way coupled to the reaction coordinate.

Our study provides a fresh perspective on current hypotheses that seek to understand the relationship between enzyme vibrational modes and (the temperature-dependence of) catalysis, incorporating a difference in enzyme heat capacity (and thus vibrational modes) along the reaction, $\Delta C_P^{\ddagger}$. Our data point to a model that links small changes in the vibrational modes of the substrate (or reacting species) to large changes in enzyme fluctuations in different states along the reaction. $\Delta C_P^{\ddagger}$ reflects the change in the *distribution* (and/or magnitude) of protein vibrational modes between the ground and

transition state. Therefore, we expect that the apparent disconnect between the scale of substrate isotopic mass changes and the (thermodynamic) heat capacity changes might be resolved by a deeper understanding of the distribution of these protein vibrational modes and how these modes are affected by subtle changes in substrate vibrations. For example, based on our present understanding of the physical origin of $\Delta C_P^{\ddagger}$, we suggest a physical model where the isotopic changes in the substrate are translated to a shift in the conformational landscape (structural, energetic or both) of the enzyme, resulting in a difference in fluctuations between the reactant and transition state complexes.[50]

Materials and methods

ssGDH expression and purification.

*ss*GDH was expressed with AmpR in a pET3a plasmid. It was transformed into BL21 (DE3) *Escherichia coli* using heat shock and grown on LB agar with ampicillin (100 μg/ml) at 37 °C. A 50 ml LB starter culture was used to inoculate 5 x 1L LB until an OD_{600} of 0.5-0.6 was reached. Cells were harvested by centrifugation (4 °C, 8000 rpm, 10 min) before being lysed by sonication using a lysis buffer (pH 7) containing 100 mM HEPES, lysozyme, DNAase and a protease inhibitor cocktail tablet. Soluble and insoluble fractions were separated by centrifugation at 4 °C (25,000 rpm, 10 min). Due to the thermostability of *ss*GDH, the soluble fraction was purified by heating the sample to 70 °C for 50 min. To remove precipitated protein, samples were centrifuged (4 °C 13,000 rpm, 10 min) before being dialysed for 4 hours in 100 mM HEPES buffer (pH 7). Samples were further purified/concentrated through the use of Vivaspin centrifugal concentrators (MWCO = 30 kDa). The concentration of purified samples was measured by the absorbance at 280 nm ($\varepsilon 280$ = 49,390 M^{-1} cm^{-1}), obtained via the input of *ss*GDH amino acid sequence into the ExPASy ProtParam tool.[179] Approximately 8 ml of 35 mg/ml purified sample was obtained.

Substrates and coenzymes.

D-glucose, D-xylose, D_2O and $NADP^+$ were obtained from Sigma Aldrich. D-glucose (1-D), D-glucose (1,2,3,4,5,6,6-D7) and D-xylose (1-D) were obtained from Cambridge Isotope Laboratories. In this manuscript the varying isotopes and D_2O combinations will be described with the following nomenclature: D-glucose (1-D) – D_1 , D-xylose (1-D) – D_1, D-glucose + D_2O – D_5 , D-glucose (1,2,3,4,5,6,6-D7) – D_7 , D-glucose (1,2,3,4,5,6,6-D7) + D_2O – D_{12}.

Enzyme assays.

Steady-state *ss*GDH kinetic measurements were carried out using a lidded 1 ml quartz cuvette to prevent evaporation at high temperatures and a UV⁄ Vis spectro-photometer (Agilent Cary 60 UV-Vis spectrometer) in 100 mM HEPES (pH 8). Accurate concentrations of $NADP^+$ were determined using NADP ε_{260} = 17,800 M^{-1} cm^{-1}. Enzyme activity was measured for each condition at 85 °C by following the formation of NADPH at 340 nm using ε_{340} = 6220 M^{-1} cm^{-1} as a direct measurement of ssGDH steady-state rates

; the data fitted well to Michaelis-Menten kinetics. Temperature-dependences were carried out from 60 °C – 90 °C at 5 °C intervals using initial velocity measurements at substrate concentrations maintained above 10x K_m to ensure saturation. The data were fitted to Eq 34 or Eq 19 as described in the manuscript using OriginPro 2016 (MicroCal). The measured pH for experiments performed in D_2O was adjusted accordingly to match that of the pH in H_2O.[180]

Molecular dynamics simulations.

The *ss*GDH crystal structure 2CDB[70] was prepared for simulation using scwrl4[181] to revert the T41A mutation and modeller[182] to model in the missing loop at positions 50-59 (based on chain A). To obtain similar starting points for the glucose and xylose complexes, this loop was used for all four chains and coordinates from 2CDB were also used for the xylose complex (where xylose was placed based on alignment with 2CDC[70]). The Amber16 suite of programs was used for periodic boundary simulation and analysis[183], with the ff14SB force-field for protein atoms[184], GLYCAM-06j for glucose/xylose[185], parameters from Ryde *et al.* for NADP+,[186] TIP3P for water and ZAFF[187] for the Zn^{2+} coordinated by Cys93, Cys96, Cys99 and Cys107. For the Zn^{2+} directly adjacent to the substrate binding site, restraints were used to maintain the crystallographically observed coordination with Cys39 and His66. After brief minimization of the complex and added water, the system was heated to 300 K and subsequently equilibrated to 1 atm in the NPT ensemble (with positional restraints on Cα atoms). After gradual release of Cα positional restraints, 50 ns NPT production simulations were performed at 300 K and 1 atm. Histograms of the D-A distances were calculated over all four binding sites using 10-50 ns of four independent simulations for each substrate. (Further details of model setup, restraints and simulation procedures are included in the Supporting Information.)

QM Cluster Model.

The aforementioned X-ray crystal structure of *ss*GDH in complex with glucose and $NADP^+$ (PDB ID 2CDB[70]) was used to create a 148 atom model of the active site (Figure S5). To preserve the overall structure of the active site, several atoms were fixed throughout the optimisation process and care was taken to ensure non-reacting groups stayed in the same local minima throughout the reaction. The T41A mutation was reversed *in silico* with the rotamer selected based on our MD simulations. All Calculations were performed using Gaussian16,[188] employing the M06-2X functional.[189] Geometry optimisations and frequency calculations were performed *in vacuo* with the 6-31G(d,p) basis set. All models were optimised on an ultrafine integration grid and under tight convergence criteria. Single point energies were obtained using the 6-311++G(2d,2p) basis set, with the surrounding protein environment accounted for using the SMD solvation model with a dielectric constant of 4.[190] Thermal corrections to the obtained energies were taken from the aforementioned frequency calculations, employing a scale factor of 0.97.[191] Contributions to tunneling on the rate of reaction were estimated using Wigner's correction.[192] Further details about calculation methodology and the coordinates of all stationary points obtained can be found in the Supporting Information.

ASSOCIATED CONTENT

Supporting Information. Molecular dynamics simulations, QM cluster model calculations, supporting data and cartesian coordinates of all stationary points. This material is available free of charge via the Internet at http://pubs.acs.org.

AUTHOR INFORMATION

Corresponding Author

*Christopher R Pudney, Department of Biology and Biochemistry, University of Bath, Bath, United Kingdom. c.r.pudney@bath.ac.uk.

*Marc W van der Kamp, School of Biochemistry, University of Bristol, Cantock's Close, Bristol BS8 1TS, United Kingdom. marc.vanderkamp@bristol.ac.uk.

*Vickery L Arcus, School of Science, Faculty of Science and Engineering, University of Waikato, Hamilton 3240, New Zealand. varcus@waikato.ac.nz.

Author Contributions

HBLJ and CM performed experimental work. RMC, MWK and ABT performed computational simulations and calculations. All authors discussed and interpreted data. The manuscript was written through contributions of all authors. All authors have given approval to the final version of the manuscript. Δ, these authors contributed equally.

ABBREVIATIONS

D-glucose (1-D), D_1 ; D-xylose (1-D), D_1 ; D-glucose + D_2O, D_5 ; D-glucose (1,2,3,4,5,6,6-D7) , D_7 ; D-glucose (1,2,3,4,5,6,6-D7) + D_2O, D_{12}.

ACKNOWLEDGMENT

HBLJ's studentship is funded by the University of Bath. RMC's studentship is funded by the EPSRC. MWvdK is a BBSRC David Phillips Fellow (BB/M026280/1). We thank Katarzyna Świderek (Universitat Jaume I), Ian H. Williams (University of Bath) and Vicent Moliner (Universitat Jaume I) for helpful discussions and critical review of the manuscript.

Supporting information

Uncovering the relationship between the change in heat capacity for enzyme catalysis and vibrational frequency through isotope effect studies

Hannah BL Jones[†Δ], Rory M Crean[#†Δ], Christopher Matthews[†], Anna B Troya[†], Michael J Danson[†], Steven D Bull[‡], Vickery L Arcus[§*], Marc W Van der Kamp[%*] and Christopher R Pudney[†*].

†Department of Biology and Biochemistry, ‡Department of Chemistry, # Doctoral Training Centre in Sustainable Chemical Technologies, University of Bath, Bath BA2 7AY, United Kingdom

§School of Science, Faculty of Science and Engineering, University of Waikato, Hamilton 3240, New Zealand

% School of Biochemistry, University of Bristol, Biomedical Sciences building, University Walk, Bristol BS8 1TD, United Kingdom

*Christopher R Pudney, Department of Biology and Biochemistry, University of Bath, Bath, United Kingdom. c.r.pudney@bath.ac.uk.
*Marc W van der Kamp, School of Biochemistry, University of Bristol, Cantock's Close, Bristol BS8 1TS, United Kingdom. marc.vanderkamp@bristol.ac.uk.
*Vickery L Arcus, School of Science, Faculty of Science and Engineering, University of Waikato, Hamilton 3240, New Zealand. varcus@waikato.ac.nz.

Author Contributions

HBLJ and CM performed experimental work. RMC, MWK and ABT performed computational simulations and calculations. All authors discussed and interpreted data. The manuscript was written through contributions of all authors. All authors have given approval to the final version of the manuscript. Δ, these authors contributed equally.

Supporting Information Materials and Methods

Molecular dynamics simulations: Model setup, restraints and simulation details

The *ss*GDH crystal structure 2CDB[70] was prepared for simulation using scwrl4[181] to revert the T41A mutation and modeller[193] to model in the missing loop at positions 50-59, based on the coordinates of the surrounding residues in chain A. The same loop conformation was subsequently transferred to the other three chains. To avoid a clash with this loop in chain C, conformer B (assigned 50% occupancy) was chosen for His118. (If not mentioned, conformer A was chosen for other residues with multiple conformers defined, including for the glucose O6.) Asn/Gln flips and His tautomers and were selected based on optimal hydrogen bonding contacts through the AmberTools facility reduce, with His66 and His319 singly protonated on Nδ1, others on Nε2. The exception was His297, which was protonated on Nδ1: test simulations indicated that this tautomer better retained the crystallographically determined enzyme-ligand conformation structure. All ionizable residues (with exception of the Cys residues coordinating Zn^{2+}, see below) were modelled in their standard protonation states (in agreement with pK_a predictions by PropKa 3.1)[194]. To obtain similar starting points for the glucose and xylose complexes, the same protein starting model was used for the xylose complex (where xylose was placed based on alignment with 2CDC [70]).

The Amber16 suite of programs was used for periodic boundary simulations and analysis,[183] with the ff14SB force-field for protein atoms,[184] GLYCAM-06j for glucose/xylose,[185] parameters from Ryde *et al.* for NADP+,[186] TIP3P for water and ZAFF[187] for the Zn^{2+} coordinated by Cys93, Cys96, Cys99 and Cys107. These Cys residues were thus modelled as thiolates (CYM). For the Zn^{2+} directly adjacent to the substrate binding site, the default Amber ion parameters were used. To avoid coordination changes around the Zn^{2+} ion, the following one-sided harmonic restraints were applied if: 1) the His66 NE2–Zn^{2+} distance was larger than 2 Å (force constant 70 kcal mol^{-1} $Å^{-2}$); 2) the Asp42 OD2–Cys39 N distance was larger than 1.95 Å (force constant 70 kcal mol^{-1} $Å^{-2}$); 3) the Asp42 OD2–Zn2+ distance was smaller than 4.2 Å (force constant 100 kcal mol^{-1} $Å^{-2}$).

In addition to the water molecules present in the crystal structure, a rectangular box of water was added using the AmberTools facility tleap such that all protein atoms were at least 11.5 Å away from the edge of the box (closeness parameter of 0.9). 20 water molecules (at least 5 Å away from the protein) were replaced with Na^+ ions to neutralize the system. After minimization of solvent and hydrogens (100 steps steepest descent, 400 steps conjugate gradient), the full system was briefly minimized (400 steps) with positional restraints of 5 kcal mol^{-1} $Å^{-2}$ on all Cα atoms. Maintaining these positional restraints on Cα atoms, velocities were assigned at 25 K and the system was heated to 300 K in 50 ps using Langevin temperature control in the NVT ensemble (with a 1 ps^{-1} collision frequency). Subsequently, 100 ps of equilibration was performed in the NPT ensemble at 1 atm, using the Berendsen barostat (1 ps pressure relaxation time) and

Langevin dynamics for temperature control (5 ps^{-1} collision frequency). Thereafter, the positional restraints on Cα atoms were gradually removed in four consecutive 10 ps simulations under the same conditions (4, 3, 2, and 1 kcal mol^{-1} $Å^{-2}$ as force constants). Production MD (without positional restraints) was then performed in the NPT ensemble at 1 atm and 300 K for 50 ns, saving coordinates every 10 ps. All MD simulations were performed with the default direct-space cut-off for non-bonded interactions and particle-mesh Ewald summation for long-range electrostatics, run with pmemd.cuda. Four independent simulations were run for each complex (GDH-glucose and GDH-xylose).

QM Cluster Model Calculations: **Model** ***Construction, pKa and KIE Calculations***

The X-ray crystal structure of *ss*GDH in complex with glucose and $NADP^+$ (2CDB)[70] was used to create a 148 atom model of the active site. Truncations of the enzyme active site were made across non-polar bonds. All titratable residues included in the model were in their standard protonation state. The T41A mutation used to crystallise *ss*GDH was reverted in silico, with the rotamer (side chain alcohol group acting as a hydrogen bond acceptor to the alcohol group of the glucose C1) chosen based on its prevalence in our MD simulations. To preserve the overall structure of the active site, several atoms were fixed throughout the optimisation process and care was taken to ensure non-reacting groups stayed in the same local minima throughout the reaction.

All Calculations were performed using Gaussian16,[188] employing the M06-2X functional.[189] Geometry optimisations and frequency calculations were performed in vacuo with the 6-31G(d,p) basis set. All models were optimised on an ultrafine integration grid and under tight convergence criteria. Single point energies were obtained using the 6-311++G(2d,2p) basis set, with the surrounding protein environment accounted for using the SMD solvation model with a dielectric constant of 4.[190] Thermal corrections to the obtained energies were taken from the aforementioned frequency calculations, employing a scale factor of 0.97.[191] Contributions to tunnelling on the rate of reaction were estimated using Wigner's correction.[192]

In order to simulate the deprotonation of the Zn coordinated water to a Zn coordinated hydroxide by the bulk milieu (reactant to reactive intermediate), a proton on the Zn coordinated water (reactant model) was removed and the structure re-optimised, giving the reactive intermediate. During optimisation, the Zn coordinated hydroxide abstracted the sugar C1 alcohol group's proton, forming an alkoxide on the sugar. This therefore led us to propose the stepwise mechanism as seen in Scheme S1. To calculate the barrier for the transition from reactant to reactive intermediate, the experimentally determined barrier at 298 K (73.5 kJ mol^{-1}) was subtracted from the computationally determined hydride transfer barrier (32.6 kJ mol^{-1}), with the subsequent energy difference used to predict a pKa of 7.2.

All polar hydrogen atoms in the cluster model were considered deuterated when modelling the SKIE (see Figure S5). Heat capacities of activation (Table S2) were

calculated from the differences in constant volume heat capacity for the reactive intermediate and transitions state models.

Supporting Tables

Table S1. Change in Hydride Transfer Frequency Upon Deuteration.

	Reactant Symmetric[a] $\bar{\upsilon}$ (cm^{-1})	Reactant Asymmetric[a] $\bar{\upsilon}$ (cm^{-1})	Reactive Intermediate $\bar{\upsilon}$ (cm^{-1})	Transition State $\bar{\upsilon}$ (cm^{-1})
glucose	3040.20	3047.13	2674.38	-576.79
D_1-glucose[c]	2236.61		1956.13	-523.85
D_5-glucose	3035.95	3047.03	2674.34	-574.96
D_7-glucose	2233.24	2239.84	1955.35	-523.10
D_{12}-glucose	2240.46	2237.05	1959.64	-521.65
D_5-glucose + D_20[b]	3036.01	3047.03	2677.49	-573.86
D_{12}-glucose + D_20[b]	2236.86	2240.33	1958.40	-520.76

[a], Reactant symmetric and asymmetric stretches are coupled to additional C–H groups on glucose. [b], Mono-deuteration breaks symmetry leaving only one major C-H stretch, not significantly coupled to another other glucose C–H bond. [c], D_2O specifies a solvent kinetic isotope effect. Protons considered deuterated for SKIE calculations are indicated in Figure S5.

Table S2. Computationally Predicted Heat Capacity of Activation at Different Temperatures

Temperature (K)	glucose (j mol^{-1} K^{-1})	D_1-glucose (j mol^{-1} K^{-1})	D_5-glucose (j mol^{-1} K^{-1})	D_5-glucose + D_20 (j mol^{-1} K^{-1})	D_7-glucose[a] (j mol^{-1} K^{-1})	D_{12}-glucose[a] (j mol^{-1} K^{-1})	D_{12}-glucose + D_20 (j mol^{-1} K^{-1})
298	-0.255	0.351	-0.351	-0.690	0.309	0.222	-0.121
333	-0.142	0.502	-0.405	-0.890	0.468	0.205	-0.280
338	-0.134	0.510	-0.422	-0.924	0.472	0.184	-0.314
343	-0.134	0.506	-0.443	-0.957	0.477	0.167	-0.347
348	-0.134	0.510	-0.468	-0.999	0.477	0.142	-0.385
353	-0.134	0.506	-0.489	-1.032	0.472	0.117	-0.426
358	-0.142	0.497	-0.514	-1.070	0.464	0.088	-0.468
363	-0.146	0.489	-0.543	-1.112	0.460	0.063	-0.510

[a], D_7-glucose and D_{12}-glucose are not possible to measure experimentally and correspond to deuteration of only the alcohol groups on glucose (D_7), and deuteration of both the alcohol and aliphatic hydrogens on glucose (D_{12}).

Supporting Figures

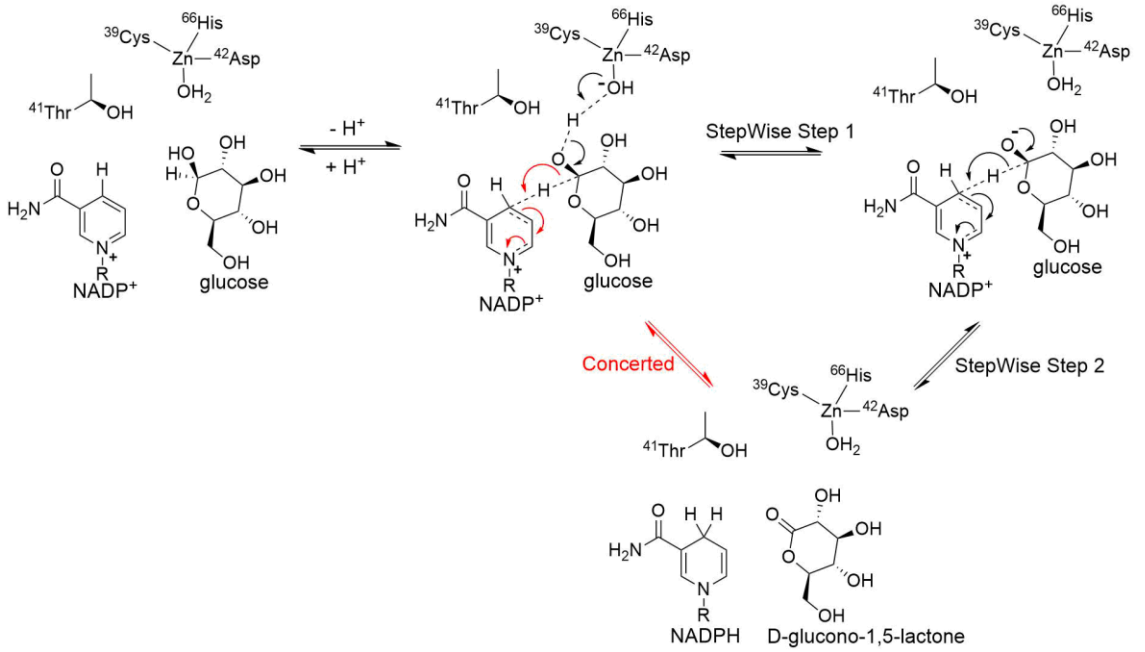

Scheme S1. Two possible mechanisms for the oxidation of glucose by *ss*GDH. Proton abstraction and hydride transfer can occur in either a single concerted step (red and black curly arrows) or by a 2-step (black curly arrows only) mechanism, whereby a stable alkoxide intermediate is formed prior to hydride transfer.

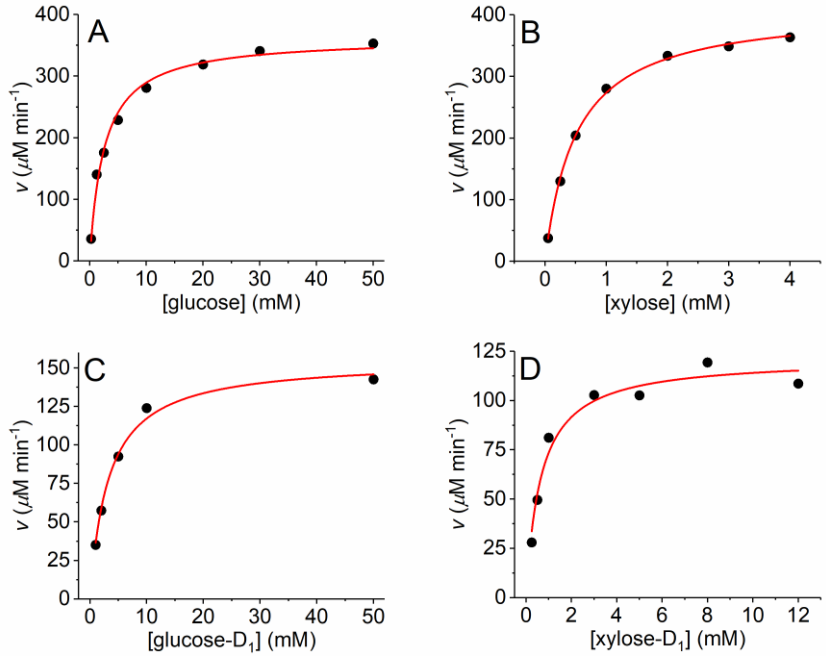

Figure S1. Michaelis-Menten plots for glucose **(A)**, xylose **(B)**, glucose-D_1 **(C)** and xylose-D_1 **(D)** with a saturating concentration of NADP. The solid red line is the fit to the Michaelis-Menten equation. Note that the enzyme concentrations are not identical for each plot and *k*cat values are given in the main text.

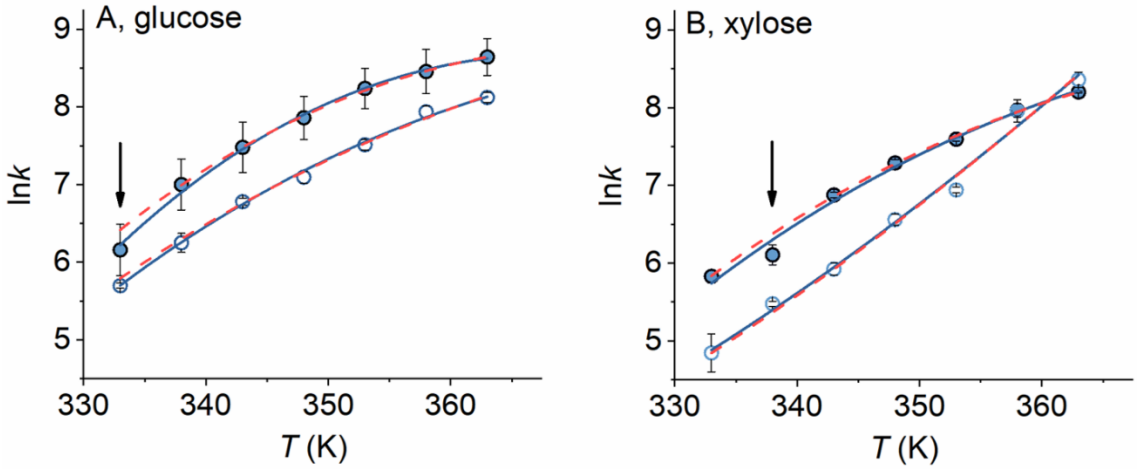

Figure S2. Alternative fitting of glucose (A) and xylose (B) temperature-dependencies. Data corresponds to that shown in Figure 21A and 21B respectively. The solid lines are the fit to Eq 19 using all data points and the red dashed lines are the fit to Eq 19 omitting the 'outlier' data points shown with the black arrow. The corresponding $\Delta\Delta C_P^{\ddagger}$ values for the omitted data point fits are glucose $\Delta\Delta C_P^{\ddagger} = -1.44 \mp 1.33$ kJ mol^{-1} K^{-1} and xylose $\Delta\Delta C_P^{\ddagger} = -3.61 \mp 2.30$ kJ mol^{-1} K^{-1}, which is essentially the same as the fit including all data points.

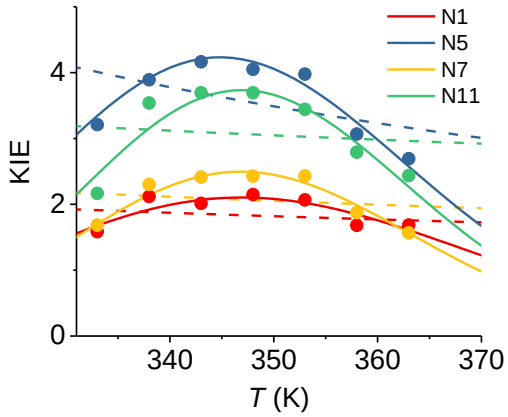

Figure S3. Comparison of the fit of the KIE data (Figure 23B) to either Eq 34 (dashed lines) or Eq 19 (solid lines). The curves are the numerical subtraction between the fits for the protiated and deuterated data sets and serves to show the trend in the data.

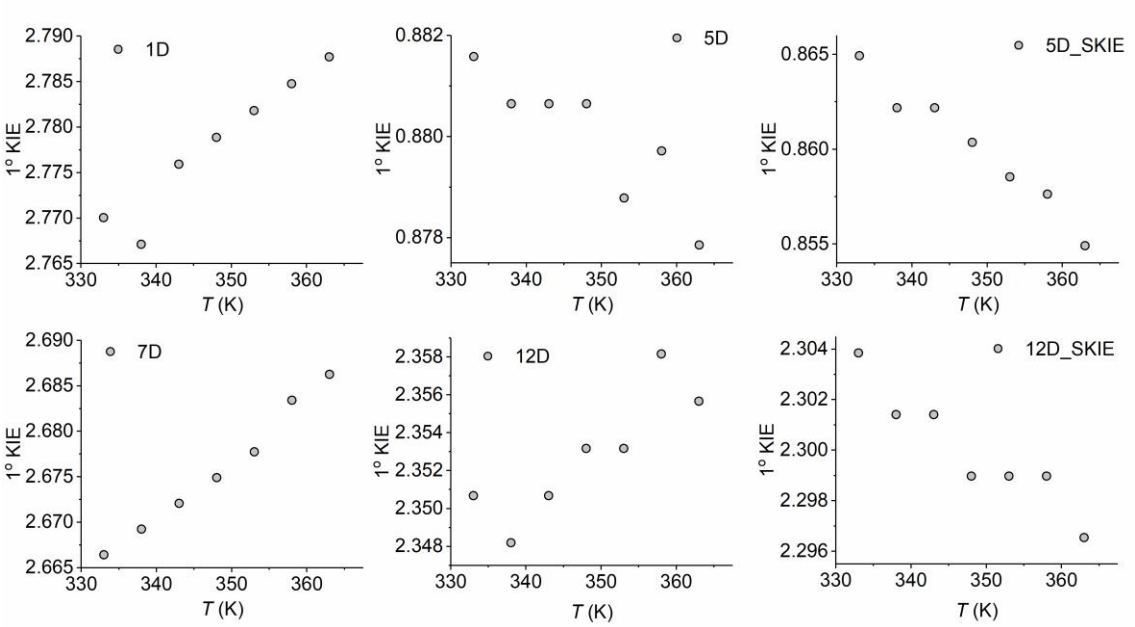

Figure S4. Temperature-dependence of computationally calculated KIEs.

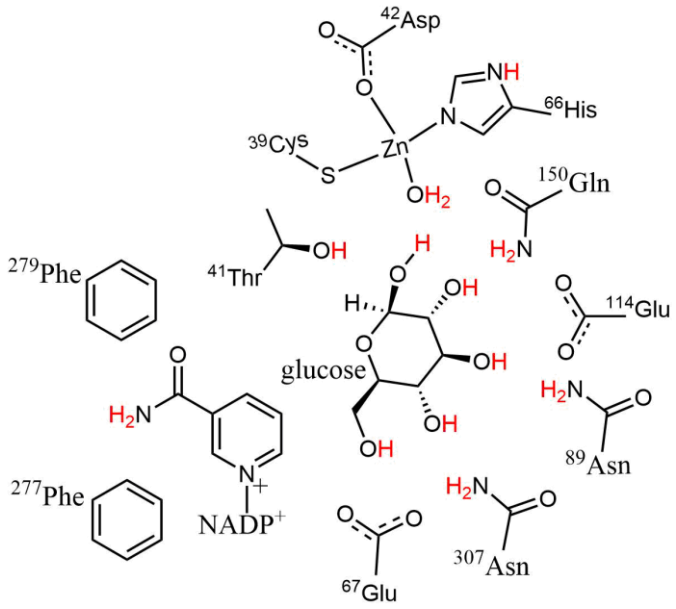

Figure S5. Molecules included in the QM cluster model of *ss*GDH. Red hydrogen atoms indicate those considered deuterated for the *in silico* measurement of the solvent kinetic isotope effect (SKIE).

Cartesian Coordinates of All Stationary Points Obtained

Reactant: Charge -1, Multiplicity 1

N	-5.72700	-0.86300	2.25800
N	-4.29200	-1.65700	0.81500
N	-3.18700	3.99300	-0.24300
N	-3.04800	1.31500	-2.64500
N	0.34200	5.82300	-0.96300
N	3.92800	-3.15100	-0.12100
N	6.39400	0.35000	-0.49800
C	-2.95300	-5.80200	0.06100
C	-1.56700	-4.32600	5.10600
C	-1.20800	-3.12100	4.23200
C	-1.12800	-1.81500	5.02600
C	-6.17400	1.46500	1.31100
C	-5.50900	0.14500	1.32500
C	-4.60700	-0.37300	0.44600
C	-4.97300	-1.94800	1.91700
C	-6.45700	-1.96800	-2.31700
C	-6.16900	-3.46500	-2.13400
C	-5.52700	4.71800	-0.53600
C	-4.20600	4.21000	-1.10800
C	-1.29800	6.60100	4.31500
C	-0.49100	5.31900	4.10000
C	-5.10000	1.38200	-3.97300
C	-3.91000	0.63000	-3.41300
C	2.64100	1.30300	-4.67700
C	1.47900	1.36300	-3.66600
C	7.85000	-1.85300	-3.37400
C	7.38000	-0.60500	-3.79700
C	6.95400	-2.91900	-3.21600
C	6.01900	-0.42300	-4.06700
C	5.59400	-2.73600	-3.49200
C	5.12700	-1.48900	-3.92100
C	6.74000	-2.20400	3.89000
C	5.35400	-2.18400	3.68900
C	7.50400	-1.05500	3.64300
C	4.72600	-1.01800	3.22900
C	6.87500	0.10700	3.18000
C	5.48900	0.12700	2.97400
C	2.72900	6.14900	-1.20200
C	1.31000	6.63500	-1.45900
C	0.35900	-0.49800	0.79800
C	-0.53600	0.31400	-0.15800
C	0.03600	1.74400	-0.23000

C	0.10900	2.35800	1.17200
C	0.83200	1.38700	2.14100
C	0.79600	1.82800	3.59900
C	4.44200	-4.41300	0.43500
C	4.71300	-2.04500	-0.13500
C	4.29000	-0.89000	-0.77500
C	3.03100	-0.89500	-1.38100
C	2.22900	-2.03600	-1.34900
C	2.69600	-3.15800	-0.70100
C	5.10000	0.38500	-0.91000
O	0.06100	-3.41000	3.61400
O	-6.99900	-4.28400	-2.53900
O	-5.03700	-3.79600	-1.58100
O	-4.09600	3.99000	-2.32100
O	-0.56500	4.44400	5.00900
O	0.12400	5.22200	2.99700
O	-3.79500	-0.59000	-3.65000
O	0.98300	2.46000	-3.33400
O	1.14400	0.21600	-3.18900
O	1.06600	7.66300	-2.09800
O	0.10400	-1.87700	0.86000
O	-0.64600	-0.27600	-1.44200
O	-0.72900	2.55200	-1.11800
O	0.82100	3.57400	1.08100
O	0.27000	0.05800	2.08700
O	-0.52400	1.94900	4.07500
O	4.58300	1.38700	-1.38200
O	-2.41100	-2.15600	-2.00300
S	-2.62100	-4.35200	1.14300
Zn	-3.54900	-3.05800	-0.55800
H	-2.10600	-5.88700	-0.62900
H	-3.88100	-5.73000	-0.53500
H	-1.97000	-3.02100	3.44600
H	0.16400	-2.81500	2.84900
H	-0.38200	-1.90300	5.82700
H	-0.84300	-0.97500	4.38300
H	-2.09700	-1.57400	5.48300
H	-5.93200	2.01700	0.38600
H	-5.85300	2.09700	2.15500
H	-6.32800	-0.79600	3.06900
H	-4.18200	0.08900	-0.43600
H	-4.93300	-2.89200	2.44100
H	-6.01300	-1.61400	-3.25900
H	-6.07800	-1.33600	-1.51400
H	-5.57500	4.59300	0.54700
H	-6.34300	4.14600	-0.99500

H	-2.29300	3.61500	-0.57700
H	-3.26300	4.20200	0.74200
H	-1.12800	7.33600	3.52500
H	-1.16300	7.07800	5.28700
H	-5.00600	2.47700	-4.00400
H	-5.99900	1.13700	-3.39300
H	-3.14200	2.32600	-2.55800
H	-2.18800	0.88300	-2.31000
H	2.64100	0.31100	-5.12900
H	3.56900	1.46200	-4.12200
H	8.07300	0.22300	-3.92600
H	7.32100	-3.89500	-2.90600
H	5.65200	0.54700	-4.38700
H	4.89800	-3.56600	-3.38700
H	4.07200	-1.34100	-4.13000
H	4.75600	-3.06500	3.91300
H	8.58500	-1.08000	3.76900
H	3.64700	-0.99600	3.09400
H	7.46000	1.00200	2.98600
H	5.00400	1.03400	2.62400
H	2.83100	5.76000	-0.18000
H	3.46700	6.94300	-1.35200
H	-0.62200	6.07500	-1.13500
H	0.52800	5.00000	-0.38700
H	-0.84700	-2.09700	0.81600
H	1.40400	-0.42300	0.45800
H	-1.54600	0.34100	0.27500
H	1.06400	1.68900	-0.62000
H	-0.91000	2.51800	1.55600
H	1.89000	1.33600	1.82000
H	0.06300	0.04000	-2.11500
H	-0.21200	2.63300	-1.96200
H	1.34600	1.06900	4.18300
H	1.33200	2.78300	3.68400
H	0.59100	4.14800	1.87100
H	-0.59700	2.86000	4.47700
H	4.76100	-5.06600	-0.38200
H	5.65500	-2.14100	0.38800
H	2.66100	-0.01700	-1.89500
H	1.23900	-2.02200	-1.79000
H	2.12000	-4.07100	-0.60200
H	6.96900	1.17200	-0.62400
H	6.88000	-0.49600	-0.21400
H	-2.92800	-1.65200	-2.69800
H	-0.72200	-4.54600	5.75900

H	-1.77100	-5.21900	4.50400
H	-2.44800	-4.11000	5.72300
H	-2.36100	6.31700	4.27600
H	-7.54100	-1.82800	-2.39000
H	-5.27700	1.00400	-4.98500
H	2.55300	2.08600	-5.43400
H	-7.26800	1.37600	1.36000
H	-5.65700	5.77500	-0.79200
H	-2.99900	-6.71700	0.66400
H	8.91400	-2.01200	-3.22000
H	7.22100	-3.10900	4.25600
H	3.65000	-4.91800	1.04100
H	5.28700	-4.22400	1.11900
H	2.95200	5.32300	-1.88900
H	-1.67000	-1.54300	-1.75900

Reactive Intermediate: Charge -2, Multiplicity 1

N	-5.80700	-0.99900	2.23200
N	-4.38900	-1.77500	0.76500
N	-3.29700	3.85600	-0.29800
N	-3.06700	1.60300	-2.79300
N	0.23300	5.91100	-0.84800
N	3.82500	-3.22200	-0.19000
N	6.29800	0.27500	-0.56400
C	-3.04000	-5.89600	-0.07100
C	-1.54800	-4.23000	5.05200
C	-1.22000	-3.04600	4.12500
C	-1.06400	-1.72600	4.88600
C	-6.26000	1.34300	1.33100
C	-5.59900	0.02000	1.30600
C	-4.70900	-0.49000	0.40800
C	-5.05400	-2.07900	1.86700
C	-6.56000	-2.02100	-2.35900
C	-6.05500	-3.46700	-2.17400
C	-5.62600	4.63200	-0.45800
C	-4.30200	4.24300	-1.11300
C	-1.37300	6.42700	4.40600
C	-0.40900	5.23500	4.23700
C	-5.21400	1.36100	-3.95900
C	-4.01500	0.74700	-3.22400
C	2.52300	1.30200	-4.70400
C	1.35400	1.37900	-3.70500
C	7.74100	-1.87200	-3.48800
C	7.27300	-0.62300	-3.90800
C	6.83500	-2.91900	-3.27100

C	5.90500	-0.41700	-4.11100
C	5.46600	-2.71200	-3.47800
C	5.00000	-1.46100	-3.89800
C	6.65900	-2.34600	3.81100
C	5.27100	-2.31600	3.61900
C	7.43200	-1.20700	3.54500
C	4.64600	-1.15300	3.15100
C	6.80400	-0.04600	3.07400
C	5.41800	-0.01800	2.87900
C	2.62500	6.08300	-1.14000
C	1.23300	6.64800	-1.38000
C	0.48900	-0.37200	0.58000
C	-0.50300	0.59200	-0.17300
C	0.12800	1.99100	-0.23700
C	0.33500	2.51800	1.18100
C	1.19300	1.49700	1.97300
C	1.31600	1.84900	3.45700
C	4.35600	-4.50700	0.29000
C	4.59500	-2.09500	-0.17700
C	4.14000	-0.91500	-0.73100
C	2.83700	-0.88300	-1.28500
C	2.07800	-2.06700	-1.33500
C	2.56900	-3.20400	-0.74700
C	4.96600	0.33900	-0.86900
O	-0.01200	-3.35800	3.41700
O	-6.81800	-4.41000	-2.43400
O	-4.82300	-3.61000	-1.79100
O	-4.19500	4.28600	-2.34600
O	-0.50400	4.30800	5.09100
O	0.38000	5.28100	3.24900
O	-3.93600	-0.47600	-3.05200
O	0.88300	2.49500	-3.38500
O	0.99800	0.24300	-3.23800
O	1.04500	7.68300	-2.03600
O	0.17700	-1.65300	0.61400
O	-0.87500	0.14600	-1.46600
O	-0.65500	2.88900	-1.03100
O	0.99600	3.77300	1.11300
O	0.68100	0.16200	1.90300
O	0.06600	1.84500	4.11200
O	4.45700	1.37700	-1.27600
O	-1.62200	-2.38000	-1.17700
S	-2.84000	-4.61900	1.22000
Zn	-3.40600	-3.11400	-0.50200
H	-2.17700	-5.93800	-0.74600

H	-3.95200	-5.79300	-0.68600
H	-2.03900	-2.94900	3.39800
H	0.02700	-2.80000	2.61300
H	-0.27600	-1.81800	5.64600
H	-0.78500	-0.90800	4.21200
H	-2.00000	-1.44800	5.39200
H	-6.00800	1.91600	0.42100
H	-5.93800	1.95100	2.19100
H	-6.39100	-0.94000	3.05400
H	-4.29900	-0.03900	-0.48600
H	-5.00000	-3.02900	2.37900
H	-6.07500	-1.60500	-3.25300
H	-6.24200	-1.41000	-1.51300
H	-5.63000	4.50100	0.62600
H	-6.42800	4.02300	-0.89200
H	-2.38600	3.54400	-0.66300
H	-3.41100	3.83700	0.70500
H	-1.42300	7.00100	3.48000
H	-1.07500	7.08800	5.21900
H	-5.39200	2.40900	-3.69500
H	-6.10600	0.77900	-3.70800
H	-3.18400	2.60800	-2.87700
H	-2.24100	1.22400	-2.32000
H	2.51700	0.32000	-5.17500
H	3.44800	1.44300	-4.14200
H	7.97300	0.19400	-4.07100
H	7.19600	-3.89300	-2.94700
H	5.53700	0.55800	-4.41600
H	4.75700	-3.51700	-3.30300
H	3.93600	-1.29000	-4.03300
H	4.66900	-3.19400	3.84500
H	8.51300	-1.23300	3.66400
H	3.56800	-1.12700	3.00600
H	7.39500	0.84200	2.85900
H	4.93500	0.88500	2.51300
H	2.73100	5.68200	-0.12000
H	3.38400	6.84900	-1.30300
H	-0.72100	6.16600	-1.06800
H	0.39700	5.05300	-0.31600
H	-0.96200	-2.20800	-0.42100
H	1.50200	-0.21200	0.04400
H	-1.42500	0.61500	0.42200
H	1.11600	1.91600	-0.71400
H	-0.63600	2.61900	1.68700
H	2.20700	1.52800	1.52700
H	-0.12300	0.24600	-2.13800

H	-0.26200	2.85700	-1.93900
H	1.97300	1.09200	3.91800
H	1.80600	2.82900	3.54300
H	0.80300	4.28800	1.94300
H	-0.10500	2.74800	4.49300
H	4.61100	-5.15400	-0.55400
H	5.56500	-2.20900	0.29000
H	2.49800	-0.01700	-1.83400
H	1.09700	-2.06900	-1.79100
H	2.00600	-4.12900	-0.69400
H	6.87200	1.10000	-0.67700
H	6.78700	-0.57500	-0.29800
H	-1.62600	-1.49200	-1.60700
H	-0.70100	-4.44400	5.70600
H	-1.74300	-5.13000	4.45700
H	-2.42800	-4.00700	5.66800
H	-2.37200	6.04800	4.65900
H	-7.64800	-2.01000	-2.46600
H	-5.04800	1.28600	-5.04000
H	2.45800	2.09600	-5.45500
H	-7.35600	1.26200	1.37400
H	-5.83800	5.67900	-0.69500
H	-3.09900	-6.88900	0.40100
H	8.80600	-2.03400	-3.34200
H	7.13600	-3.25300	4.17900
H	3.58200	-4.99600	0.93600
H	5.23900	-4.34000	0.92600
H	2.79600	5.25100	-1.83400

Transition State: Charge -2, Multiplicity 1

N	-5.80500	-0.91700	2.35600
N	-4.36200	-1.68200	0.90500
N	-3.26000	3.94700	-0.18800
N	-3.21600	1.46800	-2.55700
N	0.27900	5.93600	-0.80300
N	3.82800	-3.26900	-0.17400
N	6.38500	0.13200	-0.69000
C	-3.13000	-5.84000	0.02000
C	-1.48600	-4.26900	5.04000
C	-1.13400	-3.08300	4.12300
C	-0.94600	-1.77600	4.90000
C	-6.22900	1.43800	1.46900
C	-5.58100	0.10900	1.44200
C	-4.67500	-0.39400	0.55700

C	-5.04600	-1.99500	1.99400
C	-6.66100	-1.93700	-2.19300
C	-6.23900	-3.40900	-2.02400
C	-5.60000	4.71300	-0.34300
C	-4.29500	4.26000	-1.00000
C	-1.20900	6.47300	4.41100
C	-0.26100	5.27400	4.19600
C	-5.31600	1.42200	-3.84200
C	-4.10800	0.72000	-3.22800
C	2.40500	1.27900	-4.78500
C	1.26800	1.34300	-3.74200
C	7.61100	-1.95500	-3.67700
C	7.15600	-0.71600	-4.13900
C	6.68800	-2.94500	-3.31700
C	5.78300	-0.46500	-4.23900
C	5.31500	-2.69300	-3.42000
C	4.86100	-1.45200	-3.87800
C	6.69000	-2.38000	3.64700
C	5.29600	-2.30800	3.51200
C	7.48300	-1.26100	3.35700
C	4.68600	-1.12300	3.08000
C	6.87000	-0.07800	2.92100
C	5.47800	-0.00800	2.78500
C	2.64600	6.06700	-1.23400
C	1.24300	6.59700	-1.48500
C	0.70600	-0.45300	0.66000
C	-0.33700	0.46100	-0.10300
C	0.18700	1.89700	-0.25000
C	0.42700	2.46500	1.14600
C	1.43600	1.54900	1.88600
C	1.63000	1.95600	3.35100
C	4.31100	-4.56300	0.32200
C	4.59000	-2.13400	-0.11800
C	4.14400	-0.93100	-0.61200
C	2.78800	-0.83600	-1.11500
C	2.10800	-2.08000	-1.33400
C	2.59500	-3.23100	-0.80600
C	5.01900	0.27600	-0.78900
O	0.06800	-3.42200	3.42200
O	-7.03200	-4.29800	-2.36900
O	-5.05200	-3.62800	-1.55600
O	-4.22500	4.17300	-2.23400
O	-0.31600	4.34300	5.04700
O	0.47300	5.32000	3.16600
O	-4.00100	-0.51400	-3.35400
O	0.77500	2.44800	-3.41500

O	0.96100	0.20200	-3.25100
O	1.01600	7.51800	-2.28100
O	0.41900	-1.68700	0.76200
O	-0.74100	-0.07500	-1.34700
O	-0.71800	2.69800	-1.02300
O	0.95300	3.77700	1.03900
O	1.03900	0.16900	1.90100
O	0.42500	1.90100	4.08300
O	4.53000	1.36200	-1.09600
O	-2.38000	-2.08000	-1.82000
S	-2.82700	-4.51300	1.23800
Zn	-3.50900	-3.05200	-0.43100
H	-2.28100	-5.90400	-0.67200
H	-4.05200	-5.73100	-0.57300
H	-1.94900	-2.95600	3.39600
H	0.14300	-2.85600	2.62500
H	-0.16700	-1.89800	5.66500
H	-0.63600	-0.96100	4.23700
H	-1.87900	-1.47500	5.40100
H	-5.99000	2.00500	0.55600
H	-5.88000	2.04400	2.32400
H	-6.40700	-0.86700	3.16600
H	-4.24000	0.08300	-0.31100
H	-5.00700	-2.95300	2.49400
H	-6.19000	-1.53200	-3.10100
H	-6.31400	-1.32600	-1.35900
H	-5.58000	4.58200	0.73800
H	-6.42200	4.11300	-0.75800
H	-2.36700	3.58300	-0.55500
H	-3.33300	4.02500	0.81700
H	-1.28100	7.04500	3.47500
H	-0.87500	7.14100	5.19800
H	-5.25300	2.51200	-3.91900
H	-6.23000	1.15800	-3.30300
H	-3.30800	2.48100	-2.55000
H	-2.35600	1.05500	-2.18800
H	2.36400	0.28900	-5.24800
H	3.34000	1.38800	-4.23500
H	7.86900	0.06100	-4.40600
H	7.03800	-3.90800	-2.94900
H	5.42800	0.50500	-4.57200
H	4.59300	-3.44800	-3.12000
H	3.79600	-1.24400	-3.92400
H	4.67900	-3.17100	3.74800
H	8.56800	-1.30100	3.44700

H	3.60500	-1.06500	2.96900
H	7.47700	0.79400	2.68700
H	5.00500	0.90900	2.44400
H	2.77400	5.66600	-0.22100
H	3.41100	6.81800	-1.42800
H	-0.68500	6.06400	-1.07500
H	0.51600	5.17700	-0.15600
H	-1.65800	-1.45500	-1.52700
H	1.73800	-0.33300	-0.03800
H	-1.22600	0.45300	0.54100
H	1.14800	1.88600	-0.78200
H	-0.51600	2.47500	1.71400
H	2.40300	1.64500	1.35700
H	-0.05900	0.09900	-2.08700
H	-0.33000	2.72900	-1.93400
H	2.35600	1.25400	3.79200
H	2.06900	2.96400	3.37900
H	0.82400	4.26400	1.89800
H	0.20500	2.80200	4.44200
H	4.54500	-5.23800	-0.50900
H	5.57000	-2.26600	0.32700
H	2.53700	0.00400	-1.74700
H	1.15100	-2.08000	-1.83900
H	2.05600	-4.17000	-0.84600
H	6.97900	0.93700	-0.82900
H	6.84800	-0.72200	-0.39200
H	-2.92900	-1.55800	-2.46400
H	-0.62700	-4.48900	5.67600
H	-1.69100	-5.16000	4.43500
H	-2.35800	-4.04100	5.66600
H	-2.20200	6.10600	4.70100
H	-7.74900	-1.86900	-2.28600
H	-5.43600	1.00800	-4.85000
H	2.33100	2.08100	-5.52600
H	-7.32400	1.36800	1.53500
H	-5.78300	5.76400	-0.58700
H	-3.19000	-6.81000	0.53400
H	8.67600	-2.13500	-3.56400
H	7.15500	-3.30400	3.98700
H	3.52600	-5.01300	0.97200
H	5.20400	-4.40400	0.94400
H	2.80900	5.22800	-1.92500

Product: Charge -2, Multiplicity 1

N	-5.83300	-1.02400	2.24100

N	-4.37300	-1.76300	0.79300
N	-3.20900	3.95800	-0.21900
N	-3.10100	1.39400	-2.63000
N	0.27800	5.91300	-0.86800
N	4.07000	-3.09100	-0.16400
N	6.54400	0.41700	-0.50100
C	-3.06500	-5.89200	-0.03000
C	-1.51300	-4.17400	5.13800
C	-1.21200	-2.99800	4.20000
C	-1.05000	-1.67400	4.95400
C	-6.22700	1.36700	1.40300
C	-5.58900	0.02700	1.35800
C	-4.67400	-0.46400	0.47300
C	-5.07600	-2.10100	1.86200
C	-6.55900	-1.98200	-2.29800
C	-6.16100	-3.45700	-2.09700
C	-5.57200	4.65600	-0.37600
C	-4.26200	4.21700	-1.02800
C	-1.29600	6.40200	4.49000
C	-0.47900	5.13400	4.20600
C	-5.19000	1.39500	-3.89000
C	-3.98200	0.66600	-3.33200
C	2.54600	1.27800	-4.64900
C	1.34900	1.38100	-3.68600
C	7.73800	-1.95500	-3.43200
C	7.23800	-0.71100	-3.82900
C	6.85600	-3.02500	-3.22200
C	5.86300	-0.53400	-4.01200
C	5.48200	-2.84600	-3.40500
C	4.98400	-1.60000	-3.80000
C	6.67200	-2.33800	4.04900
C	5.29400	-2.31000	3.80000
C	7.48500	-1.27700	3.63000
C	4.72400	-1.22400	3.12500
C	6.91100	-0.19200	2.95500
C	5.53500	-0.16600	2.70400
C	2.68700	6.04500	-1.06600
C	1.31600	6.64900	-1.33000
C	-0.09400	-0.35600	0.81600
C	-0.67100	0.63900	-0.21100
C	0.09800	1.96000	-0.30900
C	0.28100	2.50100	1.10500
C	1.12600	1.50300	1.91900
C	1.12500	1.79000	3.41900
C	4.61100	-4.36700	0.27800

C	4.84600	-1.95800	-0.23400
C	4.39000	-0.76700	-0.70700
C	2.94100	-0.60600	-1.11900
C	2.24700	-1.93700	-1.23000
C	2.78900	-3.06400	-0.75900
C	5.23400	0.42100	-0.93100
O	-0.01400	-3.31200	3.47900
O	-6.98600	-4.34000	-2.38000
O	-4.96200	-3.68600	-1.66700
O	-4.19500	4.10300	-2.25800
O	-0.69800	4.15000	4.96800
O	0.29700	5.16800	3.20800
O	-3.86900	-0.56200	-3.51300
O	0.93300	2.52100	-3.35100
O	0.90200	0.26500	-3.25600
O	1.17000	7.71500	-1.94300
O	-0.38700	-1.53600	0.79500
O	-0.85800	0.02500	-1.46300
O	-0.62000	2.86600	-1.13800
O	0.94900	3.74300	1.06000
O	0.69900	0.10800	1.79000
O	-0.18100	1.73000	3.94600
O	4.78300	1.43300	-1.48400
O	-2.33000	-2.13400	-1.91700
S	-2.73200	-4.54700	1.16500
Zn	-3.43900	-3.11200	-0.51800
H	-2.28700	-5.90100	-0.80500
H	-4.04300	-5.83400	-0.53900
H	-2.04400	-2.91100	3.48700
H	-0.04500	-2.85000	2.62000
H	-0.23400	-1.75600	5.68500
H	-0.80800	-0.84900	4.27500
H	-1.97200	-1.41000	5.49200
H	-6.01200	1.92800	0.47800
H	-5.85400	1.97400	2.24300
H	-6.44900	-0.99100	3.04100
H	-4.22900	0.02800	-0.38200
H	-5.04400	-3.06800	2.34400
H	-6.07600	-1.58700	-3.20300
H	-6.24400	-1.36800	-1.45500
H	-5.58900	4.50800	0.70500
H	-6.39300	4.08200	-0.82400
H	-2.30700	3.64900	-0.60800
H	-3.26400	4.07400	0.78300
H	-1.03200	7.22600	3.82600
H	-1.25300	6.73800	5.52500

H	-5.10400	2.49100	-3.88600
H	-6.08300	1.12600	-3.31100
H	-3.19700	2.40500	-2.59100
H	-2.23300	0.96500	-2.29200
H	2.56200	0.29100	-5.11300
H	3.45600	1.41300	-4.04700
H	7.91700	0.12500	-3.98700
H	7.24200	-3.99400	-2.91200
H	5.47200	0.44100	-4.28600
H	4.78900	-3.66100	-3.21200
H	3.91400	-1.45100	-3.90500
H	4.66100	-3.13200	4.12600
H	8.55800	-1.31300	3.79800
H	3.65700	-1.21000	2.91600
H	7.53400	0.63200	2.61300
H	5.10100	0.66600	2.15700
H	2.77500	5.63600	-0.04900
H	3.46000	6.80300	-1.21200
H	-0.65900	6.20300	-1.11000
H	0.40700	5.02900	-0.37400
H	-1.64400	-1.48500	-1.61400
H	2.41400	0.03500	-0.39300
H	-1.67400	0.88100	0.17900
H	1.08600	1.79400	-0.75700
H	-0.70200	2.60600	1.59200
H	2.15400	1.54600	1.53400
H	-0.08900	0.19300	-2.15000
H	-0.16800	2.84000	-2.03000
H	1.76300	1.03500	3.90400
H	1.57500	2.78000	3.57800
H	0.74100	4.25000	1.89400
H	-0.38800	2.61600	4.35600
H	5.05400	-4.95200	-0.54200
H	5.86900	-2.10500	0.10000
H	2.87200	-0.06600	-2.06200
H	1.26100	-1.96400	-1.68000
H	2.27800	-4.02100	-0.78700
H	7.14700	1.17300	-0.78100
H	7.01200	-0.42600	-0.18400
H	-2.87000	-1.63200	-2.58600
H	-0.66100	-4.38000	5.78800
H	-1.70900	-5.08200	4.55500
H	-2.38900	-3.95800	5.76300
H	-2.35200	6.15400	4.30500
H	-7.64600	-1.91100	-2.41500

H	-5.35800	1.04000	-4.91100
H	2.51400	2.06900	-5.40400
H	-7.32000	1.30200	1.49800
H	-5.74000	5.71500	-0.59800
H	-3.01700	-6.86500	0.47900
H	8.80900	-2.11300	-3.33100
H	7.11100	-3.18700	4.57000
H	3.79100	-4.94900	0.75100
H	5.36300	-4.18600	1.06500
H	2.85700	5.21600	-1.76400

Chapter 5:
Applying MMRT to Investigate the Role of the Membrane Environment on Monoamine Oxidase B Catalysis

The work in chapters 3 & 4 demonstrates that MMRT is an important consideration when investigating the temperature-dependence of enzymatic reactions. It also provides evidence that the value of $\Delta C_P^{\ddagger}$ can reflect the extent to which enzyme dynamics are linked to catalysis in comparative systems. In this chapter, MMRT is applied to MAO-B, to gain insight into whether the membrane environment of the enzyme is influencing the dynamics associated with turnover. The difference in the temperature-dependences, as confirmed by values of $\Delta C_P^{\ddagger}$, in different membrane environments, led to in-depth MD simulations. Consequently, MMRT led to computational investigations that established potential new entrances to the substrate binding site of the enzyme, and an asymmetry in the substrate accessibility to the dimer. This provides a valuable insight into the influence of the membrane environment on the mechanism of MAO-B, which is a drug target for Parkinson's disease and depression. This study demonstrates that MMRT can be used as a tool to inform on the temperature-dependences, and therefore the dynamics, of medically relevant enzyme systems. This viable application of the theory is an important step towards MMRT being considered and used in both medical and industrial applications, with the potential to inform on enzyme engineering in the future.

<table>
<tr><td colspan="10">This declaration concerns the article entitled:</td></tr>
<tr><td colspan="10">Exposing the Interplay Between Enzyme Turnover, Protein Dynamics and the Membrane Environment in Monoamine Oxidase B</td></tr>
<tr><td colspan="10">Publication status (tick one)</td></tr>
<tr><td>draft manuscript</td><td></td><td>Submitted</td><td>✓</td><td>In review</td><td></td><td>Accepted</td><td></td><td>Published</td><td></td></tr>
<tr><td>Publication details (reference)</td><td colspan="9"></td></tr>
<tr><td>Candidate's contribution to the paper (detailed, and also given as a percentage).</td><td colspan="9">The candidate contributed to/ considerably contributed to/predominantly executed the…

Formulation of ideas:
Laboratory experiment ideas were formulated by HBLJ and CRP
Computational experiment ideas were formulated by RMC, MvdK & HBLJ.
(30%)

Design of methodology:
Methodology for steady state kinetics, anaerobic reduction, and fluorescence matrix was formulated by HBLJ and CRP
Methodology for EPR experiments was formulated by AM and FM
Methodology for MD simulations and analysis was formulated by RMC, HBLJ and MvdK
(40%)

Experimental work:
EPR experiments were carried out by AM and HBLJ
Steady state kinetics, anaerobic reduction, and fluorescence matrix was carried out by HBLJ
MD simulations were carried out by RC and HBLJ
Caver analysis was carried out by HBLJ
All other MD simulation analysis was carried out by RC
(65%)

Presentation of data in journal format:
Main text by HBLJ, SI by RC
All authors edited and reviewed manuscript.
(70%)</td></tr>
</table>

Statement from Candidate	This paper reports on original research I conducted during the period of my Higher Degree by Research candidature.		
Signed	H B L Jones	**Date**	17/01/19

the following is the author accepted manuscript of a paper published in final form in Jones, HBL, Crean, RM, Mullen, A, Kendrick, E, Bull, SD, Wells, SA, Carbery, DR, MacMillan, F, van der Kamp, MW & Pudney, CR 2019, 'Exposing the Interplay Between Enzyme Turnover, Protein Dynamics and the Membrane Environment in Monoamine Oxidase B', Biochemistry, vol. 58, no. 18, pp. 2362-2372 and available online via https://doi.org/10.1021/acs.biochem.9b00213

Exposing the Interplay Between Enzyme Turnover, Protein Dynamics and the Membrane Environment in Monoamine Oxidase B

Hannah B. L. Jones[†‖], Rory M. Crean[#†‖], Anna Mullen[§], Emanuele G. Kendrick[†], Steven D Bull[Δ], Stephen A. Wells[‡], David R. Carbery[Δ], Fraser MacMillan[§], Marc W. Van der Kamp*[%], Christopher R. Pudney*[†|].

[†]Department of Biology and Biochemistry, [Δ]Department of Chemistry, [‡]Department of Chemical Engineering University of Bath, [#]Doctoral Training Centre in Sustainable Chemical Technologies, [|]Centre for Therapeutic Innovation, University of Bath, Bath BA2 7AY, United Kingdom.

[%]School of Biochemistry, University of Bristol, Biomedical Sciences building, University Walk, Bristol BS8 1TD, United Kingdom.

[§]School of Chemistry, University of East Anglia, Norwich Research Park, Norwich NR4 7TJ, United Kingdom.

Abstract: There is an increasing realization that structure-based drug design may show improved success rates by understanding the ensemble of conformations and sub-states accessible to an enzyme and how the environment affects this ensemble. Human m**o**noamine oxidase B (MAO-B) catalyzes the oxidation of amines and is inhibited for the treatment of both Parkinson's disease and depression. Despite its clinical importance, its catalytic mechanism remains unclear and routes to drugging this target would be valuable and relevant. Evidence of a radical in either the transition state or resting state of MAO-B is present throughout the literature, and is suggested to be a flavin semiquinone, a tyrosyl radical or both. Here we see evidence of a resting state flavin semiquinone, via absorption redox studies and electron paramagnetic resonance, suggesting that the anionic semiquinone is biologically relevant. Based on enzyme kinetic studies, enzyme variants and molecular dynamics simulations we find evidence for the crucial importance of the membrane environment in mediating the activity of MAO-B and that this mediation is related to effects on the protein dynamics of MAO-B. Further, our MD simulations identify a hitherto undescribed entrance for substrate binding, membrane modulated substrate access, and indications for half-site reactivity: only one active site is accessible to binding at a time. Our study combines both experimental and computational evidence to illustrate the subtle interplay between enzyme activity, protein dynamics and the immediate membrane environment. Understanding key biomedical enzymes to this level of detail will be crucial to inform strategies (and binding sites) for rational drug design for these drug targets.

KEYWORDS *EPR, Molecular Dynamics, Monoamine Oxidase B, semiquinone, enzyme, flavin, membrane*

Human monoamine Oxidase B (MAO-B) catalyzes the oxidative deamination of amines, by electron transfer, via its flavin adenine dinucleotide (FAD) cofactor (Scheme 1).[195] It is located in the outer mitochondrial membrane,[196] as a dimer, with bipartite substrate

binding and active site cavities.[195] MAO-B is the target of treatment for both depression and Parkinson's disease, with inhibitors of the enzyme first being approved as pharmaceuticals in the 1960's.[197,198]

Despite the important medical applications associated with MAO-B its chemical mechanism remains unclear and there is debate over the role of MAO-B conformational change and protein dynamics. Reduction of the FAD has been shown to proceed by a tunneling mechanism via primary (1°) and secondary (2°) kinetic isotope effect (KIE) studies.[199] These studies have suggested that MAO-B catalysis is not linked to fast (pico/nanosecond) dynamics.[199,200] MAO-B catalysis has been investigated via experimental and computational studies, with at least seven different proposed mechanisms, including polar nucleophilic,[201] radical,[202] direct hydride transfer[203–205] and two step hydride transfer[206] (Scheme S2).

Although the direct single electron transfer (SET) radical mechanism (Scheme S2) has previously been discounted experimentally[207] and by quantum mechanics/molecular mechanics (QM/MM),[208] a separate radical mechanism has been proposed by Murray *et al*.[209] This was established via a model small molecule reaction that mimics MAO-B to provide evidence for a neutral semiquinone flavin that can be formed aerobically. The authors suggest that a neutral semiquinone flavin is the reactive species for the oxidation of benzylamine (BZA).[209] This led to the hypothesis of a radical mechanism whereby MAO-B forms a neutral semiquinone flavin via a proximal tyrosine radical (Y398). The presence of a stable anionic semiquinone flavin and tyrosyl radical intermediate are also reported in MAO-A and MAO-N.[210,211]

In our hands, we find spectroscopic evidence for a stable semiquinone in resting state MAO-B (vida infra). Here, MAO-B was expressed and purified in *Pichia pastoris* as outlined by Newton-Vinson et al. [212] This protocol attributes observations of oxidized/semiquinone MAO-B FAD to reactive oxygen species (ROS) that form upon the disruption of the mitochondrial membrane, which they observe upon purification from bovine liver, but not from *P. pastoris*.[212]

Previous observation of a stable anionic semiquinone FAD in MAO-B[213,214] led to a hypothesis of half-site reactivity. This mechanism posits that one monomer of the MAO-B dimer is inaccessible to oxygen and substrate, resulting in the formation of the stable semiquinone species, whilst the other contains oxidized FAD. Electrons are then shuttled

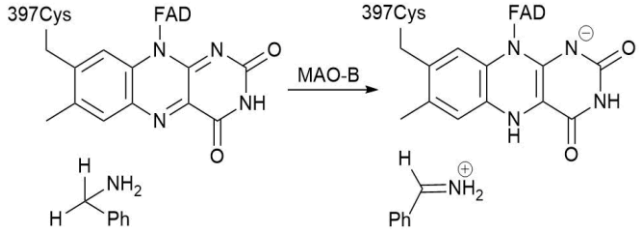

Scheme 1. General reaction catalyzed by MAO-B.

to the semiquinone species, allowing for the oxidation of the reduced FAD upon turnover.[214] The authors suggest this might arise from electron shuttling between specific amino acids. Potentially, such a mechanism might require significant conformational change associated with turnover in each monomer. Indeed, conformational changes have been found to be associated with MAO-B turnover, with a molecular dynamics (MD) study demonstrating the potential for the membrane to regulate access to the active site entrance via two gating loops (residues 85-119 and 155-165).[73] Other MD studies have been carried out on MAO-B, both with and without a membrane environment, with the focus on identifying or improving inhibitors for MAO-B[215–219], or ascertaining how MAO-B binds to the membrane.[220]

Herein, we find evidence for a resting-state anionic semiquinone, and through kinetic and computational studies, evidence for conformationally controlled enzyme activity at each MAO-B monomer. Crucially, we find that the membrane environment exposes novel substrate/product channels that could be potential new drug targets. We thereby link the membrane environment, substrate binding and MAO-B conformational change to enzyme turnover.

Results and Discussion

Evidence for a resting-state semiquinone in MAO-B.

The presence of purified MAO-B was established by SDS-PAGE (Figure S6; essentially a single band via size exclusion chromatography) and via electrospray ionization quadrupole time-of-flight (ESI-Q TOF) mass spectrometry in combination with the MASCOT server.[221] The absorption spectrum of purified MAO-B is shown in Figure 24A. The spectra share characteristics of an anionic semiquinone FAD (FAD·-) with an absorption feature at ~415 nm.[222] The preparation protocol of MAO-B was the same as that used by Newton-Vinson *et al.*,[212] with small differences outlined in the *Materials and Methods*. Multiple preparations were completed, including the final polymer partition step outlined by Newton-Vinson *et al.* and without EDTA present, with the ~415 nm spectral feature consistently present. The effect of incubation with BZA, under anaerobic conditions, on the MAO-B absorption feature at ~415 nm was monitored over time (Figure 24A *inset*). From Figure 24A *inset*, we find a decrease in absorption at 415nm with respect to time on incubation with BZA, suggesting the ~415 nm spectral feature is redox sensitive with a natural MAO-B substrate.

We note that the absorption spectrum shown in Figure 24A lacks a defined feature around ~450 nm where one would expect oxidized flavin as well as spectral features at ~475 nm that would also characterize a putative anionic semiquinone. We do not have a clear explanation for the lack of these features and the complexity of the absorption spectrum; the protein is purified to homogeneity, it is identified as MAO-B by mass spectrometry and is catalytically active with the natural substrates (Figure 24A *inset*, Figure S7 and as described below). The electronic environment around both flavins is highly complex, with a large number of proximal Tyr residues (Y60, 398 and 435 positioned 3.1, 3.3 and 3.5 Å from the alloxan moiety, respectively). Potentially, this gives rise to a complex absorption

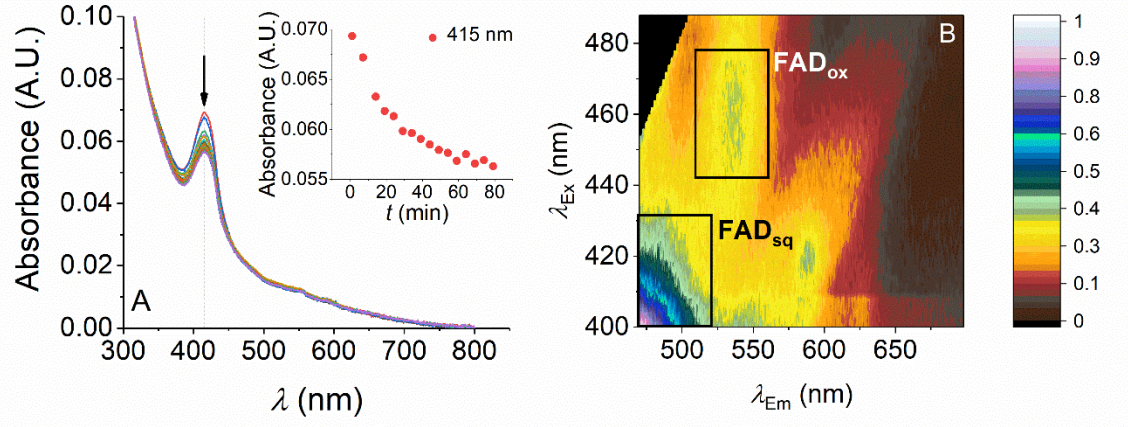

Figure 24. A, The absorbance spectra of MAO-B after treatment with BZA over time. Inset, the effect on the 415 nm peak over time. **B,** Fluorescence excitation/emission matrix resolves oxidized and semiquinone flavin states (highlighted in solid black boxes). Scale bar is relative intensity Conditions: 50 mM HEPES 0.5 % w/v Triton X-100, 20 °C. For absorption experiments 40 mM BZA, anaerobic conditions as Materials and Methods.

spectrum arising from different electronic environments for a sub-set of active site conformational states. This hypothesis requires MAO-B to be able to explore different conformational states and we consider this in more detail below. Given the complexity of the absorption spectrum, we turned to fluorescence and electron paramagnetic resonance (EPR) spectroscopy to provide more specific evidence for the oxidation state(s) of the MAO-B flavin.

Previously, MAO-B steady-state fluorescence spectroscopy has demonstrated that there are two different chromophores present in resting state MAO-B.[223] The authors concluded that these two different species were consistent with oxidized and semiquinone flavin. To establish if we similarly have both oxidized and semiquinoid flavin present (which is not obvious from the absorption spectrum), we have monitored the fluorescence excitation-emission matrix (Figure 24B). Similar to the previous report, the spectra resolve at least two different emission peaks suggesting the presence of two different oxidation states of the flavin with λ_{Ex} ~ 400-420 and 460 nm. Notably, the excitation/emission profile at λ_{Ex} ~ 460 and λ_{Em} ~ 540 nm (Figure 24B) indicates the presence of oxidized flavin.

The ~415 nm absorption feature could be potentially attributed to a tyrosyl radical, which has a characteristic absorbance peak at 410 nm,[224] or a mixture of both an FAD semiquinone and tyrosyl radical, as seen as intermediates in MAO-A.[210,211] Murray *et al.* postulated that the reactive semiquinone FAD was formed by a proximal tyrosyl radical (Y398). However, the UV-vis absorption spectrum of Y398F MAO-B also shows the spectral feature at ~415 nm (Figure S8A), indicating that this feature is not attributable to a Y398 tyrosyl radical. The Y398F variant also shows a slight increase in K_m (Figure S9), similar in magnitude to previously reported changes in K_m for Y398F.[225]

A stringent approach to identifying the nature of the flavin oxidation state is EPR. The EPR X-band spectrum of the wild type MAO-B (*wt*MAO-B) clearly indicates that the signal arises from a semiquinone radical (Figure 25), in agreement with the UV-Vis and fluorescence spectroscopy (Figure 24). The measured spectra lack the defining features which would identify the signal as arising from a tyrosyl radical: the typical 'wings' or 'shoulders' around the central signal at around g = 2 [210,226] at X-band (Figure 25), and increased g-value anisotropy at higher frequency (and therefore resonant field), i.e. Q-band (data not shown). Furthermore, the signal persists in the Y398F variant, confirming that it is not caused by the proximal tyrosine. Further, computational simulation and fitting of the experimental X-band data of the WT and Y398F MAO-B (Table 3) suggests that the semiquinone radical species is anionic; the hyperfine environment of a neutral semiquinone radical would contain a contribution from an additional hydrogen atom.[214,227] This is not the case for the signals seen in the X-band spectra.

Previous studies have illustrated the importance of the membrane environment in mediating the normal enzymatic activity of MAO-B.[73] To probe if the putative semiquinoid species (inferred from spectroscopic studies above) was also stably present in the membrane environment, we have conducted spectroscopic studies in an artificial membrane environment using l-α-phosphatidylcholine styrene maleic acid co-polymer (SMA) nanodiscs, prepared as reported previously.[228] We find that the absorption feature at ~415 nm is present in both reduced Triton X-100 and nanodisc environments (Figure S8A), implying that the putative anionic semiquinone is not an artifact of the buffer system used, and that its presence is not affected by the specific membrane environment used. It is clear from these data (Figures 24 and 25) that the FAD of resting state MAO-B

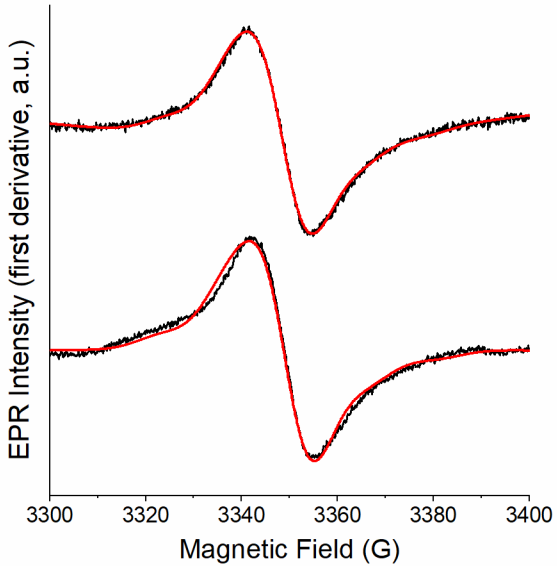

Figure 25. X-band cw-EPR spectra of WT (top, black) and Y398F (bottom, black) MAO-B, with their respective fitted simulations (red). EPR microwave frequency = 9.3916 GHz (WT) & 9.3926 GHz (Y398F), microwave power = 0.2 mW, modulation amplitude = 0.5 mT, temperature = 16 K.

Table 3. Spectral Parameters of EPR Data Extracted by Simulation and Fitting

		WT MAO-B	Y398F MAO-B
g-tensor	g_x	2.00444	2.00444
	g_y	2.00429	2.00429
	g_z	2.00191	2.00191
	g_{iso}	2.00355	2.00355
A(^{14}N) (MHz)	$A_{\parallel}$	39.3	38.4
	$A_{\perp}$	0	0
A(^{14}N) (MHz)	$A_{\parallel}$	34.1	40.1
	$A_{\perp}$	0	0
Linewidth (mT)		1.1	1.1
RMSD		0.0255	0.0440

is able to stably occupy oxidation states other than fully oxidized FAD. Evidence for this is recurring in the literature, demonstrated by Raman[213], fluorescence[223], and EPR[212,214] spectroscopy. We suggest that these different observations could be rationalized by an equilibrium of energetically similar conformational states, which allow differently stable oxidation states. Indeed, below we provide evidence that shows MAO-B is able to sample a range of conformational states.

Influence of the membrane environment on MAO-B turnover.

To assess how/if the membrane environment affects enzyme turnover, we measured MAO-B turnover with both BZA and kynuramine dihydrobromide (KYN) at a range of temperatures. We monitor enzyme turnover based on the absorption features of benzaldehyde product formation at 250 nm for BZA,[207] and 4-hydroxyquinoline product formation at 316 nm for KYN.[229] This assay notionally primarily reflects the rate of reduction of the flavin.[207] Our temperature-dependence studies allow us to analyze not just the observed rate of enzyme turnover but also the thermodynamics of the system. The temperature-dependence of the observed rate is shown in Figure 26.

There has been a recent move to fitting enzyme temperature-dependence data to physical models that allow for curvature in the associated plots. Such models often provide a more realistic fit to experimental data. We fit the MAO-B temperature-dependence data to a model that incorporates the heat capacity of catalysis ($\Delta C_P^{\ddagger}$) (Eq 19) into the Eyring equation (Eq 34).[1]

$$k = (k_{\mathrm{B}}T/h)e^{\Delta S^{\ddagger}/R}e^{-\Delta H^{\ddagger}/RT} \qquad \text{(Eq34)}$$

$$lnk = ln\frac{k_B T}{h} - \left[\frac{\Delta H_{T_R}^{\ddagger} + \Delta C_P^{\ddagger}(T - T_R)}{RT}\right] + \left[\frac{\Delta S_{T_R}^{\ddagger} + \Delta C_P^{\ddagger}(lnT - lnT_R)}{R}\right] \qquad \text{(Eq19)}$$

Where $\Delta H^{\ddagger}$ is the change in enthalpy and $\Delta S^{\ddagger}$ is the change in entropy between the ground and transition state of the reaction at an arbitrary reference temperature (T_0). This model has recently gained traction in studying enzyme temperature-dependencies.[46,162,166,230] In the absence of other confounding factors, $\Delta C_P^{\ddagger}$ quantifies the temperature-dependence of $\Delta H^{\ddagger}$ and $\Delta S^{\ddagger}$ and reflects the difference in the distribution and frequency of vibrational modes between the ground state and transition state.[1,42] We have recently suggested that $\Delta C_P^{\ddagger}$ can be used as a proxy for the changes in these vibrational modes during enzyme turnover and thus relates to some aspect of the protein's molecular dynamics.[46] This is relevant in the present study where the membrane environment may not alter the tertiary structure of the enzyme, but potentially alters protein fluctuations, which have previously been proposed to affect small molecule binding to the active site.[73]

From Figure 26 and Table S3, we find $\Delta C_P^{\ddagger}$ to be the same within error for both KYN and BZA substrates when in a reduced Triton X-100 environment. However, when in nanodiscs, the difference in $\Delta C_P^{\ddagger}$ for the different substrates is $\Delta\Delta C_P^{\ddagger}$ = 2.4 ± 1.0 kJ mol^{-1}. The $\Delta C_P^{\ddagger}$ increases in magnitude from reduced Triton to nanodiscs with KYN, and decreases with BZA (Figure 26). These data suggest that the difference in conformational fluctuations in the reactant and transition states is different in a more native membrane environment and for different substrates. Moreover, we find a significant difference in the observed rate of enzyme turnover in the nanodiscs (~5 times faster). These data therefore provide experimental evidence of the notion that the membrane environment has a role in 'tuning' the molecular dynamics of MAO-B. However, given we observe a retention of the putative anionic flavin semiquinone, we would suggest the membrane does not affect the chemical mechanism of enzyme turnover *per se*.

Computational evidence for a new entrance to the MAO-B active site mediated by the protein-membrane interaction.

To obtain detailed insight into the role of the membrane environment on protein dynamics, we performed MD simulations of the MAO-B dimer embedded in a phospholipid membrane. We explore (i) the influence of the phospholipid membrane in modulating substrate/inhibitor binding, (ii) the accessibility of small molecules to the active site of MAO-B, and (iii) the potential for half-site reactivity, as discussed above.

MD simulations of MAO-B in complex with FAD in a POPC/POPE lipid bilayer (similar to the native environment in the mitochondrial membrane)[231] were performed in triplicate for 150 ns in 3 different states: no BZA present (BZA_0), one active site occupied with BZA (BZA_1), and both active sites occupied with BZA (BZA_2). Protein Cα RMSD and area per lipid head groups (Figure S10) indicated equilibration of both the protein and membrane after 50 ns of production MD. The analysis described below is therefore from 50 to 150 ns.

Prior simulations of BZA_0-MAO-B in a bilayer established that MAO-B ligand binding site access is modulated by the membrane.[73] We investigate this further using longer simulations (150 ns vs. 50 ns) and with substrate (BZA) bound. To measure possible

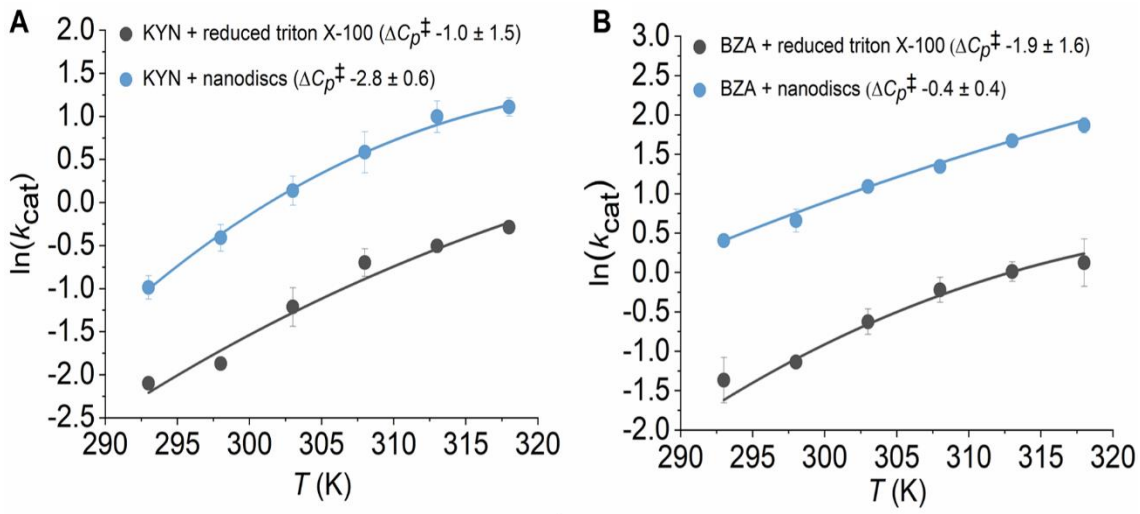

Figure 26. The temperature-dependence of MAO-B with BZA (**A**) and KYN (**B**) with reduced Triton and nanodisc environments, fit to the MMRT equation. Conditions, 50 mM HEPES 0.5 % w/v reduced Triton X-100 pH 7.5. Reduced Triton X-100: 1.5 mM BZA, 0.75 mM KYN. Nanodiscs: 3 mM BZA, 0.66 mM KYN.

access to the substrate cavity of MAO-B via the membrane, we quantify the occurrence and features of tunnels in our simulations using Caver 3.0.[102] Tunnels identified are grouped into clusters, allowing for the quantification of various characteristics, such as the frequency of occurrence and smallest width (bottleneck radius), as used here.[232] This tool has previously been used to identify tunnels for ligand-induced protein flexibility analysis,[233] to rationalize change in mechanism and kinetics of an enzyme upon a point mutation,[234] and to identify a tunnel to the FAD moiety in MAO-A.[235]

Two main possible entrances for ligands into the MAO-B active site are found at either side of the gating loop residues 99 to 112 (Figure 27). Entrance A (Figure 27A) is accessed via the membrane and its opening has previously been observed.[73] Briefly, a π-π stacking interaction between Tyr97 and Trp107 is lost as Trp107 buries into the aliphatic lipid tails of the bilayer, establishing an additional interaction of MAO-B with the phospholipid bilayer.

Entrance B (Figure 27B) is solvent accessible, and its opening is controlled by the conformation of three loop regions (81 to 88, 99 to 112 and 198 to 208). To the best of our knowledge, its opening has not yet been observed through protein crystallography or simulation. To provide a qualitative description of the open and closed conformations of this entrance, we have performed clustering analysis on the entrance loop residues (see *Materials and Methods*). Opening of Entrance B (Figure S11) can be described by: 1) loop 81-88 separates from loop 199-206, breaking a number of transiently formed electrostatic interactions and instead forming interactions with the solvent in the open conformation; 2) the central region of the gating loop (residues P102, F103, P104) rotates

down and away from the hydrophobic core of the entrance cavity. The opening of both entrance A and B involves residues directly interacting with the bilayer. This indicates that the membrane is important in modulating access to the substrate binding pocket of MAO-B.

Evidence of asymmetry in MAO-B from MD simulation.

Previous studies have suggested that the presence of an anionic semiquinone could be mechanistically significant as part of a half-site reactivity mechanism.[214] To investigate the potential for half-site reactivity in MAO-B, tunnels from the N5 of the flavin to the solvent were first identified from all MD trajectories with BZA_0, BZA_1 and BZA_2 (with three replicates). These data are useful to determine the size of species that could access the active site and to investigate whether access to the active site is half-site specific. To avoid identifying numerous tunnels that cannot accommodate substrate/product molecules, a minimum tunnel radius was set to 1.5 Å. (This avoids identifying water tunnels, as water has a Van der Waals radius of ~1.4 Å.[236]) With this criterion, no tunnels were found, which demonstrates a closed active-site on the timescales of our simulations. Whilst larger conformational changes may be occurring on longer time-scales (or in presence of substrate in the vicinity of a bottleneck) to enable substrate access to the active site, a generally closed off active site is in agreement with previous experimental findings.[214]

Next, tunnels were identified from the substrate binding cavity towards the protein surface. The starting point was defined as the center of mass between the alpha carbon (Cα) atoms of residues 168 and 316 (Figure S12). This starting point was chosen as it is located within the substrate binding cavity and is common to both previously described substrate entrance tunnels (Figure 27). Tunnel frequency and the average bottleneck

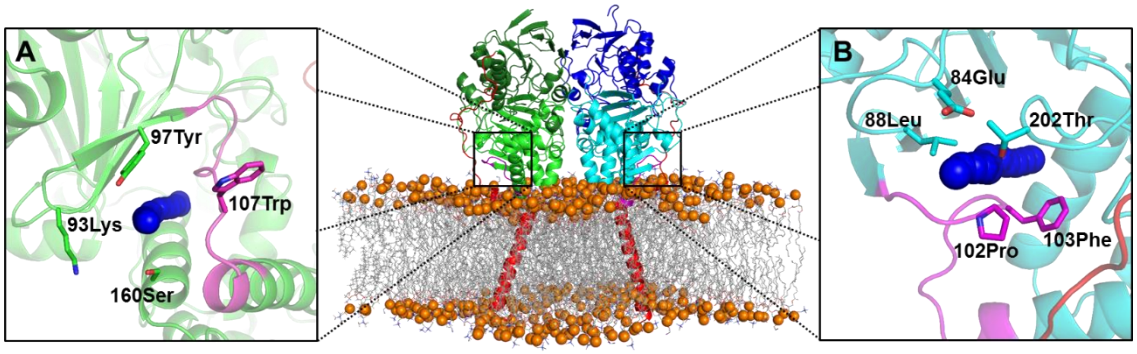

Figure 27. MAO-B in POPC/POPE membrane environment. The substrate binding area is shown in light green and light blue (residues 80-210, 286-390) for each monomer. The active site area is shown in dark green and dark blue (residues 4-79, 211-285, and 391-452). The C-terminal tail and transmembrane helix are shown in red (residues 453-520). The binding site gating loop is shown in magenta (residues 99-112). Images A and B inset denote the two main entrances (or tunnels) to the binding site (denoted Entrance A and Entrance B throughout the manuscript), with a representative tunnel (navy spheres) shown for both entrances. Key residues which describe the location of the entrance are shown as sticks and labelled. Entrance B is newly identified here, Entrance A has been previously described.[73]

radius of all tunnels identified in both monomers were obtained for BZA_0 and BZA_1 (Figure 28A and B). To aid discussion, we designate each monomer as monomer 1 or monomer 2, noting that this does not imply a structural or other difference between monomers.

Notably, both the frequency and maximum bottleneck radius of tunnels to the substrate binding cavity of MAO-B is significantly different for each monomer. In the absence of BZA, monomer 1 presents a higher frequency of tunnels, with a larger average maximum bottleneck radius. When BZA is present in monomer 1 and not monomer 2, the frequency of tunnels and maximum bottleneck measurements are higher for monomer 2 (Figure 28 A and B and Table S4). In Figure 28C and D, the pathways are colored according to the entrance pathway they use from the starting point to the solvent, with the majority of tunnels passing the aforementioned entrances A and B (Figure 27).

The observed 'closing' of the active site entrance in the $BZA_{1\text{-bound}}$ monomer and 'opening' in the $BZA_{1\text{-unbound}}$ monomer are particularly notable. This indicates that when BZA is bound to the active site cavity of one monomer, a subsequent BZA is more likely to enter the binding site of the opposite monomer. Such asymmetry may prevent binding of subsequent BZA into the same monomer, allowing for the release of products, whilst increasing the efficiency of binding in the opposite 'free' monomer. Previous experimental work indicated that binding of inhibitor to the intermediate binding site of MAO-B was increased where inhibitor was already bound into the active site (see Figure 27 for binding/active site differentiation).[237] Whilst it is not known whether this is within

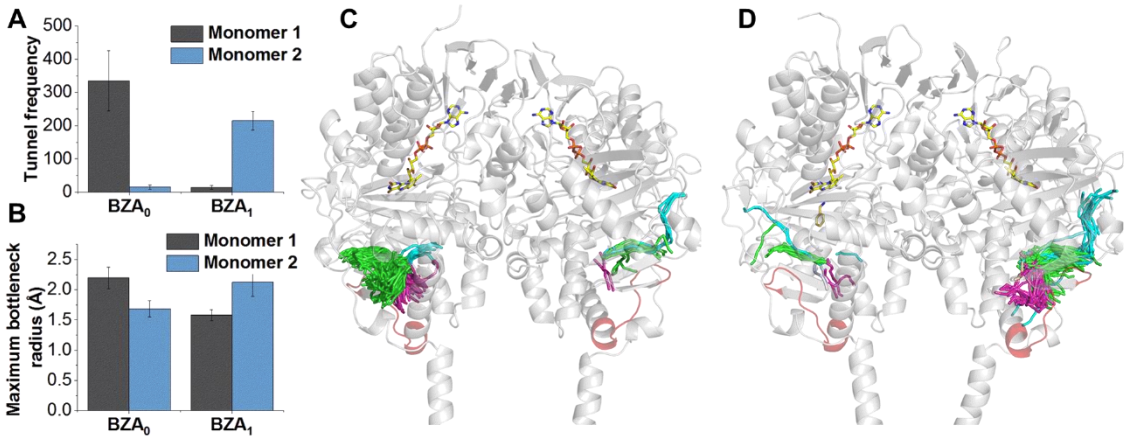

Figure 28. A, The summed tunnel frequency from the substrate binding site of MAO-B to solvent, identified by Caver.[102] BZA_0 – No BZA is bound in either monomer. BZA_1 – BZA is bound only in monomer 1. All are from triplicate MD runs. **B**, The average maximum bottleneck (Å) from the substrate binding site of MAO-B to the solvent, as identified by Caver. **C** + **D**, All tunnels identified by Caver over all three MD simulation repeats for BZA_0 (**C**) and BZA_1 (**D**). FAD and BZA (when present) are shown as yellow sticks. Tunnels are colored according to entrance/exit pathway used, with magenta and green representing Entrances A and B respectively. Blue tunnels indicate pathways which go through neither of the two main entrances described.

the same monomer, it could explain the asymmetry in binding site access seen here when BZA_1 is present.

BZA_2 was not considered for half-site reactivity analysis. This was due to BZA leaving the active site altogether in one simulation trajectory (Figure S13), meaning that the identified tunnels would not be comparable to those where BZA does not leave. This BZA movement may indicate that BZA_2 is potentially an unstable configuration, providing further evidence towards asymmetry in MAO-B.

Mutagenesis reveals long-range networks of motion are important in MAO-B.

Our findings above suggest a model where MAO-B intramolecular dynamics are intimately linked to the environment. That is, we hypothesize, that functionally important MAO-B conformational changes are at least in part controlled by the membrane environment. We expect that those conformational changes (or protein dynamics) are influenced by the global protein scaffold. To explore this hypothesis, we have turned to computationally informed mutagenesis studies.

We identify enzyme variants that are predicted to affect networks of flexible motion throughout MAO-B using the FIRST (floppy inclusion and rigid substructure topography) algorithm.[104] FIRST uses a single conformation (e.g. a crystal structure) to define a constraint-network of movement for a protein. This constraint-network is composed of terms describing covalent and non-covalent contributions to the rigidity of the protein, allowing prediction of the relative rigidity/flexibility of each residue. These calculations can therefore be used to predict the relative rigidity (and therefore stability) of MAO-B variants, both on a local (per-residue) and global (sum of all residues) level.

FIRST was used to perform high-throughput screening to identify point variants that were predicted to significantly rigidify the network of flexible motion of *wt*MAO-B, without significantly perturbing the flexibility of residues considered

In short, we perform computational alanine scanning, by applying FIRST with the contribution of each amino-acid side chain to the constraint network discounted in turn. This allows us to identify residues with side chains that make a negligible contribution to the overall rigidity of MAO-B. All residues identified with the above approach were then subjected to *in silico* mutagenesis to all other canonical amino acids and subsequent FIRST analysis.

From these calculations, we selected three enzyme variants (W184F, F402V and E466Y) that, based on our calculations, were predicted to increase the rigidity of the protein scaffold, but are distal to the active site (between 13-21 Å from BZA) and do not significantly alter the rigidity of catalytically relevant residues (Figure S14 A-C; see SI *Materials and Methods*). We find that these variants retain the absorption feature at ~415 nm (Figure S8A) and their overall structure is not significantly perturbed, at least as assessed from their far-UV circular dichroism spectra (Figure S8B). However, despite the variants being located a significant distance from the active site, we find that enzyme

activity is ablated. Given that these variants are expected to alter the network of flexible motion, we suggest these data reflect the importance of protein conformational changes in MAO-B turnover. Moreover, the importance of such changes may also provide a rationale for the differences of our temperature-dependence studies when MAO-B is in different environments (Figure 26).

The FIRST calculations have the advantage that they are rapid and so enable very large *in silico* screening. However, they are thus necessarily approximate and do not reflect the realistic (and complex) protein molecular dynamics. An additional important caveat of our FIRST calculations is that they do not include the membrane environment. Therefore, in an attempt to rationalize the loss of activity for the variants, and explore our hypothesis above, we have performed 3 independent 100 ns MD simulations on each variant in the BZA_1 state (as above, see *SI Materials and Methods*).

Based on the flexibility in MD simulations (root-mean square fluctuations, RMSF), each variant is predicted to be slightly more rigid (Figure S14 D-F) than *wt*MAO-B. Comparison of predictions of relative rigidity (by FIRST) and flexibility (by MD) for *wt*MAO-B show only moderate correlation (Figure S15). Poor correlation is particularly found for residues near the bilayer, which is not taken into account in our FIRST calculations; this demonstrates the importance of modelling the molecule in a native-like environment.

Figure 29A-D, (additional measurements can be found in Figures S16 and S17) shows the fluctuation in the catalytic distance between BZA and FAD (BZA CH_2 and FAD N5) for each variant and *wt*MAO-B. There is clearly some fluctuation in individual simulations (with excursions to longer distances), but no significant differences are observed between the variants and *wt*MAO-B. That is, we do not find any evidence (at least on these timescales) that catalytically competent conformations are disadvantaged in the variants. Therefore, based on these data, we do not expect the immediate active site environment to be compromised in the enzyme variants, which correlates with the observation of the retention of the putative anionic semiquinone peak in the absorption spectrum of each variant (Figure S8).

To explore the changes in global protein dynamics for the MAO-B variants in more detail, we performed principal component analysis (PCA) on the Cα carbon of residues 1-455 for all BZA_1 simulations (Figures 29 and S18). The vector which describes each PC can be projected onto a static structure (to create a porcupine plot; Figure 29G), with the magnitude of the vector describing the relative change in each residues position over the PC. Analysis of the porcupine plot of PC1 (Figure S18B) shows a global motion dependent on several flexible regions of MAO-B, whereas PC2 is dominated by the movement of the gating loop (residues 99–112) region and residues around it (Figure 29G). This gating loop sits between Entrance A and B (Figure 27) and is key for substrate binding and product release. Histograms of PC2 (Figure 29E and F) show reduced/differential conformational sampling of PC2 for all variants compared to

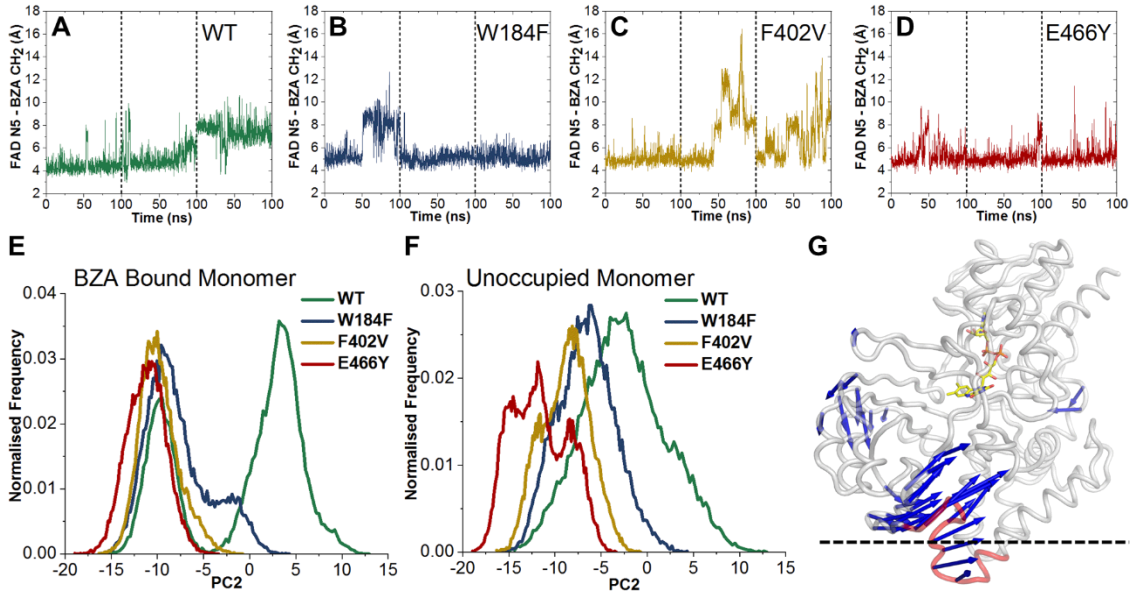

Figure 29. A – D, Distance between the N5 (FAD) and CH2 group of BZA for wtMAO-B and all three enzyme variant simulations. A black dotted line indicates the start of each new trajectory (all runs performed in triplicate). Additional measurements for all BZA containing simulations can be found in Figures S16 and S17. E + F, Normalized histograms (bin width 0.25 Å) of principle principal component 2 (PC2) for all BZA1 simulations of the bound (**E**) and unoccupied monomers (**F**). **G**, 'Porcupine' plot of PC2, with arrows indicating the direction of the PC2 eigenvector and arrow size indicating the magnitude of the corresponding eigenvalue, for all Cα atoms with eigenvalues greater than 4 Å. The gating loop residues (99 – 112) are colored in red, and the approximate location of the bilayer is indicated with a black dotted line. (A mobility plot of PC2 is provided in Figure S18A.). key for catalysis (see *Supporting Information Materials and Methods* and Table S5).

*wt*MAO-B. Our MD simulations therefore suggest that the variants have lost activity because the mutations have altered the normal dynamics of the gating loop, potentially affecting substrate entrance/exit to the active site. The fact that these variants (distal from the gating loop) have such a significant and specific effect on the gating loop sampling implies the presence of a long-range network of motions in MAO-B (Figure 29G) through which dynamics of the gating loop are affected.

Conclusions

MAO-B is an important biomedical target, and as with many such targets, is associated with a biological membrane. Such association places enzymes in specific physiological contexts, can promote interaction with other species and enable specific structural features. Less obvious is the role of the membrane environment in mediating the conformational dynamics of enzymes, and whether this is functionally important.

Previous molecular dynamics studies have illustrated that the immediate membrane environment of MAO-B is involved in controlling substrate entrance to channels leading to the active site. Here, using enzyme kinetic and mutagenesis studies, we consider the role of the membrane environment in tuning the molecular dynamics of MAO-B more

widely, including its influence on turnover and catalysis. We find that placement of MAO-B in SMA nanodiscs instead of in reduced Triton X-100 has a significant effect on the heat capacity of catalysis ($\Delta C_P^{\ddagger}$). Differences in $\Delta C_P^{\ddagger}$ reflect differences in the distribution and frequency of vibrational modes between the ground (reactant) and transition states and implies that the membrane environment is affecting the global protein dynamics of MAO-B *and* that these dynamics influence the thermodynamics of enzyme turnover. Indeed, k_{cat} is ~5 times faster in the nanodisc environment versus reduced Triton X-100. These data further hint at the role of the specific lipid composition and fine structure of the membrane to tune MAO-B turnover efficiency. These findings are corroborated by studying enzyme variants that are predicted to alter the network of flexible motion in the enzyme, but do not affect the overall structure. These variants, which are distal to the active site, all lead to inactive enzyme, indicating the critical role of 'optimized' global protein dynamics of MAO-B.

Through atomistic molecular dynamics simulations with and without substrate bound, we find two substrate entrance/product exit channels that are mediated by membrane interaction, one of which was not previously described. The simulations further indicate an asymmetry in substrate access in the MOA-B dimer. Specifically, either one or the other monomer may allow substrate access at any one time, with active site occupation in one monomer preferentially allowing substrate access to the other. Moreover, the gating loop dynamics appear to be highly sensitive to the global enzyme dynamics, potentially reflecting long-range networks of enzyme motion.

Taken together, our study suggests that the global protein dynamics of MAO-B are 'tuned' by the specific immediate membrane environment. These protein dynamics have a major effect on MAO-B function, through tuning fluctuations linked to enzyme turnover, including controlling the opening and closing of substrate/product channels. The finding that two different channels mediated by the membrane environment are present in MAO-B illustrates the potential to exploit novel small molecule binding sites with rational drug design. Therefore, our study illustrates that when searching for novel small molecule binding sites, one should consider not just the static structure of the system in isolation, but time-dependent changes in the population of conformational sub-states and in the 'native' environment.[238,239] The finding that there may be long range networks of motions that can, in particular, affect the gating loop also indicates the potential for allosteric inhibitors. Further, as MAO-B resides in the outer mitochondrial membrane of cells, the finding of a solvent accessible entrance is important for rational drug design efforts. That is, inhibitors that target MAO-B may not need to enter the mitochondrial membrane in order to access the active site of MAO-B.

Materials and Methods

Unless otherwise stated, all reagents were obtained from Sigma-Aldrich.

MAO-B expression and purification.

MAO-B was expressed and purified following the purification protocol by Newton-Vinson *et al*.[212] Small variations from the protocol include shake flask fermentation instead of bioreactor fermentation, with BMMY (buffered methanol-complex medium) media instead of MM (minimal methanol) media for induction, storage of cell pellets in a buffer with protease inhibitor tablets instead of PMSF, suspension of pellet in 100 ml of breaking buffer instead of 1 L, and cell breakage of 30 s on 30 s off x 10 sonication in addition to bead beating. The purification was completed after MAO-B was passed over a DEAE-sepharose FF column, achieving satisfactory purity. The additional polymer partition step detailed by Newton-Vinson et al.[212] did not change the state of the semiquinone MAO-B species seen here, with additional purity achieved by size exclusion chromatography if necessary. MAO-B concentration was determined spectroscopically using ε_{415} = 11 000 M^{-1} cm^{-1}.[240]

Nanodisc preparation.

Nanodiscs were prepared following methods by McDowall *et al*.,[228] suspended in 50 mM HEPES, pH 7.5. and incubated with MAO-B in a 10x molar excess, for 2 hours prior to experiments.

Enzyme assays.

MAO-B was transferred from Triton X-100 containing buffer to reduced Triton X-100 or nanodisc containing buffer using detergent removal spin columns (Thermo Scientific Pierce). Steady-state MAO-B kinetic measurements were carried out using a 1 ml quartz cuvette and a UV⁄Vis spectro-photometer (Agilent Cary 60 UV-Vis spectrometer) in 50 mM HEPES (pH 7.5), containing 0.5 % (w/v) reduced Triton X-100 or SMA l-α-Phosphatidylcholine nanodiscs. Enzyme activity was measured by following the formation of benzaldehyde using ε_{250} = 12,800 M^{-1} cm^{-1} for BZA,[207] and 4-hydroxyquinoline using ε_{316} = 12,300 M^{-1} cm^{-1} for KYN.[229] For each condition substrate dependences were monitored at 40 °C ; the data fitted well to Michaelis-Menten kinetics (Figure S7). Temperature-dependences were carried out from 20 °C - 45 °C at 5 °C intervals using initial velocity measurements at substrate concentrations maintained above 10x K_m to ensure saturation. The data were fitted to Eq 19 as described in the manuscript using OriginPro 2017.

Redox assays.

These experiments were performed anaerobically, all buffer was purged with nitrogen and samples were prepared in an anaerobic box. Glucose and glucose oxidase were added to maintain anaerobic conditions.

EPR.

Measurements were performed using WT and Y398F variant MAO-B in 50 mM HEPES 0.5% Triton, pH 7.5, flash-frozen in liquid nitrogen in suprasil quartz sample tubes. X-

band cw-EPR spectra were recorded on a Bruker eleXsys E500 spectrometer using a standard rectangular Bruker EPR cavity (ER4102T) equipped with an Oxford helium cryostat (ESR900). Experimental parameters: microwave power, 0.2 mW; field modulation amplitude, 5 G; field modulation frequency, 100 kHz; measuring time 10 s; temperature 16 K. Q-band cw-EPR spectra were performed on a Bruker eleXsys E-560 spectrometer using a ER 5106QT-W1 resonator equipped with a home-built ARS cryogen-free cryostat (data not shown). Spectral simulations were performed using the Matlab-based Easyspin package.[241]

Computational materials and methods.

The X-ray crystal structure of MAO-B in complex with 6-hydroxy-N-propargyl-1(R)-aminoindan (1S3E)[242] was used as the starting point for all MD simulations. The missing C-terminal residues (502 – 520 Chain A and 497 – 520 Chain B) which form the remainder of the transmembrane helix were built using Avogadro[243] (assuming the standard backbone dihedral angles of an α-helix). MAO-B was then inserted into a lipid bilayer comprised of a 4:3 ratio of palmitoyloleoylphosphatidylcholine (POPC) and palmitoyloleoyl-phosphatidylethanolamine (POPE) using CHARMM-GUI.[244] This composition has been used in prior bilayer MD simulations of MAO-B, and was chosen to represent the composition of the outer mitochondrial membrane.[73,220,231] BZA was placed in the active site by alignment with the crystal structure of MAO-B in complex with nitrobenzylamine (2C70,[245] Cα RMSD 0.118 Å to 1S3E; the latter was used due to its higher resolution). All simulations of BZA were performed with the amino group in its neutral form, as this is widely believed to be the catalytically competent state of BZA.[202,208,246] Titratable residues were simulated in their standard protonation states, based on calculations with PropKa 3.0[194]. MolProbity was used to determine the optimum tautomerisation states of every His residue, and any required Asn/Gln side chain flips, based on optimizing the hydrogen bonding network[247]. Histidines 91, 115 and 452 were singly protonated on their Nδ1, with all others singly protonated on their Nε2. The system was then solvated such that there was no protein or lipid atom within 20 Å of the edge of the periodic box along the z-coordinate (bilayer normal). The total number of atoms for each system simulated was approximately 90,000.

Periodic boundary simulations were performed with Amber16, using the CHARMM36 force field to describe protein[248] and lipid[249] atoms, and TIP3P for water. Parameters for FAD in its oxidized form and BZA in its neutral form were taken from Abad *et al.*[208] Following minimization, heating and equilibration (see SI Materials and Methods), production MD simulations were run in the NpT ensemble at 310 K, with semi-isotropic coupling to a Monte Carlo barostat. Temperature was regulated using Langevin dynamics with a collision frequency of 1 ps^{-1}. A time step of 2 fs was applied with the covalent bonds to hydrogen constrained by the SHAKE algorithm. A 12 Å non-bonded cut-off was applied with a force switch smoothing function from 10 to 12 Å. Long range electrostatics were evaluated with the particle mesh Ewald method.[250] For *wt*MAO-B simulations, a total of 9 simulations were performed for 150 ns each, with the first 50 ns of simulation

used to equilibrate the protein and bilayer (see Figure S10). The BZA_2 run in which a BZA escapes the active site cavity was extended for a further 50 ns. Enzyme variant simulations (W184F, F402V, E466Y) were performed for 3 x 100 ns each in the BZA1 state (see SI Materials and Methods for further details). Coordinates were saved every 10 ps for further analysis. Routine analysis of trajectories was performed using CPPTRAJ[251], from the AmberTools suite. Area per lipid calculations were performed with GridMAT-MD,[252] using a grid resolution of 200 x 200 points for each measurement. Tunnel analysis was performed with Caver 3.0[102]. All settings were kept default apart from bottleneck radius (1.5 Å).

ASSOCIATED CONTENT

Supporting Information. FIRST calculations methodology, molecular dynamics simulation methodology, MAO-B mechanisms, table of caver data, MAO-B variant and environment spectra, Michealis-Menten of Y398F MAO-B, MD RMSD and area per lipid calculations, Entrance B structure, Caver calculation starting point, RMSF of gating loop, BZA leading the active site by MD simulations, Michaelis-Mentens of *wt*MAO-B. This information is available free of charge on the ACS Publications website.

AUTHOR INFORMATION

Corresponding Authors

*Christopher R Pudney, Department of Biology and Biochemistry, University of Bath, Bath, United Kingdom. c.r.pudney@bath.ac.uk.
*Marc W van der Kamp, School of Biochemistry, University of Bristol, Cantock's Close, Bristol BS8 1TS, United Kingdom. marc.vanderkamp@bristol.ac.uk.

Author Contributions

HBLJ and AM performed experimental work. RMC and HBLJ performed computational calculations and simulations. All authors discussed and interpreted data. The manuscript was written through contributions of all authors. All authors have given approval to the final version of the manuscript. HBLJ and RMC contributed equally‖.

ABBREVIATIONS

Alpha carbon (Cα), benzylamine (BZA), electron paramagnetic resonance (EPR), flavin adenine dinucleotide (FAD), heat capacity of catalysis ($\Delta C_P^{\ddagger}$), kynuramine (KYN), molecular dynamics (MD), monoamine oxidase (MAO), principal component analysis (PCA), palmitoyloleoylphosphatidylcholine (POPC), palmitoyloleoyl-phosphatidylethanolamine (POPE), root mean square fluctuation (RMSF), reactive oxygen species (ROS).

ACKNOWLEDGMENT

HBLJ's studentship is funded by the University of Bath. RMC's studentship is funded by the EPSRC. MWvdK is a BBSRC David Phillips Fellow (BB/M026280/1). SAW has received funding from the European Research Council (ERC) under the European Union's Horizon 2020 research and innovation programme (grant agreement No 648283

“GROWMOF”). This research made use of the Balena High Performance Computing (HPC) Service at the University of Bath

Supporting information

Exposing the Interplay Between Enzyme Turnover, Protein Dynamics and the Membrane Environment in Monoamine Oxidase B

Hannah B. L. Jones[†‖], Rory M. Crean[#†‖], Anna Mullen[§], Emanuele G. Kendrick[†], Steven D Bull[Δ], Stephen A. Wells[‡], David R. Carbery[Δ], Fraser MacMillan[§], Marc W. Van der Kamp*[%], Christopher R. Pudney*[†|].

[†]Department of Biology and Biochemistry, University of Bath, Bath BA2 7AY, United Kingdom.

[Δ]Department of Chemistry, University of Bath, Bath BA2 7AY, United Kingdom.

[‡]Department of Chemical Engineering, University of Bath, Bath BA2 7AY, United Kingdom.

[#] Doctoral Training Centre in Sustainable Chemical Technologies, University of Bath, Bath BA2 7AY, United Kingdom.

[|]Centre for Therapeutic Innovation, University of Bath, Bath BA2 7AY, United Kingdom.

[%]School of Biochemistry, University of Bristol, Biomedical Sciences building, University Walk, Bristol BS8 1TD, United Kingdom.

[§]School of Chemistry, University of East Anglia, Norwich Research Park, Norwich NR4 7TJ, United Kingdom.

*Christopher R Pudney, Department of Biology and Biochemistry, University of Bath, Bath, United Kingdom. c.r.pudney@bath.ac.uk.

*Marc W van der Kamp, School of Biochemistry, University of Bristol, Cantock’s Close, Bristol BS8 1TS, United Kingdom. marc.vanderkamp@bristol.ac.uk.

Author Contributions

[‖]H.B.L.J. and R.M.C. contributed equally. HBLJ and AM performed experimental work. RMC and HBLJ performed computational calculations and simulations. All authors discussed and interpreted data. The manuscript was written through contributions of all authors. All authors have given approval to the final version of the manuscript.

FIRST calculations

FIRST[104] (floppy inclusion and rigid substructure topography) calculations, as mentioned in the main text, were carried out on a crystal structure of Monoamine oxidase B (MAO-B) (PDB 1S3E)[242]. The aim of this procedure was to establish rigidified mutations of MAO-B, and to access their impact on catalysis. Scwrl4[181] was used to optimize the side-chain conformations of 1S3E MAO-B, and calculations were run on both the original and optimized structures. Structures that were optimized using Scwrl4 were constrained against their FAD cofactor (FAD atoms are treated as non-interacting particles that provide steric restraints). Of mutants carried forward for experimental testing, F402V and W184F arose from Scwrl4 optimized 1S3E, and E466Y arose from the original 1S3E crystal structure. Prior to running calculations, the X-ray structure was pre-processed by removing all hetero atoms (apart from FAD), and water molecules with PyMOL, and adding hydrogens to all residues (all residues were at their standard protonation state for pH 7) using Molprobity[247].

An initial FIRST run was used to generate the constraint files for wildtype (WT) MAO-B, which describe the strength of the covalent bonds, hydrogen bonds, hydrophobic interactions and pi-pi stacking interactions throughout the protein. FIRST was then run over 20 energy cut offs (Ecuts), using rigid cluster decomposition (RCD) as previously described.[105] Results are quantified as 'the fraction of residues in rigid clusters' for each Ecut. Ecuts ranged from 0-4 kcal mol^{-1} with a step size of 0.2 kcal mol^{-1}. The fraction of residues in rigid clusters from all Ecuts were then averaged to give a single value to reflect the overall rigidity of the protein. This was used as the background value for comparison to all further calculations.

To replicate the premise of alanine scanning, a protocol ‘Sidescan’ (available upon request) was developed to produce the constraint files calculated by FIRST with the constraint contribution of a specified amino acid side chain past the beta carbon (Cβ) missing from the files. These altered constraint files were produced sequentially for each amino acid (not including alanine or glycine) of MAO-B, and the RCD analysis was carried out to determine the rigidity value of MAO-B without each amino acid. A random sample of residues whose side chains were identified as making no contribution to the rigidity of MAO-B, were taken forward for *in silico* mutagenesis and additional screening within FIRST. Scwrl4 was used to mutate these residues to each possible amino acid alternative, and the FIRST/RCD calculations were implemented, to predict the relative rigidity of each mutant compared to the WT.

Mutations that improved the overall rigidity of MAO-B were then analyzed using the protocol ‘GetRCD’ (available upon request). GetRCD assigned each amino acid in MAO-B an E_{cut} (kcal mol^{-1}) value, which reflects the amount of energy required to free that residue from its constraint network. This was carried out on the selected mutants to ascertain whether they would significantly affect the flexibility/rigidity of the catalytically

relevant residues of *wt*MAO-B (Table S5). If a mutation altered the flexibility/rigidity of a catalytically relevant residue by more than 1 kcal mol^{-1} it was disregarded.

From these calculations we selected three single point mutations to experimentally test (W184F, F402V, E466Y). W184F is located in the FAD binding domain of MAO-B and is 13.3 Å away from BZA and 15.9 Å away from the flavin ring of FAD. F402V is located in the FAD binding domain of MAO-B and is 15.3 Å away from BZA and 15.3 Å away from the flavin ring of FAD. E466Y is located on the C-terminal tail of MAO-B and is 21.4 Å away from BZA and 16.6 Å away from the flavin ring of FAD. All measurements are based on PDB 2C70 (chosen because it is co-crystallized with nitrobenzylamine) and based on the closest atom to atom distance of the amino acid backbone and FAD or BZA. Graphical representations of the location of each mutant, alongside their predicted change in rigidity from FIRST calculations can be found in Figure S14 A-C.

Molecular Dynamics (MD) Simulations

Equilibration Procedure

Following structure preparation (as described in the main text), all systems were subjected to the same equilibration procedure as detailed below. First, all water molecules and hydrogen atoms were minimized with 500 steps of steepest descent followed by 500 steps of conjugate gradient minimization. The system was then rapidly heated from 100 K to 310 K in the NVT ensemble over 100 ps, with 10 kcal mol^{-1} positional restraints on all protein and lipid atoms. Whilst retaining the 10 kcal mol^{-1} restraints on protein atoms, lipid restraints were gradually reduced to 2.5 kcal mol^{-1} over the course of 200 ps. During NVT simulation, the timestep was set to 1 fs and a collision frequency of 1 ps^{-1} was used with Langevin temperature control. Systems were then simulated in the NPT ensemble (1 atm, 310 K, semi-isotropic coupling to a Monte Carlo barostat, Langevin temperature control with a collision frequency of 1 ps^{-1}, 2 fs time step), with lipid restraints reduced from 2.5 to 0 kcal mol^{-1} over the course of 200 ps. Finally, protein restraints were reduced from 10 kcal mol^{-1} to 0 kcal mol^{-1} over the course of 1 ns. At this point 50 ns of production MD simulations were performed to equilibrate the bilayer and protein (as described in the main text).

Mutant Simulations

The point mutants (W184F, F402V and E466Y) were each subjected to 3 x 100 ns of MD simulation in the BZA_1 bound state. The structure of *wt*MAOB-BZA_1 at 50 ns into each of the three independent simulations was used to generate three unique starting structures for the point mutant MD simulations. BZA was re-orientated to a catalytically competent state for Run 3 simulations based on the structure of nitrobenzylamine in complex with MAO-B (PDB 2C70). Mutations were made in silico using PyMOL[253], and any overlapping water molecules with the newly introduced sidechains were removed. For the E466Y mutation a single sodium atom was removed from each simulation box to ensure

the system had an overall charge zero. Each system was then prepared as described above (see Equilibration Procedure). Trajectory analysis was performed without the first 10 ns of simulation time, which was used to equilibrate each mutant simulation.

Trajectory Analysis

Trajectory analysis was performed using CPPTRAJ[251], (part of the AmberTools suite of programmes). Per residue Root Mean Square Fluctuations (RMSFs) were performed on snapshots at 10 ps intervals using average structures calculated from 1 ns time windows over the course of each trajectory. Performing RMSF calculations in this way reduces the influence of larger scale conformational changes on the calculation, providing a more realistic indication of backbone mobility.[254] RMS fitting was performed on the Cα carbon of residues 1-455 of each monomer. Clustering analysis was performed using the DBSCAN algorithm[255], using all backbone heavy atoms of the three loop regions (81–85, 100–108 and 202–207) which describe the opening of Entrance B. Principal Component Analysis was performed on all BZA_1 simulations (WT, W184F, F402V and E466Y) simultaneously using the Cα carbon of residues 1-455 of each monomer (with monomers inputted separately).

Supporting Data

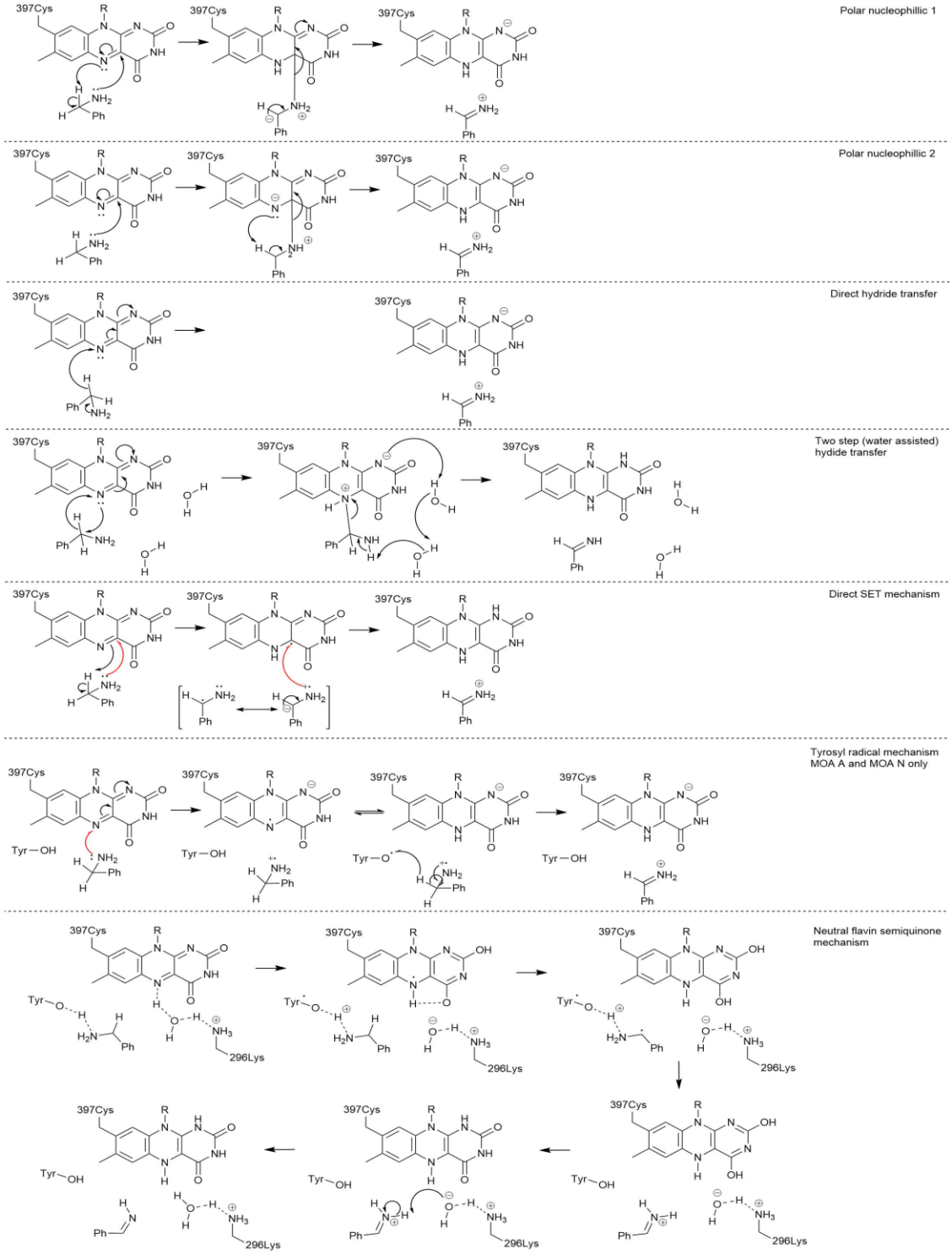

Scheme S2. Proposed mechanisms for MAO-B catalysis: Polar nucleophilic,[201] direct hydride transfer,[203–205] two step hydride transfer,[206] radical (single electron transfer),[202] tyrosyl radical mechanism[211], and neutral semiqunione[209]. For clarity, double electron transfers are shown as black (double headed) arrows and single electron transfers are shown as red (single headed) arrows.

Supporting Tables

Table S3. Kinetic parameters extracted from temperature-dependence of MAO-B fit to the MMRT equation as shown in Figure 26.

	$\Delta H^{\ddagger}$ (kJ mol^{-1})[a]	$\Delta S^{\ddagger}$ (kJ mol^{-1} K^{-1}) [a]	$\Delta C_P^{\ddagger}$ (kJ mol^{-1} K^{-1})
KYN			
MAO-B in nanodiscs	83.5 ± 4.8	1.3 ± 0.02	−2.8 ± 0.6
MAO-B in reduced Triton X-100	66.1 ± 12.0	1.3 ± 0.04	−1.0 ± 1.5
BZA			
MAO-B in nanodiscs	47.7 ± 2.1	1.2 ± 0.01	−0.4 ± 0.4
MAO-B in reduced Triton X-100	68.4 ± 12.4	1.3 ± 0.04	−1.9 ± 1.6

a, Data at 298 K.

Table S4. Caver values for the maximum bottleneck radius (Å) and the tunnel frequency of monomer 1 and 2 of MAO-B, with benzylamine in neither side (BZA_0), in monomer 1 (BZA_1) and in both sides of the MAOB dimer (BZA_2).

	Monomer 1	**Monomer 2**
Maximum bottleneck radius (Å)		
BZA_0	2.2 +/- 0.2	1.7 +/- 0.1
BZA_1	1.6 +/- 0.1	2.1 +/- 0.2
BZA_2	1.9 +/- 0.5	2.1 +/- 0.2
Tunnel Frequency		
BZA_0	335 +/- 90.4	15 +/- 6.2
BZA_1	14 +/- 5.5	215 +/- 28.4
BZA_2	51 +/- 91.5	124 +/- 15.0

Table S5. Residues considered catalytically relevant for FIRST and RCD calculations.

Residues	**Catalytic Relevance**
296[256], 388[256], 398[256], 435[256]	Key active site residues
156[257], 365[257], 382[258]	Distal from active site, but mutagenesis removes or seriously reduces activity.
85 – 112[73], 155-165[73], 199[73], 326[73]	Substrate binding/product release
34[259], 44[259], 222-227[259], 397[256]	FAD binding

Supporting Figures

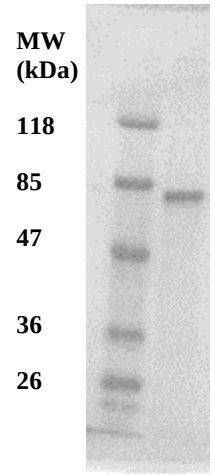

Figure S6. SDS-page of MAO-B eluted after gel filtration chromatography. Band corresponds to MAO-B MW ~59 kDa.

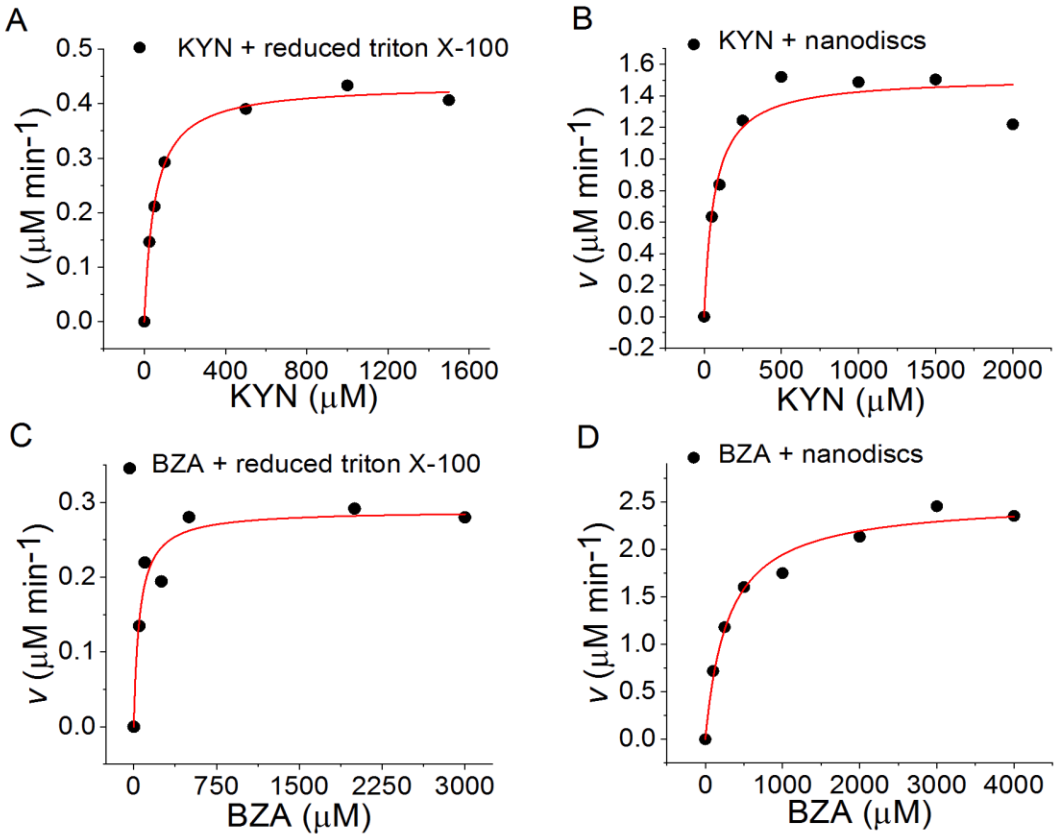

Figure S7. Michaelis-Menten plots A. KYN + reduced Triton X-100 (K_m 50.5 ± 4.2). B. KYN + PC nanodiscs (K_m 66.1 ± 20.1). C. BZA + reduced Triton X-100 (K_m 51.8 ± 16.6). D. BZA + nanodiscs (K_m 295.7 ± 45.6). Conditions, 25 °C, 50 mM HEPES, pH 7.5, the same concentration of enzyme used in each panel.

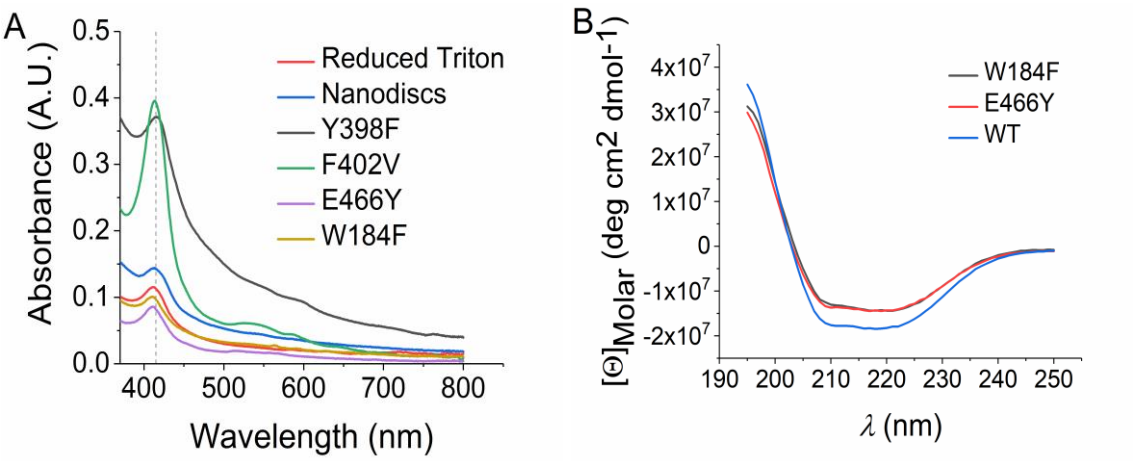

Figure S8. A. The absorbance spectrum of MAO-B in a reduced Triton X-100 and in a nanodisc environment, and of various MAO-B point mutations. 50 mM HEPES, pH 7.5. The spectral feature at 415 nm is marked by a horizontal dashed line. B. The circular dichroism spectrum of wtMAO-B, W184F and E466Y in 50 mM potassium phosphate, 0.5 % w/v Triton X-100, pH 7.5.

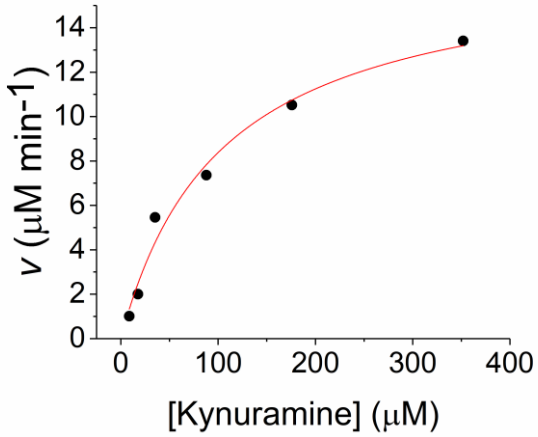

Figure S9. A. Michaelis-Menten plot of MAO-B Y398F with KYN at 40 °C

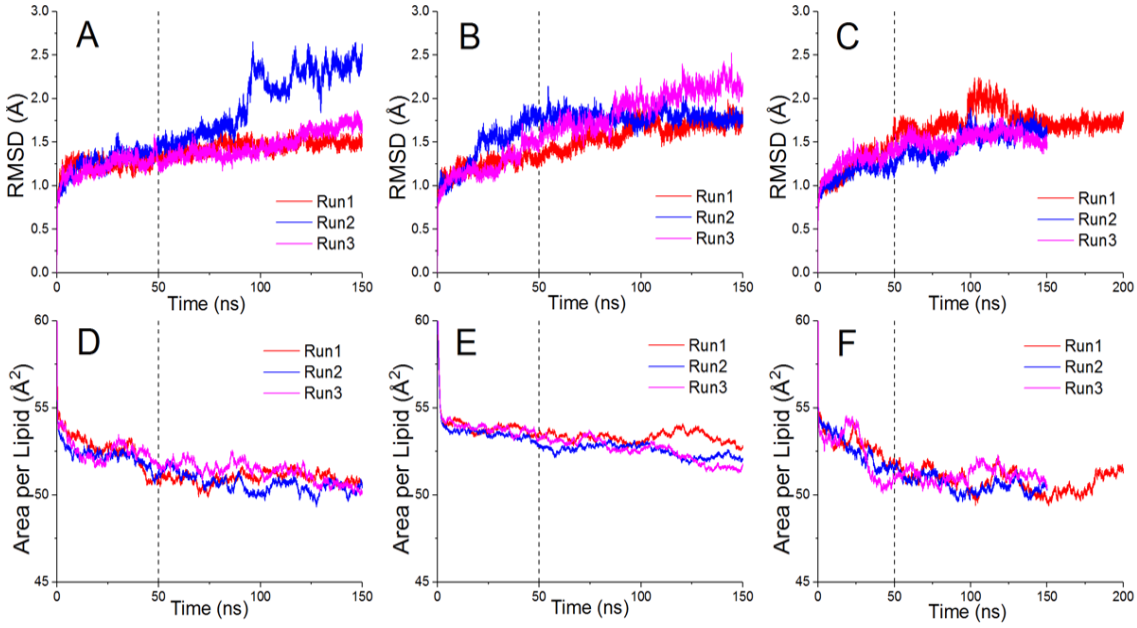

Figure S10. **A** to **C**; Cα RMSDs of residues 1-485 in each monomer of BZA_0 (**A**), BZA_1 (**B**) and BZA_2 (**C**) for each run. **D** to **F**; Area per Lipid against simulation time for BZA_0 (**D**), BZA_1 (**E**) and BZA_2 (**F**). A dotted line at 50 ns is placed on all graphs to indicate the point at which all simulations were considered equilibrated.

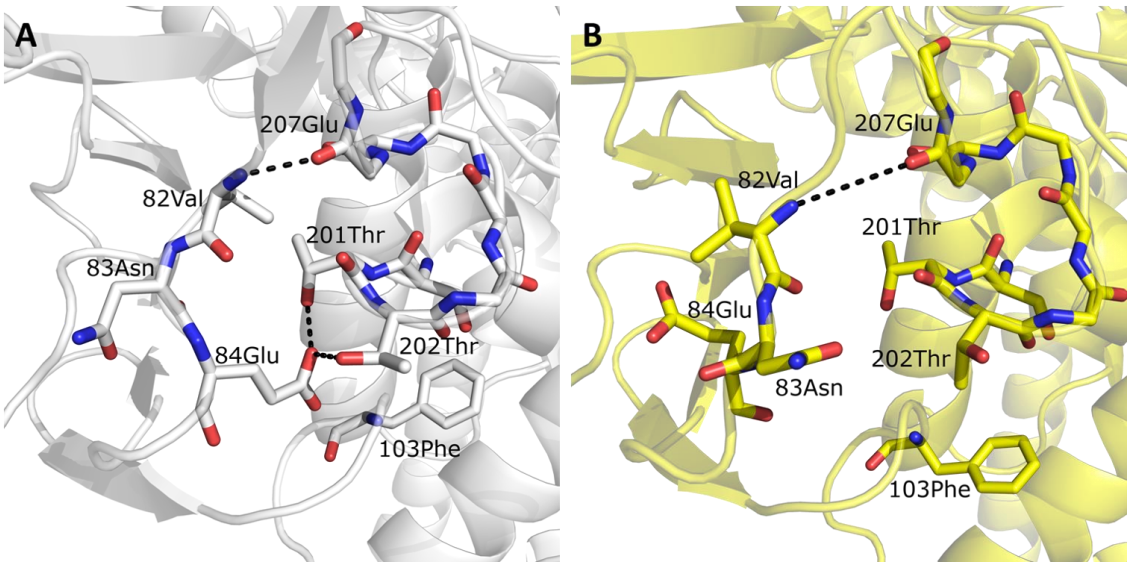

Figure S11. A and **B**: Representative structures of open (**A**) and closed (**B**) conformations of Entrance B. Side chains of non-important residues and all hydrogens have been hidden for clarity. The native (crystal structure) contacts between 82Val and 207Gly as well as 84Glu and 201Thr and 202Thr are lost upon opening of Entrance B. Alongside this observation, the gating loop (residues 99 to 112) are observed to rotate down and away from the entrance, further increasing the size of the entrance cavity.

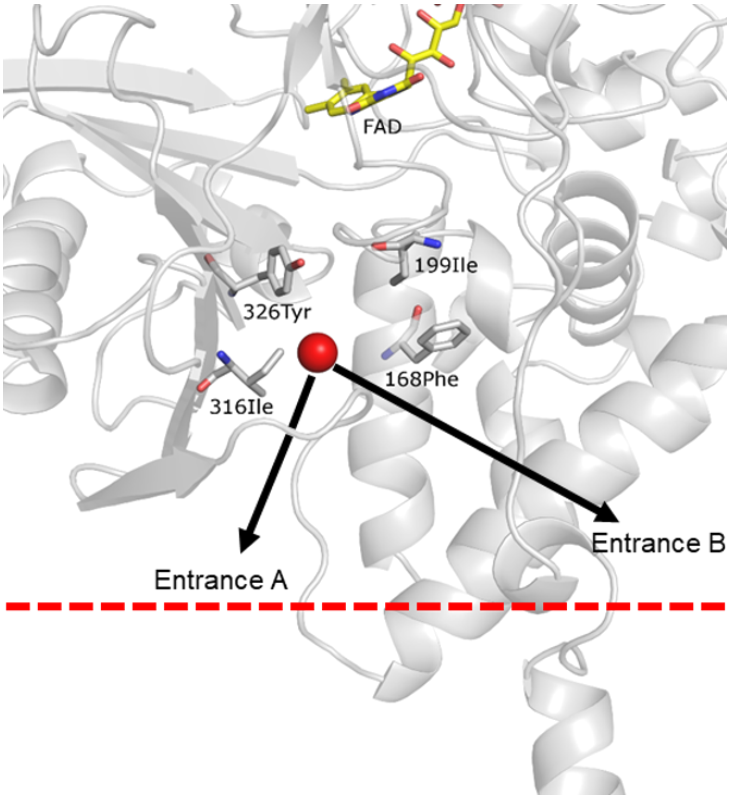

Figure S12. The starting point for Caver 3.0 analysis of MAO-B MD simulations. The 199Ile 326Tyr 'gate' is which forms a bottleneck closing off the active site from both Entrance A and B is indicated. The average starting point is shown as a red sphere and is positioned based on the center of mass of the Cα of residues 168Phe and 316Ile for each snapshot. A red dashed line is used to indicate the approximate starting point of the membrane.

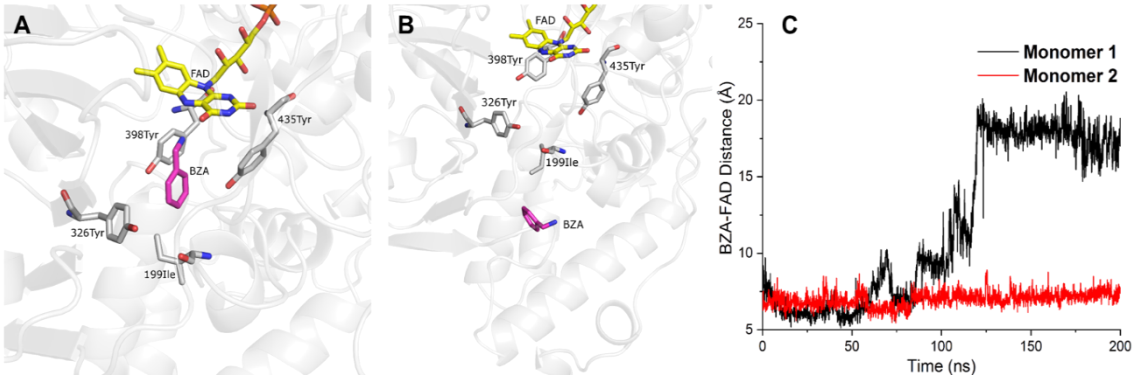

Figure S13. BZA leaving the active site of one monomer when it is placed in both sides of MAO-B during one of the three MD simulation repeats. **A** – Representative structure of BZA in coordination with FAD, showing the active site coordinating tyrosine's (398 and 435), as well as the 199Ile 326Tyr gate, which closes off the active site. **B** – Position of BZA at its furthest point from the FAD recorded over the course of the simulation. **C** – Measurement of the distance between FAD and BZA for each monomer. Distances are calculated as the center of mass between all heavy atoms on BZA to the piperazine (central) ring heavy atoms of FAD.

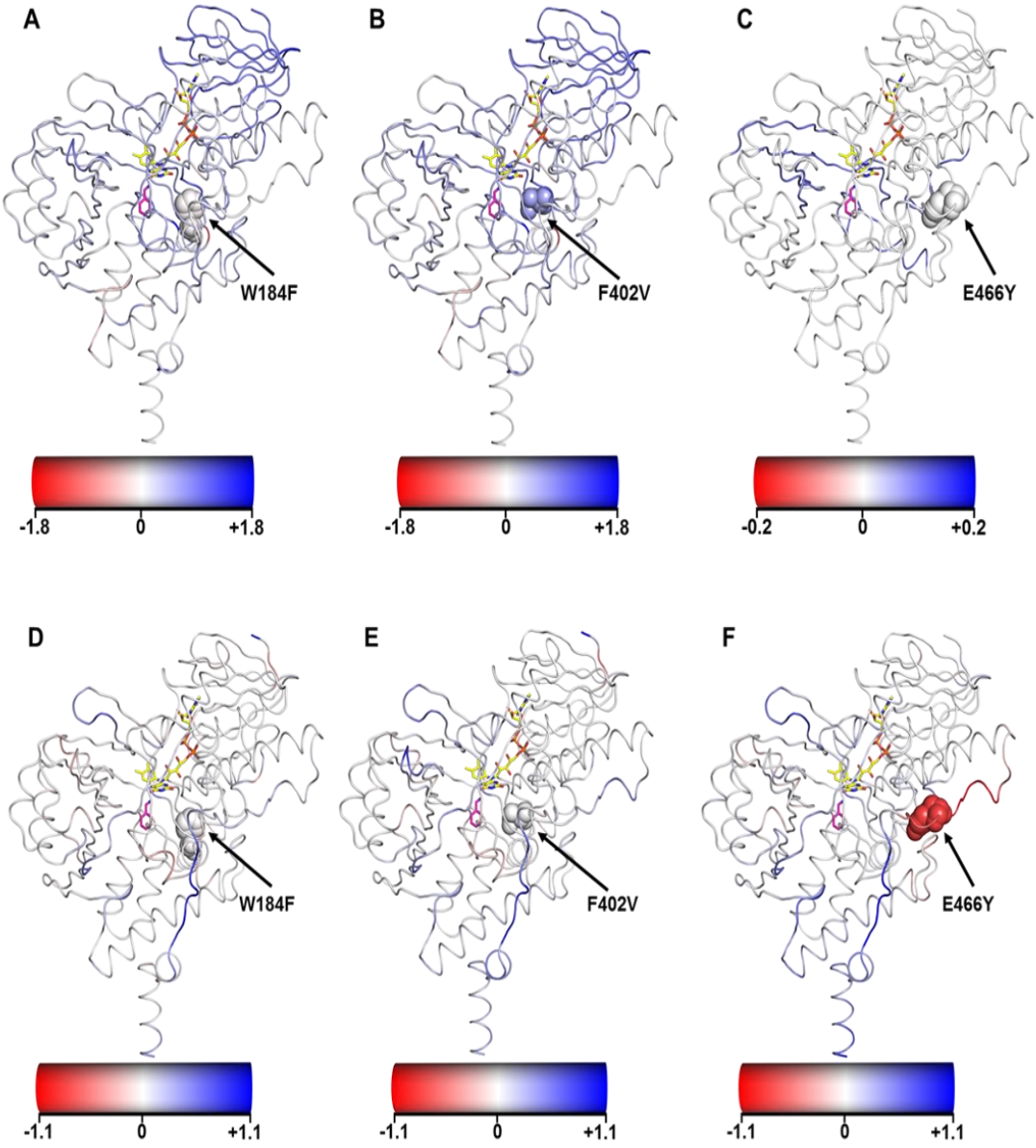

Figure S14. Predicted Rigidification of MAO-B point mutations W184F (**A)**, F402V (**B**) and E466Y (**C**) from FIRST calculations. Per-residue changes in rigidity (in kcal mol^{-1}) against the wtMAO-B are colour mapped onto each structure, whereby a predicted increase or decrease in rigidity upon mutation is shown as blue or red respectively. Predicted change in flexibility of MAO-B point mutations W184F (**D)**, F402V (**E**) and E466Y (**F**) from MD simulations. Per residues differences in RMSF (in Å) are coloured mapped onto each structure such that an increase or decrease in rigidity upon mutation is shown as blue or red respectively. For all figures, the site of each mutation is indicated and shown as spheres. The locations of FAD and BZA are indicated on all structures.

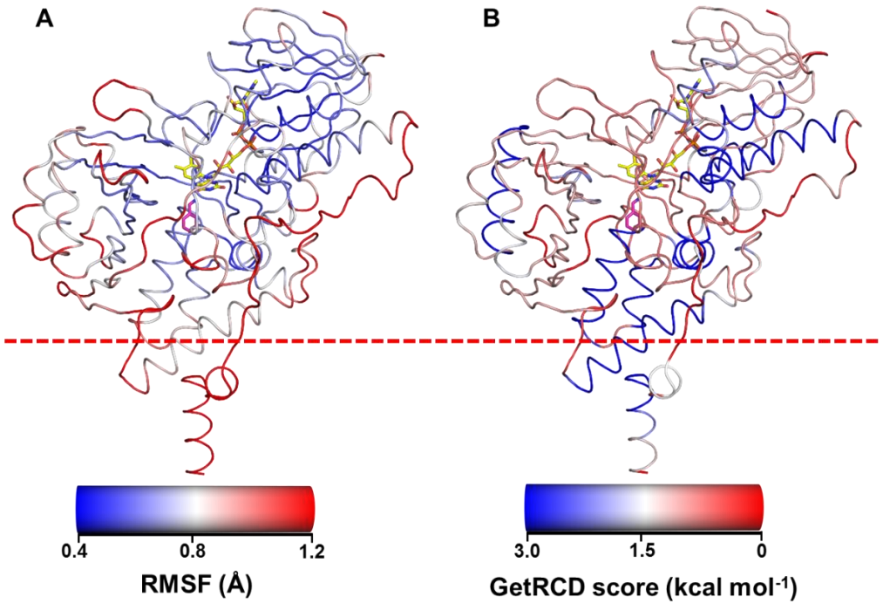

Figure S15. Comparison of the calculated Cα RMSF for wtMAO-B (averaged over all BZA_0 runs) and the GetRCD score calculated by FIRST. The location of FAD and BZA are indicated on both structures. A red dashed line is used to indicate the approximate location of the bilayer where the most disagreement is observed, likely due to the lack of consideration of a bilayer in FIRST calculations. In both cases, going from red to blue indicates increased stability/rigidity of that residue.

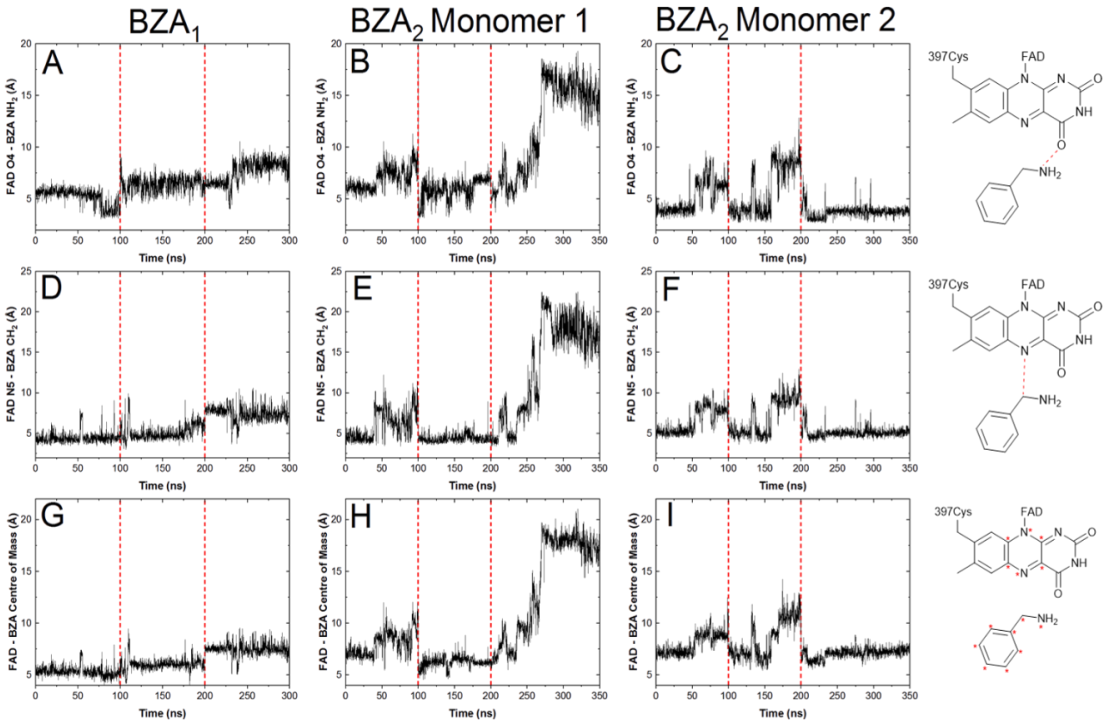

Figure S16. Measurement of three distances between FAD and BZA for all wtMAO-B simulations. A schematic of the measurement made is provided for each column. For **G**, **H** and **I**, the distance is measured between the centre of mass of the heavy atoms of the central FAD ring and BZA, with those atoms considered in the measurement indicated with an asterix.

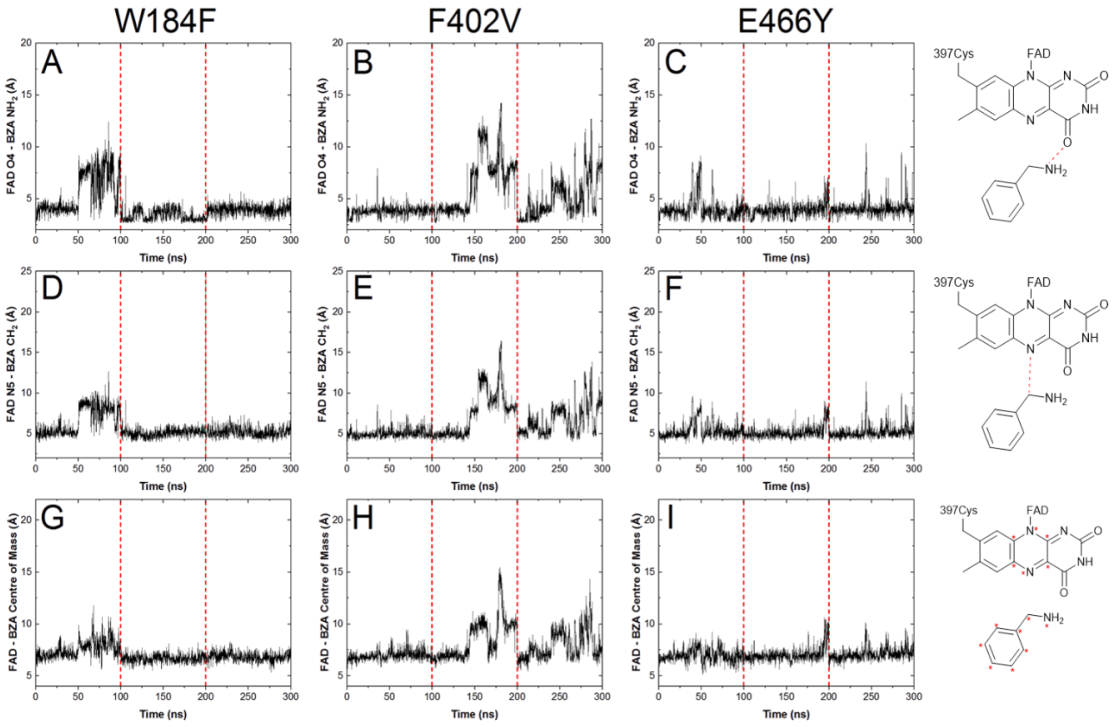

Figure S17. Measurement of three distances between FAD and BZA for all Mutant MAO-B simulations. A schematic of the measurement made is provided for each column. For **G**, **H** and **I**, the distance is measured between the centre of mass of the heavy atoms of the central FAD ring and BZA, with those atoms considered in the measurement indicated with an asterix.

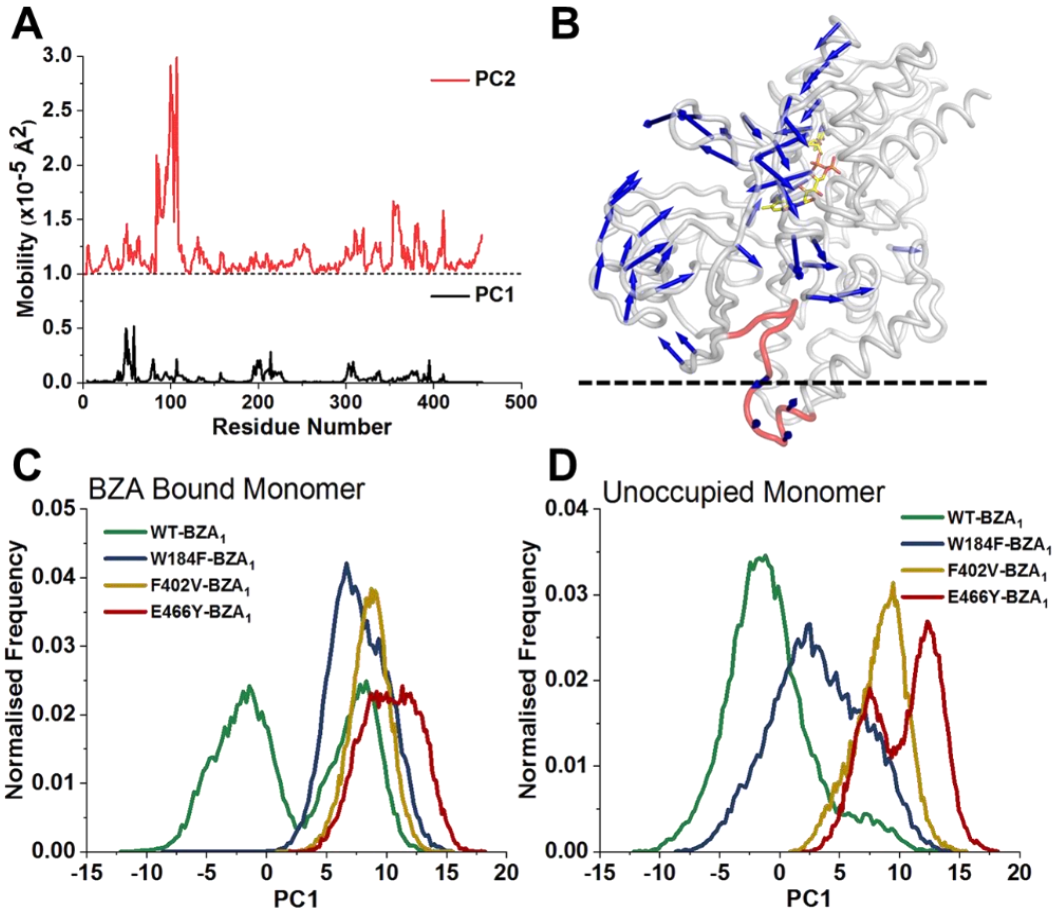

Figure S18. A. Mobility plots of principal components 1 and 2 (PC1 and PC2) for all BZA_1 simulations. Both plots are to the same scale, with PC2 plotted using a y + 1 offset. **B**. Porcupine' plot of PC1, with arrows indicating the direction of the PC1 eigenvector and arrow size indicating the magnitude of the corresponding eigenvalue, for all Cα atoms with eigenvalues greater than 4 Å. The gating loop residues (99 – 112) are colored in red, and the approximate location of the bilayer is indicated with a black dotted line. **C** + **D**. Normalized histograms (bin width 0.25 Å) of PC1 for all BZA_1 simulations of the bound (**C**) and unoccupied monomers (**D**).

Chapter 6:
Conclusions and Future Work

The work presented in this thesis explored the influence of $\Delta C_p^{\ddagger}$ on the curvature of enzymatic temperature-dependences, as proposed by the MMRT. $\Delta C_p^{\ddagger}$ is hypothesized to arise predominantly from alterations in the vibrational motions of an enzyme between the ground and transition state of its reaction coordinate. To validate this notion, chapter 3 establishes the influence of dynamical perturbations via pressure and viscosity studies, on the temperature-dependences of two comparable enzyme systems. Here, the curvature of the temperature-dependences, and consequently the value of $\Delta C_p^{\ddagger}$ was found to be sensitive to enzyme dynamics linked to catalysis. This validated both the notion of MMRT, and the relationship between MMRT and the dynamics of enzymes linked to the reaction coordinate.

Chapter 4 cleanly links vibrational motion on a small scale to the curvature of temperature-dependences using KIEs, which is reflected in the value of $\Delta C_p^{\ddagger}$. This work demonstrates that $\Delta C_p^{\ddagger}$ is sensitive to low level vibrational changes and to alterations in the vibrational motion of substrates, in the system studied. Chapter 5 provides evidence for the importance of considering the value of $\Delta C_p^{\ddagger}$, where the value supplied insight, and directed further research, into the mechanism of the medically relevant enzyme MAO-B.

All three studies presented in this thesis aimed to minimise the impact of other causes of curvature linked to enzyme temperature-dependences, which were detailed in chapter 1. This included minimising denaturation through short assay times, conservative temperature ranges and the use of a hyper-thermophile. Additionally, the experimentation in all three cases invokes the use of comparable systems to minimise or cancel out additional impact from other variables, such as temperature-dependent changes in the rate-limiting step, the influence of changes in the hydration term over the reaction coordinate and the temperature-dependence of $\Delta C_p^{\ddagger}$ itself.

This work does not categorically disprove alternative hypotheses for the curvature of enzyme temperature-dependences, such as the equilibrium and N-state models detailed in chapter one.[9,30] However, neither of these models provide full explanations for the phenomenon. The equilibrium model lacks a proven molecular basis or an understanding of the timescales on which the proposed reversible enzyme inactivation occurs.[29] Additionally, although the N-state model allows for the addition of multiple terms for multiple conformational states, arguably the integrity of this numerical fit is reduced with each additional conformation considered. Also, the N-state model is very difficult to prove

or disprove, as we are currently limited by a lack of computational and experimental techniques that could be used to thoroughly sample the various catalytically relevant conformational states proposed. The time/dynamical scales on which the N-state model occurs may be extremely small and may remain immeasurable.

Furthermore, neither the equilibrium model or the N-state model considers the change in heat capacity that can occur during a reaction. It is possible that all three models are influencing the temperature-dependence of enzyme reactions and could even be applied in conjunction with each other. For instance, the temperature dependence of the enzyme sub-states proposed by the N-state model may also be further influenced by the temperature-dependence of their individual enthalpy and entropy contributions to turnover. Future work should focus on elucidating which models are contributing and to what extent.

Even in the case that the value of $\Delta C_p^{\ddagger}$ is not fully attributable to changes in heat capacity, all three chapters demonstrate that the value itself is effectively reporting on the extent to which enzyme dynamics are linked to catalysis. This highlights the importance of fitting enzyme temperature-dependences to the MMRT equation rather than the Eyring equation. It may even explain the break points that are often reported in temperature-dependence plots, and in KIEs.[24,260,261] Perhaps they are not break points, but instead are prominent curvature. The application of MMRT to the temperature-dependence of enzymatic reactions is beginning to gain traction with other enzymologists.[21,166,262] The ability to measure the extent to which dynamics are linked to catalysis, without carrying out lengthy studies such as MD simulations or NMR experiments, as well as being able to rationalise perceived curvature of enzyme temperature-dependences, makes the application of MMRT appealing. When applied in circumstances where all the caveats detailed in section 1.10 are accounted for, $\Delta C_p^{\ddagger}$ becomes a powerful probe of enzyme turnover.

This thesis validates the theory and application of MMRT to enzymatic temperature-dependences, and in turn, opens multiple avenues for future development of the theory and its applications. In chapter 1 the contribution of enzyme dynamics to catalysis is discussed. The work presented here cannot prove whether enzyme dynamics are directly linked to the catalytic step or whether temperature-dependent shifts in the populations of enzymatic sub-states are influencing the rate of turnover. However, it does provide substantial evidence that enzyme dynamics are influencing turnover. Future work to elucidate whether the dynamics reported by the value of $\Delta C_p^{\ddagger}$ are directly linked to the catalytic step, or whether it is reporting on shifted equilibriums at different temperatures, or both, would allow for $\Delta C_p^{\ddagger}$ to be applied and interpreted more directly.

Additionally, future work should focus on identifying the true origin of $\Delta C_p^{\ddagger}$. Work by van der Kamp *et al*., suggests that vibrational motions involved with catalysis, and therefore the value of $\Delta C_p^{\ddagger}$, are both local to and distal from the active site of the enzyme[46], implying a network of vibrational modes are influencing catalysis. This is also demonstrated in the

results of chapter 4, where the experimental value of $\Delta C_p^{\ddagger}$ was much larger than that calculated computationally from a QM cluster model. Here the main difference is the lack of surrounding protein included in the QM calculations, which implies the origin of $\Delta C_p^{\ddagger}$ lies not only at the active site, but also distally. This may provide further evidence for the hypothesis that enzymes are large to carry out difficult chemistry, to increase their 'energy reservoir', which is reflected in the value of $\Delta C_p^{\ddagger}$, as proposed by Arcus *et al*.[42] Identifying the origin of $\Delta C_p^{\ddagger}$ is currently difficult. The most appropriate technique that exists is explicit computational calculations of enzyme turnover (QM), which is currently too computationally demanding to be viable. As computational techniques improve, the future evaluation of numerous systems considered in full may identify both the origin of $\Delta C_p^{\ddagger}$ and the contribution of dynamics to catalysis.

The MMRT equation can also be further developed to account for the value of $\Delta C_p^{\ddagger}$ being temperature-dependent in itself. This corresponds with the theory of the temperature-dependence of the entropic and enthalpic terms of catalysis. If these two terms are not opposingly temperature-dependent to the same extent, then the value of $\Delta C_p^{\ddagger}$ will vary depending on the temperature range at which it is measured. In the future, the MMRT equation will include an extra term to account for the temperature-dependence of $\Delta C_p^{\ddagger}$, which will require additional data points to maintain the integrity of the fit.

Ultimately, applications of the MMRT for medicine and industry should be the focus of the future direction of this work. For example, chapter 5 demonstrates the utility of the value of $\Delta C_p^{\ddagger}$, and further studies can continue to apply $\Delta C_p^{\ddagger}$ as a metric to assess the influence of an enzyme's environment on its turnover. In turn this can direct the focus of mechanistic studies, which are valuable in both medical and industrial applications.

Additionally, if the link between restricted enzyme dynamics, a reduced value of $\Delta C_p^{\ddagger}$ and a subsequently increased enzyme T_{opt} and rate, as seen in chapter 3, is universal in all enzyme systems, $\Delta C_p^{\ddagger}$ could be applied to enzyme engineering. Future methods could aim to computationally predict and screen enzyme mutations for desired $\Delta C_p^{\ddagger}$ values. This could be implemented via a high-throughput approach, such as the FIRST method outlined in chapter 5. FIRST could be applied to screen for mutations that lead to the global rigidification of an enzyme. Selected mutations could then be validated and screened for alterations that may negatively impact catalysis by MD, as outlined in chapter 5, followed by experimentally measuring the value of $\Delta C_p^{\ddagger}$ for validation. Ultimately MD simulations would provide a more direct and stringent approach than FIRST calculations to engineer values of $\Delta C_p^{\ddagger}$, and therefore an enzyme's T_{opt} and rate at T_{opt}. $\Delta C_p^{\ddagger}$ can be accurately measured by the MD simulations, as demonstrated by van der Kamp *et al.*[46] However, MD simulations are currently not high-throughput enough for this approach to

be viable, and so this may only become a valuable method in the future, as computational power increases.

Another approach could involve tuning the value of $\Delta C_p^{\ddagger}$ using varied solvents with different viscosities for enzyme rigidification, as shown in chapter three. Conditions could be screened in a multi-well plate using the fluorescence REES effect outlined in Chapter 2 and utilized in Chapter 3. Conditions where an enzyme is rigidified at a desired temperature could then be carried forward and $\Delta C_p^{\ddagger}$ values could be measured, allowing for the T_{opt} and rate at T_{opt} of enzymes to be tuned for medical and industrial applications.

The increase in enzymatic efficiency associated with an increased T_{opt} and rate at T_{opt} could be applied where increased enzyme turnover at high temperatures is required, or where the quantity of product formed is a key focus. For example, a keto-reductase is used to form intermediates in the production of multiple pharmaceuticals. The enzyme was stabilised and its activity was enhanced by the company Codexis, as the enzyme's substrate is only soluble when exposed to high temperatures and organic solvents.[263] Additionally, altering the value of $\Delta C_p^{\ddagger}$ could also aid in reducing the T_{opt} of enzymes, where reactions are required to take place in colder conditions, such as for use in washing detergents.

In conclusion, the work presented here has both validated the MMRT and provided evidence for the influence of dynamics on enzyme turnover. It is a valuable first step towards the potential future role of applying the MMRT to engineer the rate and T_{opt} of enzymes.

References

(1) Hobbs, J. K.; Jiao, W.; Easter, A. D.; Parker, E. J.; Schipper, L. a.; Arcus, V. L. Change in Heat Capacity for Enzyme Catalysis Determines Temperature Dependence of Enzyme Catalyzed Rates. *ACS Chem. Biol.* **2013**, *8*, 2388–2393.

(2) Kirk, O.; Borchert, T. V.; Fuglsang, C. C. Industrial Enzyme Applications. *Curr. Opin. Biotechnol.* **2002**, *13*, 345–351.

(3) Huang, X.; Dixit, V. M. Drugging the Undruggables: Exploring the Ubiquitin System for Drug Development. *Cell Res.* **2016**, *26*, 484–498.

(4) Ramsay, R. R.; Tipton, K. F. Assessment of Enzyme Inhibition: A Review with Examples from the Development of Monoamine Oxidase and Cholinesterase Inhibitory Drugs. *Molecules* **2017**, *22*, 1192.

(5) Bornscheuer, U. T.; Kazlauskas, R. J. Catalytic Promiscuity in Biocatalysis: Using Old Enzymes to Form New Bonds and Follow New Pathways. *Angew. Chemie Int. Ed.* **2004**, *43*, 6032–6040.

(6) Silva, C.; Martins, M.; Jing, S.; Fu, J.; Cavaco-Paulo, A. Practical Insights on Enzyme Stabilization. *Crit. Rev. Biotechnol.* **2018**, *38*, 335–350.

(7) Cleenewerck, M.; Grootaert, M. O. J.; Gladysz, R.; Adriaenssens, Y.; Roelandt, R.; Joossens, J.; Lambeir, A.-M.; De Meyer, G. R. Y.; Declercq, W.; Augustyns, K.; Martinet, W.; Van der Veken, P. Inhibitor Screening and Enzymatic Activity Determination for Autophagy Target Atg4B Using a Gel Electrophoresis-Based Assay. *Eur. J. Med. Chem.* **2016**, *123*, 631–638.

(8) Eijsink, V. G. H.; Gåseidnes, S.; Borchert, T. V.; van den Burg, B. Directed Evolution of Enzyme Stability. *Biomol. Eng.* **2005**, *22*, 21–30.

(9) Glowacki, D. R.; Harvey, J. N.; Mulholland, A. J. Taking Ockham's Razor to Enzyme Dynamics and Catalysis. *Nat. Chem.* **2012**, *4*, 169–176.

(10) Logan, S. R. The Origin and Status of the Arrhenius Equation. *J. Chem. Educ.* **1982**, *59*, 279.

(11) Eyring, H. The Activated Complex and the Absolute Rate of Chemical Reactions. *Chem. Rev.* **1935**, *17*, 65–77.

(12) Cornish-Bowden, A.; Cornish-Bowden, A. *Fundamentals of Enzyme Kinetics*; Wiley-Blackwell Weinheim, Germany, 2012.

(13) Laidler, K. J. The Development of the Arrhenius Equation. *J. Chem. Educ.* **1984**, *61*, 494.

(14) Barton, J. S. Denaturation at the Optimum Temperature. *Biochem. Educ.* **1979**, *7*, 13–14.

(15) Vieille, C.; Zeikus, G. J. Hyperthermophilic Enzymes: Sources, Uses, and Molecular Mechanisms for Thermostability. *Microbiol. Mol. Biol. Rev.* **2001**, *65*, 1–43.

(16) Feller, G. Psychrophilic Enzymes: From Folding to Function and Biotechnology. *Scientifica (Cairo).* **2013**, *2013*, 1–28.

(17) Konermann, L. Protein Unfolding and Denaturants; eLS. John Wiley & Sons, Ltd: Chichester., 2012.

(18) Halliday, D.; Walker, J.; Resnick, R. *Fundamentals of Physics*; 2013.

(19) Masgrau, L.; González-Lafont, À.; Lluch, J. M. The Curvature of the Arrhenius Plots Predicted by Conventional Canonical Transition-State Theory in the Absence of Tunneling. *Theor. Chem. Acc.* **2003**, *110*, 352–357.

(20) Morild, E. The Theory of Pressure Effects on Enzymes. *Adv. Protein Chem.* **1981**, *34*, 93–166.

(21) Machado, T. F. G.; Gloster, T. M.; da Silva, R. G. Linear Eyring Plots Conceal a Change in the Rate-Limiting Step in an Enzyme Reaction. *Biochemistry* **2018**, *57*, 6757–6761.

(22) Kistiakowsky, G. B.; Lumry, R. Anomalous Temperature Effects in the Hydrolysis of Urea by Urease. *J. Am. Chem. Soc.* **1949**, *71*, 2006–2013.

(23) Truhlar, D.; Kohen, A. Convex Arrhenius Plots and Their Interpretation. *Proc. Natl. Acad. Sci. U. S. A.* **2001**, *98*, 848–851.

(24) Massey, V.; Curti, B.; Ganther, H. A Temperature-Dependent Conformational Change in D-Amino Acid Oxidase and Its Effect on Catalysis. *J. Biol. Chem.* **1966**, *241*, 2347–2357.

(25) Kavanau, J. L. Enzyme Kinetics and the Rate of Biological Processes. *J. Gen. Physiol.* **1950**, *34*, 193–209.

(26) Thomas, T.; Scopes, R. The Effects of Temperature on the Kinetics and Stability of Mesophilic and Thermophilic 3-Phosphoglycerate Kinases. *Biochem. J.* **1998**, *330*, 1087–1095.

(27) Feller, G.; Gerday, C. Psychrophilic Enzymes: Hot Topics in Cold Adaptation. *Nat. Rev. Microbiol.* **2003**, *1*, 200–208.

(28) Buchanan, C. L.; Connaris, H.; Danson, M. J.; Reeve, C. D.; Hough, D. W. An Extremely Thermostable Aldolase from Sulfolobus Solfataricus with Specificity for Non-Phosphorylated Substrates. *Biochem. J.* **1999**, *343*, 563–570.

(29) Daniel, R. M.; Danson, M. J. A New Understanding of How Temperature Affects the Catalytic Activity of Enzymes. *Trends Biochem. Sci.* **2010**, *35*, 584–591.

(30) Daniel, R. M.; Danson, M. J.; Eisenthal, R. The Temperature Optima of Enzymes: A New Perspective on an Old Phenomenon. *Trends Biochem. Sci.* **2001**, *26*, 223–225.

(31) Sizer, I. W. Temperature Activation and Inactivation of the Crystalline Catalase-Hydrogen Peroxide System. *J. Biol. Chem.* **1944**, *154*, 461–473.

(32) Wright, G. G.; Schomaker, V. Studies on the Denaturation of Antibody. III. Kinetic Aspects of the Inactivation of Diphtheria Antitoxin by Urea. *J. Am. Chem. Soc.* **1948**, *70*, 356–364.

(33) Daniel, R. M.; Danson, M. J.; Eisenthal, R.; Lee, C. K.; Peterson, M. E. The Effect of Temperature on Enzyme Activity: New Insights and Their Implications. *Extremophiles* **2008**, *12*, 51–59.

(34) Peterson, M. E.; Eisenthal, R.; Danson, M. J.; Spence, A.; Daniel, R. M. A New Intrinsic Thermal Parameter for Enzymes Reveals True Temperature Optima. *J. Biol. Chem.* **2004**, *279*, 20717–20722.

(35) Eisenthal, R.; Peterson, M. E.; Daniel, R. M.; Danson, M. J. The Thermal Behaviour of Enzyme Activity: Implications for Biotechnology. *Trends Biotechnol.* **2006**, *24*, 289–292.

(36) Agmon, N.; Hopfield, J. J. CO Binding to Heme Proteins: A Model for Barrier Height Distributions and Slow Conformational Changes. *J. Chem. Phys.* **1983**, *79*, 2042–2053.

(37) Prabhu, N. V.; Sharp, K. A. Heat Capacity in Proteins. *Annu. Rev. Phys. Chem.* **2005**, *56*, 521–548.

(38) Chouard, T. Structural Biology: Breaking the Protein Rules. *Nature* **2011**, *471*, 151–153.

(39) Mills, J. L.; Liu, G.; Skerra, A.; Szyperski, T. NMR Structure and Dynamics of the Engineered Fluorescein-Binding Lipocalin FluA Reveal Rigidification of β-Barrel and Variable Loops upon Enthalpy-Driven Ligand Binding. *Biochemistry* **2009**, *48*, 7411–7419.

(40) Grutsch, S.; Fuchs, J. E.; Freier, R.; Kofler, S.; Bibi, M.; Asam, C.; Wallner, M.; Ferreira, F.; Brandstetter, H.; Liedl, K. R.; Tollinger, M. Ligand Binding Modulates the Structural Dynamics and Compactness of the Major Birch Pollen Allergen. *Biophys. J.* **2014**, *107*, 2972–2981.

(41) Hanson, W. M.; Domek, G. J.; Horvath, M. P.; Goldenberg, D. P. Rigidification of a Flexible Protease Inhibitor Variant upon Binding to Trypsin. *J. Mol. Biol.* **2007**, *366*, 230–243.

(42) Arcus, V. L.; Prentice, E. J.; Hobbs, J. K.; Mulholland, A. J.; van der Kamp, M. W.; Pudney, C. R.; Parker, E. J.; Schipper, L. A. On the Temperature Dependence of Enzyme-Catalyzed Rates. *Biochemistry* **2016**, *55*, 1681–1688.

(43) Seewald, M. J.; Pichumani, K.; Stowell, C.; Tibbals, B. V.; Regan, L.; Stone, M. J. The Role of Backbone Conformational Heat Capacity in Protein Stability: Temperature Dependent Dynamics of the B1 Domain of *Streptococcal* Protein G. *Protein Sci.* **2000**, *9*, 1177–1193.

(44) Gómez, J.; Hilser, V. J.; Xie, D.; Freire, E. The Heat Capacity of Proteins. *Proteins Struct. Funct. Genet.* **1995**, *22*, 404–412.

(45) Arcus, V. L.; Pudney, C. R. Change in Heat Capacity Accurately Predicts Vibrational Coupling in Enzyme Catalyzed Reactions. *FEBS Lett.* **2015**, *589*, 2200–2206.

(46) van der Kamp, M. W.; Prentice, E. J.; Kraakman, K. L.; Connolly, M.; Mulholland, A. J.; Arcus, V. L. Dynamical Origins of Heat Capacity Changes in Enzyme-Catalysed Reactions. *Nat. Commun.* **2018**, *9*, 1177.

(47) Bingham, R. J.; Findlay, J. B. C.; Hsieh, S. Y.; Kalverda, A. P.; Kjellberg, A.; Perazzolo, C.; Phillips, S. E. V.; Seshadri, K.; Trinh, C. H.; Turnbull, W. B.; Bodenhausen, G.; Homans, S. W. Thermodynamics of Binding of 2-Methoxy-3-Isopropylpyrazine and 2-Methoxy-3-Isobutylpyrazine to the Major Urinary Protein. *J. Am. Chem. Soc.* **2004**, *126*, 1675–1681.

(48) MacRaild, C. A.; Daranas, A. H.; Bronowska, A.; Homans, S. W. Global Changes in Local

Protein Dynamics Reduce the Entropic Cost of Carbohydrate Binding in the Arabinose-Binding Protein. *J. Mol. Biol.* **2007**, *368*, 822–832.

(49) Kazemi, M.; Himo, F.; Åqvist, J. Enzyme Catalysis by Entropy without Circe Effect. *Proc. Natl. Acad. Sci.* **2016**, *113*, 2406–2411.

(50) Åqvist, J.; Kazemi, M.; Isaksen, G. V.; Brandsdal, B. O. Entropy and Enzyme Catalysis. *Acc. Chem. Res.* **2017**, *50*, 199–207.

(51) Wolfenden, R. Primordial Chemistry and Enzyme Evolution in a Hot Environment. *Cell. Mol. Life Sci.* **2014**, *71*, 2909–2915.

(52) Siddiqui, K. S.; Cavicchioli, R. Cold-Adapted Enzymes. *Annu. Rev. Biochem.* **2006**, *75*, 403–433.

(53) Cornish-Bowden, A. Enthalpy—entropy Compensation: A Phantom Phenomenon. *J. Biosci.* **2002**, *27*, 121–126.

(54) Göbl, C.; Tjandra, N.; Göbl, C.; Tjandra, N. Application of Solution NMR Spectroscopy to Study Protein Dynamics. *Entropy* **2012**, *14*, 581–598.

(55) Chao, F.-A.; Byrd, R. A. Protein Dynamics Revealed by NMR Relaxation Methods. *Emerg. Top. Life Sci.* **2018**, *2*, 93–105.

(56) Lindorff-Larsen, K.; Maragakis, P.; Piana, S.; Shaw, D. E. Picosecond to Millisecond Structural Dynamics in Human Ubiquitin. *J. Phys. Chem. B* **2016**, *120*, 8313–8320.

(57) Seo, M.-H.; Park, J.; Kim, E.; Hohng, S.; Kim, H.-S. Protein Conformational Dynamics Dictate the Binding Affinity for a Ligand. *Nat. Commun.* **2014**, *5*, 3724.

(58) Davulcu, O.; Skalicky, J. J.; Chapman, M. S. Rate-Limiting Domain and Loop Motions in Arginine Kinase. *Biochemistry* **2011**, *50*, 4011–4018.

(59) Watt, E. D.; Shimada, H.; Kovrigin, E. L.; Loria, J. P. The Mechanism of Rate-Limiting Motions in Enzyme Function. *Proc. Natl. Acad. Sci.* **2007**, *104*, 11981–11986.

(60) Pisliakov, A. V.; Cao, J.; Kamerlin, S. C. L.; Warshel, A. Enzyme Millisecond Conformational Dynamics Do Not Catalyze the Chemical Step. *Proc. Natl. Acad. Sci. U. S. A.* **2009**, *106*, 17359–17364.

(61) Hay, S.; Scrutton, N. S. Good Vibrations in Enzyme-Catalysed Reactions. *Nat. Chem.* **2012**, *4*, 161–168.

(62) Hay, S.; Scrutton, N. S. Incorporation of Hydrostatic Pressure into Models of Hydrogen Tunneling Highlights a Role for Pressure-Modulated Promoting Vibrations. *Biochemistry* **2008**, *47*, 9880–9887.

(63) Knapp, M. J.; Rickert, K.; Klinman, J. P. Temperature-Dependent Isotope Effects in Soybean Lipoxygenase-1: Correlating Hydrogen Tunneling with Protein Dynamics. *J. Am. Chem. Soc.* **2002**, *124*, 3865–3874.

(64) Basner, J. E.; Schwartz, S. D. Donor−Acceptor Distance and Protein Promoting Vibration Coupling to Hydride Transfer: A Possible Mechanism for Kinetic Control in Isozymes of Human Lactate Dehydrogenase. *J. Phys. Chem. B* **2004**, *108*, 444–451.

(65) Caratzoulas, S.; Mincer, J. S.; Schwartz, S. D. Identification of a Protein-Promoting Vibration in the Reaction Catalyzed by Horse Liver Alcohol Dehydrogenase. *J. Am. Chem.*

Soc. **2002**, *124*, 3270–3276.

(66) Roca, M.; Moliner, V.; Tuñón, I.; Hynes, J. T. Coupling between Protein and Reaction Dynamics in Enzymatic Processes: Application of Grote-Hynes Theory to Catechol O-Methyltransferase. *J. Am. Chem. Soc.* **2006**, *128*, 6186–6193.

(67) Kamerlin, S. C. L.; Mavri, J.; Warshel, A. Examining the Case for the Effect of Barrier Compression on Tunneling, Vibrationally Enhanced Catalysis, Catalytic Entropy and Related Issues. *FEBS Lett.* **2010**, *584*, 2759–2766.

(68) Warshel, A.; Bora, R. P. Perspective: Defining and Quantifying the Role of Dynamics in Enzyme Catalysis. *J. Chem. Phys.* **2016**, *144*, 180901.

(69) Tuñón, I.; Laage, D.; Hynes, J. T. Are There Dynamical Effects in Enzyme Catalysis? Some Thoughts Concerning the Enzymatic Chemical Step. *Arch. Biochem. Biophys.* **2015**, *582*, 42–55.

(70) Milburn, C. C.; Lamble, H. J.; Theodossis, A.; Bull, S. D.; Hough, D. W.; Danson, M. J.; Taylor, G. L. The Structural Basis of Substrate Promiscuity in Glucose Dehydrogenase from the Hyperthermophilic Archaeon Sulfolobus Solfataricus. *J. Biol. Chem.* **2006**, *281*, 14796–14804.

(71) Takagi, Y.; Taira, K. Temperature-Dependent Change in the Rate-Determining Step in a Reaction Catalyzed by a Hammerhead Ribozyme. *FEBS Lett.* **1995**, *361*, 273–276.

(72) Weber, J. P.; Fink, A. L. Temperature-Dependent Change in the Rate-Limiting Step of Beta-Glucosidase Catalysis. *J. Biol. Chem.* **1980**, *255*, 9030–9032.

(73) Allen, W. J.; Bevan, D. R. Steered Molecular Dynamics Simulations Reveal Important Mechanisms in Reversible Monoamine Oxidase B Inhibition. *Biochemistry* **2011**, *50*, 6441–6454.

(74) Librizzi, F.; Carrotta, R.; Peters, J.; Cupane, A. The Effects of Pressure on the Energy Landscape of Proteins. *Sci. Rep.* **2018**, *8*, 2037.

(75) Pudney, C. R.; Hay, S.; Levy, C.; Pang, J.; Sutcliffe, M. J.; Leys, D.; Scrutton, N. S. Evidence to Support the Hypothesis That Promoting Vibrations Enhance the Rate of an Enzyme Catalyzed H-Tunneling Reaction. *J. Am. Chem. Soc.* **2009**, *131*, 17072–17073.

(76) Masson, P.; Balny, C. Linear and Non-Linear Pressure Dependence of Enzyme Catalytic Parameters. *Biochimica et Biophysica Acta - General Subjects*. Elsevier August 5, 2005, pp 440–450.

(77) Northrop, D. B. Effects of High Pressure on Enzymatic Activity. *Biochim. Biophys. Acta - Protein Struct. Mol. Enzymol.* **2002**, *1595*, 71–79.

(78) Suzuki, K. Studies on the Kinetics of Protein Denaturation under High Pressure. *J. Chem. Inf. Model.* **1960**, *29*, 91–98.

(79) Rauscher, A.; Derényi, I.; Gráf, L.; Málnási-Csizmadia, A. Internal Friction in Enzyme Reactions. *IUBMB Life* **2013**, *65*, 35–42.

(80) Ansari, A.; Jones, C. M.; Henry, E. R.; Hofrichter, J.; Eaton, W. A. The Role of Solvent Viscosity in the Dynamics of Protein Conformational Changes. *Science* **1992**, *256*, 1796–1798.

(81) Frauenfelder, H.; Chen, G.; Berendzen, J.; Fenimore, P. W.; Jansson, H.; McMahon, B. H.; Stroe, I. R.; Swenson, J.; Young, R. D. A Unified Model of Protein Dynamics. *Proc. Natl. Acad. Sci.* **2009**, *106*, 5129–5134.

(82) Beece, D.; Eisenstein, L.; Frauenfelder, H.; Good, D.; Marden, M. C.; Reinisch, L.; Reynolds, A. H.; Sorensen, L. B.; Yue, K. T. Solvent Viscosity and Protein Dynamics. *Biochemistry* **1980**, *19*, 5147–5157.

(83) Finkelstein, I. J.; Massari, A. M.; Fayer, M. D. Viscosity-Dependent Protein Dynamics. *Biophys. J.* **2007**, *92*, 3652–3662.

(84) Wensley, B. G.; Batey, S.; Bone, F. A. C.; Chan, Z. M.; Tumelty, N. R.; Steward, A.; Kwa, L. G.; Borgia, A.; Clarke, J. Experimental Evidence for a Frustrated Energy Landscape in a Three-Helix-Bundle Protein Family. *Nature* **2010**, *463*, 685–688.

(85) Priev, A.; Almagor, A.; Yedgar, S.; Gavish, B. Glycerol Decreases the Volume and Compressibility of Protein Interior. *Biochemistry* **1996**, *35*, 2061–2066.

(86) Gekko, K.; Timasheff, S. N. Mechanism of Protein Stabilization by Glycerol: Preferential Hydration in Glycerol-Water Mixtures. *Biochemistry* **1981**, *20*, 4667–4676.

(87) Born, M.; Oppenheimer, R. Zur Quantentheorie Der Molekeln. *Ann. Phys.* **1927**, *389*, 457–484.

(88) Thornton, E. R. Physical Organic Chemistry. *Annu. Rev. Phys. Chem.* **1966**, *17*, 349–372.

(89) Morse, P. M. Diatomic Molecules According to the Wave Mechanics. II. Vibrational Levels. *Phys. Rev.* **1929**, *34*, 57–64.

(90) Kohen, A.; Limbach, H.-H. *Isotope Effects in Chemistry and Biology*; CRC Press, 2006.

(91) Bell, R. P. *The Application of Tunnel Corrections in Chemical Kinetics*; Springer US: Boston, MA, 1980.

(92) Heisenberg, W. Über Den Anschaulichen Inhalt Der Quantentheoretischen Kinematik Und Mechanik. In *Original Scientific Papers Wissenschaftliche Originalarbeiten*; Springer Berlin Heidelberg: Berlin, Heidelberg, 1985; pp 478–504.

(93) de Broglie, L. The Reinterpretation of Wave Mechanics. *Found. Phys.* **1970**, *1*, 5–15.

(94) Caldin, E. F. Tunneling in Proton-Transfer Reactions in Solution. *Chem. Rev.* **1969**, *69*, 135–156.

(95) Marcus, R. A.; Sutin, N. Electron Transfers in Chemistry and Biology. *Biochim. Biophys. Acta - Rev. Bioenerg.* **1985**, *811*, 265–322.

(96) Salomon-Ferrer, R.; Case, D. A.; Walker, R. C. An Overview of the Amber Biomolecular Simulation Package. *Wiley Interdiscip. Rev. Comput. Mol. Sci.* **2013**, *3*, 198–210.

(97) Braun, E.; Gilmer, J.; Mayes, H.; Mobley, D.; Prasad, S.; Zuckerman, D.; Monroe, J. Best Practices for Foundations in Molecular Simulations [Article v1.0]. *Living J. Comput. Mol. Sci.* **2018**, *1*, 5957.

(98) Allen, M. Introduction to Molecular Dynamics Simulations. *Comput. soft matter from Synth. Polym. to proteins* **2004**, *23*, 1–28.

(99) Gelpi, J.; Hospital, A.; Goñi, R.; Orozco, M. Molecular Dynamics Simulations: Advances

and Applications. *Adv. Appl. Bioinforma. Chem.* **2015**, 37.

(100) Tieleman, D. P.; Kandt, C.; Ash, W. L. Setting up and Running Molecular Dynamics Simulations of Membrane Proteins. *Methods* **2007**, *41*, 475–488.

(101) David, C. C.; Jacobs, D. J. Principal Component Analysis: A Method for Determining the Essential Dynamics of Proteins. *Methods Mol. Biol.* **2014**, *1084*, 193–226.

(102) Chovancova, E.; Pavelka, A.; Benes, P.; Strnad, O.; Brezovsky, J.; Kozlikova, B.; Gora, A.; Sustr, V.; Klvana, M.; Medek, P.; Biedermannova, L.; Sochor, J.; Damborsky, J. CAVER 3.0: A Tool for the Analysis of Transport Pathways in Dynamic Protein Structures. *PLoS Comput. Biol.* **2012**, *8*, e1002708.

(103) Jacobs, D. J.; Rader, a. J.; Kuhn, L. a; Thorpe, M. F. Protein Flexibility Predictions Using Graph Theory. *Proteins Struct. Funct. Bioinforma.* **2001**, *44*, 150–165.

(104) Wells, S.; Menor, S.; Hespenheide, B.; Thorpe, M. F. Constrained Geometric Simulation of Diffusive Motion in Proteins. *Phys. Biol.* **2005**, *2*, S127–S136.

(105) Wells, S. A.; Crennell, S. J.; Danson, M. J. Structures of Mesophilic and Extremophilic Citrate Synthases Reveal Rigidity and Flexibility for Function. *Proteins Struct. Funct. Bioinforma.* **2014**, *82*, 2657–2670.

(106) Garcia-Viloca, M.; Gao, J.; Karplus, M.; Truhlar, D. G. How Enzymes Work: Analysis by Modern Rate Theory and Computer Simulations. *Science (80-.).* **2004**, *303*, 186–195.

(107) Kamerlin, S. C. L.; Warshel, A. At the Dawn of the 21st Century: Is Dynamics the Missing Link for Understanding Enzyme Catalysis. *Proteins Struct. Funct. Bioinforma.* **2010**, *78*, 1339–1375.

(108) Adamczyk, A. J.; Cao, J.; Kamerlin, S. C. L.; Warshel, A. Catalysis by Dihydrofolate Reductase and Other Enzymes Arises from Electrostatic Preorganization, Not Conformational Motions. *Proc. Natl. Acad. Sci. U. S. A.* **2011**, *108*, 14115–14120.

(109) Pudney, C. R.; Guerriero, A.; Baxter, N. J.; Johannissen, L. O.; Waltho, J. P.; Hay, S.; Scrutton, N. S. Fast Protein Motions Are Coupled to Enzyme H-Transfer Reactions. *J. Am. Chem. Soc.* **2013**, *135*, 2512–2517.

(110) Pudney, C. R.; Hay, S.; Sutcliffe, M. J.; Scrutton, N. S. α-Secondary Isotope Effects as Probes Of "tunneling-Ready" configurations in Enzymatic H-Tunneling: Insight from Environmentally Coupled Tunneling Models. *J. Am. Chem. Soc.* **2006**, *128*, 14053–14058.

(111) Ma, B.; Tsai, C. J.; Nussinov, R. A Systematic Study of the Vibrational Free Energies of Polypeptides in Folded and Random States. *Biophys. J.* **2000**, *79*, 2739–2753.

(112) Hay, S.; Sutcliffe, M. J.; Scrutton, N. S. Promoting Motions in Enzyme Catalysis Probed by Pressure Studies of Kinetic Isotope Effects. *Proc. Natl. Acad. Sci. U. S. A.* **2007**, *104*, 507–512.

(113) Hoeven, R.; Heyes, D. J.; Hay, S.; Scrutton, N. S. Does the Pressure Dependence of Kinetic Isotope Effects Report Usefully on Dynamics in Enzyme H-Transfer Reactions? *FEBS J.* **2015**, *282*, 3243–3255.

(114) Hu, S.; Cattin-Ortolá, J.; Munos, J. W.; Klinman, J. P. Hydrostatic Pressure Studies Distinguish Global from Local Protein Motions in C−H Activation by Soybean

Lipoxygenase-1. *Angew. Chemie - Int. Ed.* **2016**, *55*, 9361–9364.

(115) Sturtevant, J. M. Heat Capacity and Entropy Changes in Processes Involving Proteins. *Proc. Natl. Acad. Sci. U. S. A.* **1977**, *74*, 2236–2240.

(116) Kanehisa, M. I.; Ikegami, A. Structural Changes and Fluctuations of Proteins. *Biophys. Chem.* **1977**, *6*, 131–149.

(117) Hay, S.; Johannissen, L. O.; Hothi, P.; Sutcliffe, M. J.; Scrutton, N. S. Pressure Effects on Enzyme-Catalyzed Quantum Tunneling Events Arise from Protein-Specific Structural and Dynamic Changes. *J. Am. Chem. Soc.* **2012**, *134*, 9749–9754.

(118) Johannissen, L. O.; Scrutton, N. S.; Sutcliffe, M. J. How Does Pressure Affect Barrier Compression and Isotope Effects in an Enzymatic Hydrogen Tunneling Reaction? *Angew. Chemie - Int. Ed.* **2011**, *50*, 2129–2132.

(119) Good, N. E.; Winget, G. D.; Winter, W.; Connolly, T. N.; Izawa, S.; Sing, R. M. M. Hydrogen Ion Buffers for Bifological Research. *Biochemistry* **1966**, *5*, 467–477.

(120) Kitamura, Y.; Itoh, T. Reaction Volume of Protonic Ionization for Buffering Agents. Prediction of Pressure Dependence of pH and pOH. *J. Solution Chem.* **1987**, *16*, 715–725.

(121) Brandts, J. F. The Thermodynamics of Protein Denaturation. I. The Denaturation of Chymotrypsinogen. *J. Am. Chem. Soc.* **1964**, *86*, 4291–4301.

(122) Brandts, J. F.; Oliveira, R. J.; Westort, C. Thermodynamics of Protein Denaturation. Effect of Pressure on the Denaturation of Ribonuclease A. *Biochemistry* **1970**, *9*, 1038–1047.

(123) Hawley, S. A. Reversible Pressure-Temperature Denaturation. *Biochemistry* **1971**, *10*, 2436–2442.

(124) Dellarole, M.; Kobayashi, K.; Rouget, J. B.; Caro, J. A.; Roche, J.; Islam, M. M.; Garcia-Moreno E., B.; Kuroda, Y.; Royer, C. a. Probing the Physical Determinants of Thermal Expansion of Folded Proteins. *J. Phys. Chem. B* **2013**, *117*, 12742–12749.

(125) Lin, L.-N.; Brandts, J. F.; Brandts, J. M.; Plotnikov, V. Determination of the Volumetric Properties of Proteins and Other Solutes Using Pressure Perturbation Calorimetry. *Anal. Biochem.* **2002**, *302*, 144–160.

(126) Catici, D. A. M.; Amos, H. E.; Yang, Y.; van den Elsen, J. M. H.; Pudney, C. R. The Red Edge Excitation Shift Phenomenon Can Be Used to Unmask Protein Structural Ensembles: Implications for NEMO–ubiquitin Interactions. *FEBS J.* **2016**, 2272–2284.

(127) Chattopadhyay, A.; Haldar, S. Dynamic Insight into Protein Structure Utilizing Red Edge Excitation Shift. *Acc. Chem. Res.* **2014**, *47*, 12–19.

(128) Cushing, S.; Li, M.; Huang, F.; Wu, N. Origin of Strong Excitation Wavelength Dependent Fluorescence of Graphene Oxide. *ACS Nano* **2014**, *8*, 1002–1013.

(129) Khan, S.; Gupta, A.; Verma, N. C.; Nandi, C. K. Time-Resolved Emission Reveals Ensemble of Emissive States as the Origin of Multicolor Fluorescence in Carbon Dots. *Nano Lett.* **2015**, *15*, 8300–8305.

(130) Karshikoff, A.; Nilsson, L.; Ladenstein, R. Rigidity versus Flexibility: The Dilemma of Understanding Protein Thermal Stability. *FEBS J.* **2015**, *282*, 3899–3917.

(131) David, C. C.; Jacobs, D. J. Characterizing Protein Motions from Structure. *J. Mol. Graph.*

Model. **2011**, *31*, 41–56.

(132) Suhre, K.; Sanejouand, Y. H. ElNémo: A Normal Mode Web Server for Protein Movement Analysis and the Generation of Templates for Molecular Replacement. *Nucleic Acids Res.* **2004**, *32*, 610–614.

(133) Wells, S. A.; Van Der Kamp, M. W.; McGeagh, J. D.; Mulholland, A. J. Structure and Function in Homodimeric Enzymes: Simulations of Cooperative and Independent Functional Motions. *PLoS One* **2015**, *10*, 1–21.

(134) Römer, R. A.; Wells, S. A.; Emilio Jimenez-Roldan, J.; Bhattacharyya, M.; Vishweshwara, S.; Freedman, R. B. The Flexibility and Dynamics of Protein Disulfide Isomerase. *Proteins Struct. Funct. Bioinforma.* **2016**, *84*, 1776–1785.

(135) Erskine, P. T.; Fokas, A.; Muriithi, C.; Rehman, H.; Yates, L. A.; Bowyer, A.; Findlow, I. S.; Hagan, R.; Werner, J. M.; Miles, A. J.; Wallace, B. A.; Wells, S. A.; Wood, S. P.; Cooper, J. B. X-Ray, Spectroscopic and Normal-Mode Dynamics of Calexcitin: Structure-Function Studies of a Neuronal Calcium-Signalling Protein. *Acta Crystallogr. Sect. D Biol. Crystallogr.* **2015**, *71*, 615–631.

(136) Mincer, J. S.; Schwartz, S. D. Evolutionary Motif. **2003**, *2*, 437–439.

(137) Singh, P.; Francis, K.; Kohen, A. Network of Remote and Local Protein Dynamics in Dihydrofolate Reductase Catalysis. *ACS Catal.* **2015**, *5*, 3067–3073.

(138) Heyes, D. J.; Sakuma, M.; Scrutton, N. S. Solvent-Slaved Protein Motions Accompany Proton but Not Hydride Tunneling in Light-Activated Protochlorophyllide Oxidoreductase. *Angew. Chemie - Int. Ed.* **2009**, *48*, 3850–3853.

(139) Davidson, V. L. Protein Control of True, Gated, and Coupled Electron Transfer Reactions. *Accounts of Chemical Research*. 2008, pp 730–738.

(140) Ivković-Jensen, M. M.; Kostić, N. M. Effects of Viscosity and Temperature on the Kinetics of the Electron- Transfer Reaction between the Triplet State of Zinc Cytochrome c and Cupriplastocyanin. *Biochemistry* **1997**, *36*, 8135–8144.

(141) Liu, L.; Hong, J.; Ogawa, M. Y. Gated Electron Transfer as a Probe of the Configurational Dynamics of Peptide-Protein Complexes. *J. Am. Chem. Soc.* **2004**, *126*, 50–51.

(142) Qin, L. Photoinduced Electron Transfer from the Triplet State of Zinc Cytochrome. *Biochemistry* **1994**, *33*, 12592–12599.

(143) Cheng, N. Formula for the Viscosity of a Glycerol- Water Mixture. *Ind. Eng. Chem. Res.* **2008**, *47*, 3285–3288.

(144) Luk, L.; Ruiz-Pernía, J.; Adesina, A. Chemical Ligation and Isotope Labeling to Locate Dynamic Effects during Catalysis by Dihydrofolate Reductase. *Angew. Chemie* **2015**, *127*, 9144–9148.

(145) Wang, Z.; Chang, E. P.; Schramm, V. L. Triple Isotope Effects Support Concerted Hydride and Proton Transfer and Promoting Vibrations in Human Heart Lactate Dehydrogenase. *J. Am. Chem. Soc.* **2016**, *138*, 15004–15010.

(146) Nashine, V. C.; Hammes-Schiffer, S.; Benkovic, S. J. Coupled Motions in Enzyme Catalysis. *Curr. Opin. Chem. Biol.* **2010**, *14*, 644–651.

(147) Ben-David, M.; Sussman, J. L.; Maxwell, C. I.; Szeler, K.; Kamerlin, S. C. L.; Tawfik, D. S. Catalytic Stimulation by Restrained Active-Site Floppiness - The Case of High Density Lipoprotein-Bound Serum Paraoxonase-1. *J. Mol. Biol.* **2015**, *427*, 1359–1374.

(148) Jiménez Roldán, J. E.; Freedman, R. B.; Roemer, R. a.; Wells, S. a. Rapid Simulation of Protein Motion : Merging Flexibility, Rigidity and Normal Mode Analyses. *Phys. Biol.* **2012**, *9*, 16008.

(149) Cook, P. F. Mechanism from Isotope Effects. *Isotopes Environ. Health Stud.* **1998**, *34*, 3–17.

(150) Schwartz, S. D.; Schramm, V. L. Enzymatic Transition States and Dynamic Motion in Barrier Crossing. *Nat. Chem. Biol.* **2009**, *5*, 551–558.

(151) Allemann, R. K.; Evans, R. M.; Tey, L.; Maglia, G.; Pang, J.; Rodriguez, R.; Shrimpton, P. J.; Swanwick, R. S. Protein Motions during Catalysis by Dihydrofolate Reductases. *Philos. Trans. R. Soc. London B Biol. Sci.* **2006**, *361*, 1317–1321.

(152) Luk, L. Y. P.; Javier Ruiz-Pernia, J.; Dawson, W. M.; Roca, M.; Loveridge, E. J.; Glowacki, D. R.; Harvey, J. N.; Mulholland, A. J.; Tunon, I.; Moliner, V.; Allemann, R. K. Unraveling the Role of Protein Dynamics in Dihydrofolate Reductase Catalysis. *Proc. Natl. Acad. Sci.* **2013**, *110*, 16344–16349.

(153) Knapp, M. J.; Klinman, J. P. Environmentally Coupled Hydrogen Tunneling. *Eur. J. Biochem.* **2002**, *269*, 3113–3121.

(154) Roy, S.; Schopf, P.; Warshel, A. Origin of the Non-Arrhenius Behavior of the Rates of Enzymatic Reactions. *J. Phys. Chem. B* **2017**, *121*, 6520–6526.

(155) Francis, K.; Sapienza, P. J.; Lee, A. L.; Kohen, A. The Effect of Protein Mass Modulation on Human Dihydrofolate Reductase. *Biochemistry* **2016**, *55*, 1100–1106.

(156) Wang, Z.; Singh, P.; Czekster, C. M.; Kohen, A.; Schramm, V. L. Protein Mass-Modulated Effects in the Catalytic Mechanism of Dihydrofolate Reductase: Beyond Promoting Vibrations. *J. Am. Chem. Soc.* **2014**, *136*, 8333–8341.

(157) Kipp, D. R.; Silva, R. G.; Schramm, V. L. Mass-Dependent Bond Vibrational Dynamics Influence Catalysis by HIV-1 Protease. *J. Am. Chem. Soc.* **2011**, *133*, 19358–19361.

(158) Soriano, A.; Silla, E.; Tuñón, I.; Martí, S.; Moliner, V.; Bertrán, J. Electrostatic Effects in Enzyme Catalysis: A Quantum Mechanics/molecular Mechanics Study of the Nucleophilic Substitution Reaction in Haloalkane Dehalogenase. *Theor. Chem. Acc.* **2004**, *112*, 327–334.

(159) García-Meseguer, R.; Martí, S.; Ruiz-Pernía, J. J.; Moliner, V.; Tuñón, I. Studying the Role of Protein Dynamics in an SN2 Enzyme Reaction Using Free-Energy Surfaces and Solvent Coordinates. *Nat. Chem.* **2013**, *5*, 566–571.

(160) Olsson, M. H. M.; Parson, W. W.; Warshel, A. Dynamical Contributions to Enzyme Catalysis: Critical Tests of A Popular Hypothesis. *Chem. Rev.* **2006**, *106*, 1737–1756.

(161) Schramm, V. L.; Schwartz, S. D. Promoting Vibrations and the Function of Enzymes. Emerging Theoretical and Experimental Convergence. *Biochemistry* **2018**, *57*, 3299–3308.

(162) Jones, H. B. L.; Wells, S. A.; Prentice, E. J.; Kwok, A.; Liang, L. L.; Arcus, V. L.; Pudney,

C. R. A Complete Thermodynamic Analysis of Enzyme Turnover Links the Free Energy Landscape to Enzyme Catalysis. *FEBS J.* **2017**, *284*, 2829–2842.

(163) Bigeleisen, J. Effect of Isotopic Substitution on the Entropy, Enthalpy, and Heat Capacity of Ideal Gases. I. Systems in Thermal Equilibrium. II. Chemically Reacting Systems. *J. Chem. Phys.* **1953**, *21*, 1333–1339.

(164) Tjahjono, M.; Garland, M. Deuterium Isotope Effect on Molar Heat Capacities and Apparent Molar Heat Capacities in Dilute Aqueous Solutions: A Multi-Channel Heat-Flow Microcalorimeter Study. *J. Chem. Thermodyn.* **2008**, *40*, 1600–1606.

(165) Ibberson, R. M.; David, W. I. F.; Yamamuro, 0; Miyoshi, Y.; Matsuo, T.; Suga, H. Calorimetric, Dielectric, and Neutron Diffraction Studies on Phase Transitions in Ordinary and Deuterated Acetone Crystals'. *J. Phys. Chem* **1995**, *99*, 14167–14173.

(166) Longbotham, J. E.; Hardman, S. J. O.; Görlich, S.; Scrutton, N. S.; Hay, S. Untangling Heavy Protein and Cofactor Isotope Effects on Enzyme-Catalyzed Hydride Transfer. *J. Am. Chem. Soc.* **2016**, *138*, 13693–13699.

(167) Lamble, H.; Heyer, N.; Bull, S.; Hough, D. Metabolic Pathway Promiscuity in the Archaeon Sulfolobus Solfataricus Revealed by Studies on Glucose Dehydrogenase and 2-Keto-3-Deoxygluconate Aldolase. *J. Biol.* **2003**, *278*, 34066–34072.

(168) Blomberg, M. R. A.; Borowski, T.; Himo, F.; Liao, R.-Z.; Siegbahn, P. E. M. Quantum Chemical Studies of Mechanisms for Metalloenzymes. *Chem. Rev.* **2014**, *114*, 3601–3658.

(169) Giardina, P.; De Biasi, M.-G.; De Rosa, M.; Gambacortat, A.; Buonocore, V. Glucose Dehydrogenase from the Thermoacidophilic Archaebacterium Sulfolobus Solfataricus. *Biochem. J* **1986**, *239*, 517–522.

(170) Pudney, C.; Johannissen, L.; Sutcliffe, M. Direct Analysis of Donor− Acceptor Distance and Relationship to Isotope Effects and the Force Constant for Barrier Compression in Enzymatic H-Tunneling Reactions. *J. Am. Chem. Soc.* **2010**, *132*, 11329–11335.

(171) Moser, C. C.; Dutton, P. L. Engineering Protein Structure for Electron Transfer Function in Photosynthetic Reaction Centers. *Biochim. Biophys. Acta - Bioenerg.* **1992**, *1*, 171–176.

(172) Huskey, W. P.; Schowen, R. L. Reaction-Coordinate Tunneling in Hydride-Transfer Reactions. *J. Am. Chem. Soc.* **1983**, *105*, 5704–5706.

(173) Hay, S.; Pudney, C. R.; Sutcliffe, M. J.; Scrutton, N. S. Probing Active Site Geometry Using High Pressure and Secondary Isotope Effects in an Enzyme-Catalysed "deep" H-Tunnelling Reaction. *J. Phys. Org. Chem.* **2010**, *23*, 696–701.

(174) Antoniou, D.; Ge, X.; Schramm, V. L.; Schwartz, S. D. Mass Modulation of Protein Dynamics Associated with Barrier Crossing in Purine Nucleoside Phosphorylase. *J. Phys. Chem. Lett.* **2012**, *3*, 3538–3544.

(175) Ranasinghe, C.; Guo, Q.; Sapienza, P. J.; Lee, A. L.; Quinn, D. M.; Cheatum, C. M.; Kohen, A. Protein Mass Effects on Formate Dehydrogenase. *J. Am. Chem. Soc.* **2017**, *139*, 17405–17413.

(176) Jordi, V.; Warshel, A. Energetics and Dynamics of Enzymatic Reactions. *J. Phys. Chem. B* **2001**, *105*, 7887–7907.

(177) Boekelheide, N.; Salomón-Ferrer, R.; Miller, T. F. Dynamics and Dissipation in Enzyme Catalysis. *Proc. Natl. Acad. Sci. U. S. A.* **2011**, *108*, 16159–16163.

(178) Loveridge, E. J.; Behiry, E. M.; Guo, J.; Allemann, R. K. Evidence That a "dynamic Knockout" in Escherichia Coli Dihydrofolate Reductase Does Not Affect the Chemical Step of Catalysis. *Nat. Chem.* **2012**, *4*, 292–297.

(179) Gasteiger, E.; Hoogland, C.; Gattiker, A.; Duvaud, S.; Wilkins, M. R.; Appel, R. D.; Bairoch, A. *Protein Identification and Analysis Tools on the ExPASy Server*; Humana press, 2005.

(180) Mikkelsen, K.; Siguri, A.; Nielsen, O. Acidity Measurements Jyith the Glass Electrode Is H,o-D,o Mixtures. *J. Phys. Chem.* **1960**, *64*, 632–637.

(181) Krivov, G. G.; Shapovalov, M. V.; Dunbrack, R. L. Improved Prediction of Protein Side-Chain Conformations with SCWRL4. *Proteins Struct. Funct. Bioinforma.* **2009**, *77*, 778–795.

(182) Webb, B.; Sali, A.; Webb, B.; Sali, A. Comparative Protein Structure Modeling Using MODELLER. In *Protein Structure Prediction*; John Wiley & Sons, Inc.: Hoboken, NJ, USA, 2014; pp 1–15.

(183) Case, D. A.; Cerutti, D. S.; Cheatham, III, T. E.; Darden, T. A.; Duke, R. E.; Giese, T. J.; Gohlke, H.; Goetz, A. W.; Greene, D.; Homeyer, N,; Izadi, S.; Kovalenko, A.; Lee, T. S.; LeGrand, S.; Li, P.; Lin, C.; Liu, J.; Luchko, T.; Luo, R.; Mermelstein, P. A. AMBER 2016. University of Calafornia: San Francisco 2017.

(184) Maier, J. A.; Martinez, C.; Kasavajhala, K.; Wickstrom, L.; Hauser, K. E.; Simmerling, C. ff14SB: Improving the Accuracy of Protein Side Chain and Backbone Parameters from ff99SB. *J. Chem. Theory Comput.* **2015**, *11*, 3696–3713.

(185) Kirschner, K. N.; Yongye, A. B.; Tschampel, S. M.; González-Outeiriño, J.; Daniels, C. R.; Foley, B. L.; Woods, R. J. GLYCAM06: A Generalizable Biomolecular Force Field. Carbohydrates. *J. Comput. Chem.* **2008**, *29*, 622–655.

(186) Holmberg, N.; Ryde, U.; Bülow, L. Redesign of the Coenzyme Specificity in L-Lactate Dehydrogenase from Bacillus Stearothermophilus Using Site-Directed Mutagenesis and Media Engineering. *Protein Eng.* **1999**, *12*, 851–856.

(187) Peters, M. B.; Yang, Y.; Wang, B.; Füsti-Molnár, L.; Weaver, M. N.; Merz, K. M. Structural Survey of Zinc-Containing Proteins and Development of the Zinc AMBER Force Field (ZAFF). *J. Chem. Theory Comput.* **2010**, *6*, 2935–2947.

(188) Frisch, M. J.; Trucks, G. W.; Schlegel, H. B.; Scuseria, G. E.; Robb, M. A.; Cheeseman, J. R.; Scalmani, G.; Barone, V.; Petersson, G. A.; Nakatsuji, H.; Li, X.; Caricato, M.; Marenich, A. V.; Bloino, J.; Janesko, B. G.; Gomperts, R.; Mennucci, B.; Hratch, D. J. Gaussian 16 Revision 16.A.03. 2016.

(189) Zhao, Y.; Truhlar, D. G. The M06 Suite of Density Functionals for Main Group Thermochemistry, Thermochemical Kinetics, Noncovalent Interactions, Excited States, and Transition Elements: Two New Functionals and Systematic Testing of Four M06-Class Functionals and 12 Other Functionals. *Theor. Chem. Acc.* **2008**, *120*, 215–241.

(190) Marenich, A. V.; Cramer, C. J.; Truhlar, D. G. Universal Solvation Model Based on Solute Electron Density and on a Continuum Model of the Solvent Defined by the Bulk Dielectric Constant and Atomic Surface Tensions. *J. Phys. Chem. B* **2009**, *113*, 6378–6396.

(191) Alecu, I. M.; Zheng, J.; Zhao, Y.; Truhlar, D. G. Computational Thermochemistry: Scale Factor Databases and Scale Factors for Vibrational Frequencies Obtained from Electronic Model Chemistries. *J. Chem. Theory Comput.* **2010**, *6*, 2872–2887.

(192) Wigner, E. Crossing of Potential Thresholds in Chemical Reactions. *Zeitschrift für Phys. Chemie* **1932**, *19*, 203–216.

(193) Eswar, N.; Webb, B.; Marti-Renom, M. A.; Madhusudhan, M. S.; Eramian, D.; Shen, M.; Pieper, U.; Sali, A. Comparative Protein Structure Modeling Using Modeller. In *Current Protocols in Bioinformatics*; John Wiley & Sons, Inc.: Hoboken, NJ, USA, 2006; Vol. 24, p 5.6.1-5.6.30.

(194) Søndergaard, C. R.; Olsson, M. H. M.; Rostkowski, M.; Jensen, J. H. Improved Treatment of Ligands and Coupling Effects in Empirical Calculation and Rationalization of P K a Values. *J. Chem. Theory Comput.* **2011**, *7*, 2284–2295.

(195) Binda, C.; Newton-Vinson, P.; Hubálek, F.; Edmondson, D. E.; Mattevi, A. Structure of Human Monoamine Oxidase B, a Drug Target for the Treatment of Neurological Disorders. *Nat. Struct. Biol.* **2002**, *9*, 22–26.

(196) Schnaitman, C.; Erwin, V. G.; Greenawalt, J. W. The Submitochondrial Localization of Monoamine Oxidase. An Enzymatic Marker for the Outer Membrane of Rat Liver Mitochondria. *J. Cell Biol.* **1967**, *32*, 719–735.

(197) Knoll, J.; Ecseri, Z.; Kelemen, K.; Nievel, J.; Knoll, B. Phenylisopropylmethylpropinylamine (E-250), a New Spectrum Psychic Energizer. *Arch. Int. Pharmacodyn. Ther.* **1965**, *155*, 154–164.

(198) Riederer, P.; Laux, G. MAO-Inhibitors in Parkinson's Disease. *Exp. Neurobiol.* **2011**, *20*, 1–17.

(199) Jonsson, T.; Edmondson, D. E.; Klinman, J. P. Hydrogen Tunneling in the Flavoenzyme Monoamine Oxidase B. *Biochemistry* **1994**, *33*, 14871–14878.

(200) Nagel, Z. D.; Klinman, J. P. Tunneling and Dynamics in Enzymatic Hydride Transfer. *Chem. Rev.* **2006**, *106*, 3095–3118.

(201) MacMillar, S.; Edmondson, D. E.; Matsson, O. Nitrogen Kinetic Isotope Effects for the Monoamine Oxidase B-Catalyzed Oxidation of Benzylamine and (1,1- $^{2}H_{2}$)Benzylamine: Nitrogen Rehybridization and CH Bond Cleavage Are Not Concerted. *J. Am. Chem. Soc.* **2011**, *133*, 12319–12321.

(202) Silverman, R. B. Radical Ideas about Monoamine Oxidase. *Acc. Chem. Res.* **1995**, *28*, 335–342.

(203) Akyüz, M. A.; Erdem, S. S. Computational Modeling of the Direct Hydride Transfer Mechanism for the MAO Catalyzed Oxidation of Phenethylamine and Benzylamine: ONIOM (QM/QM) Calculations. *J. Neural Transm.* **2013**, *120*, 937–945.

(204) Kurtz, K. A.; Rishavy, M. A.; Cleland, W. W.; Fitzpatrick, P. F. Nitrogen Isotope Effects as Probes of the Mechanism of D-Amino Acid Oxidase. *J. Am. Chem. Soc.* **2000**, *122*, 12896–12897.

(205) Fitzpatrick, P. F. Oxidation of Amines by Flavoproteins. *Arch. Biochem. Biophys.* **2010**, *493*, 13–25.

(206) Vianello, R.; Repič, M.; Mavri, J. How Are Biogenic Amines Metabolized by Monoamine Oxidases? *European J. Org. Chem.* **2012**, *2012*, 7057–7065.

(207) Walker, M. C.; Edmondson, D. E. Structure-Activity Relationships in the Oxidation of Benzylamine Analogs by Bovine Liver Mitochondrial Monoamine Oxidase B. *Biochemistry* **1994**, *33*, 7088–7098.

(208) Abad, E.; Zenn, R. K.; Kästner, J. Reaction Mechanism of Monoamine Oxidase from QM/MM Calculations. *J. Phys. Chem. B* **2013**, *117*, 14238–14246.

(209) Murray, A. T.; Dowley, M. J. H.; Pradaux-Caggiano, F.; Baldansuren, A.; Fielding, A. J.; Tuna, F.; Hendon, C. H.; Walsh, A.; Lloyd-Jones, G. C.; John, M. P.; Carbery, D. R. Catalytic Amine Oxidation under Ambient Aerobic Conditions: Mimicry of Monoamine Oxidase B. *Angew. Chemie - Int. Ed.* **2015**, *54*, 8997–9000.

(210) Rigby, S. E. J.; Hynson, R. M. G.; Ramsay, R. R.; Munro, A. W.; Scrutton, N. S. A Stable Tyrosyl Radical in Monoamine Oxidase A. *J. Biol. Chem.* **2005**, *280*, 4627–4631.

(211) Dunn, R. V.; Munro, A. W.; Turner, N. J.; Rigby, S. E. J.; Scrutton, N. S. Tyrosyl Radical Formation and Propagation in Flavin Dependent Monoamine Oxidases. *ChemBioChem* **2010**, *11*, 1228–1231.

(212) Newton-Vinson, P.; Hubalek, F.; Edmondson, D. E. High-Level Expression of Human Liver Monoamine Oxidase B in Pichia Pastoris. *Protein Expr. Purif.* **2000**, *20*, 334–345.

(213) Yue, K. T.; Bhattacharyya, A. K.; Zhelyaskov, V. R.; Edmondson, D. E. Resonance Raman Spectroscopic Evidence for an Anionic Flavin Semiquinone in Bovine Liver Monoamine Oxidase. *Arch. Biochem. Biophys.* **1993**, *300*, 178–185.

(214) DeRose, V. J.; Woo, J. C. G.; Hawe, W. P.; Hoffman, B. M.; Silverman, R. B.; Yelekci, K. Observation of a Flavin Semiquinone in the Resting State of Monoamine Oxidase B by Electron Paramagnetic Resonance and Electron Nuclear Double Resonance Spectroscopy. *Biochemistry* **1996**, *35*, 11085–11091.

(215) Is, Y. S.; Durdagi, S.; Aksoydan, B.; Yurtsever, M. Proposing Novel MAO-B Hit Inhibitors Using Multidimensional Molecular Modeling Approaches and Application of Binary QSAR Models for Prediction of Their Therapeutic Activity, Pharmacokinetic and Toxicity Properties. *ACS Chem. Neurosci.* **2018**, *9*, 1768–1782.

(216) Braun, G. H.; M Jorge, D. M.; Ramos, H. P.; Alves, R. M.; da Silva, V. B.; Giuliatti, S.; Vilela Sampaio, S.; Taft, C. A.; T P Silva, C. H. Molecular Dynamics, Flexible Docking, Virtual Screening, ADMET Predictions, and Molecular Interaction Field Studies to Design Novel Potential MAO-B Inhibitors. *J. Biomol. Struct. Dyn.* **2008**, *254*, 347–355.

(217) La Regina, G.; Silvestri, R.; Artico, M.; Lavecchia, A.; Novellino, E.; Befani, O.; Turini, P.; Agostinelli, E. New Pyrrole Inhibitors of Monoamine Oxidase: Synthesis, Biological Evaluation, and Structural Determinants of MAO-A and MAO-B Selectivity. *J. Med. Chem.* **2007**, *50*, 922–931.

(218) Maccioni, E.; Alcaro, S.; Cirilli, R.; Vigo, S.; Cardia, M. C.; Sanna, M. L.; Meleddu, R.; Yanez, M.; Costa, G.; Casu, L.; Matyus, P.; Distinto, S. 3-Acetyl-2,5-Diaryl-2,3-Dihydro-1,3,4-Oxadiazoles: A New Scaffold for the Selective Inhibition of Monoamine Oxidase B. *J. Med. Chem.* **2011**, *54*, 6394–6398.

(219) Chimenti, F.; Maccioni, E.; Secci, D.; Bolasco, A.; Chimenti, P.; Granese, A.; Befani, O.; Turini, P.; Alcaro, S.; Ortuso, F.; Cirilli, R.; Torre, F. La; Cardia, M. C.; Distinto, S.

Synthesis, Molecular Modeling Studies, and Selective Inhibitory Activity against Monoamine Oxidase of 1-Thiocarbamoyl-3,5-Diaryl-4,5-Dihydro-(1H)- Pyrazole Derivatives. *J. Med. Chem.* **2005**, *48*, 7113–7122.

(220) Fowler, P. W.; Balali-Mood, K.; Deol, S.; Coveney, P. V.; Sansom, M. S. P. Monotopic Enzymes and Lipid Bilayers: A Comparative Study. *Biochemistry* **2007**, *46*, 3108–3115.

(221) Perkins, D. N.; Pappin, D. J. C.; Creasy, D. M.; Cottrell, J. S. Probability-Based Protein Identification by Searching Sequence Databases Using Mass Spectrometry Data. *Electrophoresis* **1999**, *20*, 3551–3567.

(222) Kao, Y. T.; Saxena, C.; He, T. F.; Guo, L.; Wang, L.; Sancar, A.; Zhong, D. Ultrafast Dynamics of Flavins in Five Redox States. *J. Am. Chem. Soc.* **2008**, *130*, 13132–13139.

(223) Woo, J. C. G.; Silverman, R. B. Observation of Two Different Chromophores in the Resting State of Monoamine Oxidase B by Fluorescence Spectroscopy. *Biochem. Biophys. Res. Commun.* **1994**, *202*, 1574–1578.

(224) Candeias, L. P.; Turconi, S.; Nugent, J. H. A. Tyrosine Y(Z) and Y(D) of Photosystem II Comparison of Optical Spectra to Those of Tyrosine Oxidised by Pulsed Radiolysis. *Biochim. Biophys. Acta - Bioenerg.* **1998**, *1363*, 1–5.

(225) Geha, R. M.; Chen, K.; Wouters, J.; Ooms, F.; Shih, J. C. Analysis of Conserved Active Site Residues in Monoamine Oxidase A and B and Their Three-Dimensional Molecular Modeling. *J. Biol. Chem.* **2002**, *277*, 17209–17216.

(226) Aubert, C.; Brettel, K.; Mathis, P.; Eker, A. P. M.; Boussac, A. EPR Detection of the Transient Tyrosyl Radical in DNA Photolyase from *Anacystis Nidulans*. *J. Am. Chem. Soc.* **1999**, *121*, 8659–8660.

(227) Okafuji, A.; Schnegg, A.; Schleicher, E.; Möbius, K.; Weber, S. G-Tensors of the Flavin Adenine Dinucleotide Radicals in Glucose Oxidase: A Comparative Multifrequency Electron Paramagnetic Resonance and Electron−Nuclear Double Resonance Study. *J. Phys. Chem. B* **2008**, *112*, 3568–3574.

(228) McDowall, J. S.; Ntai, I.; Hake, J.; Whitley, P. R.; Mason, J. M.; Pudney, C. R.; Brown, D. R. Steady-State Kinetics of α-Synuclein Ferrireductase Activity Identifies the Catalytically Competent Species. *Biochemistry* **2017**, *56*, 2497–2505.

(229) Weyler, W.; Salach, J. I. Purification and Properties of Mitochondrial Monoamine Oxidase Type A from Human Placenta. *J. Biol. Chem.* **1985**, *260*, 13199–13207.

(230) Jones, H. B. L.; Crean, R. M.; Matthews, C.; Troya, A. B.; Danson, M. J.; Bull, S. D.; Arcus, V. L.; van der Kamp, M. W.; Pudney, C. R. Uncovering the Relationship between the Change in Heat Capacity for Enzyme Catalysis and Vibrational Frequency through Isotope Effect Studies. *ACS Catal.* **2018**, *8*, 5340–5349.

(231) van Meer, G.; Voelker, D. R.; Feigenson, G. W. Membrane Lipids: Where They Are and How They Behave. *Nat. Rev. Mol. Cell Biol.* **2008**, *9*, 112–124.

(232) Pavelka, A.; Sebestova, E.; Kozlikova, B.; Brezovsky, J.; Sochor, J.; Damborsky, J. CAVER: Algorithms for Analyzing Dynamics of Tunnels in Macromolecules. *IEEE/ACM Trans. Comput. Biol. Bioinforma.* **2016**, *13*, 505–517.

(233) Kingsley, L. J.; Lill, M. A. Including Ligand-Induced Protein Flexibility into Protein

Tunnel Prediction. *J. Comput. Chem.* **2014**, *35*, 1748–1756.

(234) Biedermannová, L.; Prokop, Z.; Gora, A.; Chovancová, E.; Kovács, M.; Damborský, J.; Wade, R. C. A Single Mutation in a Tunnel to the Active Site Changes the Mechanism and Kinetics of Product Release in Haloalkane Dehalogenase LinB. *J. Biol. Chem.* **2012**, *287*, 29062–29074.

(235) Zapata-Torres, G.; Fierro, A.; Miranda-Rojas, S.; Guajardo, C.; Saez-Briones, P.; Salgado, J. C.; Celis-Barros, C. Influence of Protonation on Substrate and Inhibitor Interactions at the Active Site of Human Monoamine Oxidase-A. *J. Chem. Inf. Model.* **2012**, *52*, 1213–1221.

(236) Tabbutt, F. Water: A Matrix of Life, 2nd Edition (Franks, Felix). *J. Chem. Educ.* **2001**, *78*, 593.

(237) Bonivento, D.; Milczek, E. M.; McDonald, G. R.; Binda, C.; Holt, A.; Edmondson, D. E.; Mattevi, A. Potentiation of Ligand Binding through Cooperative Effects in Monoamine Oxidase B. *J. Biol. Chem.* **2010**, *285*, 36849–36856.

(238) Oleinikovas, V.; Saladino, G.; Cossins, B. P.; Gervasio, F. L. Understanding Cryptic Pocket Formation in Protein Targets by Enhanced Sampling Simulations. *J. Am. Chem. Soc.* **2016**, *138*, 14257–14263.

(239) Beglov, D.; Hall, D. R.; Wakefield, A. E.; Luo, L.; Allen, K. N.; Kozakov, D.; Whitty, A.; Vajda, S. Exploring the Structural Origins of Cryptic Sites on Proteins. *Proc. Natl. Acad. Sci. U. S. A.* **2018**, *115*, 3416–3425.

(240) Evans, E. W.; Dodson, C. A.; Maeda, K.; Biskup, T.; Wedge, C. J.; Timme, C. R. Magnetic Field Effects in Flavoproteins and Related Systems. *Interface Focus* **2013**, *3*.

(241) Stoll, S.; Schweiger, A. EasySpin, a Comprehensive Software Package for Spectral Simulation and Analysis in EPR. *J. Magn. Reson.* **2006**, *178*, 42–55.

(242) Binda, C.; Hubálek, F.; Li, M.; Herzig, Y.; Sterling, J.; Edmondson, D. E.; Mattevi, A. Crystal Structures of Monoamine Oxidase B in Complex with Four Inhibitors of the N-Propargylaminoindan Class. *J. Med. Chem.* **2004**, *47*, 1767–1774.

(243) Hanwell, M. D.; Curtis, D. E.; Lonie, D. C.; Vandermeersch, T.; Zurek, E.; Hutchison, G. R. Avogadro: An Advanced Semantic Chemical Editor, Visualization, and Analysis Platform. *J. Cheminform.* **2012**, *4*, 17.

(244) Wu, E. L.; Cheng, X.; Jo, S.; Rui, H.; Song, K. C.; Dávila-Contreras, E. M.; Qi, Y.; Lee, J.; Monje-Galvan, V.; Venable, R. M.; Klauda, J. B.; Im, W. CHARMM-GUI *Membrane Builder* toward Realistic Biological Membrane Simulations. *J. Comput. Chem.* **2014**, *35*, 1997–2004.

(245) Li, M.; Binda, C.; Mattevi, A.; Edmondson, D. E. Functional Role of The "aromatic Cage" in Human Monoamine Oxidase B: Structures and Catalytic Properties of Tyr435 Mutant Proteins. *Biochemistry* **2006**, *45*, 4775–4784.

(246) Edmondson, D. E.; Binda, C.; Wang, J.; Upadhyay, A. K.; Mattevi, A. Molecular and Mechanistic Properties of the Membrane-Bound Mitochondrial Monoamine Oxidases. *Biochemistry* **2009**, *48*, 4220–4230.

(247) Chen, V. B.; Arendall, W. B.; Headd, J. J.; Keedy, D. A.; Immormino, R. M.; Kapral, G. J.; Murray, L. W.; Richardson, J. S.; Richardson, D. C. *MolProbity* : All-Atom Structure

Validation for Macromolecular Crystallography. *Acta Crystallogr. Sect. D Biol. Crystallogr.* **2010**, *66*, 12–21.

(248) Best, R. B.; Zhu, X.; Shim, J.; Lopes, P. E. M.; Mittal, J.; Feig, M.; MacKerell, A. D. Optimization of the Additive CHARMM All-Atom Protein Force Field Targeting Improved Sampling of the Backbone Φ, ψ and Side-Chain χ1and χ2Dihedral Angles. *J. Chem. Theory Comput.* **2012**, *8*, 3257–3273.

(249) Klauda, J. B.; Venable, R. M.; Freites, J. A.; O'Connor, J. W.; Tobias, D. J.; Mondragon-Ramirez, C.; Vorobyov, I.; MacKerell, A. D.; Pastor, R. W. Update of the CHARMM All-Atom Additive Force Field for Lipids: Validation on Six Lipid Types. *J. Phys. Chem. B* **2010**, *114*, 7830–7843.

(250) Darden, T.; York, D.; Pedersen, L. Particle Mesh Ewald: An $N \cdot \log(N)$ Method for Ewald Sums in Large Systems. *J. Chem. Phys.* **1993**, *98*, 10089–10092.

(251) Roe, D. R.; Cheatham, T. E. PTRAJ and CPPTRAJ: Software for Processing and Analysis of Molecular Dynamics Trajectory Data. *J. Chem. Theory Comput.* **2013**, *9*, 3084–3095.

(252) Allen, W. J.; Lemkul, J. A.; Bevan, D. R. GridMAT-MD: A Grid-Based Membrane Analysis Tool for Use with Molecular Dynamics. *J. Comput. Chem.* **2009**, *30*, 1952–1958.

(253) DeLano W.L. *PyMol Molecular Graphics System*; 2002.

(254) van der Kamp, M. W.; Daggett, V. Influence of pH on the Human Prion Protein: Insights into the Early Steps of Misfolding. *Biophys. J.* **2010**, *99*, 2289–2298.

(255) Ester, M.; Kriegel, H.-P.; Sander, J.; Xu, X. A Density-Based Algorithm for Discovering Clusters in Large Spatial Databases with Noise. *Data Min Knowl Discov* **1996**, *90*, 226–231.

(256) Li, M.; Binda, C.; Mattevi, A.; Edmondson, D. E. Functional Role of The "aromatic Cage" in Human Monoamine Oxidase B: Structures and Catalytic Properties of Tyr435 Mutant Proteins. *Biochemistry* **2006**, *45*, 4775–4784.

(257) Wu, H. F.; Chen, K.; Shih, J. C. Site-Directed Mutagenesis of Monoamine Oxidase A and B: Role of Cysteines. *Mol. Pharmacol.* **1993**, *43*, 888–893.

(258) Cesura, A. M.; Gottowik, J.; Lahm, H.-W.; Lang, G.; Imhof, R.; Malherbe, P.; Rothlisberger, U.; Prada, M. Da. Investigation on the Structure of the Active Site of Monoamine Oxidase-B by Affinity Labeling with the Selective Inhibitor Lazabemide and by Site-Directed Mutagenesis. *Eur. J. Biochem.* **1996**, *236*, 996–1002.

(259) Zhou, B. P.; Wu, B.; Kwan, S.-W.; Abell, C. W. Characterization of a Highly Conserved FAD-Binding Site in Human Monoamine Oxidase B. *J. Biol. Chem.* **1998**, *273*, 14862–14868.

(260) Klinman, J. P.; Kohen, A.; Cannio, R.; Bartolucci, S.; Klinman, J. P. Enzyme Dynamics and Hydrogen Tunnelling in a Thermophilic Alcohol Dehydrogenase. *Nature* **1999**, *399*, 496–499.

(261) di Rigano, V. M.; Vona, V.; Lobosco, O.; Carillo, P.; Lunn, J. E.; Carfagna, S.; Esposito, S.; Caiazzo, M.; Rigano, C. Temperature Dependence of Nitrate Reductase in the Psychrophilic Unicellular Alga Koliella Antarctica and the Mesophilic Alga Chlorella Sorokiniana. *Plant. Cell Environ.* **2006**, *29*, 1400–1409.

(262) Firestone, R. S.; Cameron, S. A.; Karp, J. M.; Arcus, V. L.; Schramm, V. L. Heat Capacity Changes for Transition-State Analogue Binding and Catalysis with Human 5'-Methylthioadenosine Phosphorylase. *ACS Chem. Biol.* **2017**, *12*, 464–473.

(263) Choi, J.-M.; Han, S.-S.; Kim, H.-S. Industrial Applications of Enzyme Biocatalysis: Current Status and Future Aspects. *Biotechnol. Adv.* **2015**, *33*, 1443–1454.